

The Role of Compositional and Configurational Disorder on Thermal Conductivity

A Dissertation Presented to the
Faculty of the School of Engineering and Applied Science
University of Virginia

In Partial Fulfillment
of the Requirements for the Degree of
Doctor of Philosophy
Mechanical and Aerospace Engineering

Jeffrey L. Braun
May 2019

APPROVAL SHEET

The dissertation is submitted in partial fulfillment of the
requirements for the degree of

Doctor of Philosophy in Mechanical and Aerospace Engineering

Jeffrey L. Braun, *Author*

This dissertation has been read and approved by the Examining Committee:

Prof. Pamela M. Norris, *Chair*

Prof. Patrick E. Hopkins, *Advisor*

Prof. Keivan Esfarjani

Prof. Jon F. Ihlefeld

Dr. Sean W. King

Accepted for the School of Engineering and Applied Science:

Craig H. Benson, Dean
School of Engineering and Applied Science

May 2019

Abstract

The rapid advancements in modern technology have largely been driven by the miniaturization of devices and improvements in materials engineering at the nanoscale. The intentional introduction of atomic-scale compositional disorder through doping and alloying has enabled a direct process to tune electrical and mechanical properties of materials. Furthermore, random solid solutions and high-entropy materials have demonstrated that the random configuration of atoms, configurational disorder, can lead to enhanced mechanical properties and improved thermodynamic stability. From a thermal transport perspective, compositional and configurational disorder at the atomic scale can significantly limit the ability for electrons and phonons to carry heat, resulting in a reduced thermal conductivity. While significant advances have been made in modeling the thermal conductivity of crystals, disorder beyond simple perturbations, especially in the case of amorphous solids which lack atomic periodicity, proves challenging to capture within the framework of these models, motivating the need for experimental study. Advancing the understanding of how disorder affects thermal conductivity under a common framework, this dissertation fills the void of current understanding in highly configurationally disordered crystals as well as compositionally disordered amorphous thin films.

Three experimental techniques are used to measure thermal properties of materials: time-domain thermoreflectance, frequency-domain thermoreflectance, and a newly developed steady-state thermoreflectance. These non-contact, optical pump-probe techniques ensure the capability to measure both thin films and bulk materials. After establishing the advances made in these experiments, this dissertation reports the thermal conductivity of configurationally disordered thin film entropy-stabilized oxides to demonstrate that the thermal conductivity decreases with increasing configurational entropy. Probing the local structure of these materials reveals that local ionic charge disorder enables amorphous-like thermal properties in these crystalline materials without diminishing elastic properties. Next, four new classes of bulk high-entropy ceramics – high-entropy oxides, carbides, borides, and silicides – are investigated to show that high configurational entropy again reduces the thermal conductivity of these materials relative to their constituent components. Using a thermal conductivity imaging technique, it is shown that grain boundaries and secondary phases can further reduce the local thermal conductivity. Finally, thermal transport in amorphous thin films is investigated. It is shown that film thickness can limit the thermal conductivity of amorphous silicon to reveal that propagating vibrational modes can significantly contribute to the thermal transport, an attribute typically associated with crystalline solids. The introduction of compositional disorder in amorphous solids is studied through hydrogenated amorphous silicon nitride to reveal that the atomic bond coordination dictates thermal conductivity and suggests a means for tuning thermal conductivity through hydrogenation and thermal annealing.

By considering the extreme cases of configurational, compositional, and structural disorder, this dissertation provides evidence that crystalline materials can behave thermally as if amorphous, while amorphous films can possess crystalline-like thermal properties. Taken together, this suggests a common framework of how disorder affects the thermal conductivity in all materials.

Acknowledgements

Coming soon...

Contents

1	Introduction	1
1.1	Applications	5
1.2	Statement of Objectives and Scope	9
2	Theory of Thermal Conductivity	12
2.1	Crystals	15
2.1.1	Phonon Dispersion	16
2.1.2	Phonon Density of States and Occupation	18
2.1.3	Phonon Heat Capacity	19
2.1.4	Phonon Thermal Conductivity	21
2.2	Amorphous Solids	26
2.2.1	Minimum Limit to Thermal Conductivity	27
2.2.2	Locons, Diffusons, and Propagons	30
3	Time- and Frequency-Domain Thermoreflectance	32
3.1	Background	33
3.2	Experimental Details	35
3.3	Core Concepts	38
3.4	Mathematical Formalism	42
3.4.1	Pump Heating	42
3.4.2	Probe Detection and Signal Analysis	52
3.4.3	Post Processing	59
3.5	Thermal Penetration Depth	61
3.6	Steady-State Temperature Rise	69
3.6.1	Experimental Case Study: Au on a-SiO ₂	77
3.6.2	Consideration of Optical Absorption Depth	81
3.7	Model Limitations	83
3.8	Summary	85
4	Steady-State Thermoreflectance	86
4.1	Background	86
4.2	Principles of Operation	89
4.3	Theory	90
4.3.1	Transient Temperature Rise	90
4.3.2	Quasi Steady-State via a Sine Wave Heat Source	92

4.4	Experimental Details	94
4.5	Signal Analysis	97
4.5.1	Periodic Waveform Analyzer / Boxcar Averager	98
4.5.2	Lock-in Amplifier	100
4.5.3	Parameter Sensitivity	102
4.6	Results and Discussion	105
4.7	Sources of Uncertainty	107
4.8	Thin Film Measurement Sensitivity	108
4.9	Summary	109
5	Entropy-Stabilized Oxides	111
5.1	Motivation	111
5.2	Experimental Details	113
5.3	Results and Discussion	115
5.4	Summary	125
6	High-Entropy Ceramics	126
6.1	Motivation	127
6.2	High-Entropy Fluorite Oxides	128
6.3	High-Entropy Carbides	131
6.4	High-Entropy Borides	139
6.5	High-Entropy Silicides	145
6.6	Summary	147
7	Amorphous Thin Films	148
7.1	Amorphous Silicon: Size Effects on Thermal Conductivity	148
7.1.1	Background	148
7.1.2	Experimental Details	152
7.1.3	Thin Film Analysis	153
7.1.4	Results and Discussion	155
7.2	Amorphous Hydrogenated Silicon Nitride: Composition Effects on Thermal Conductivity	159
7.2.1	Background	159
7.2.2	Experimental Details	163
7.2.3	Results and Discussion	165
7.3	Summary	173
8	Summary and Future Projects	175
8.1	Summary	176
8.2	Opportunities for Future Investigation	178
A	Transient Temperature Rise in SSTR	180
B	Published Work	183

List of Figures

1.1	Types of disorder in solid-state materials	3
2.1	Dispersion relation for 1-D atomic chain	16
2.2	Phonon dispersion relations for MgO and NiO	18
2.3	Heat capacities vs. temperature for MgO and NiO	20
2.4	Phonon scattering mechanisms in crystals	22
2.5	Thermal conductivity of MgO and NiO	24
2.6	Einstein and Cahill-Pohl models applied to MgO	29
3.1	TDTR schematic	36
3.2	Temperature rises in TDTR and FDTR	39
3.3	Phase lag FDTR	40
3.4	Lock-in amplification process	41
3.5	Sample schematic	43
3.6	Total, AC, and DC temperature rises	53
3.7	Unmodulated, CW spatial temperature rise	63
3.8	Unmodulated, pulsed spatial temperature rise	64
3.9	Effect of pulse repetition rate on TPD	65
3.10	Modulated temperature rise in a-SiO ₂	67
3.11	TPD theory vs. calculation	68
3.12	Modulated and steady-state temperature profiles in a-SiO ₂	72
3.13	Steady-state radial temperature distribution	74
3.14	Transducer effect on steady-state temperature rise	75
3.15	Transducer effect on steady-state heat flux	76
3.16	Sensitivity to thermal parameters for 65 nm Au on a-SiO ₂	78
3.17	Experimental thermal conductivities for 65 nm Au on a-SiO ₂	80
3.18	Effect of optical penetration depth on steady-state temperature rise	82
4.1	Transient temperature Rise to laser heating	90
4.2	Normalized temperature rise vs. modulation frequency	93
4.3	Schematic of the two-color SSTR experiment	94
4.4	Pump periodic waveform analysis	99
4.5	Probe periodic waveform analysis	100
4.6	Lockin Amplifier Analysis	101
4.7	Model sensitivity to parameters	102

4.8 Thermal conductivity vs. thermal boundary conductance	103
4.9 Measured thermal conductivity vs. literature thermal conductivity	105
4.10 Sensitivity to thin film thermal conductivity	108
5.1 Structural and thermal characterization of ESOs	113
5.2 Thermal and elastic properties of crystals	117
5.3 ESO thermal conductivity vs. temperature	120
5.4 Local structure determination from EXAFS	123
5.5 Modified local structure	124
6.1 Thermal conductivity of high-entropy fluorite oxides	130
6.2 Thermal conductivity and heat capacity of high-entropy carbides	133
6.3 HEC thermal conductivity vs. valence electron concentration	135
6.4 SEM and TDTR images for HEC3	136
6.5 Thermal conductivity map of HEC3	138
6.6 SEM and TDTR images for HEB	140
6.7 Thermal conductivity map of HEB	141
6.8 High Resolution Thermal Image of HEB1 with 50 \times objective	142
6.9 Deconvolution of thermal conductivity image with grain and phase	144
6.10 Thermal conductivity of high-entropy silicide	146
7.1 Literature thermal conductivity vs. thickness of amorphous silicon	151
7.2 Measured thermal conductivity vs. thickness of amorphous silicon	154
7.3 Model for propagon thermal conductivity with experimental data	157
7.4 Literature thermal conductivity vs. thickness for amorphous silicon nitride	161
7.5 Measured thermal conductivity vs. thickness	165
7.6 Thermal conductivity vs. annealing temperature for a-SiN:H	168
7.7 a-SiN:H thermal conductivity dependence on composition	169
7.8 FTIR spectrum for annealed a-SiN:H	170

List of Tables

2.1	Fitting parameters for MgO and NiO	23
3.1	Input parameters to models	54
4.1	Thermal conductivities measured with SSTR	104
5.1	Thermal and physical properties of ESOs at room temperature	115
5.2	VCA model parameters	119
5.3	EXAFS fitting parameters	122
6.1	Thermal and mechanical properties of high-entropy fluorite oxides	129
6.2	Thermal properties of high-entropy carbides	132
7.1	Properties of annealed a-SiN _x :H samples	167

Chapter 1

Introduction

The science and engineering progress fueling the recent nanotechnology boom have enabled revolutionary advances in fields ranging from information and medicine, to energy technology. Development of bottom-up synthesis methods have pushed the lower limits of feature size to enable the fabrication of nanoscale and atomic scale particles, wires, and films [1]. As these length scales diminish to the order of those of fundamental energy carriers, continuum-based models to describe transport phenomena and material properties break down, necessitating a quantum-based description to precisely describe material behavior [2]. This is particularly true in the field of thermal transport and energy conversion, where the macroscopic descriptor of thermal transport, a material's thermal conductivity, can be significantly influenced by sample dimension and atomic-scale features. Therefore, as technologies develop and devices become smaller, a fundamental understanding of nanoscale thermal transport becomes increasingly important for thermal management [3].

The field of nanoscale thermal transport is rooted in understanding how energy carriers interact on the nanoscale to dictate macroscopic transport properties. From this understanding, we can then engineer materials to obtain more desirable thermal properties for specific applications. Thermal conductivity is the quantity that defines a material's ability to carry heat. From a macroscopic perspective, the thermal conductivity relates the heat flux to the temperature gradient. On the nanoscale it defines the net power carried per unit distance per unit temperature that an ensemble

of individual particles (or waves) carry. These energy carriers include any such particle that can transport energy, but in most solids are limited to electrons and phonons (quantized lattice vibrations). Furthermore, phonons are generally the overwhelmingly dominant carrier in nonmetals. While great strides have been made in predicting the thermal conductivity of perfect crystals and small variations thereof using first principals [4, 5], very rarely do materials fall into this paragon. Deviation from a perfect crystal, i.e. disorder, proves to play a critical role in reducing thermal conductivity.

We can define disorder as the breaking of translational symmetry within a crystal. From this definition, it follows that disorder exists within all materials, as even geometric boundaries break translational symmetry. Indeed, Haas and Biermasz first reported that the finite nature of the samples they measured limited the observed thermal conductivity. They noted that the thermal conductivities of bulk quartz [6], KCl, and KBr [7] reach a maximum (Umklapp peak) near 10 K and have decreasing trend with temperature thereafter. Casimir later generalized these findings to demonstrate that this result was due to long-wavelength phonons reflecting from the sample boundaries when their propagation length becomes comparable to the sample dimensions at very low temperatures [8]; this condition is now known as the Casimir limit.

Beyond these cryogenic temperatures, this spatial confinement effect on thermal conductivity seemingly becomes insignificant. However, the extent to which any disorder affects thermal conductivity is determined based on the relative length scales of this disorder as compared to the characteristic length scales of the heat carriers. For example, in bulk silicon, the thermal conductivity at room temperature is not affected by geometric boundaries since the phonon mean free paths carrying heat are generally limited to below 10 microns [9]. By contrast, both silicon nanowires [10] and silicon thin films [11] exhibit a strong reduction in thermal conductivity with reduced characteristic length.

Beyond physical boundaries, disorder can manifest itself in isotopic impurities, compositional and chemical impurities, and lattice imperfections to include dislocations, point defects, and grain boundaries. These concepts are summarized in Fig. 1.1, showing how deviation from an ideal crystal can be driven by both structural or compositional disorder. The limit of structural disorder is

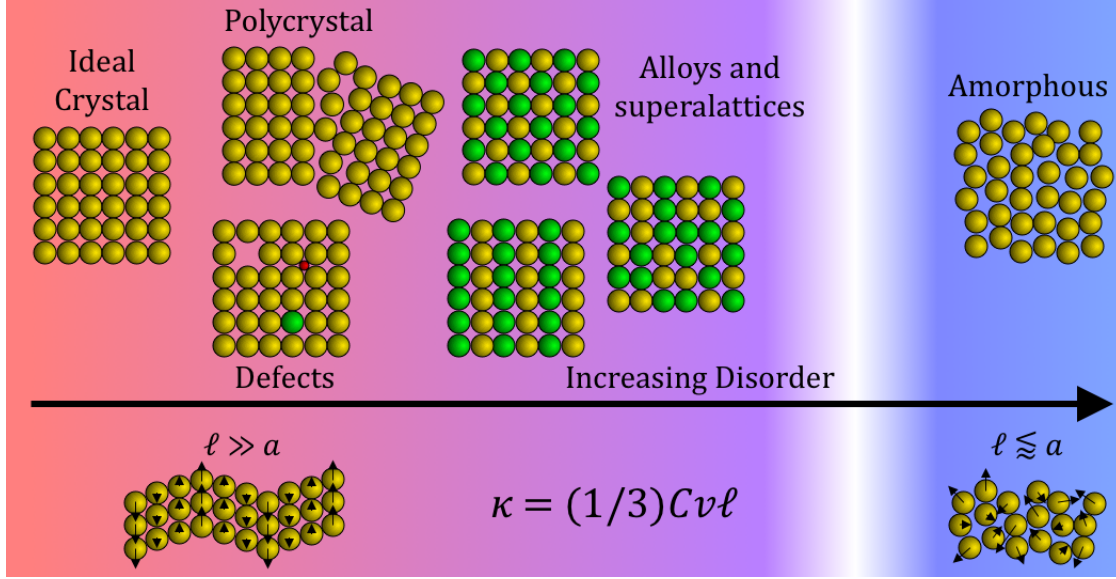


Figure 1.1: Representation of various types of disorder for crystalline solids. Disorder can include any deviation from an ideal crystal; examples shown include defects, polycrystals, alloys and superlattices, and the limit of solid-state structural disorder – the amorphous phase. The vibrational thermal conductivity is described by Eq. (1.1); for crystals ℓ is, on average, much greater than the interatomic spacing, a . As disorder increases, $\ell \rightarrow a$ so that for amorphous solids, however, ℓ can be equivalent to or smaller than a .

the amorphous phase of the material, where no long-range periodicity exists in the atomic arrangement. Current understanding of thermal conductivity on the nanoscale comes from kinetic theory, treating energy carriers as particles. In its simplest form, the microscopic definition of thermal conductivity (κ) is

$$\kappa = \frac{1}{3} C_v v \ell = \frac{1}{3} C_v v^2 \tau \quad (1.1)$$

where C_v is the specific heat capacity per unit volume (the amount of energy the heat carrier can hold), v is the velocity of the heat carrier, ℓ is the mean free path (the average distance the carrier travels before scattering with another carrier), and τ is the relaxation time of the carrier (the average time it takes before the carrier scatters). Because this dissertation is focused primarily on materials having phonon-dominated thermal transport, we consider only the phonon thermal conductivity. In an ideal crystal, intrinsic phonon-phonon scattering is known to dominate the mean-free path (relaxation time) to dictate thermal conductivity. Small perturbations from this ideal crystal have

a known affect on τ , so that κ can be modeled with reasonably accurate predictive power. Even binary and ternary alloys have well-defined frameworks for predicting thermal conductivity [12]. However, as disorder becomes large these theories break down. In fact, in highly disordered solids, phonon mean free paths can be reduced so much that the materials behave thermally as if they are amorphous [13]. In this transition region, shown in white in Fig. 1.1, the mechanisms dictating thermal transport are unknown. The goal of this dissertation is to determine how structural and compositional disorder in this regime can influence phonon relaxation times to reduce thermal conductivity. To do so, the research presented here will focus on configurationally disordered solid solutions to include entropy stabilized oxides, as well as high-entropy carbides, borides, and silicides. Comparing experimental results with analytical and computational models, we can elucidate the mechanisms of thermal transport in these highly disordered crystals.

Using these disordered crystals, we can approach this transition regime from the crystalline side. Another way to approach this regime is from the amorphous side. In semiconductor devices and applications, amorphous materials play critical roles in electrical and thermal insulation. Amorphous solids are used for electrophotography [14], sensors [15], and are ubiquitous in photovoltaic (PV) solar cells, gate dielectrics, thermoelectric (TE) devices, solid-state non-volatile phase change memory (PCM), memristors, and displays [16]. Because material properties dictating device performance are highly dependent on operating temperature, a thorough understanding of thermal transport in amorphous materials is necessary for thermal management. However, a fundamental understanding of thermal transport in amorphous materials has remained underdeveloped, particularly when compared with the development of predictive models governing thermal transport in crystalline materials from first principals [4, 5].

Perhaps Freeman and Anderson said it best: “It is emphasized that the thermal conductivity of an amorphous solid is not understood in any temperature range” [17]. While this remains true, great strides have been made in modeling and physical understanding of thermal transport in amorphous solids. From an atomic-level picture first proposed by Einstein, thermal transport in amorphous dielectrics has largely been understood as a random walk of energy in which atoms vibrate as uncorrelated oscillators with random phases, transferring energy to one another elastically. In this

framework, vibrational mean free paths are intrinsically on the order of the interatomic spacing. Although originally developed to describe thermal transport in crystals, this concept was eventually adopted to successfully describe the temperature-dependent thermal conductivity of amorphous materials and glasses above the plateau [18]. Slack [19] and later Cahill and Pohl [20] refined this idea to establish the “minimum limit” to thermal conductivity by adopting the ideas of Debye to include coupled oscillators as opposed to the single uncorrelated oscillators considered by Einstein. Still, this physical picture preserves the core idea that localized oscillators (now having a range of frequencies) transfer energy in a random walk, having lifetimes of half a period of oscillation and preserving the notion that the dominant energy transport is between nearest neighbors. While this physical picture has been adopted with much success, experimental and computational results regarding the dominating nature of propagating modes on thermal transport in certain amorphous materials, most notably amorphous silicon (a-Si) [21–24], have raised questions about the validity of this random walk theory and about the physical origins of these heat carrying propagating modes. Thus, we will approach this transition regime in Fig. 1.1 from the amorphous side by studying amorphous silicon and silicon nitride to reveal how propagating, phonon-like, modes can arise to give these materials crystalline-like thermal conductivity characteristics.

1.1 Applications

While the fundamental understanding of how disorder affects thermal transport is the focus of this dissertation, this research is further motivated by several application areas where engineering disorder into systems can be used to create better thermally-insulating materials to improve performance. Below are four such applications where this dissertation research can have a direct impact in manufacturing devices with improved performances.

Thermoelectric Devices

Thermoelectric devices convert heat into electricity and vice-versa [25]. A thermoelectric generator is a solid-state device that converts a temperature difference directly to electrical voltage via

the Seebeck effect. Thermoelectric refrigerators work in reverse, converting electrical current into a heat flux via the Peltier effect to cool one side of the device. In either application, the efficiency of the device is based on the thermoelectric properties of the active materials comprising the device. The efficiency can be quantified by the thermoelectric figure of merit, Z , defined as [26]

$$Z = \frac{\sigma S^2}{\kappa}, \quad (1.2)$$

where σ is electrical conductivity and S is the Seebeck coefficient. The Seebeck coefficient defines the proportionality constant between the generated voltage and thermal gradient, having units of [V/K]. Z has units of [1/K], so that often the dimensionless figure of merit, ZT is used instead; thermoelectric efficiency is increased by making ZT as large as possible. We see that the ZT is inversely proportional to κ , which occurs because the thermoelectric elements act as the thermal insulation between hot and cold sides [27]. Thus, decreasing κ increases the temperature gradient and by extension the generated voltage. Metals have relatively low Seebeck coefficients and electron-dominated thermal conductivities, as dictated by the Wiedmann-Franz law; as a result, semiconductors are generally targeted for thermoelectric devices [28, 29]. While the thermal conductivity of semiconductors has contributions from both electrons and phonons, in general the phonon contribution is much larger. Therefore, a major avenue of research has been to engineer materials with reduced phonon thermal conductivities; this reduction is achieved through the introduction of disorder in ways that reduce κ without significantly altering σ and S .

Various types of disorder have been engineered into materials to reduce the thermal conductivity. One approach that has been proven successful is alloying, which was shown in 1958 to achieve a ZT of 0.75 in p-type $\text{Bi}_x\text{Sb}_{2-x}\text{Te}_3$ ($x \approx 1$) near room temperature [30]. Only incremental progress has been made in enhancing ZT since then – the best bulk materials today only have ZT values of around 1, equivalent to about 10% Carnot efficiency in refrigeration [25]. To compete with conventional home refrigeration, this ZT needs to be over 4, equating to a Carnot efficiency of 30% [25]. These low efficiencies have limited the use of TE devices to niche applications, such as cooling laser diodes. The introduction of interfaces in thin films, i.e., the use of superlattices, has also proven to be effective [31]. In fact, the highest room temperature ZT reported comes from

p-type $\text{Bi}_2\text{Te}_3/\text{Sb}_2\text{Te}_3$ superlattices, having $ZT = 2.4$ [32]. This extreme jump in ZT compared to predecessors represents optimism for thermoelectric devices and makes clear the benefits of engineering disorder into thermoelectric materials for improving performance. Understanding the limits of this disorder on thermal conductivity, therefore, will be valuable towards thermoelectric materials research.

Thermal Barrier Coatings

A large application area for disordered and amorphous solids is in thermal insulation, where low thermal conductivity coatings are needed to insulate critical device components. A primary example of this is thermal barrier coatings (TBCs). Gas turbines need to operate at as high temperature as possible to maximize their efficiency [33]. While typical metal components have melting temperatures within the range of desired operating temperatures, coating these components with a protective film can shield them from such temperatures; TBCs do just that [34]. TBCs are multi-functional films having thicknesses ranging from $100 \mu\text{m}$ to 2 mm [35, 36]. Typically made of a refractory material, they serve to protect the metal components of a gas turbine from the extreme temperatures in the gas [33]. This is achieved by inducing a large temperature drop within the TBC when exposed to a heat flux so that the temperature at the TBC-metal interface is low enough to avoid damage [37]. This temperature drop is entirely dictated by the TBC thermal conductivity.

To not only reduce thermal conductivity, but also to improve strain tolerance to mitigate stresses due to the thermal-expansion mismatch between the metal and TBC [38], defects are deliberately engineered into these materials [39]. For example, the most common material used for TBC applications is yttria-stabilized zirconia (YSZ) [39]. YSZ has very low thermal conductivity of $3 \text{ W m}^{-1} \text{ K}^{-1}$ at typical operating temperatures [39, 40]. This is achieved by taking an already highly thermally insulating ceramic, ZrO_2 , and heavily doping it with Y_2O_3 . The result is a nearly amorphous-like thermal conductivity relation with temperature [41]. Building off the success of YSZ, understanding the implications of various other types of disorder, including high entropy, on thermal conductivity can offer new avenues towards developing novel TBCs.

Phase-Change Memory Devices

In an endless pursuit to reach smaller dimensions to comply with Moore’s law [42], phase-change memory (PCM) has emerged as a promising non-volatile random access memory due to its higher memory capacity and integration density than dynamic random-access memory (DRAM) [43, 44]. PCM exploits the large resistance contrast between the amorphous and crystalline phases of a phase-change material [45]. Whereas the crystalline state generally exhibits low electrical resistivity, the amorphous phase typically exhibits high resistivity, often three or four orders of magnitude higher [46]. Although the difference is not as stark in most cases, the same general relation holds true with the thermal resistivity [13]. The reversible electrical switching that occurs between these states was shown by Ovshinsky in 1968 [47], but strong interest in its application to memory did not come until the discovery of fast-switching materials such as $\text{Ge}_2\text{Sb}_2\text{Te}_5$ (GST) [48], which have crystallization times < 100 ns.

PCM works via induction of a phase-change to alter states between high and low resistance. To achieve a low resistance (crystalline) state, an electrical pulse is used to heat a large portion of the memory cell above the crystallization temperature of the phase change material to induce a crystalline phase transition. To return to the high resistance (amorphous) state, called the reset operation [46], a larger electrical pulse is applied to melt the phase-change material, followed by an abrupt end to the pulse to rapidly quench the material so that it stays in the amorphous phase. The state of resistance determines the bit state of the material (0 or 1), and is read by applying a small voltage not large enough to induce a phase-transition. Because PCM relies on rapid heating and cooling of these materials, understanding the thermal conductivity is critical to determining the optimal operating conditions of the PCM device. In particular, because the amorphous-to-crystalline phase change needs to occur within specific temperature range (high enough for crystallization but low enough not to melt), the thermal conductivity of the amorphous phase is imperative to determining the amplitude of electrical pulse needed to heat the sample. Understanding the general role of size, structure, and composition on the thermal conductivity of amorphous materials will help guide both material discovery and device optimization.

1.2 Statement of Objectives and Scope

The first overarching objective of this work is to understand the mechanisms that dictate thermal transport in highly disordered crystals and amorphous solids. To do so, the materials selected for study include entropy-stabilized oxides having increasing number of components to systematically increase compositional disorder, as well as high-entropy bulk oxides, borides, carbides, and silicides. These high-entropy ceramics are included to understand the effects of extrinsic disorder such as grain boundaries, porosity, and phase segregation on thermal conductivity. Finally, amorphous silicon films are studied in order to show how propagating vibrational modes can give crystalline-like thermal transport characteristics to fully amorphous solids, while amorphous hydrogenated silicon nitride thin films are investigated to understand how composition effects thermal transport in amorphous solids.

Just as importantly, the second overarching objective of this work is to rigorously develop the experimental advances made in thermoreflectance experiments that were key to conducting this research. Therefore, a large portion of this dissertation is devoted to the theory, mathematical models, and experiments I have used and developed to study heat transfer in disordered materials. The remainder of this dissertation is organized as follows:

- *Chapter 2 - Theory of Thermal Conductivity* - The concepts and equations governing thermal conductivity are presented. Starting with the macroscale picture and working down to the microscale picture, I will detail the necessary background to model thermal conductivity of both crystalline and amorphous materials. This framework will be used later to compare with experimental data to assess the role of disorder on thermal conductivity.
- *Chapter 3 - Time- and Frequency-Domain Thermoreflectance* - The primary measurement technique used in this work is time-domain thermoreflectance (TDTR). Having a spatial resolution downwards of nanometers, this non-contact pump-probe technique is ideal for the measurement of thermal properties of thin films and microscale features. Also used in this work is the sister technique, frequency-domain thermoreflectance (FDTR), which adds an additional controlled variable to widen the space of thermal property extraction. In this

chapter, I discuss the core concepts behind these techniques, derive all equations needed to model the temperature rise resulting from laser heating, derive the model used to interpret experimental data, and discuss implications of the temperature rise and thermal length scales on the experiment.

- *Chapter 4 - Steady-State Thermoreflectance* - In this chapter, I introduce an entirely new technique that is a natural extension to FDTR: steady-state thermoreflectance (SSTR). This technique works in principle by inducing a steady-state temperature rise in a material via a long enough exposure to constant laser heating. Because of the steady-state nature of the technique, the analysis is governed by Fourier's law of heat conduction, rather than the heat diffusion equation. As a result, this technique is sensitive only to thermal conductivity, rather than thermal effusivity or diffusivity.
- *Chapter 5 - Entropy-Stabilized Oxides* - The effects of configurational entropy on thermal transport are explored. In entropy-stabilized oxides with 2 to 6 metal cations contained in a single-crystal oxide thin film, the temperature-dependent thermal conductivity reveals amorphous-like behavior for the 5- and 6-cation oxides. Comparison of these results with the analytical models derived in Chapter 2 suggest that mass-disorder scattering cannot explain experimental results. Instead, observation of the local structure reveals that the highly disordered charges present in the anion-cation pairs, resulting from the random distribution of cations, creates a large oxygen sublattice distortion. This charge-induced disorder controls the thermal conductivity in entropy-stabilized oxides.
- *Chapter 6 - High-Entropy Ceramics* - The study of high configurational entropy on thermal conductivity is extended to bulk ceramics. The thermal properties of four new classes of high-entropy ceramics are explored: high-entropy oxides, high-entropy carbides, high-entropy borides, and high-entropy silicides. It is shown that the high configurational entropy greatly reduces the phonon thermal conductivity relative to binary constituents. However, there can still be a significant electronic contribution to thermal conductivity that enables the carbides and borides to maintain a relatively high thermal conductivity. Finally, the effects

of microstructure are revealed through the use of TDTR to locally probe the thermal conductivity as a function of real space in two dimensions to create a thermal conductivity image. It is shown that the carbides possess a relatively uniform thermal conductivity across the sample, whereas large variation in the local thermal conductivity of the borides is attributed to secondary oxide phases.

- *Chapter 7 - Amorphous Thin Films* - The role of size and composition on the thermal conductivity of amorphous materials is investigated. Measurement of the thermal conductivity of amorphous silicon as a function of film thickness reveals how long wavelength propagating vibrational modes can contribute to thermal transport, in opposition to conventional models. Furthermore, amorphous hydrogenated silicon nitride is used to show how composition effects thermal conductivity in amorphous solids. In particular, the introduction of hydrogen and depletion thereof through thermal annealing allows for tunable thermal conductivity through manipulation of the coordination number of the material.
- *Chapter 8 - Summary and Future Projects* - The major conclusions of this dissertation are summarized to reveal the connection between each study towards supporting the overarching goals of this research. Finally, several future projects are proposed that could build on the results of this work.

Chapter 2

Theory of Thermal Conductivity

In this chapter, I will provide some fundamental concepts and mathematical equations governing heat conduction that will be used to compare to experimental findings later in this dissertation. The concept of thermal conductivity was first formalized by Joseph Fourier in 1807 [49] and subsequently made available to the broader scientific community in 1822 [49, 50]. In these works, Fourier noted that the flow of heat is proportional to temperature difference, so that in one-dimension (1-D) this can be written

$$Q_z = -\kappa \frac{\partial T}{\partial z}, \quad (2.1)$$

where Q_z is the heat flux in the z direction, T is temperature, and the proportionality constant between heat flux and temperature gradient is defined as the thermal conductivity, κ . This phenomenological expression defines Fourier's law of heat conduction, and is valid for any snapshot in time. When transient heat flow is considered, Fourier's law is only one part of a larger governing equation. Transient heat flow within a material is governed by (i) how much energy a material can hold per unit volume (volumetric heat capacity) and (ii) how quickly the heat can be dissipated within that material (thermal conductivity). Heat conduction, a diffusion process, is mathematically described by the transient heat diffusion equation,

$$C_v \frac{\partial T}{\partial t} = \nabla \cdot (\kappa \nabla T) + Q_{\text{gen}}, \quad (2.2)$$

where C_v is the volumetric heat capacity [energy per unit temperature per unit volume], t is time, and Q_{gen} is a volumetric heat energy generation term. Each side of Eq. 3.7 describes an energy per unit time per unit volume, typically given in units of [W m^{-3}]. In general, there is little variation in volumetric heat capacity between fully dense solids at and above room temperature; variation is generally contained to approximately 1 to 4 $\text{MJ m}^{-3} \text{ K}^{-1}$. In contrast, thermal conductivity can vary by orders of magnitude. For example, disordered C_{60} and other fullerene derivatives have thermal conductivities $< 0.1 \text{ W m}^{-2} \text{ K}^{-1}$ [51] whereas diamond has a thermal conductivity $> 2000 \text{ W m}^{-2} \text{ K}^{-1}$ [52]. Moreover, the volumetric heat capacity is an intensive property readily determined for most materials based on analytical expressions detailed later. Finally, it is very common that heat transfer can be assumed to be in steady-state (i.e., no time dependence), in which case the heat diffusion equation simplifies to Fourier's law such that the heat capacity plays no role in heat conduction. For these reasons, the thermal conductivity is the primary quantity we use to describe a material's ability to transport heat; it is therefore the property of interest for this dissertation. Strictly speaking, κ is a second order tensor and the gradient operator in Eq. (2.2) necessitates the consideration of off-diagonal terms when the coordinate system of interest, in this case the experimental coordinate system, is not aligned to the principal directions of thermal conductivity for an anisotropic material. In most cases, such as for most amorphous materials, κ can be assumed isotropic so as to become a scalar.

This macroscopic view of heat diffusion is valid at length and time scales large enough that energy carriers at any spatial and temporal point can be described by an equilibrium energy distribution. From a microscopic point of view, energy is fluctuating among carriers at all times. Heat carriers transfer energy to one another through energy conserving scattering events. In the solid-state, these energy carriers consist of electrical carriers (electrons or holes), lattice waves (phonons), coupled electromagnetic waves (plasmons), spin waves (magnons), and other excita-

tions [53]. In all such cases, the wave-particle duality of these carriers means we can treat them as particles, so that their heat transfer can be analyzed through the kinetic theory of gases [54]. Note, an alternative approach to analyze heat transfer using wave mechanics is provided by Chen [2]. In the simple kinetic theory picture, for a given energy carrier the *net* heat flux in the z -direction at a given point in space is

$$Q_z = Q_{+z} - Q_{-z} = \frac{1}{2} ((n\epsilon v_z)|_{z+v_z\tau} - (n\epsilon v_z)|_{z-v_z\tau}) \approx -v_z \tau \frac{\partial(n\epsilon v_z)}{\partial z}, \quad (2.3)$$

where n is the number of carriers per unit volume, ϵ is the energy of each carrier, v_z is the velocity of each carrier in z , and τ is the relaxation time - the average time the carrier travels before scattering with another carrier. An alternative description for $v_z \tau$ is the carrier mean free path, ℓ . Assuming isotropy, $v_z^2 = v^2/3$, where v is the total velocity of the heat carrier. Additionally, note that $n\epsilon$ describes the internal energy per unit volume (U). Taken together, Q_z is

$$Q_z = \frac{-v^2 \tau}{3} \frac{\partial U}{\partial z} = \frac{-v^2 \tau}{3} \frac{\partial U}{\partial T} \frac{\partial T}{\partial z}. \quad (2.4)$$

Finally, note that the volumetric heat capacity is defined by the change in internal energy (per unit volume) with temperature, i.e. $C_v = \partial U / \partial T$. Thus,

$$Q_z = \frac{-1}{3} C_v v^2 \tau \frac{\partial T}{\partial z}. \quad (2.5)$$

Comparing Eq. (2.5) with Eq. (2.1), the thermal conductivity is defined as

$$\kappa = \frac{1}{3} C_v v^2 \tau, \quad (2.6)$$

the same relationship given by Eq. 1.1. This simple derivation assumed a single heat capacity, velocity, and relaxation time for all carriers. In reality, these quantities can vary widely, so that the total thermal conductivity is the summation of all individual carriers. Furthermore, although energies are discrete, the minimum $\Delta\epsilon$ between carriers is small enough so that a continuum approximation is valid [2]. Therefore, the general expression for thermal conductivity is

$$\kappa = \sum_{\varepsilon} \frac{1}{3} C_{v,\varepsilon} v_{\varepsilon}^2 \tau_{\varepsilon} \approx \int \frac{1}{3} C_{v,\varepsilon} v_{\varepsilon}^2 \tau_{\varepsilon} d\varepsilon. \quad (2.7)$$

This summation includes the contribution from each type of carrier over all energies. However, in practice, one carrier typically dominates the thermal conductivity in a given material. In metals, the concentration of free electrons is typically over 10^{21} cm^{-3} so that electrons carry the majority of the heat. Some highly doped semiconductors can also have a significant contribution of electronic thermal conductivity. In insulators and intrinsic semiconductors, the free electron concentration is not large enough to support significant electronic thermal transport, so phonons dominate the thermal conductivity. For example, intrinsic silicon has a carrier concentration of only $8.9 \times 10^9 \text{ cm}^{-3}$, whereas doped silicon has typical concentrations of 10^{18} cm^{-3} [55]. While a substantial increase, this is still four orders of magnitude below the concentration in Cu, which is $8.47 \times 10^{22} \text{ cm}^{-3}$ [55]. As a comparison, typical phonon number densities at room temperature are around 10^{23} cm^{-3} for fully dense materials [55]. Thus, differences in free electron number density are indicative of the relative contribution of electrons to thermal conductivity in most materials. In this dissertation, although electronic contribution is considered in Ch 6, the focus will be primarily on the lattice thermal conductivity.

2.1 Crystals

In order to model the thermal conductivity given by Eq. (2.7), we need to define each term comprising κ . In crystalline materials, the atoms are arranged in an ordered and periodic nature on a length scale much larger than the lattice constant. Atoms can move about their equilibrium positions in collective excitations to form normal modes of vibration. These vibrational modes, which carry energy, are quantized and described as quasiparticles called phonons.

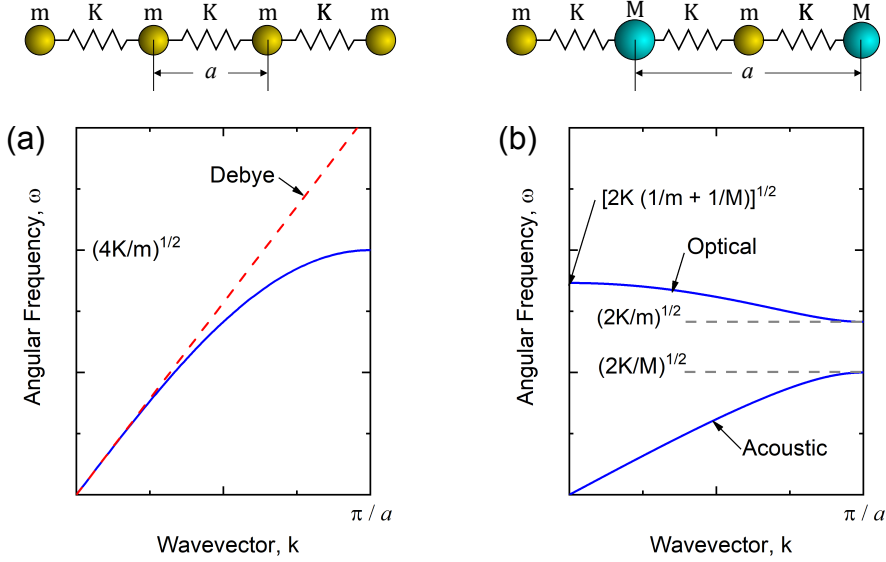


Figure 2.1: (a) Solid line is the real dispersion relation for a 1-D atomic chain given by Eq. 2.8, while dashed line represents the Debye dispersion. (b) Dispersion relation for 1-D atomic chain with two distinct masses. In this case, $M = 2m$.

2.1.1 Phonon Dispersion

The phonon dispersion relation defines the phonon angular frequency (ω) dependence on wavevector (k). In real crystals, the phonon dispersion relation depends on the crystal structure, number of atoms in the unit cell, atomic masses, and atomic bond strengths. Additionally, this relation can be defined along any line of symmetry, so that different relations are defined along any high symmetry direction. Given these parameters, lattice dynamics provide a framework with which to calculate the phonon dispersion [56]. Experimentally, inelastic neutron scattering [57] provides a way to obtain this relation at finite points in k -space.

To generalize the important concepts used later, an instructive example of how this phonon dispersion arises is the one-dimensional (1-D) atomic chain. Depicted in Fig. 2.1(a), an infinite spring mass system is assumed; the spacing between atoms is a , the mass is m and the spring constant is K . The governing equation of motion for each atom is simply Hooke's Law ($m \frac{d^2x_i}{dt^2} = -Kx_i$, where x is the displacement of atom i). The solution to this simple problem is [58]

$$\omega(k) = \left(\frac{4K}{m} \right)^{1/2} \left| \sin \left(\frac{ka}{2} \right) \right|. \quad (2.8)$$

Thus, the dispersion relation is described by a simple analytical function. Although we have not defined any bounds on k , physically, a phonon wavelength cannot be shorter than the atomic spacing, a . This implies that k is limited $[-\pi/a, \pi/a]$, i.e., the first Brillouin zone. Note that periodicity of Eq. 2.8 implies that $\omega(k) = \omega(\pi/a + k)$, an aspect that will be considered later when considering how phonon wavevectors add together. Next, the evenness of Eq. 2.8 implies that $\omega(k) = \omega(-k)$, so that $\omega(k)$ can be completely described by k in $[0, \pi/a]$. The resulting relation is shown in Fig. 2.1(a).

The phonon group velocity, v_g , is defined by

$$v_g(k) = \frac{\partial \omega}{\partial k}. \quad (2.9)$$

In the limit as $k \rightarrow 0$, $v_g(k) \rightarrow v_s$, where v_s is constant defining the speed of sound of a material in the direction and branch defining the dispersion relation. Under the Debye approximation, the phonon dispersion is modeled as $\omega(k) = v_s k$. This is shown for the 1-D chain in Fig. 2.1(a), where $v_s = a(K/m)^{1/2}$. Since only one dimension is defined, atoms are limited to one phonon polarization (branch), the longitudinal branch. However, in 3-D crystals, the motion of atoms can be perpendicular to the wave propagation, giving rise to transverse branches.

Often materials have multiple atoms in the unit cell, giving rise to optical phonons. Taking the previous 1-D example and making every other mass equal to M (see Fig. 2.1(b)), the phonon dispersion becomes [56]

$$\omega(k) = K \left(\frac{1}{m} + \frac{1}{M} \right) \pm K \left[\left(\frac{1}{m} + \frac{1}{M} \right)^2 - \frac{4}{mM} \sin^2 \left(\frac{ka}{2} \right) \right]^{1/2}. \quad (2.10)$$

There are two solutions, giving rise to an acoustic and an optical branch in the dispersion, shown in Fig. 2.1(b). Note that optical branches are distinct from acoustic in that they do not approach 0 as $k \rightarrow 0$. Comparing the dispersions in Fig. 2.1(a) and (b), one notes that the latter has lower group velocity and lower maximum frequency, both of which result from the heavier mass of M , which was taken as $M = 2m$ for the figure.

Having established the essential concepts about the phonon dispersion through these simple

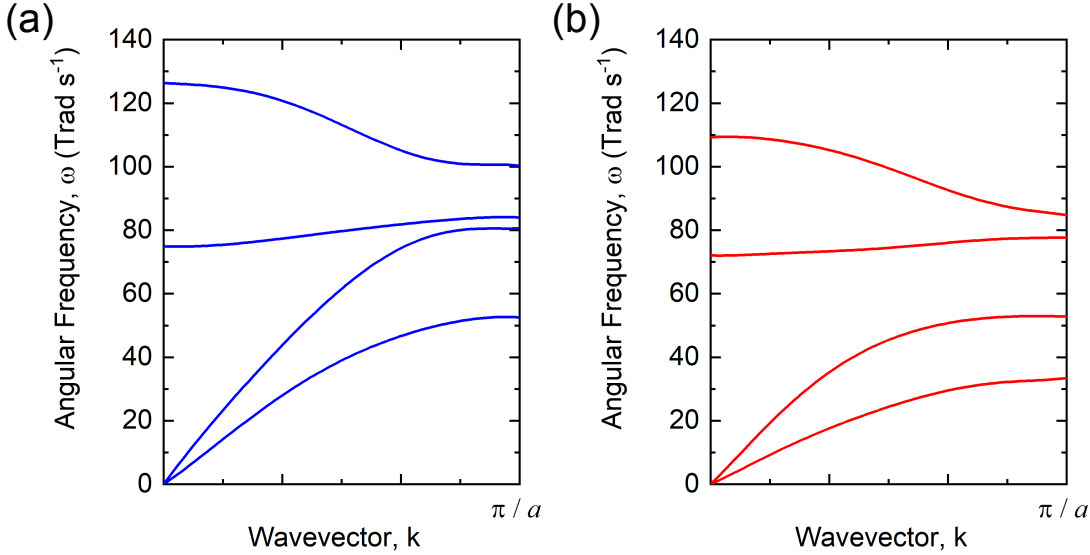


Figure 2.2: Phonon dispersion relations in the $\Gamma \rightarrow X$ (100) direction for (a) MgO [59] and (b) NiO [60].

examples, next we consider two realistic dispersions that will be used in Chapter 5, that of MgO and NiO along the $\Gamma \rightarrow X$ (100) direction, shown in Fig. 2.2, taken from Refs. [59, 60]. MgO and NiO have the same rocksalt crystal structure and similar lattice and interatomic force constants. Therefore, the primary difference between the two is that Nickel has a $\sim 2.4 \times$ higher mass than magnesium. Comparison of the two dispersion relations reveals that the sound speed and maximum frequencies of each branch is reduced in NiO as compared to MgO, in agreement with the simple 1-D chain model considered previously. To incorporate these dispersions later in calculating thermal conductivity, we model each branch as a 4th order polynomial.

2.1.2 Phonon Density of States and Occupation

The phonon density of states (sometimes referred to as density of normal modes) is defined as the number of phonon energy states per unit volume per unit energy. For a given phonon branch, the density of states, $D_j(\omega)$, is described for an isotropic crystal by

$$D_j(\omega) = \frac{\omega^2}{2\pi^2 v_j^3(\omega)}. \quad (2.11)$$

$D(\omega)$ describes the *available* states that phonons can occupy. To determine the *occupied* states, we need to invoke statistical mechanics. Noting that phonons are bosons, their equilibrium occupation function is described by the Bose-Einstein distribution,

$$f(\omega, T) = \frac{1}{\exp\left[\frac{\hbar\omega}{k_B T}\right] - 1}, \quad (2.12)$$

where \hbar is the reduced Planck's constant, k_B is Boltzmann's constant, and T is temperature. The occupied density of states, then, is simply $D(\omega)f(\omega, T)$.

2.1.3 Phonon Heat Capacity

The lattice heat capacity (at constant volume) is defined as the change in internal energy (U) with temperature,

$$C_v = \frac{\partial U}{\partial T}. \quad (2.13)$$

To determine the total internal energy from phonons, we can simply add the contribution from each individual phonon. Since we have described all functions thus far as continuum, this summation becomes an integral so that the total energy of phonons per unit volume can be understood as the number of occupied phonons (per unit volume per unit energy) multiplied by the energy of each phonon. This can be written

$$U = \sum_j \int_0^{\omega_{\max,j}} \hbar\omega f(\omega, T) D_j(\omega) d\omega. \quad (2.14)$$

where the sum is taken over all branches of the dispersion relation and $\omega_{\max,j}$ is the maximum angular frequency of branch j . Taking the derivative of U with temperature, the heat capacity becomes

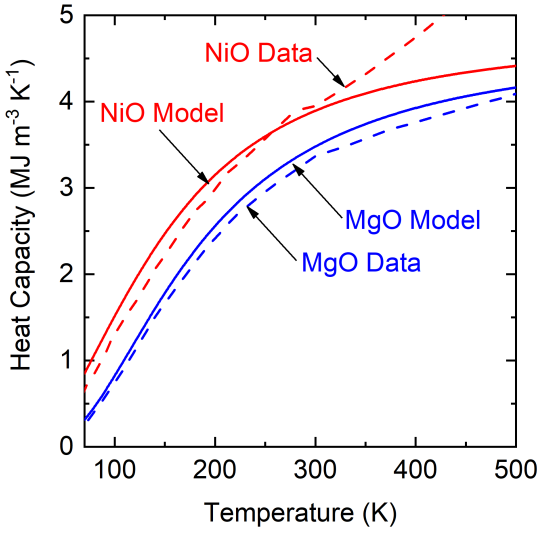


Figure 2.3: Heat capacities vs. temperature for MgO and NiO. Data is taken from Ref. [61], while the models are calculated from (2.15).

$$C_v = \sum_j \int_0^{\omega_{\max,j}} \hbar\omega \frac{\partial f(\omega, T)}{\partial T} D_j(\omega) d\omega = \sum_j \frac{\hbar^2}{2\pi^2 k_B T^2 v_j^3} \int_0^{\omega_{\max,j}} \frac{\omega^4 \exp\left[\frac{\hbar\omega}{k_B T}\right]}{\left(\exp\left[\frac{\hbar\omega}{k_B T}\right] - 1\right)^2} d\omega. \quad (2.15)$$

Thus, heat capacity can be solved as a function of temperature given the phonon dispersion. Using a polynomial dispersion to capture all branches of the polynomial and integrating over k -space (note, all integrals over ω can be converted to integrals over k), we use Eq. 2.15 calculate the heat capacity as a function of temperature for MgO and NiO; calculations are shown and compared with literature data [61] in Fig. 2.3. This relatively simple model, having no fitting parameters, shows remarkable agreement with literature heat capacities up to ~ 350 K for NiO and up to the maximum temperature considered, 500 K, for MgO. The deviation in heat capacity observed in NiO at high temperatures is due to a magnetic transition. Near 523 K, NiO undergoes a magnetic disordering transition from an antiferromagnetic to a paramagnetic insulator [62], giving rise to a so-called lambda-type anomaly in the heat capacity [63].

2.1.4 Phonon Thermal Conductivity

Like heat capacity, the phonon thermal conductivity is a summation of contributions from all phonons, given by

$$\begin{aligned}\kappa &= \frac{1}{3} \sum_j \int_0^{\omega_{\max,j}} \hbar\omega D_j(\omega) \frac{\partial f(\omega, T)}{\partial T} v_j^2(\omega) \tau_j(\omega) d\omega \\ &= \frac{1}{3} \sum_j \int_0^{k_{\max}} \hbar\omega_j(k) D_j(k) \frac{\partial f(k)}{\partial T} v_j^2(k) \tau_j(k) dk.\end{aligned}\quad (2.16)$$

where κ is expressed as a function of both k and ω to emphasize that integration can be done with respect to either variable; often it is more convenient to work with one over the other. The relaxation time comes from consideration of all individual scattering processes and is described by Matthiessen's rule,

$$\tau_j^{-1} = \sum_i \tau_{i,j}^{-1}, \quad (2.17)$$

where the summation is over all possible scattering processes. Thus, the key to modeling thermal conductivity is to accurately model τ_j . This description of thermal conductivity and its relaxation time was pioneered by works from Klemens, Callaway, and Ziman [64–67], and is based on a semi-classical formalism where τ_j is defined phenomenologically.

There are three major categories of phonon scattering processes: intrinsic scattering, boundary scattering, and point defect scattering. Figure 2.4 depicts each mechanism. In the absence of extrinsic mechanisms, intrinsic scattering processes are the only phonon scattering events that would dictate thermal conductivity in an ideal crystal. This phonon-phonon scattering process includes momentum conserving Normal and momentum destroying Umklapp processes [64, 66, 68–70]. Shown in Fig. 2.4(a), Normal scattering involves a three-phonon process in which two phonon momentums add ($k_1 + k_2$) such that the sum (k_3) is within $[0, \pi/a]$. Umklapp scattering, on the other hand, involves the resultant phonon wavevector falling outside the first Brillouin zone,

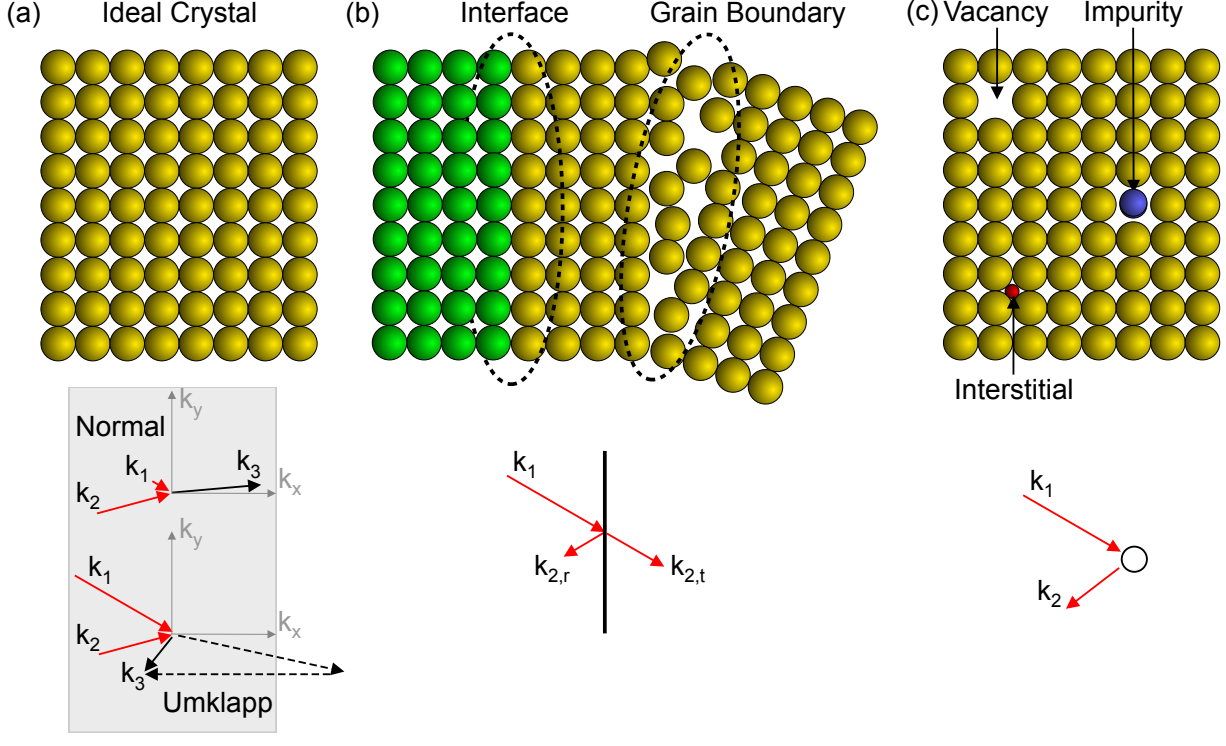


Figure 2.4: Representation of atomic structure, phonon scattering, and corresponding mathematical description of scattering time, τ for (a) an ideal crystal, (b) interfaces and boundaries, and (c) vacancies, impurities, and interstitials.

such that k_3 is reduced by the $2\pi/a$ so that the net momentum is negative. Hence, Umklapp scattering is a resistive process, since two positive-momentum phonons can scatter to result in a negative momentum phonon. Although Normal processes are not directly resistive, they ensure redistribution of the phonon population so that Umklapp processes become more likely, thereby indirectly contributing to this resistance. Although shown in Fig. 2.4(a) is the addition of two phonons into one (three-phonon process), intrinsic processes can also involve higher-order phonon scattering (four-phonon scattering, etc.) and the decay of one phonon into multiple (the reverse process to what is shown). The probability of higher-order phonon scattering is not significant at room temperature for most materials, but can become so at high temperatures [71]. The combined Normal and Umklapp scattering process used in this work takes the form [66]

Table 2.1: Fitting parameters corresponding to the terms described in Eq. (2.20) and Eq. (2.18), determined by fitting Eq. (2.16) to the experimental data shown in Fig. 2.5.

Material (dispersion)	A [s ³]	B [s K ⁻¹]	C [K]
MgO (full)	1.86×10^{-38}	4.61×10^{-19}	80.3
MgO (Debye)	4.02×10^{-48}	5.68×10^{-19}	41.0
NiO (full)	1.12×10^{-39}	9.20×10^{-19}	146.3
NiO (Debye)	-8.51×10^{-49}	1.24×10^{-18}	81.66

$$\tau_{\text{ph},j}^{-1} = B\omega^2 T \exp\left(\frac{-C}{T}\right) \quad (2.18)$$

B and C are constants and “ph” denotes “phonon.”

The next phonon scattering process to consider is boundary scattering. Shown in Fig. 2.4(b), boundary scattering occurs when phonons scatter at geometric boundaries such as material interfaces or grain boundaries. A phonon can partially transmit and reflect at such an interface so that the process is net resistive. Boundary scattering becomes increasingly significant when material dimensions become comparable to phonon mean free paths. It takes the form [2]

$$\tau_{\text{b},j}^{-1} = (1-p)\frac{v_j}{d}, \quad (2.19)$$

where “b” denotes “boundary,” d is the characteristic length, and p is the specularity parameter that accounts for sample dimension and interface roughness, varying between 0 and 1.

The final scattering category considered is impurity scattering from point defects, isotope atoms, and alloy atoms. This scattering results from randomly distributed mass fluctuations within the periodic lattice. It takes a Rayleigh scattering form [66, 72],

$$\tau_{\text{I},j}^{-1} = A\omega^4, \quad (2.20)$$

where “I” denotes “impurity” and A is a constant.

With these three scattering times defined, we can now determine A , B , and C by fitting Eq. (2.16) to experimental data and adjusting these parameters to minimize the difference between model and

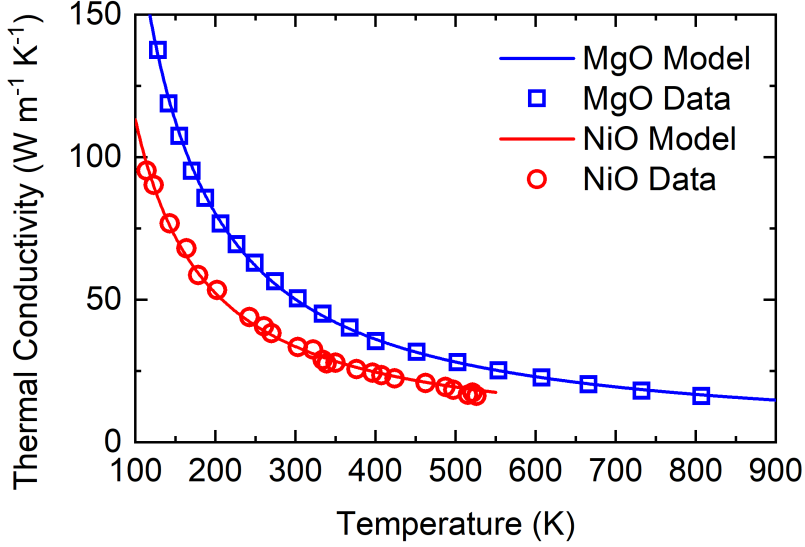


Figure 2.5: Thermal conductivity vs. temperature for MgO and NiO. Data is obtained from Ref. [73] for MgO and Ref. [74] for NiO. Models depict the thermal conductivity calculated by Eq. 2.16 with best-fit values for parameters A , B , and C .

data. Returning again to MgO and NiO, Fig. 2.5 shows the experimental thermal conductivity data vs. temperature for MgO [73] and NiO [74] as well as the best fit model. Two models are considered, one using the full phonon dispersion described by a polynomial function, and the other using a Debye dispersion. In both MgO and NiO, similarly good fits are found for both the full dispersion and Debye dispersion. The best-fit parameters are listed in Table 2.1. As expected for intrinsic MgO and NiO with little impurity concentrations, the fitted values for A in each case are negligible in determining the best fit; changing this value by several orders of magnitude made little difference to the fit. However, in alloys and solid solutions, A can dominate the scattering.

For random alloys and solid solutions, Abeles developed the virtual crystal approximation (VCA) [12], whereby a random alloy is treated as an effective crystal possessing the compositionally-weighted average properties (sound speed, mass, atomic radii, dispersion, intrinsic scattering rates) of the elements or compounds constituting the virtual crystal; additional phonon scattering results from differences in constituent and virtual crystal properties. In general, these Rayleigh scattering mechanisms are derived from perturbation theory [72], such that their use, and the phonon gas picture in general, become dubious when disorder becomes large [75]. Still, this formalism has

been used to adequately model the thermal conductivity in a variety of materials, including SiGe [12, 76, 77], InGaN [78], InAsP [12], and GaInAs [12] across a range of compositions, and remains the standard to model alloy thermal conductivity, even within first principles frameworks [4]. Under the VCA, Rayleigh scattering includes an addition term resulting from mass-impurity scattering (τ_m), which is described by

$$\tau_{m,j}^{-1} = \left(\frac{\Gamma\Omega}{12\pi\nu_j^3} \right) \omega^4, \quad (2.21)$$

where the mass-impurity scattering is a Rayleigh scattering mechanism describing how mass, strain, and atomic radius affect the phonon scattering rate through the constant, Γ . Ω is the volume per atom and Γ is described by [12]

$$\Gamma = \Gamma_m + \Gamma_f = \sum_i x_i \left[\left(\frac{\Delta m_i}{\bar{m}} \right)^2 + 2 \left(\frac{\Delta G_i}{\bar{G}} - 6.4\gamma \left(\frac{\Delta \delta_i}{\bar{\delta}} \right) \right)^2 \right], \quad (2.22)$$

where x_i is the fraction of element i , m_i denotes the atomic mass of species i , G_i represents the average stiffness constant of nearest neighbor bonds of species i within the host lattice, γ is the Grüneisen parameter describing the average anharmonicity between bonds, and δ_i denotes atomic radius of species i . Under the VCA, \bar{m} , \bar{G} and $\bar{\delta}$ are the average mass, strain, and atomic radius of the perturbed atoms. From this analytical expression, we observe that three terms dictate the Rayleigh scattering of phonons within a multi-component alloy or solid solution: (1) mass difference, (2) bond strength difference, and (3) atomic radii difference between impurity and host atom. While the mass differences are easily quantifiable, the latter terms, which are all related to the interatomic force constants, are not. Therefore, we split the summation in Eq. (2.22) to distinguish the contribution from mass and interatomic forces, $\Gamma = \Gamma_m + \Gamma_f$. In Chapter 5, we will model the thermal conductivity with and without the Γ_f term to assess its contribution to the model.

The VCA also implies a modified form of Normal scattering form [68, 78],

$$\tau_{N,j}^{-1} = \left(\frac{k_B \gamma^2 \Omega^{1/3}}{\bar{m} \nu_j^3} \right) T \omega_j^2, \quad (2.23)$$

so that the total relaxation time according to Matthiessen's rule becomes

$$\tau_j^{-1} = \tau_{I,j}^{-1} + \tau_{m,j}^{-1} + \tau_{ph,j}^{-1} + \tau_{N,j}^{-1} + \tau_{b,j}^{-1}. \quad (2.24)$$

Under the VCA, all atoms are assumed to have the same mass equal to the average atomic mass, \bar{m} , such that mass differences in Eq. (2.22) are with respect to \bar{m} . Additionally, the differences in stiffness constants and atomic radii are with respect to those average quantities of all atoms. In this case, the B and C used in Eq. (2.18) will take the form of the average B and C for each constituent composition.

2.2 Amorphous Solids

In contrast to crystals, amorphous solids lack long-range translational and orientational order. Because of the lack of atomic periodicity, it is no longer valid to describe vibrational modes in amorphous solids as phonons, since they do not have well-defined wavevectors. Similarly, phonon group velocity and mean free path become ill-defined, making modeling thermal transport in amorphous materials very challenging. However, if the kinetic theory ideas defining thermal conductivity in crystals holds true in amorphous materials, the lack of long-range order in these materials suggests that vibrational mean free paths must be significantly lower than in crystalline materials. Experiments in amorphous materials support this idea in that measured thermal conductivities for amorphous materials are generally significantly lower than their crystalline counterparts. For example, Si has a thermal conductivity of up to $\sim 150 \text{ W m}^{-1} \text{ K}^{-1}$ in the crystalline phase at room temperature [79], whereas amorphous silicon has a thermal conductivity as low as $\sim 1 \text{ W m}^{-1} \text{ K}^{-1}$ [80]. In fact, using Eq. (2.6), Birch and Clark [81] first noted that the mean free paths interpreted by thermal conductivity measurements suggested that in glasses, mean free paths above 30 K approach the interatomic spacing. Since the interatomic spacing represents the minimum possible wavelength of a vibrational mode, the concept of a wave carrying heat loses significance below

this length scale [18]. These findings suggest a modified framework is necessary to model thermal transport in amorphous materials.

2.2.1 Minimum Limit to Thermal Conductivity

A fairly successful and conceptually appealing framework on which to model thermal conductivity in amorphous solids is based on ideas originally developed by Einstein [82] and later refined by Slack [19]. In this description, atoms are treated as independent oscillators, so that energy hops from one atom to another through a random walk at the same frequency but having random phases with respect to one another [20]. According to Einstein, heavily damped atomic vibrations will transfer energy within half a period of their oscillation [82]. With all atoms vibrating at the same angular frequency ω_E (the Einstein frequency), the internal energy is then

$$U = 3n\hbar\omega_E f(\omega_E, T) = \frac{3n\hbar\omega_E}{\exp\left[\frac{\hbar\omega_E}{k_B T}\right] - 1}, \quad (2.25)$$

where n in this case is the *atomic* number density. The factor of 3 accounts for the three possible polarizations of modes. Using this internal energy, the heat capacity is

$$C_v = 3nk_B \left(\frac{\hbar\omega_E}{k_B T}\right)^2 \frac{\exp\left[\frac{\hbar\omega_E}{k_B T}\right]}{\left(\exp\left[\frac{\hbar\omega_E}{k_B T}\right] - 1\right)^2}. \quad (2.26)$$

Finally, the thermal velocity of atoms is equal to the distance traveled divided by the relaxation time, i.e., $v = n^{-1/3}/\tau_E$. As previously mentioned, this relaxation time is half a period of oscillation, $\tau_E = \omega_E/\pi$. Substituting these expressions into Eq. (2.6), the thermal conductivity becomes

$$\kappa_{\text{Einstein}} = \frac{n^{1/3}k_B\omega_E}{\pi} \left(\frac{\hbar\omega_E}{k_B T}\right)^2 \frac{\exp\left[\frac{\hbar\omega_E}{k_B T}\right]}{\left(\exp\left[\frac{\hbar\omega_E}{k_B T}\right] - 1\right)^2}. \quad (2.27)$$

To slightly simplify this expression, we can define the Einstein temperature as $\Theta_E = \hbar\omega_E/k_B$ so that thermal conductivity is

$$\kappa_{\text{Einstein}} = \frac{k_B^2 n^{1/3}}{\hbar \pi} \Theta_E \frac{x^2 e^x}{(e^x - 1)^2}, \quad (2.28)$$

where $x = (\Theta_E/T)$. Θ_E , due to the ambiguity of ω_E , is unknown; however, it can be obtained by fitting Eq. 2.26 to experimental heat capacity data. Still, this single-frequency assumption is not justified from any physical evidence. Instead, Slack later followed the ideas of Debye to suggest that atoms could vibrate together as larger entities to obtain a spectrum of frequencies [19]. Thus, the thermal conductivity takes the same integral form presented in Eq. (2.16). However, the relaxation time is taken to be half a period of oscillation, consistent with the Einstein model. This is what Slack called the *model of the minimum thermal conductivity*. Furthermore, within the Debye model, the maximum frequency of oscillation is equal to $\omega_{D,j} = v_j(6\pi^2 n)^{1/3}$. Taken together, the minimum thermal conductivity is

$$\kappa_{\min} = \sum_j \frac{\hbar^2}{6\pi k_B T^2 v_j} \int_0^{v_j(6\pi^2 n)^{1/3}} \frac{\omega^3 \exp\left[\frac{\hbar\omega}{k_B T}\right]}{\left(\exp\left[\frac{\hbar\omega}{k_B T}\right] - 1\right)^2} d\omega. \quad (2.29)$$

This can be simplified to [18, 80]

$$\kappa_{\min} = \left(\frac{\pi}{6}\right)^{1/3} k_B n^{2/3} \sum_j v_j \left(\frac{T}{\theta_j}\right)^2 \int_0^{\theta_{D,j}/T} \frac{x^3 e^x}{(e^x - 1)^2} dx, \quad (2.30)$$

where $\theta_{D,j}$ is the Debye temperature, equal to $\theta_{D,j} = v_j(\hbar/k_B)(6\pi^2 n)^{1/3}$. This model was formalized by Cahill and Pohl [18] so that it is often referred to as the Cahill-Pohl model. It has been successful in describing the thermal conductivity in a variety of highly disordered crystals and amorphous solids [80]. Although this model comes with the unsubstantiated assumption of no dispersion, it comes with a major advantage over the Einstein model – it is an absolute model that does not require fitting parameters.

To understand the differences between these models, we turn back to the example of MgO. Figure 2.6 shows the thermal conductivity vs. temperature for the Cahill-Pohl model (κ_{\min} calculated

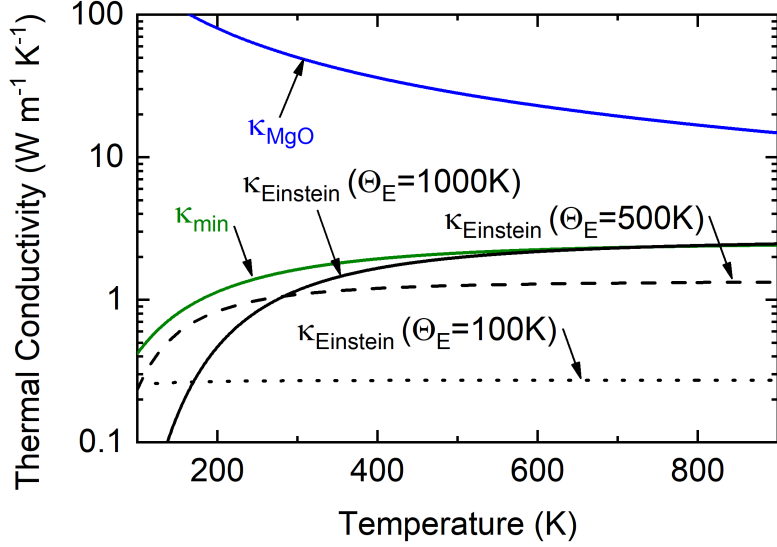


Figure 2.6: Thermal conductivity models vs. temperature for MgO. κ_{MgO} is determined using Eq. (2.16) with best-fit values for parameters A , B , and C listed in Table 2.1, κ_{min} is determined using Eq. (2.30), and κ_{Einstein} is determined using Eq. (2.28) considering three values for Θ_E , 100 K, 500 K, and 1000 K.

using Eq. (2.30)) and the Einstein model (κ_{Einstein} calculated using Eq. (2.27)). To understand the role of Θ_E on this model, κ_{Einstein} is shown for $\Theta_E = 100$, 500, and 1000 K. Finally, for comparison, The thermal conductivity model for crystalline MgO (κ_{MgO}), equivalent to that from Fig. 2.5, is shown. Comparison of both κ_{min} and κ_{Einstein} to κ_{MgO} reveals that the former are orders of magnitude lower in value and have an increasing, rather than decreasing trend with temperature over the range considered. This increasing trend with temperature is a signature for amorphous and highly structurally disordered solids [13]. It arises from the fact that relaxation times in the model are no longer temperature-dependent, but rather are reduced to a half period of oscillation. Because the group velocity is temperature-independent, the only term that has temperature dependence is heat capacity, which increases with temperature (see Fig. 2.3); therefore, the thermal conductivity will have the same temperature dependence. Comparing κ_{min} to κ_{Einstein} , a higher thermal conductivity is predicted for κ_{min} than κ_{Einstein} for the temperature range and Θ_E considered. There is generally better agreement between κ_{min} with experimental data [18, 20].

2.2.2 Locons, Diffusons, and Propagons

While the “minimum limit” description of thermal conductivity has been adopted with much success, many computational and experimental works have suggested this picture is not complete. Moreover, κ_{\min} is still derived from the original idea that vibrational modes can be described using the phonon gas model. An alternative description of thermal conductivity comes from consideration of vibrational mode diffusivities. As mentioned previously, vibrational modes having wavelengths below the interatomic spacing do not make physical sense. Therefore, a more appropriate descriptor of energy transport is given by the diffusivity, since this descriptor has no need for a well-defined wavevector [83]. Diffusivity, having units of [m^2/s] describes the *rate* of heat transfer; the quantized quasi-particle used to describe this is the diffuson [84].

In this picture, the diffuson is a subset of vibrational modes that exist in amorphous solids. In general, harmonic normal modes of vibration are classified as extended (extendons) or localized (locons). In three dimensions the vibrational spectrum has sharp boundaries called “mobility edges” that distinguish these modes. Allen *et al.* [84] used numerical studies of amorphous silicon to reveal that within the extendon spectrum of frequencies, a less pronounced boundary exists between phonon-like vibrational modes called propagons and the diffusive modes they called diffusons; Allen *et al.* called this edge the “Ioffe-Regel” crossover. Note that in the phonon picture, the Ioffe-Regel limit is the frequency edge at which the mean free path approaches the average interatomic spacing, ($\ell \rightarrow n^{-1/3}$) [85, 86], i.e., the mobility edge between extendon and locon. However, these computational simulations showed that the Ioffe-Regel crossover and mobility edge did not coincide. Propagons are phonon-like vibrational modes in that they can be reasonably well-defined by a wavevector and travel at the sound velocity over distances greater than the interatomic spacings before scattering [87]. By contrast, in the diffuson region of the vibrational frequency spectrum, only diffusive propagation occurs such that the concept of mean free path and wavevector lose significance. Allen *et al.*’s simulations showed that propagons and locons made up only 4% and 3% of the vibrational modes in amorphous silicon, respectively. Generalizing the results suggests that diffusons overwhelmingly dominate the vibration mode population in amorphous solids.

Given the overwhelmingly large diffuson population, one may expect that thermal transport should be dictated by diffusons. Indeed, this idea is generally in line with the previously defined minimum limit idea in that diffusion implies the random walk theory of vibrational modes is valid. However, recent experimental studies have suggested that propagons can significantly influence thermal conductivity. In amorphous silicon, for example, experiments have shown that reduction of sample size can reduce the thermal conductivity [21–24], suggesting that ballistic propagons are being scattered at the boundaries to reduce thermal conductivity. Evidence for such strong propagon contribution to thermal transport in other amorphous materials such as Silicon Nitride ($a\text{-SiN}_x$) and Germanium is established but less convincing as it is still a matter of contention [16]. On the other hand, several amorphous oxides such as silicon dioxide ($a\text{-SiO}_2$) and alumina ($a\text{-Al}_2\text{O}_3$) do not show any experimental evidence for significant propagon contribution to κ at the length scales typically measured (>10 nm) [16, 21, 88]. This does not mean that propagons do not exist, but rather it suggests that their mean-free paths are greatly suppressed via intrinsic scattering; in fact, recent studies suggest heat can traverse $a\text{-SiO}_2$ ballistically when its thickness is below 5 nm [89]. Taken as a whole, there is still much ambiguity in the conditions needed for a material to support significant propagon thermal transport.

Chapter 3

Time- and Frequency-Domain Thermoreflectance

In this chapter, I will present the primary experiments used this dissertation, the optical pump-probe techniques, time- and frequency-domain thermoreflectance. After briefly discussing the background, concepts, and implementation used in this work, I will focus primarily on the mathematical basis used to model laser heating of materials. This formalism will be generalized to model the spatial and temporal evolution of the temperature rise in samples with an arbitrary number of layers. There is tremendous benefit to understanding this underlying temperature rise and its implications on thermoreflectance experiments. In fact, it is this mathematical basis that led to the creation of the new experimental advance as part of my dissertation work – steady-state thermoreflectance – which will be discussed in the following chapter. Here, I will derive a method to calculate the temperature rise and heat flux profiles as a function of depth and radius for bulk, homogeneous materials and samples with layered thin-film structures during pulsed and continuous wave laser heating.

3.1 Background

While Joseph Fourier's formulation of the heat conduction law that defines thermal conductivity dates back to 1822 [50], significant efforts to experimentally measure and model thermal conductivities of solid-state materials (as well as thermal boundary conductances between materials) did not take place until the 1950s [53], through pioneering works from G. White, R. Berman, G. Slack, and R. Pohl, to name just a few. Almost all experiments at the time were based on steady-state, resistive heating approaches. However, in addition to suffering from long measurement times and susceptibility to convective and radiative heat losses, these conventional techniques do not provide the spatial resolution needed to measure temperature gradients of interest to modern technologies, i.e., micrometer and nanometer length scales.

As was the case with many other scientific fields, the invention of the laser revolutionized the study heat transfer immensely, enabling a directed, localized, and controllable heat source with which to perform experiments. In addition to being a heat source, the laser can also be used as a local temperature probe by exploiting the principle of thermoreflectance. A material's dielectric function, and ultimately its reflectivity, varies with temperature. For small temperature rises, the relationship between a material's change in reflectance (ΔR) with change in temperature (ΔT) can be assumed linear, so that

$$\frac{\Delta R}{R_0} = \left(\frac{1}{R_0} \frac{\partial R}{\partial T} \right) \Delta T = \beta \Delta T. \quad (3.1)$$

where β is defined as the material's thermoreflectance coefficient and R_0 is the baseline reflectance of the material at temperature T . Thus, the idea behind any thermoreflectance-based pump-probe technique is to heat the sample with a pump beam and detect the resulting ΔR using the probe beam. In general, laser excitation of a material can alter carrier concentrations, electronic energies, local strain, and other properties, all of which contribute to ΔR . Hence, to ensure that ΔR is only dependent on ΔT , a thin metal transducer is typically deposited on the material of interest to serve as a transducer. Paddock and Eesley first reported a transient thermoreflectance-based pump-probe technique, termed picosecond transient thermoreflectance (TTR), in 1986 using two

dye lasers to generate the pulsed pump and probe [90]. Paddock and Eesley measured the thermal diffusivity of thin metal films by heating the samples with a pump beam that was amplitude modulated, and detected the change in reflectance as a function of time by physically extending the path length of the probe relative to the pump via a mechanical delay stage. A lock-in amplifier was used to monitor changes in the probe reflected power by locking into a photodetected signal at the pump modulation frequency. Note, lock-in amplification is the key to detection, as typical thermoreflectance coefficients are around $10^{-5} - 10^{-4}$ K $^{-1}$ [91–93]. Since this seminal work, much progress has been made over the past three decades to advance the metrology, including the ubiquitous use of a Ti:Sapphire oscillator to generate femtosecond laser pulses [94] as well as the extension of the thermal model used to interpret thermoreflectance data to include multiple dimensions [94] and pulse accumulation [95] when the temperature rise from a single pulse does not decay to ambient before the next pulse arrives. This pulse accumulation is what distinguishes time-domain thermoreflectance (TDTR) [94, 96, 97] from TTR [98].

The related pump-probe technique, frequency-domain thermoreflectance (FDTR), relies on the same concept as TDTR in that it locks into a modulated temperature rise resulting from modulated laser heating. However, the modulation frequency, rather than delay time, is the controlled variable in this technique. FDTR traces its roots back to 1983, when Opsal, Rosencwaig, and Willenborg used focused, continuous wave (CW) lasers to both generate and detect thermal waves in the megahertz frequency regime based on measuring the thermoelastic response of the sample to a modulated heat source via detection of the deflected probe [99]. In 1985, Rosencwaig *et al.* [100] showed the same thermal wave detection, now using thermoreflectance. Refinement of the technique to what it is known today, however, did not take place until 2009, when Schmidt, Cheaito and Chiesa [101] reported an analysis to extract the thermal conductivity, thermal boundary conductance, and heat capacity of films and bulk samples based on the frequency domain solution to the heat diffusion equation over a wide range of modulation frequencies; it is this work that established the name frequency-domain thermoreflectance. FDTR can be performed with either a CW [101, 102] or pulsed [101] laser pump-probe setup. Both TDTR and FDTR have proven to be robust techniques capable of measuring thermal conductivities ranging from <0.1 to >2000 W m $^{-1}$

K^{-1} . Moreover, the localized nature of measurements and capability to measure thin films have enabled unique scientific advances to include the measurement of the lowest fully-dense, solid-state thermal conductivity materials ever measured at $0.05 \text{ W m}^{-1} \text{ K}^{-1}$ for WSe_2 in the cross-plane direction [103] and $0.03 - 0.06 \text{ W m}^{-1} \text{ K}^{-1}$ for $\text{C}_{61}\text{-butyric acid methyl ester}$ (PCBM) [51, 104], as well as the measurement of one of the highest predicted thermal conductivities at $>1000 \text{ W m}^{-1} \text{ K}^{-1}$ for cubic Boron Arsenide [105–107].

3.2 Experimental Details

A TDTR schematic, as it is implemented in this dissertation, is shown in Figure 3.1(a). In this setup, a Ti:Sapphire oscillator, pumped externally by a Nd:YAG CW laser, outputs pulses at a repetition rate of 80 MHz with a central wavelength of 800 nm; the full-width half max of the spectrum is typically around 10 nm. The pulse width upon exiting the oscillator is $\sim 100 \text{ fs}$. The output is first sent through an optical isolator to prevent back reflections into the oscillator. Thereafter, the beam is divided into a pump and probe path via a polarizing beam splitter (PBS) and the ratio of power is controlled using a half-wave plate. The pump beam is sent through an electro-optic modulator to become amplitude modulated with a frequency of 1 to 10 MHz in a sinusoidally varying envelope (shown in Figure 3.1(b)); the pump is then sent through a Bismuth Borate (BiBO) crystal for second harmonic generation to convert the wavelength from 800 nm to 400 nm. This conversion in wavelength is done to enable better absorption in transducers such as gold and allow for wavelength filtering of the pump. Finally, the pump is reflected from a cold mirror and directed through an objective lens ($10\times$ and $20\times$ are used in this dissertation) to focus the beam onto the sample.

The probe beam is first sent through a PBS and the transmitted portion is passed through a quarter-wave plate before reaching the retroreflector mirror mounted on a computer-controlled mechanical delay stage. The probe is reflected to a zero-degree mirror where it is sent back to the retroreflector along the same path. As such, the probe then passes again through the quarter-wave plate before reaching the aforementioned PBS; because the probe passes through the quarter-wave

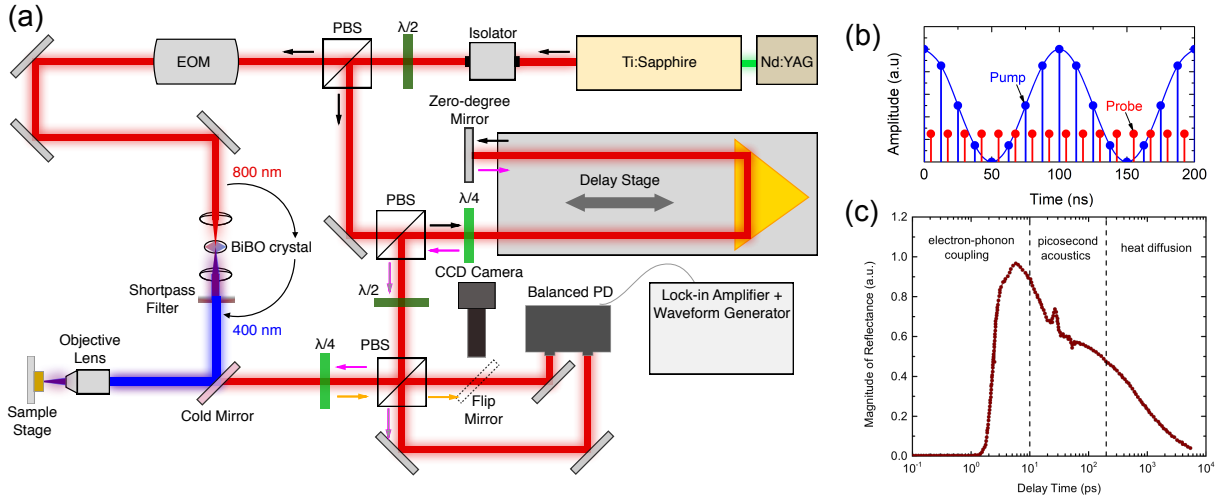


Figure 3.1: (a) Schematic of the two-color TDTR experiment: A Ti:Sapphire oscillator outputs a train of pulses at a repetition rate of 80 MHz. This is split into a pump path and a probe path, the former of which is modulated with a sinusoidal waveform via an electro-optic modulator and frequency doubled via a BiBO crystal so that the wavelength becomes 400 nm. The probe beam, is used to monitor the change in reflectance at the sample surface. (b) Amplitude of power vs. time for pump and probe before reaching the sample; the pump is modulated by a sinusoidal waveform at a frequency of 10 MHz. (c) Example of data collected by TDTR for 20 nm Au on Al₂O₃: the magnitude of reflection resulting from the modulated component to the pump heating event. The data can be separated into three time regimes: (i) electron-phonon coupling, (ii) picosecond acoustics via strain wave propagation, and (iii) heat diffusion.

plate twice before reaching the PBS, the polarization of the beam is shifted by half, allowing all of the power to be reflected away from the PBS towards the sample. The delay stage ensures that the probe pulse arrival to the sample is delayed relative to the pump heating event up to 6 ns. After exiting the PBS, the probe is transmitted through a quarter-wave plate and PBS to split the probe into a reference arm and a detection arm; the reference arm is sent to one of two photodiodes comprising the balanced photodetector (BPD). The detection arm is sent towards the sample, transmitting through the cold mirror, to be focused onto the sample via the same objective lens as the pump. The reflected probe is transmitted back through the PBS, using the same quarter-wave plate scheme used in the delay stage section, and sent into the other photodiode of the BPD. The focus of the beam onto the sample is ensured using a CCD camera to minimize the probe size by adjusting the sample stage position. The detection and reference probe powers reaching the BPD are balanced using the half-wave plate; this balanced detection scheme cancels any common

noise in the probe, significantly improving signal-to-noise ratios. The measured voltage is then sent to a lock-in amplifier which picks out the frequency component only at the pump modulation frequency. An automated LabVIEW program is used to collect the lock-in amplifier's in-phase (V_{in}) and out-of-phase (V_{out}) signals as a function of probe delay time.

The magnitude of this voltage ($\sqrt{V_{\text{in}}^2 + V_{\text{out}}^2}$) is proportional to the total change in reflectivity due to the change in temperature induced by the pump heating; a representative measurement of this magnitude as a function of delay time is shown in Figure 3.1(c) for 20 nm Au on Al₂O₃. Three regions are highlighted corresponding to the type of information this decay curve reveals: (i) electron-phonon coupling, (ii) picosecond acoustics via strain wave propagation, and (iii) heat diffusion. In the first few picoseconds after pump pulse absorption, the free electrons in the metal transducer are excited; due to the low heat capacity of these electrons, the local electron temperature can be thousands of degrees out of equilibrium with the lattice [108]. Over the first \sim 10 ps, the electron-phonon coupling facilitates restoration to equilibrium between the electrons and lattice so that they are at the same temperature. This rapid and localized heating induces a strain wave in the transducer which can propagate at the speed of sound through the film and reflect at the film/substrate interface. When the reflected strain wave reaches the surface of the transducer, it changes the piezo-optic coefficient of the probed surface volume, and thus changes ΔR . What we refer to as the “picosecond acoustics” regime, the strain wave manifests itself as a local peak or trough in the transient decay (the sign depends on the piezo-optic coefficient and relative mismatch in acoustic impedance between transducer and substrate). In this dissertation, the picosecond acoustics regime is used to determine thickness of the transducer based on the measured time between echos. Finally, the last regime is that of heat diffusion. Beyond \sim 100 ps, heat diffuses through the sample such that the surface temperature decreases exponentially in time.

All analysis for extracting thermal conductivity is obtained from the heat diffusion regime. In this regime, the ratio ($-V_{\text{in}}/V_{\text{out}}$) is generally used to extract thermal properties since sources of error, such as power variation, are canceled out upon division. A multilayer, radially symmetric thermal model is used to extract unknown parameters via a nonlinear least squares fit to experimental data. Thus, the analysis for TDTR relies on the macroscale picture of heat diffusion. This

macroscale analysis, however, can reveal a plethora of information about microscale phenomena given proper interpretation. For example, measuring the reduction of thermal conductivity in spatially confined systems such as thin films can reveal the influence phonon-boundary scattering [22, 109, 110], as well as the effects of microstructure, for example grain boundaries [111–113] and crystalline coherence length [114]. Similarly, manipulating experimental length scales to the order of the characteristic length scales of thermal transport can reveal information on phonon mean-free path accumulation [115–118].

3.3 Core Concepts

For beginners to TDTR and FDTR, often there is confusion about the various temperature rises that occur during experiment. We capture an “in-phase” and “out-of-phase” signal, and associate that with a “real” and “imaginary” component of the induced temperature rise. But what does this all mean physically? How can there be an imaginary temperature rise? In this subsection, I will elucidate the meaning of these concepts.

Physically, in both TDTR and FDTR, an amplitude modulated heating event creates an amplitude modulated temperature rise at the sample surface having the same frequency as the pump. There are two pieces of information associated with this modulated temperature rise: (1) the amplitude of the temperature (A) and (2) the phase lag (ϕ) *relative* to the pump phase. This idea is shown in Fig. 3.2. Starting the more intuitive case of FDTR with a CW laser source, Fig. 3.2(a) depicts the power of the pump as a function of time for two modulation frequencies: 10 and 5 MHz. Two frequencies are considered because FDTR relies on varying the modulation frequency as a control variable, so it is instructive to see how changing this variable changes both A and ϕ . Figure 3.2(c) shows the corresponding temperature rises for both modulation frequencies, and labels the resulting ϕ and A in each case. Note that the amplitude increases with decreasing modulation frequency. Intuitively, one would expect that when applying heat to a sample, leaving the heat source on longer will result in a higher temperature rise than quickly turning off the heat source. Similarly, leaving the source off longer will allow the sample to cool to a lower temperature. So,

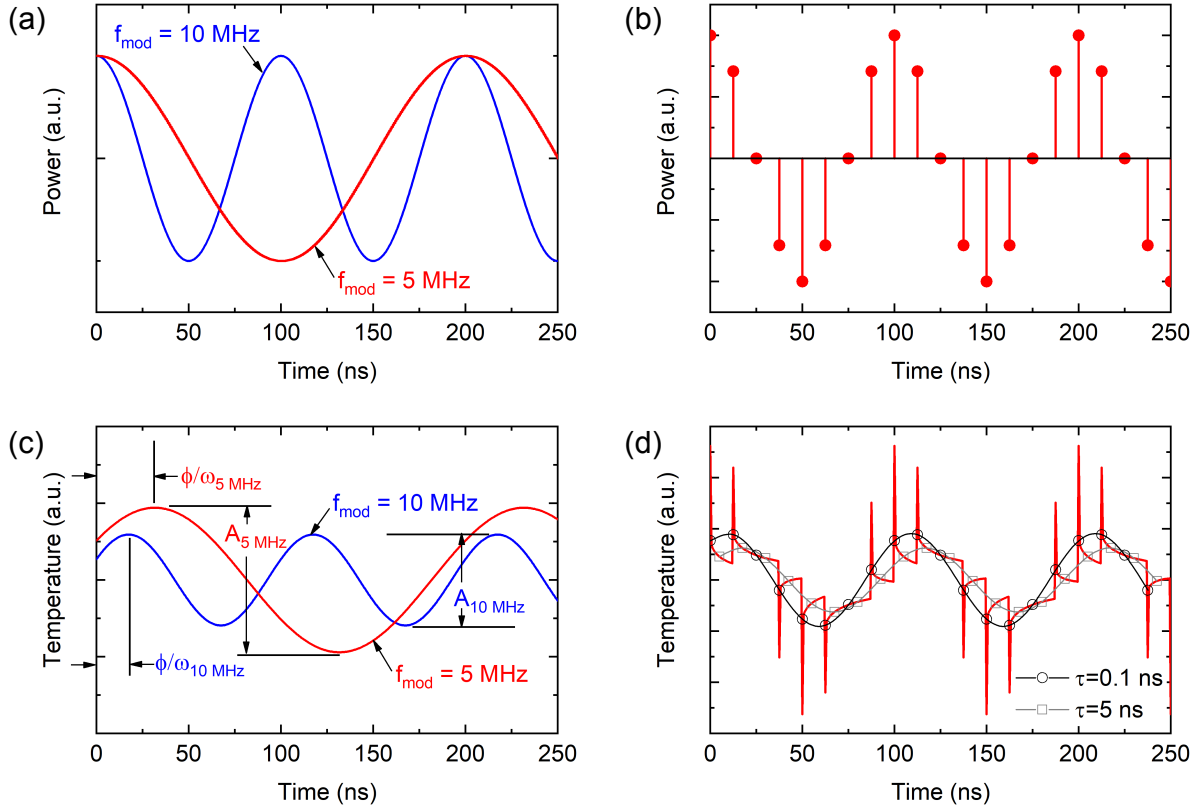


Figure 3.2: (a) Pump power vs. time for a 10 MHz and 5 MHz amplitude modulated continuous wave laser having the same average power. (b) Pump power vs. time for a 10 MHz amplitude modulated pulsed laser. (c) The resulting temperature rise vs. time resulting from the sources described in (a). ϕ is the phase lag relative to the pump phase, and A is the amplitude of the temperature oscillation. (d) The resulting temperature rise vs. time resulting from the source described in (b). The phase lag and amplitude are equivalently described as in (c). However, in TDTR, the delay time, ϕ and A vary with the probe delay time, τ . To show this, labeled are the resulting temperature oscillations for $\tau = 0.1 \text{ ns}$ and $\tau = 5 \text{ ns}$.

the lower modulation frequency having a larger temperature amplitude makes sense. The phase lag, on the other hand, decreases with decreasing modulation frequency. This result may not be intuitive, given that the time it takes to reach the maximum amplitude (ϕ/ω) actually increases with decreasing frequency. However, consider the limit as modulation frequency approaches zero. At zero modulation frequency, the pump is constant in time, so we should expect there to be no phase lag at all. Indeed, this is the basis of steady-state thermoreflectance, to be discussed later. Figure 3.3 shows the same temperature rise as Fig. 3.2(c) vs. ωt . Now the phase can be clearly shown to reduce with a lower modulation frequency.

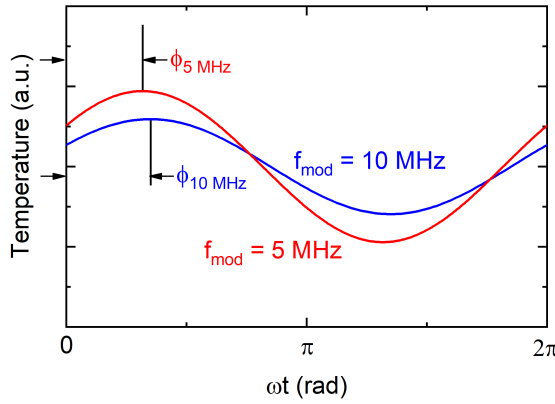


Figure 3.3: The same temperature rise as in Fig. 3.2(c) vs. ωt . The phase lag, ϕ is shown for both the 5 and 10 MHz modulated temperatures.

Turning now to the TDTR case, Fig. 3.2(b) shows the pulsed pump power vs time. Note that mathematically, the pulses are treated as delta functions, but for visualization are plotted as finite values. The resulting temperature rise vs. time is shown in Fig. 3.2(d). The same definitions for phase lag and amplitude remain the same in the pulsed case. However, in TDTR, the controlled variable is now time delay (τ) between the pump pulse and the probe pulse. Thus, the probe samples the temperature rise at discrete values of τ . The amplitude and phase lag are, as a result, functions of τ . To show this, Fig. 3.2(d) displays the sampled temperature vs. time for $\tau = 0.1$ and 5 ns. The amplitude decreases with τ due to cooling of the sample after pulse absorption, while the phase lag increases simply by definition.

Notice that I have not mentioned anything about a real or imaginary portion of temperature rise. TDTR and FDTR can be completely understood and modeled without these concepts. However, where it becomes useful to invoke these concepts is when we analyze data collected by the lock-in amplifier. Outlined in Fig. 3.4, lock-in amplification of a signal extracts the amplitude and phase of the signal by mixing (multiplying) the signal with a reference wave having a defined phase. In TDTR and FDTR, the pump is this reference. Although there is an additional phase shift the signal receives from the electronics, this can be offset or corrected after data is taken [119]. So, we can describe the reference signal (V_{ref}) by a cosine wave with angular modulation frequency ω_0 ,

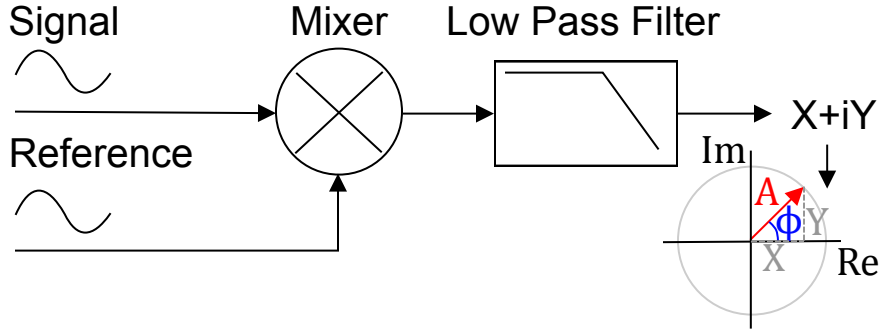


Figure 3.4: The lock-in amplifier mixes a reference and signal wave. The product is sent to a low pass filter to extract the in-phase and out-of-phase components.

$$V_{\text{ref}}(t) = V_0 \cos(\omega_0 t), \quad (3.2)$$

where V_0 is the average voltage of the reference. The signal voltage (V_{sig}), following the temperature rise, is then a cosine wave with phase shift ϕ . But to show the power of lock-in amplification, we can include any other arbitrary function $f(t)$ that might be present as noise. The signal is then

$$V_{\text{sig}}(t) = V_1 \cos(\omega_0 t + \phi) + f(t). \quad (3.3)$$

where V_1 is the average voltage of the oscillatory signal. The mixed signal is then

$$\begin{aligned} V_{\text{mixed}} &= V_{\text{sig}}(t) \times V_{\text{ref}}(t) = V_0 \cos(\omega_0 t) * [V_1 \cos(\omega_0 t + \phi) + f(t)] \\ &= \frac{1}{2} V_0 V_1 \cos(2\omega_0 t + \phi) + \frac{1}{2} V_0 V_1 \cos(\phi) + V_0 f(t) \cos(\omega_0 t). \end{aligned} \quad (3.4)$$

This signal is then sent through a low-pass filter that effectively picks out only the DC component of V_{mixed} , rejecting all components with a frequency dependence. This leaves only

$$X = \frac{1}{2} V_0 V_1 \cos(\phi), \quad (3.5)$$

where X is defined as this DC component, and is described as the *in-phase* component since we

described both the reference and source by the same oscillatory base function, in this case a cosine wave. However, the lock-in also performs this same process with another, 90° shifted reference, described mathematically by a sine wave. It is straightforward to show that this process results in a DC component of

$$Y = \frac{1}{2}V_0V_1 \sin(\phi), \quad (3.6)$$

where Y is the *out-of-phase* component because it results from mixing a second reference 90 degrees out-of-phase with the first. Instead of describing these two processes independently, we can instead describe them by complex functions, so the reference is $V_{\text{ref}} = V_0 e^{i\omega t}$. The lock-in process then results in an output of $X + iY$, which can be converted back to the signal amplitude (A) and phase (ϕ) by a simple coordinate transform, shown in the inset to Fig. 3.4. By invoking complex numbers, we see the emergence of real and imaginary components that correspond simply to the in-phase and out-of-phase components of the measured signal.

3.4 Mathematical Formalism

3.4.1 Pump Heating

The pump/probe experiments used in this dissertation rely on the same premise: using a periodic pump laser to heat a sample and a probe laser to detect the resulting change in temperature within the probed volume. Because of this common premise, we will derive a general form for the temperature rise that occurs during laser heating so that it can be applied to any pump/probe experiment, including pulsed pump/ pulsed probe, pulsed pump/ continuous wave probe, continuous wave pump/ pulsed probe, and continuous wave pump/ continuous wave probe. The basis for determining the temperature rise that occurs during laser heating is the heat diffusion equation. Because laser spots are generally circular, it is convenient to work in cylindrical coordinates so that the radial symmetry simplifies the dimension to two. The heat diffusion equation in cylindrical

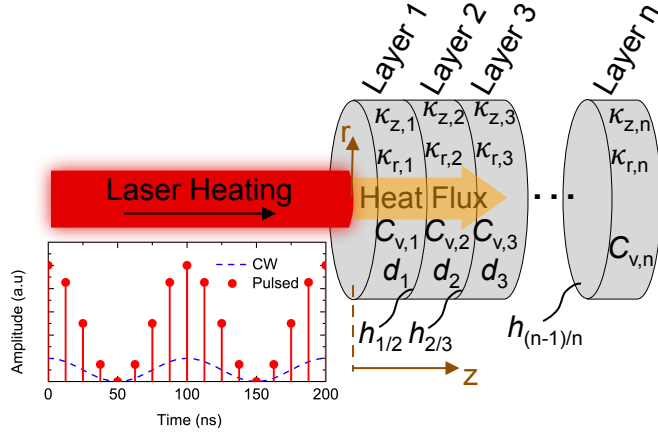


Figure 3.5: Sample schematic of a sample with n layers. All parameters used are listed within their respective layers to include in-plane and out-of-plane thermal conductivity (κ_r and κ_z), volumetric heat capacity ($C_v = \rho c_p$, where ρ is mass density and c_p is specific heat capacity), and thickness (d). Note that the final layers do not include d to emphasize that they are semi-infinite with respect to the thermal length scales of laser heating. The inset shows the time-dependent functions governing the laser heat source for both pulsed (repetition rate of 80 MHz) and CW cases with modulation at 10 MHz.

coordinates with radial symmetry and a volumetric heating source is given by

$$\kappa_r \left\{ \frac{1}{r} \frac{\partial T(z, r, t)}{\partial r} + \frac{\partial^2 T(z, r, t)}{\partial r^2} \right\} + \kappa_z \frac{\partial^2 T(z, r, t)}{\partial z^2} + S(z, r, t) = C_v \frac{\partial T(z, r, t)}{\partial t} \quad (3.7)$$

where κ_r and κ_z are in-plane and cross-plane thermal conductivity, respectively, T is the temperature (relative to some initial temperature) at a given location and time, r denotes radius (in-plane), z denotes depth (cross-plane) and is orthogonal to r , S is the heat source, C_v is the volumetric heat capacity ($C_v = \rho c_p$, where ρ is the mass density and c_p is the specific heat capacity), and t is the time. For a surface adjacent to an insulating medium (such as air), the boundary condition is given by

$$T(0, r, t) = T_{\text{top}}(r, t) \quad (3.8)$$

$$\left. \frac{\partial T(z, r, t)}{\partial z} \right|_{z=0} = -\frac{1}{\kappa_z} Q_{\text{top}}(r, t) = 0, \quad (3.9)$$

where $T_{\text{top}}(r, t)$ is the temperature rise and $Q_{\text{top}}(r, t)$ is the depth-component of heat flux at the top surface ($z = 0$) of a given material. The laser heating term is incorporated into $S(z, r, t)$ in order to include the heat deposition in depth resulting from a nonzero optical absorption depth of the laser. In some cases, as will be shown later, one can assume the heat is entirely deposited at the surface ($z = 0$) so that the laser heating can be treated instead as a boundary condition [120]. In the general case, however, S is defined as [121]

$$S(z, r, t) = F(z)P(r)G(t) = \frac{2}{\pi r_0^2 \zeta_0 \left[1 - \exp\left(-\frac{d_1}{\zeta_0}\right) \right]} \exp\left(-\frac{2r^2}{r_0^2}\right) \exp\left(-\frac{z}{\zeta_0}\right) G(t) \quad (3.10)$$

where $P(r)$ describes the radial distribution of the laser beam heating source, $G(t)$ describes the time response of this source, and $F(z)$ describes the distribution of the heating source in the cross-plane direction. Thus, the source term is decoupled into three functions. The right hand side of Eq. (3.10) assumes that $P(r)$ takes on a Gaussian profile with r_0 describing the $1/e^2$ radius of the beam, and the expression for $F(z)$ comes from consideration of the optical penetration depth, ζ_0 , and the thickness of the absorbing layer, d_1 [121]. Two cases for $G(t)$ are considered, a pulsed source and a CW source. In the pulsed case, the time dependence of the beam is represented as a train of delta functions,

$$G_{\text{pulsed}}(t) = \sum_{n=-\infty}^{\infty} \frac{\alpha_0 A_0}{f_s} \delta(t - n/f_s), \quad (3.11)$$

where the absorbed laser energy at the surface is given by the absorption of the sample, α_0 , multiplied by energy per pulse, A_0/f_s where A_0 is the time-averaged amplitude of laser power and f_s is the laser repetition rate. In this study, we consider only sub-picosecond pulses, such that the expression of laser pulses as delta functions can be assumed without significant loss of accuracy. The sum is taken over all pulses to account for any accumulation of heat over time. The continuous wave laser heating event is simple by comparison, given by

$$G_{\text{CW}}(t) = \alpha_0 A_0, \quad (3.12)$$

such that $G(t)$ is constant with time. In both cases, $G(t)$ is described in units of [W] such that $S(z, r, t)$ obtains the desired units of [W/m³].

Typically in optical pump-probe experiments such as TDTR and FDTR, an amplitude modulation at angular frequency ω_0 [rad/s] is applied to the pump beam. To keep this analysis general, all equations are derived using a modulated heat source, noting that the solution is equivalent to that of an unmodulated source when $\omega_0 = 0$. Thus, given the same absorbed average power of $\alpha_0 A_0$, the fully extinguished sinusoidally modulated source terms for pulsed and CW sources, respectively, can be expressed as

$$G_{\text{pulsed}}(t) = \frac{\alpha_0 A_0}{f_s} (\mathrm{e}^{i\omega_0 t} + 1) \sum_{n=-\infty}^{\infty} \delta(t - n/f_s) \quad (3.13)$$

$$G_{\text{CW}}(t) = \alpha_0 A_0 (\mathrm{e}^{i\omega_0 t} + 1) \quad (3.14)$$

These power functions are displayed in the inset to Fig. 3.5. Given the radial symmetry and the periodic nature of the time varying heat source, Eq. (3.7) is conveniently solved in Hankel and frequency space. Taking the Hankel and Fourier transforms, the heat diffusion equation becomes

$$-\kappa_r k^2 \tilde{T}(z, k, \omega) + \kappa_z \frac{\partial^2 \tilde{T}(z, k, \omega)}{\partial z^2} + \tilde{S}(z, k, \omega) = C_v \tilde{T}(z, k, \omega) \quad (3.15)$$

where k denotes the Hankel transform variable and ω denotes the frequency space variable upon taking the Fourier transform. The notation used here is such that for a function $Y(z, r, t)$, \tilde{Y} denotes the Fourier transform of Y , while $\tilde{\tilde{Y}}$ denotes the Hankel transform of \tilde{Y} . The transformed source term becomes

$$\tilde{S}(z, k, \omega) = \frac{\exp\left(-\frac{k^2 r_0^2}{8}\right) \exp\left(-\frac{z}{\xi_0}\right)}{2\pi \xi_0 \left[1 - \exp\left(-\frac{d_1}{\xi_0}\right)\right]} \tilde{G}(\omega). \quad (3.16)$$

Eq. (3.15) can then be simplified to

$$\frac{\partial^2 \tilde{T}(z, k, \omega)}{\partial z^2} = q^2 \tilde{T}(z, k, \omega) - \frac{\tilde{S}(z, k, \omega)}{\kappa_z}, \quad (3.17)$$

where

$$q^2 = \frac{\kappa_r k^2 + i C_v \omega}{\kappa_z}. \quad (3.18)$$

The solution to this ordinary differential equation can be obtained using the method of undetermined coefficients, such that it takes the form

$$\tilde{T}(z, k, \omega) = \tilde{a} \cosh(qz) + \tilde{b} \sinh(qz) + \tilde{c} e^{-z/\zeta_0}, \quad (3.19)$$

The last term is the particular solution resulting from the heat source term; thus, this term alone should satisfy Eq. (3.17), allowing for \tilde{c} to be obtained. Applying the boundary conditions given by Eq. (3.8) and Eq. (3.9) allows for the following solution to be obtained:

$$\tilde{T}(z, k, \omega) = \cosh(qz) \tilde{T}_{\text{top}} + \frac{\tilde{c}(k, \omega)}{\kappa_z} \left(-\frac{1}{q} \sinh(qz) + \zeta_0 \cosh(qz) - \zeta_0 e^{-z/\zeta_0} \right), \quad (3.20)$$

where

$$\tilde{c}(k, \omega) = \frac{\exp\left(-\frac{k^2 r_0^2}{8}\right) \tilde{G}(\omega)}{2\pi \left[1 - \exp\left(-\frac{d_1}{\zeta_0}\right) \right] (1 - q^2 \zeta_0^2)}. \quad (3.21)$$

the cross-plane component of heat flux is determined by

$$\tilde{Q}(z, k, \omega) \equiv -\kappa_z \frac{\partial T}{\partial z} = -\kappa_z q \sinh(qz) \tilde{T}_{\text{top}} + \tilde{c}(k, \omega) \left(\cosh(qz) - \zeta_0 q \sinh(qz) - e^{-z/\zeta_0} \right). \quad (3.22)$$

In matrix form, Eqs (3.20) and (3.22) can be expressed as

$$\begin{bmatrix} \tilde{T}(z, k, \omega) \\ \tilde{Q}(z, k, \omega) \end{bmatrix} = \begin{bmatrix} \cosh(qz) & \frac{1}{\kappa_z} \left(-\frac{1}{q} \sinh(qz) + \zeta_0 \cosh(qz) - \zeta_0 e^{-z/\zeta_0} \right) \\ -q\kappa_z \sinh(qz) & \left(\cosh(qz) - \zeta_0 q \sinh(qz) - e^{-z/\zeta_0} \right) \end{bmatrix} \begin{bmatrix} \tilde{T}_{\text{top}}(k, \omega) \\ \tilde{Q}_{\text{top}}(k, \omega) \end{bmatrix} \quad (3.23)$$

for z between 0 and d_1 . Thus, knowing the temperature at the top surface allows the acquisition of the entire depth-dependent temperature and heat flux profiles. While the solution up to this point has been generalized to account for a depth-dependent heating source, in many cases, e.g., in TDTR and FDTR relying on metal transducers, an assumption of surface heating is reasonable, in which case in the limit as $\zeta_0 \rightarrow 0$ Eq. (3.23) simplifies to

$$\begin{bmatrix} \tilde{T}(z) \\ \tilde{Q}(z) \end{bmatrix} = \begin{bmatrix} \cosh(qz) & -\frac{1}{q\kappa_z} \sinh(qz) \\ -q\kappa_z \sinh(qz) & \cosh(qz) \end{bmatrix} \begin{bmatrix} \tilde{T}_{\text{top}} \\ \tilde{Q}_{\text{top}} \end{bmatrix}, \quad (3.24)$$

where

$$\tilde{Q}_{\text{top}}(k, \omega) = \frac{1}{2\pi} \exp\left(-\frac{k^2 r_0^2}{8}\right) \tilde{G}(\omega). \quad (3.25)$$

This solution is generalized to layered systems by noting that Eq. (3.24) is valid for any layer in which \tilde{T}_{top} and \tilde{Q}_{top} for that layer are known. While the heat flux is prescribed to layer 1, the temperature at this surface is unknown. To obtain this quantity, we invoke a semi-infinite boundary condition at the back side of the final layer of some system having n layers (refer to Fig. 3.5), such that the following condition holds

$$\lim_{z \rightarrow \infty} \tilde{Q}_n(z) = 0. \quad (3.26)$$

Applying this condition to the n^{th} layer allows the determination of $\tilde{T}_{\text{top},n}$ and $\tilde{Q}_{\text{top},n}$, defined to be the temperature and heat flux at the surface of layer n , i.e., at $z = \sum_{i=1}^{n-1} d_i$. These quantities can then be related to the bottom temperature and heat flux of the $(n-1)^{\text{th}}$ layer through the thermal boundary conductance (TBC), $G_{(n-1)/n}$, mathematically represented in matrix notation by

$$\begin{bmatrix} \tilde{T}_{\text{bot},n-1} \\ \tilde{Q}_{\text{bot},n-1} \end{bmatrix} = \begin{bmatrix} 1 & -\frac{1}{G_{(n-1)/n}} \\ 0 & 1 \end{bmatrix} \begin{bmatrix} \tilde{T}_{\text{top},n} \\ \tilde{Q}_{\text{top},n} \end{bmatrix}, \quad (3.27)$$

so that the bottom temperature and heat flux of the $(n-1)^{\text{th}}$ layer are known, allowing for the solution to the temperature and heat flux at the top of this layer as well. This process can be repeated for an arbitrary number of layers until ultimately the temperature at the top of layer 1 is determined. This matrix approach [94, 95, 122, 123] can then be generalized so that the temperature and heat flux within the n^{th} layer can be determined from

$$\begin{bmatrix} \tilde{T}_n(z) \\ \tilde{Q}_n(z) \end{bmatrix} = \begin{bmatrix} \cosh(q_n z_n) & -\frac{1}{q_n \kappa_{z,n}} \sinh(q_n z_n) \\ -q_n \kappa_{z,n} \sinh(q_n z_n) & \cosh(q_n z_n) \end{bmatrix} \times \prod_{i=n-1, n-2, \dots}^{i=1} \mathbf{M}_i \mathbf{N}_i \begin{bmatrix} \tilde{T}_{\text{top}} \\ \tilde{Q}_{\text{top}} \end{bmatrix} = \begin{bmatrix} \tilde{A} & \tilde{B} \\ \tilde{C} & \tilde{D} \end{bmatrix} \begin{bmatrix} \tilde{T}_{\text{top}} \\ \tilde{Q}_{\text{top}} \end{bmatrix}, \quad (3.28)$$

where

$$\mathbf{M}_j = \begin{bmatrix} \cosh(q_j d_j) & -\frac{1}{q_j z_j} \sinh(q_j z_j) + \frac{1-f(j)}{\kappa_z} \left(\zeta_0 \cosh(q_j z_j) - \zeta_0 e^{-z_j/\zeta_0} \right) \\ -q_j \kappa_z \sinh(q_j d_j) & \cosh(q_j d_j) \end{bmatrix}, \quad (3.29)$$

$$\mathbf{N}_j = \begin{bmatrix} 1 & -\frac{f(j)}{G_{(j-1)/j}} \\ 0 & 1 \end{bmatrix}, \quad (3.30)$$

$$f(j) = \begin{cases} 1 & j \neq 1 \\ 0 & j = 1 \end{cases}, \quad (3.31)$$

$$q_j^2 = \frac{1}{\kappa_{z,j}}(i\omega C_{v,j} + \kappa_{r,j}k^2). \quad (3.32)$$

Here, z_n is defined as $z_n = z - \sum_j^{n-1} d_j$ such that $z_n = 0$ corresponds to the top surface of the n^{th} layer. Note that this set of equations can be used to solve the temperature profile in any given layer once T_{top} is obtained, since n can represent any layer of interest. To proceed, though, without loss of generality we assume the n^{th} layer denotes the final, semi-infinite layer of this geometry. Then, \tilde{T}_{top} is determined by invoking the aforementioned semi-infinite boundary condition described in Eq. (3.26), such that

$$\tilde{T}_{\text{top}} = -\frac{\tilde{D}}{\tilde{C}} \tilde{\xi}_{\text{top}}. \quad (3.33)$$

Since $\tilde{\xi}_{\text{top}}$ is a well-defined function given by Eq. (3.21), \tilde{T}_{top} can be obtained. To obtain this solution in radial space and time, the inverse Hankel and Fourier transforms are performed on \tilde{T}_{top} . Taking first the inverse Hankel transform yields

$$\begin{aligned} \tilde{T}_{\text{top}}(r, \omega) &= \int_0^\infty -\left(\frac{\tilde{D}}{\tilde{C}}\right) \tilde{\xi}_{\text{top}} J_0(kr) k dk \\ &= \frac{-\tilde{G}(\omega)}{2\pi \left[1 - \exp\left(-\frac{d_1}{\zeta_0}\right)\right]} \int_0^\infty \frac{1}{(1 - q_1^2 \zeta_0^2)} \left(\frac{\tilde{D}}{\tilde{C}}\right) \exp\left(-\frac{k^2 r_0^2}{8}\right) J_0(kr) k dk \\ &= \tilde{L}(r, \omega) \tilde{G}(\omega), \end{aligned} \quad (3.34)$$

and J_0 is the zeroth-order Bessel function of the first kind and $\tilde{L}(r, \omega)$ is defined to simplify notation.

That is,

$$\tilde{L}(r, \omega) = \frac{-1}{2\pi \left[1 - \exp\left(-\frac{d_1}{\zeta_0}\right)\right]} \int_0^\infty \frac{1}{(1 - q_1^2 \zeta_0^2)} \left(\frac{\tilde{D}}{\tilde{C}}\right) \exp\left(-\frac{k^2 r_0^2}{8}\right) J_0(kr) k dk. \quad (3.35)$$

The integration resulting from taking the inverse Hankel transform can be performed numerically; the upper bound of the integral can be set to $2/r_0$ without significant loss of accuracy [94]. Next, taking the inverse Fourier transform yields the desired temperature solution in radial and time coordinates,

$$T_{\text{top}}(r, t) = \frac{1}{2\pi} \int_{-\infty}^{\infty} \tilde{L}(r, \omega) \tilde{G}(\omega) e^{i\omega t} d\omega. \quad (3.36)$$

Thus, T_{top} is completely characterized, in principle. In practice, there are several simplifying assumptions that can be made based on the specific form of $\tilde{G}(\omega)$.

Beginning with the modulated CW source described by Eq. (3.14), $\tilde{G}(\omega)$ can be written as

$$\tilde{G}_{\text{CW}}(\omega) = \mathcal{F}\{G_{\text{CW}}(t)\} = 2\pi\alpha_0 A_0 \left(\delta(\omega - \omega_0) + \delta(\omega) \right), \quad (3.37)$$

whereas the modulated pulsed source given by Eq. (3.13) becomes

$$\tilde{G}_{\text{pulsed}}(\omega) = \mathcal{F}\{G_{\text{pulsed}}(t)\} = 2\pi\alpha_0 A_0 \left(\sum_{n=-\infty}^{\infty} \delta(\omega - \omega_0 - n\omega_s) + \delta(\omega - n\omega_s) \right) \quad (3.38)$$

where ω_s is defined as $2\pi f_s$ and \mathcal{F} denotes the Fourier transform operation. Interestingly, in the frequency domain the only difference between the pulsed and CW source terms is the additional sum over n pulses for the pulsed case. The delta function representation of these expressions makes the transformation from frequency space to time relatively simple. In the CW case, the expression for T_{top} becomes

$$\begin{aligned} T_{\text{top,CW}}(r, t) &= \alpha_0 A_0 \int_{-\infty}^{\infty} \tilde{L}(r, \omega) \left(\delta(\omega - \omega_0) + \delta(\omega) \right) e^{i\omega t} d\omega \\ &= \alpha_0 A (\tilde{L}(r, \omega_0) e^{i\omega_0 t} + \tilde{L}(r, 0)), \end{aligned} \quad (3.39)$$

whereas in the pulsed case, the expression for T_{top} takes the form

$$\begin{aligned} T_{\text{top,pulsed}}(r,t) &= \alpha_0 A_0 \int_{-\infty}^{\infty} \tilde{L}(r,\omega) e^{i\omega t} \left(\sum_{n=-\infty}^{\infty} \delta(\omega - \omega_0 - n\omega_s) + \delta(\omega - n\omega_s) \right) d\omega \\ &= \alpha_0 A_0 \left(\sum_{n=-\infty}^{\infty} \tilde{L}(r, \omega_0 + n\omega_s) e^{i(\omega_0 + n\omega_s)t} + \tilde{L}(r, n\omega_s) \right). \end{aligned} \quad (3.40)$$

It is clear that in both the CW and pulsed modulated heating cases, there are two contributions to the temperature rise at the surface: a steady state, “DC” temperature rise governed by the average power deposited into the sample, and a modulated, “AC” temperature rise associated with amplitude modulation at a fixed frequency. Decoupling the terms and recognizing that $T_{\text{top}} = T_{\text{top,DC}} + T_{\text{top,AC}}$, the temperature rises for the CW case are given by

$$T_{\text{top,DC,CW}} = \alpha_0 A_0 \tilde{L}(r, 0) \quad (3.41)$$

$$T_{\text{top,AC,CW}} = \alpha_0 A_0 \tilde{L}(r, \omega_0) e^{i\omega_0 t}, \quad (3.42)$$

while those of the pulsed case are given by

$$T_{\text{top,DC,pulsed}} = \alpha_0 A_0 \sum_{n=-\infty}^{\infty} \tilde{L}(r, n\omega_s) \quad (3.43)$$

$$T_{\text{top,AC,pulsed}} = \alpha_0 A_0 \sum_{n=-\infty}^{\infty} \tilde{L}(r, \omega_0 + n\omega_s) e^{i(\omega_0 + n\omega_s)t}. \quad (3.44)$$

These equations completely describe the temperature rise at the top surface of layer 1. With T_{top} known, $T(z, r, t)$ can be explicitly calculated in any layer within a sample having layered structures by invoking Eq. (3.28) and transforming back to real space and time.

Equations (3.41) - (3.44) completely describe the surface temperature distribution as a function of radius and time for a CW and pulsed, respectively. The change in reflectivity detected by the probe, however, is a weighted average over this temperature distribution. As detailed in the next subsection, for a near surface probe absorption, the photodetector measures a reflectance

signal proportional to a Gaussian-averaged temperature distribution about the probe radius, r_1 , represented by

$$T_{\text{probed}} = \frac{4}{r_1^2} \int_0^\infty T_{\text{top}} \exp\left(\frac{-2r^2}{r_1^2}\right) r dr. \quad (3.45)$$

where r_1 is the probe radius. Using Eq. 3.45, the probe averaged temperature rise can be modeled completely. We now calculate the probe averaged temperature rise for two samples: a-SiO₂ and Si coated with an 80 nm Al transducer (both common TDTR/FDTR calibration samples). The parameters used in the model and the rest of this chapter are listed in Table 3.1. Figure 3.6 (a)-(c) shows the pump power vs. time used in this calculation for both a pulsed and CW pump. The absorption of power is assumed to be $\alpha_0 = 0.1$, the pump and probe diameters are 10 μm, and the modulation frequency is 10 MHz. Figure 3.6 (d)-(e) show the resulting total, AC, and DC temperature rises for the case of a-SiO₂, while Fig. 3.6 (f)-(g) show the total, AC, and DC temperature rises for the case of Si. Comparison of these two cases makes clear that steady-state heating of the a-SiO₂ is significantly higher than Si. However, in TDTR and FDTR, lock-in detection ensures that only the AC temperature rise is captured. So, from a modeling perspective, only the AC temperature rise needs to be determined to compare with TDTR/FDTR data. Still, this steady-state temperature rise can have an indirect, often impactful, influence on a measurement.

3.4.2 Probe Detection and Signal Analysis

TDTR and FDTR work on the premise of detecting the time varying probe power after reflection from the heated sample. The probe beam incident absorbed flux takes a similar profile to that of the pump, given by

$$Q_1(z, r, t) = \frac{2}{\pi r_1^2 \zeta_1 \left[1 - \exp\left(-\frac{d_1}{\zeta_1}\right) \right]} \exp\left(-\frac{2r^2}{r_1^2}\right) \exp\left(-\frac{z}{\zeta_1}\right) G_1(t) \quad (3.46)$$

where ζ_1 is the optical penetration depth of the probe beam, r_1 is the probe 1/e² radius, and G_1 defines how the probe power varies with time. As with the pump, the probe can be pulsed or CW;

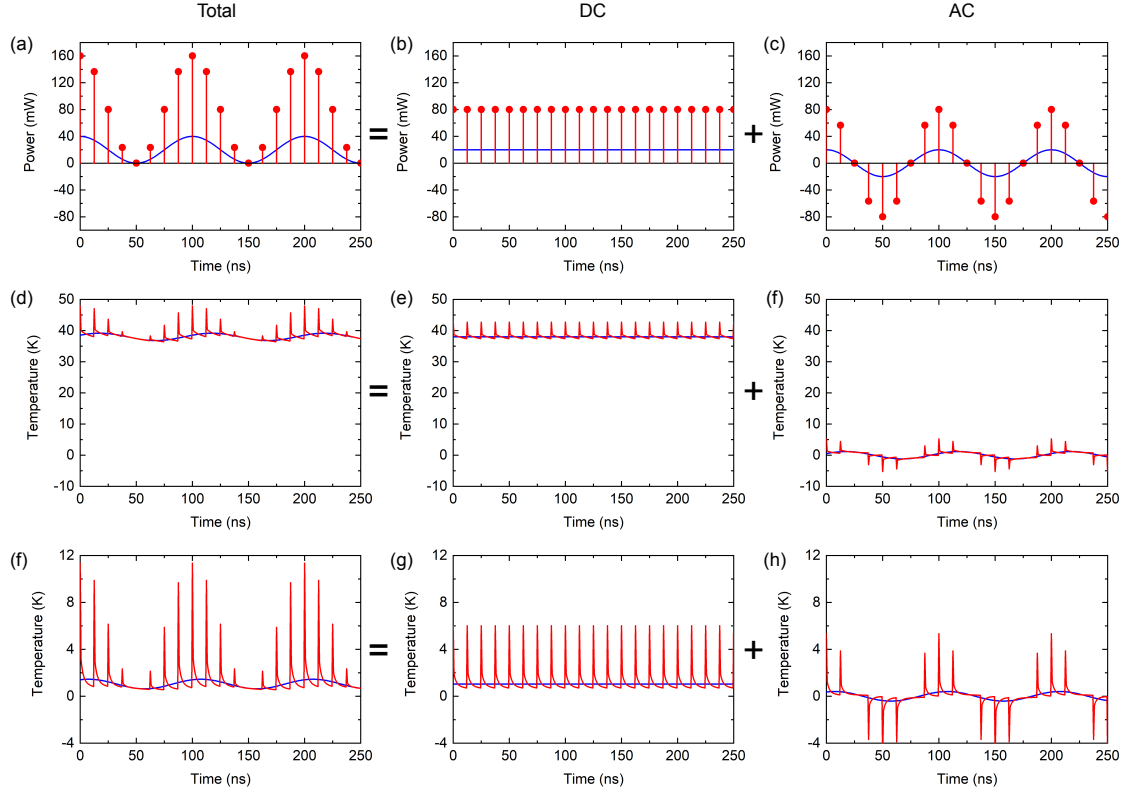


Figure 3.6: (a) Total pump power vs. time, shown for a pulsed (red) and CW (blue) source having the same average power. (b) DC component of the pump power. (c) AC component of the pump power. (d)-(e) Total, DC, and AC temperature rises for 80 nm Al on a-SiO₂. (f)-(h) Total, DC, and AC temperature rises for 80 nm Al on Si. In all cases, $r_0 = r_1 = 5 \mu\text{m}$, $\alpha_0 A_0 = 2 \text{ mW}$, and $f_{\text{mod}} = 10 \text{ MHz}$.

both cases are considered below. In the pulsed case, consider a pulsed probe separated in time with respect to the pump beam by τ . Then,

$$G_{1,\text{pulsed}}(t) = \frac{\alpha_1 A_1}{f_s} \sum_{m=-\infty}^{\infty} \delta(t - m/f_s - \tau), \quad (3.47)$$

where α_1 and A_1 are the probe absorption and power, respectively. In the CW case,

$$G_{1,\text{CW}}(t) = \alpha_1 A_1. \quad (3.48)$$

The reflected probe power is determined by

$$Q_{1,R} = (R_0 + \Delta R) Q_1, \quad (3.49)$$

Table 3.1: Room temperature thermal parameters used in calculating temperature rises in this study. κ_r is thermal conductivity [$\text{W m}^{-1} \text{K}^{-1}$] in the radial (in-plane) direction, κ_z is thermal conductivity [$\text{W m}^{-1} \text{K}^{-1}$] in the z (out-of-plane) direction, C_v is volumetric heat capacity [$\text{J cm}^{-3} \text{K}^{-1}$], and $G_{\text{Al(Au)/x}}$ is the thermal boundary conductance [$\text{MW m}^{-2} \text{K}^{-1}$] between Al(Au) and the material of interest.

Material	κ_z	κ_r	C_v	$G_{\text{Al/x}}$	$G_{\text{Au/x}}$
C_{60}	0.097 ^a	0.097 ^a	1.3 ^a	100 ^b	-
Polymer	0.2 ^c	0.2 ^c	2.0 ^c	26 ^d	-
a-Si	1.3 ^e	1.3 ^e	1.62 ^f	100 ^b	-
a-SiO ₂	1.4 ^g	1.4 ^g	1.62 ^f	100 ^b	50 ^h
Si	140 ^f	140 ^f	1.62 ^f	100 ⁱ	-
Al	135 ^b	135 ^j	2.42 ^k	∞	-
Au	220 ^b	220 ^j	2.49 ^k	-	∞

^a Reference [51]; ^b Estimated value, in practice this does not play a role in the temperature rise calculation ; ^c Reference [124]; ^d Reference [125]; ^e Reference [121]; ^f Reference [61]; ^g Reference [22]; ^h Measured using TDTR; ⁱ Reference [126]; ^j Measured using four-point probe resistivity and applying the Wiedemann-Franz law; ^k Reference [127].

where ΔR is change in reflectance due to laser heating. From Eq. (3.1) ΔR can be, for small temperature rises, estimated based on its proportionality to the change in temperature.

$$\Delta R = R_0 \beta \Delta T = \beta_0 \Delta T, \quad (3.50)$$

where for convenience β_0 , which is an alternative way to describe the thermoreflectance coefficient, is defined. From the previous section, we know that there is a DC and AC component to the temperature rise. Assuming the thermoreflectance coefficient is still linear for the DC component (we will revisit this assumption later) the reflected power in the frequency domain can be written

$$\mathcal{F}\{Q_{1,r}\} = \int_{-\infty}^{\infty} \left(R_0 + \beta_0 \Delta \tilde{T}(z, r, \omega') \right) \tilde{Q}_1(z, r, \omega - \omega') d\omega. \quad (3.51)$$

The reflected probe illuminates a photodetector to generate a photocurrent. The current through a phototransistor is directly proportional to the intensity of the incident light. The voltage measured is a function of this current and for typical PIN photodiodes has a linear relation. Therefore, the photodetector voltage can be written as

$$\begin{aligned}
v_{PD}(t) &= \gamma(1-l)(Q_{1,R})_{wa} = \gamma(1-l)((R_0 + \Delta R)(Q_1))_{wa} \\
&= \gamma(1-l) \int_0^\infty \int_0^\infty (R_0 + \beta_0 \Delta T(z, r, t)) Q_1(z, r, t) 2\pi r dr dz \\
&= \gamma(1-l) R_0 \int_0^\infty \int_0^\infty Q_1(z, r, t) 2\pi r dr dz + \gamma(1-l) \beta_0 \int_0^\infty \int_0^\infty \Delta T(z, r, t) Q_1(z, r, t) 2\pi r dr dz \\
&= v_0(t) + \Delta v(t),
\end{aligned} \tag{3.52}$$

where γ is a constant of proportionality relating to the conversion of intensity to voltage, l accounts for any losses associated with the reflected light's path to the photodetector (mirrors, lenses, absorption in the air, etc.), and the “wa” subscript denotes the weighted average intensity. In the frequency domain, this is

$$v_{PD}(\omega) = v_0(\omega) + \Delta v(\omega). \tag{3.53}$$

Consider a pulsed probe beam and modulated pulsed pump beam

$$\begin{aligned}
\tilde{Q}_1 &= \frac{2}{\pi r_1^2 \zeta_1 \left[1 - \exp \left(-\frac{d_1}{\zeta_1} \right) \right]} \exp \left(-\frac{2r^2}{r_1^2} \right) \exp \left(-\frac{z}{\zeta_1} \right) \tilde{G}_1(\omega) = P_1(z, r) \tilde{G}_1(\omega) \\
&= 2\pi \alpha_1 A_1 P_1(z, r) e^{-i\omega\tau} \left(\sum_{m=-\infty}^{\infty} \delta(\omega - m\omega_s) \right),
\end{aligned} \tag{3.54}$$

where P_1 , introduced to simplify notation, is

$$P_1(z, r) = \frac{2}{\pi r_1^2 \zeta_1 \left[1 - \exp \left(-\frac{d_1}{\zeta_1} \right) \right]} \exp \left(-\frac{2r^2}{r_1^2} \right) \exp \left(-\frac{z}{\zeta_1} \right). \tag{3.55}$$

The total temperature rise for the modulated pulsed pump is given by Eqs. 3.43 and 3.44, so that

$$\Delta \tilde{T} = \tilde{L}_0(z, r, \omega) \tilde{G}_0(\omega) = \tilde{L}_0(z, r, \omega) 2\pi\alpha_0 A_0 \left(\sum_{n=-\infty}^{\infty} \delta(\omega - n\omega_s) + \delta(\omega - \omega_0 - n\omega_s) \right). \quad (3.56)$$

Therefore, the DC voltage becomes

$$v_0(\omega) = R_0 Q_1(z, r, \omega) = R_0 \sum_{m=-\infty}^{\infty} \int_0^{\infty} \int_0^{\infty} P_1(z, r) \delta(\omega - m\omega_s) 2\pi r dr dz, \quad (3.57)$$

while the change in voltage due to a change in reflectance is

$$\begin{aligned} \Delta v(\omega) &= \gamma\beta_0(1-l) \int_0^{\infty} \int_0^{\infty} \int_{-\infty}^{\infty} \Delta \tilde{T}(z, r, \omega') \tilde{Q}_1(z, r, \omega - \omega') 2\pi r d\omega' dr dz \\ &= (2\pi)^3 \gamma\beta_0 \alpha_0 \alpha_1 A_0 A_1 (1-l) \sum_{n=-\infty}^{\infty} \sum_{m=-\infty}^{\infty} \int_0^{\infty} \int_0^{\infty} \int_{-\infty}^{\infty} P_1(z, r) \tilde{L}_0(z, r, \omega') e^{-i(\omega-\omega')\tau} \delta(\omega' - \omega_0 - n\omega_s) \delta(\omega - \omega' - m\omega_s) d\omega' r dr dz \\ &\quad + (2\pi)^3 \gamma\beta_0 \alpha_0 \alpha_1 A_0 A_1 (1-l) \sum_{n=-\infty}^{\infty} \sum_{m=-\infty}^{\infty} \int_0^{\infty} \int_0^{\infty} \int_{-\infty}^{\infty} P_1(z, r) \tilde{L}_0(z, r, \omega') e^{-i(\omega-\omega')\tau} \delta(\omega' - n\omega_s) \delta(\omega - \omega' - m\omega_s) d\omega' r dr dz \\ &= (2\pi)^3 \gamma\beta_0 \alpha_0 \alpha_1 A_0 A_1 (1-l) \sum_{n=-\infty}^{\infty} \sum_{m=-\infty}^{\infty} \int_0^{\infty} \int_0^{\infty} P_1(z, r) \tilde{L}_0(z, r, \omega - m\omega_s) e^{-im\omega_s\tau} \delta(\omega - \omega_0 - (n+m)\omega_s) r dr dz \\ &\quad + (2\pi)^3 \gamma\beta_0 \alpha_0 \alpha_1 A_0 A_1 (1-l) \sum_{n=-\infty}^{\infty} \sum_{m=-\infty}^{\infty} \int_0^{\infty} \int_0^{\infty} P_1(z, r) \tilde{L}_0(z, r, \omega - m\omega_s) e^{-im\omega_s\tau} \delta(\omega - (n+m)\omega_s) r dr dz. \end{aligned} \quad (3.58)$$

Typically ΔR is orders of magnitude smaller than R_0 such that any changes in reflected probe signal detected by the photodetector are indistinguishable from noise. Balanced photodetectors allow for a way to reduce this dependence on R_0 . Under ideal conditions, the balanced photodetector will extract only the difference in intensity of the reflected probe beam and reflected signal, effectively eliminating R_0 from the previous equation. However, the noise fluctuations associated with this resulting voltage are generally still much greater than the changes in voltage resulting from ΔR . The lock-in amplifier provides a way to bypass this predicament, as it is responsible for locking into a specific frequency response to allow for signal-to-noise ratios significant to extract changes in probe reflected power. Locking into a frequency ω_{ref} means a narrow band of frequencies around ω_{ref} will contribute to the detected voltage after lock-in amplification. Mathematically,

this requires $\omega = \omega_{\text{ref}}$. Setting ω_{ref} to be ω_0 ensures the detected signal is that of the modulated heating event. In addition, the delta function in Eq. (3.58) will only be nonzero when $n = -m$. Finally, since ω_0 is limited by the Nyquist-Shannon sampling theorem to be less than $\omega_s/2$, and because the lock-in amplification filters out all frequency responses outside a narrow band around ω_0 , $V_0(\omega)$ is always zero for nonzero modulation frequencies. Additionally these criteria require the final term in Eq (3.58) to be zero, since any integer multiple of ω_s cannot be equal to ω_0 . These conditions imply that the voltage after amplification, V_{LA} , can be written

$$V_{\text{LA}}(\omega) = (2\pi)^3 \gamma \beta_0 \alpha_0 \alpha_1 A_0 A_1 \chi (1-l) \sum_{n=-\infty}^{\infty} \int_0^{\infty} \int_0^{\infty} P_1(z, r) \tilde{L}_0(z, r, \omega + n\omega_s) e^{in\omega_s \tau} \delta(\omega - \omega_0) r dr dz \quad (3.59)$$

where χ is introduced to represent the signal scaling that results from lock-in amplification. Finally, the lock-in response can be represented in the time-domain by taking the inverse Fourier transform

$$\begin{aligned} V_{\text{LA}}(t) &= (2\pi)^2 \gamma \beta_0 \alpha_0 \alpha_1 A_0 A_1 \chi (1-l) \\ &\times \sum_{n=-\infty}^{\infty} \int_0^{\infty} \int_0^{\infty} \int_{-\infty}^{\infty} P_1(z, r) \tilde{L}_0(z, r, \omega + n\omega_s) e^{in\omega_s \tau} \delta(\omega - \omega_0) e^{i\omega t} r d\omega dr dz \quad (3.60) \\ &= (2\pi)^2 \gamma \beta_0 \alpha_0 \alpha_1 A_0 A_1 \chi (1-l) e^{i\omega_0 t} \sum_{n=-\infty}^{\infty} \int_0^{\infty} \int_0^{\infty} P_1(z, r) \tilde{L}_0(z, r, \omega_0 + n\omega_s) e^{in\omega_s \tau} r dr dz. \end{aligned}$$

To simplify this expression, we need to expand the inner integral so that

$$\begin{aligned} \int_0^{\infty} P_1(z, r) \tilde{L}_0(z, r, \omega) 2\pi r dr &= \int_0^{\infty} P_1(z, r) 2\pi r dr \\ &\times \left[\int_0^{\infty} \left(-\cosh(q_1 z) \frac{\tilde{D}}{\tilde{C}} + \frac{1}{\kappa_z} \left(-\frac{1}{q_1} \sinh(q_1 z) + \zeta_0 \cosh(q_1 z) - \zeta_0 e^{-z/\zeta_0} \right) \right) \tilde{\zeta} J_0(kr) k dk \right]. \quad (3.61) \end{aligned}$$

To simplify notation, we introduce

$$\tilde{F}(z, k, \omega) \equiv -\cosh(q_1 z) \frac{\tilde{D}}{\tilde{C}} + \frac{1}{\kappa_z} \left(-\frac{1}{q_1} \sinh(q_1 z) + \zeta_0 \cosh(q_1 z) - \zeta_0 e^{-z/\zeta_0} \right), \quad (3.62)$$

Simplifying, the integral becomes

$$\begin{aligned} \int_0^\infty P_1(z, r) \tilde{L}_0(z, r, \omega) 2\pi r dr &= \int_0^\infty P_1(z, r) 2\pi r dr \left[\int_0^\infty \tilde{F}(z, k, \omega) \left(\frac{\exp\left(-\frac{k^2 r_0^2}{8}\right)}{2\pi \left[1 - \exp\left(-\frac{d_1}{\zeta_0}\right)\right] (1 - q^2 \zeta_0^2)} \right) J_0(kr) k dk \right] \\ &= \int_0^\infty \int_0^\infty \left(\frac{2}{\pi r_1^2 \zeta_1 \left[1 - \exp\left(-\frac{d_1}{\zeta_1}\right)\right]} \exp\left(-\frac{2r^2}{r_1^2}\right) \exp\left(-\frac{z}{\zeta_1}\right) \right) \tilde{F}(z, k, \omega) \left(\frac{\exp\left(-\frac{k^2 r_0^2}{8}\right)(\omega)}{2\pi \left[1 - \exp\left(-\frac{d_1}{\zeta_0}\right)\right] (1 - q^2 \zeta_0^2)} \right) J_0(kr) k dk 2\pi r dr \quad (3.63) \\ &= \int_0^\infty \left[\int_0^\infty \frac{2 \exp\left(-\frac{z}{\zeta_1}\right)}{\pi r_1^2 \zeta_1 \left[1 - \exp\left(-\frac{d_1}{\zeta_1}\right)\right]} \exp\left(-\frac{2r^2}{r_1^2}\right) r J_0(kr) dr \right] \tilde{F}(z, k, \omega) \left(\frac{\exp\left(-\frac{k^2 r_0^2}{8}\right)(\omega)}{\left[1 - \exp\left(-\frac{d_1}{\zeta_0}\right)\right] (1 - q^2 \zeta_0^2)} \right) k dk. \end{aligned}$$

The expression within the brackets of the last term in this equation is simply the Hankel transform of the probe intensity, i.e.,

$$\int_0^\infty \frac{2 \exp\left(-\frac{z}{\zeta_1}\right)}{\pi r_1^2 \zeta_1 \left[1 - \exp\left(-\frac{d_1}{\zeta_1}\right)\right]} \exp\left(-\frac{2r^2}{r_1^2}\right) r J_0(kr) dr = \frac{\exp\left(-\frac{z}{\zeta_1}\right)}{2\pi \zeta_1 \left[1 - \exp\left(-\frac{d_1}{\zeta_1}\right)\right]} \exp\left(-\frac{k^2 r_1^2}{8}\right). \quad (3.64)$$

Substituting, we define

$$\tilde{L}_{01}(z, k, \omega) = \frac{\exp\left(-\frac{z}{\zeta_1}\right) \tilde{G}_0(\omega)}{2\pi \zeta_1 \left[1 - \exp\left(-\frac{d_1}{\zeta_1}\right)\right] \left[1 - \exp\left(-\frac{d_1}{\zeta_0}\right)\right]} \int_0^\infty \frac{\tilde{F}(z, k, \omega)}{(1 - q^2 \zeta_0^2)} \exp\left(-\frac{k^2(r_0^2 + r_1^2)}{8}\right) k dk, \quad (3.65)$$

so that $V_{LA}(t)$ becomes

$$V_{LA}(t) = 2\pi\gamma\beta_0\alpha_0\alpha_1A_0A_1\chi(1-l)e^{i\omega_0 t} \sum_{n=-\infty}^{\infty} \int_0^{\infty} \tilde{L}_{01}(z, k, \omega_0 + n\omega_s) e^{in\omega_s \tau} k dk dz = Z(\omega_0, \tau) e^{i\omega_0 t}, \quad (3.66)$$

where $Z(\omega_0, \tau)$ is the transfer function relating the lock-in voltage to the temperature rise. It is emphasized that Z is a function of both ω_0 and τ , so that either parameter can be varied to change Z ; TDTR varies τ while FDTR varies ω_0 . Z includes all thermal properties and experimental parameters involved in TDTR. Remembering that the physical temperature rise is the real component only, the lock-in voltage is the real part of $V_{LA}(t)$, so that it can be described as

$$\begin{aligned} \text{Re}\{V_{LA}(t)\} &= \text{Re}\{Z(\omega_0, \tau) e^{i\omega_0 t}\} = \text{Re}\{Z(\omega_0, \tau)\} \cos(\omega_0 t) - \text{Im}\{Z(\omega_0, \tau)\} \sin(\omega_0 t) \\ &= X(\omega_0, \tau) \cos(\omega_0 t) - iY(\omega_0, \tau) \sin(\omega_0 t). \end{aligned} \quad (3.67)$$

where X and Y are defined to be the real and imaginary components of Z . In agreement with the simple picture provided in the previous conceptual overview, X and Y are constant for a given ω_0 and τ . Equation (3.67) is valid for a pulsed pump and pulsed probe. All other scenarios can be obtained in the same manner by substituting the appropriate form for the source term of the pump and probe.

3.4.3 Post Processing

The lock-in amplifier records the X and Y voltages as a function of probe delay time (TDTR) or modulation frequency (FDTR). As discussed previously, we provide a reference signal to the lock-in amplifier to mix with the signal wave to extract X and Y . In an ideal experiment, this reference phase will have the same phase as the pump relative to the probe. However, the electronics add an additional electronic phase shift that needs to be offset. This can be done manually by, for example, allowing the pump beam to bleed through to the probe photodetector to determine its phase. In TDTR, an easy alternative solution is to phase correct via post processing by ensuring

that the out-of-phase signal is constant across $\tau = 0$ [119]. Thus, the procedure is to determine ΔX_0 and ΔY_0 , the change in X signal Y signals as the delay time crosses $\tau = 0$. To ensure $\Delta Y_0 = 0$ after post processing, we can fix X and Y as followed

$$X_{\text{fixed}} = X \cos(\Delta\phi) - Y \sin(\Delta\phi), \quad (3.68)$$

$$Y_{\text{fixed}} = Y \cos(\Delta\phi) + X \sin(\Delta\phi), \quad (3.69)$$

where the $\Delta\phi = \tan^{-1}(\Delta Y_0 / \Delta X_0)$. In principle, once the phase corrected X and Y are obtained, they can be used to fit data from the derived model. However, with so many scaling parameters, many of which are difficult to quantify, it is not practical to do this. Instead, we can normalize the data and model to a specific time delay to get rid of these constants. This is sometimes done with X to improve sensitivity to certain parameters, namely thermal boundary conductance [114]. Similarly, often the amplitude of the signal, often called the *magnitude* when describing X and Y as complex functions, can be used to fit data after normalizing. The magnitude, M , is defined as

$$M = \sqrt{X^2 + Y^2}. \quad (3.70)$$

Even this, though, is not ideal, since noise can significantly influence the signal and the choice of normalization time can be ambiguous. Instead, it is far better to work with intrinsically unitless quantities - the phase lag and the ratio, defined respectively as

$$\phi = \tan^{-1} \left(\frac{-Y}{X} \right), \quad (3.71)$$

$$R = \frac{-X}{Y}. \quad (3.72)$$

Working with these has several benefits. In addition to avoiding normalization, using the phase or ratio naturally cancels many potential experimental errors and noise; any common such errors/noise are canceled upon division. As a note, using the phase or ratio is only possible with

continuous wave or high repetition rate lasers, as the out-of-phase signal approaches zero when there is no pulse accumulation [95]. The 80 MHz repetition rate of the oscillator used in this dissertation ensures we can obtain an out-of-phase signal for all materials studied.

3.5 Thermal Penetration Depth

The derived equations are now used to determine the spatially-dependent temperature profiles in order to study the thermal penetration depth (TPD) in bulk and thin film systems. This section provides answers to the questions of how the TPD is dependent on time and length scales of the laser heat source and sample geometry. In TDTR and FDTR, the TPD is of great importance as it relates a measurement length scale to the length scale of physical phenomena of interest. For example, interpretation of TDTR/FDTR extracted thermal properties' relation to physical processes relies on the idea that the TPD resulting from a modulated heating event can be orders of magnitude smaller than the pump radius, making it the defining length scale of the thermal response within the measurement volume. In fact, many of the recent advances in mean free path spectroscopy [117] stem from relating phonon mean free paths to the TPD imposed by a modulated heating event [115, 128–132]. Therefore, it is of utmost importance to properly characterize this length scale. This length scale is highly dependent on a multitude of variables that make accurate analytical predictions difficult for realistic sample geometries and conditions, suggesting a need for the rigorous calculations presented in this section. Such variables include time, modulation frequency, material and interface properties, and heater radius.

Beyond TDTR and FDTR, accurate predictions of TPD are highly valuable to several applications; pulsed and continuous wave (CW) laser applications are ubiquitous in both industry and scientific research. Many modern applications rely on laser heating to manipulate structural, mechanical, and electrical properties of materials. Pulsed laser heating, having versatile windows of energy duration ranging from femtoseconds to nanoseconds, is routinely used in materials and microstructure fabrication [133–135], materials processing [136], laser cutting and micro-machining [137], and property measurements through pump-probe techniques [96, 138–140]. Additionally,

with picosecond and sub-picosecond pulse durations, pulsed lasers can be used to provide high energy densities locally, providing a means for surface modification [141, 142]. Continuous wave laser heating, likewise, has major applications in welding, cutting, surface treatment [143] such as near-surface melting to modify wear and corrosion [144], and surface patterning [134]. In all such applications, it is necessary to understand the spatially-varying temperature profile that results from laser heating, since this temperature dictates material response.

The $1/e$ temperature decay TPD used to interpret TDTR and FDTR results is often estimated using the analytical solution to a 1-dimensional semi-infinite sample subject to a CW heating source modulated in the high frequency limit ($\omega_0 \gg D/r_0^2$, where ω_0 is modulation angular frequency, r_0 is pump radius, and D is thermal diffusivity) taking the form

$$\text{TPD} = \sqrt{\frac{2D}{\omega_0}}. \quad (3.73)$$

However, this equation breaks down when experimental conditions deviate from those on which this expression was derived. Considering commonly studied materials like silicon (Si), amorphous silicon dioxide (a-SiO₂), and aluminum (Al) on Si and a-SiO₂ reveals that such deviations can occur at modulation frequencies and pump radii common in TDTR and FDTR. To comply with Eq. (3.73) and the definition typically used in TDTR/FDTR, the TPD is defined as the distance away from the spatial coordinate of maximum temperature at which the temperature profile has decayed to $1/e$ of this maximum temperature.

In order to establish the upper limit to the obtainable TPD from a modulated heating event, consider the TPD associated with an unmodulated heating event. Since both modulated and unmodulated temperature profiles are considered, the definition of TPD is generalized to quantify the temperature decay both radially and in depth. This distinction is made because, when considering the modulated temperature profile simulating the heating event to which lock-in detection occurs during TDTR and FDTR, the temperature profile is typically one-dimensional; that is, the temperature decay extends in depth much less than radially. However, as the modulation frequency approaches zero, the TPD becomes large, on the order of pump radius, making the radial decay length important.

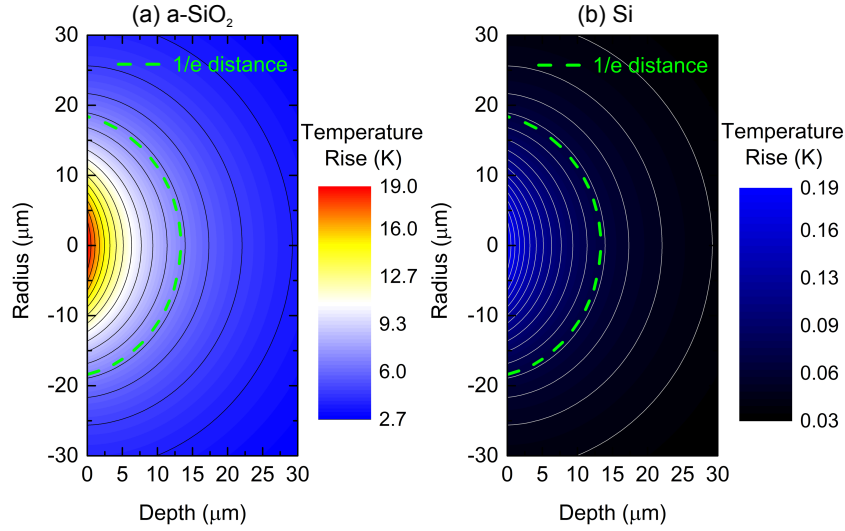


Figure 3.7: Temperature rise profiles for (a) bulk a-SiO₂ and (b) bulk Si subjected to a CW source with power $\alpha_0 A_0 = 1$ mW and $1/e^2$ gaussian radius of 15 μm . Also plotted in both cases is the $1/e$ distance away from the point of maximum temperature ($z = r = 0 \mu\text{m}$). For both SiO₂ and Si, the $1/e$ penetration depth is determined to be 13.3 μm at $r = 0 \mu\text{m}$ and is independent of absorbed power.

An unmodulated heating event is first considered to understand how the steady-state temperature profile and TPD compare when a source is constant (CW laser) vs. time-dependent (pulsed laser). Note that the unmodulated case fundamentally establishes the upper limit to the attainable TPD in the modulated case. The surface temperature for CW and pulsed sources are given by Eqs. (3.41) and (3.43). For a bulk system (homogeneous, semi-infinite material) irradiated with an unmodulated CW source, the TPD is determined to be independent of both pump power and thermal properties of the system; only radius of the heating event is directly correlated with TPD. Shown in Fig. 3.7 is the temperature profile for both bulk a-SiO₂ and bulk Si subjected to the same CW source having a heater radius $r_0 = 15 \mu\text{m}$ and average absorbed power of 1 mW. In both cases, the temperature decay from the maximum temperature is equivalent when normalized. However, it is clear that a-SiO₂, given the same heat flux, has a significantly higher temperature distribution. Nonetheless, the temperature decay with depth is proportionally the same in both cases. While this may seem counterintuitive in the context of optical thermometry techniques, as the thermal penetration depth is traditionally assumed to increase with increasing thermal con-

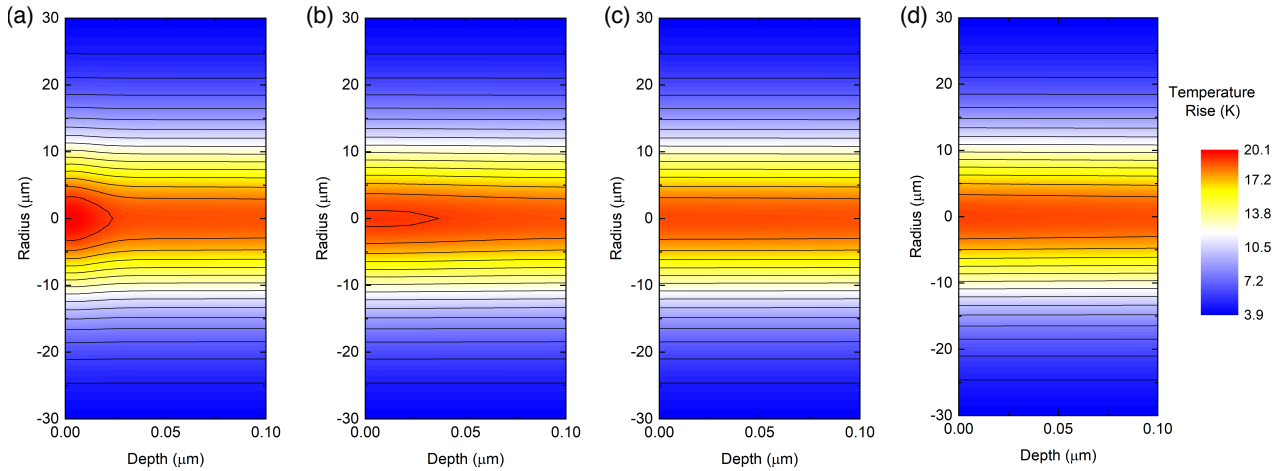


Figure 3.8: Near-surface temperature profile as a function of radius and depth for bulk a-SiO₂ subjected to a 80 MHz pulsed source as observed at (a) 100 ps, (b) 1 ns, (c) 10 ns, and (d) a CW source. In all cases, the average absorbed power is set to $\alpha_0 A_0 = 1$ mW and the 1/e² pump radius is 15 μm

ductivity, these results can be understood in the context of a simple Fourier analysis, given that the source is a constant heat flux. For example, in a one-dimensional example, given a constant heat flux boundary condition, Fourier's law implies $Q_{\text{top}} = -\kappa(dT/dz)$, so that the temperature is described by a linear function in z , $T(z) = -(Q_{\text{top}}/\kappa)z + T(0)$. The 1/e temperature decay, then, is simply $T(0)/e = -(Q_{\text{top}}/\kappa)z_{\text{TPD}} + T(0)$. Solving for TPD, $z_{\text{TPD}} = T(0)(1 - 1/e)(\kappa/Q_{\text{top}})$, but in accordance with Eq. (3.33), for a semi-infinite medium $T(0) \propto (Q_{\text{top}}/\kappa)$, so that the dependency of both heat flux and thermal conductivity are nullified. As a result, for simple isotropic homogeneous bulk materials, the TPD proves to be independent of the thermal properties and magnitude of heat flux.

In the more complex case of a pulsed laser heat source, the TPD becomes time-dependent. Fig. 3.8(a)-(d) displays the near-surface temperature distributions for SiO₂ subjected to surface heating from an 80 MHz pulsed laser source. At early times, the temperature rise is confined closer to the surface due to the initial energy deposited by the laser pulse. By 10 ns, the heat is largely distributed such that the temperature rise is nearly indistinguishable compared to the equivalent CW source case.

To further expand on the role of the repetition rate, we calculate the radial- and depth-dependent

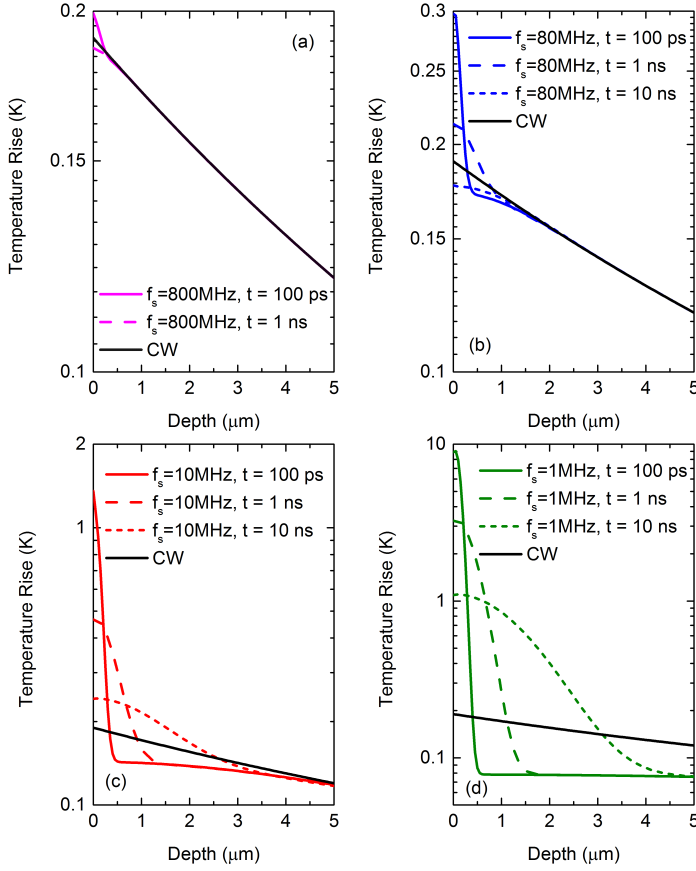


Figure 3.9: Temperature decay in depth for bulk Si along the radius = 0 profile subjected to an unmodulated pulsed source with repetition rates (a) 800 MHz, (b) 80 MHz, (c) 10 MHz, and (d) 1 MHz. In all cases, average absorbed power at the surface is 1 mW and pump $1/e^2$ radius is 15 μm .

temperature profiles for silicon at repetition rates spanning nearly four orders of magnitude (1 MHz to 800 MHz); the results are shown in Fig. 3.9 for the temperature decay in depth along the $r = 0$ contour. For higher repetition rate pulsed sources (e.g., 800 MHz), the solution is almost indistinguishable from the CW solution at any given time. 80 MHz is a commonly used repetition rate for TDTR as it is a typical output of most commercial Ti:Sapphire oscillators. For this repetition rate, the temperature decay has a time dependence, but beyond 1 to 2 μm the depth-dependent temperature decays to be equivalent to that of the CW source solution. The temperature profile resulting from a 10 MHz repetition rate source displays similar characteristics, but takes longer in time and depth to relax to the CW solution. Still, this similarity to the 80 MHz case suggests that pulse accumulation is still present; that is, the thermal decay does not reach zero before the

next pulse arrives. Finally, the 1 MHz case displays a unique trend in that the solution does not approach that of the CW source until both decay to zero. This suggests that there is little, if any, pulse accumulation. Furthermore, the $t = 100$ ps curve shows that before the temperature equilibrates, the magnitude of temperature is relatively low and shows a flat profile in depth beyond the near-surface region, confirming this lack of significant pulse accumulation.

These calculations lead to the following general conclusions. First, the steady-state temperature profile, while independent of time in the CW case, displays a strong time dependence when considering a pulsed source. This results from the heat flux being supplied by impulses of energy such that the steady-state temperature distribution after pulse accumulation has saturated still varies with time between each pulse. Second, the solution of the steady-state temperature profile for a pulsed heating event relaxes in depth to that for a CW source of equivalent average power; the depth it takes this co-incidence of solutions to occur is dependent on the repetition rate of the system. In the limit as repetition rate becomes slow enough that the temperature decays to zero between pulses, this co-incidence occurs only as $z \rightarrow \infty$. In this case, the solution is equivalent to that of the single pulse (impulse) temperature response. At the other extreme, as the repetition rate approaches infinity, the heating source becomes a CW source so that the thermal response relaxes to that of a CW solution very close to the surface.

Next, consider the spatially-dependent temperature profiles when a modulated heat flux is applied to the surface. Since the laser heating magnitude is modulated about some average power, we note that there will always be a steady-state (DC) component to temperature rise as discussed in the previous section. In this section, however, the focus will be on the modulated (AC) component to this temperature rise to comply with temperature profiles of interest to TDTR and FDTR. Equations (3.42) and (3.44) describe the surface temperature solution to such a heat flux condition. The expression given by Eq. (3.73) is commonly used in both TDTR and FDTR studies to correlate TPD with physical length scales associated with heat carriers [115, 128–132]. However, this equation, given the assumptions invoked in its derivation, is limited in its practical applicability and clearly breaks down when true conditions deviate from such idealities. For example, in agreement with the conclusion drawn from the unmodulated case, the TPD depends strongly on time after

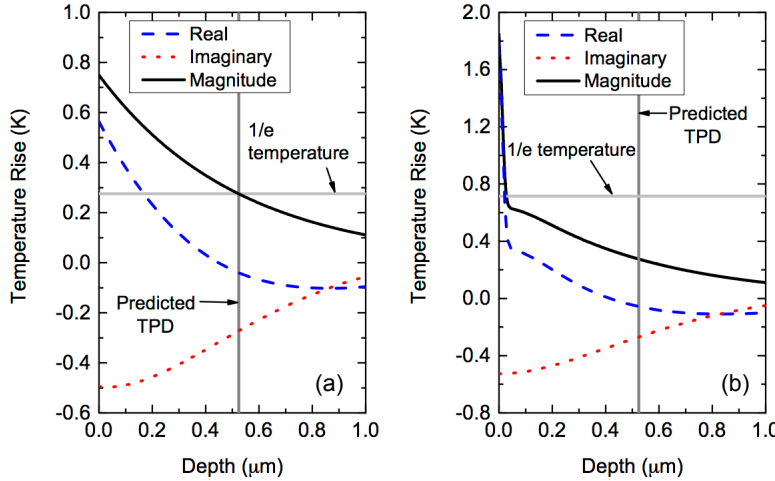


Figure 3.10: Modulated temperature profiles as a function of depth at $r = 0 \mu\text{m}$ for a bulk a-SiO₂ system. The average power absorbed at the sample surface was chosen as $\alpha_0 A_0 = 1 \text{ mW}$. The modulation frequency in both cases was set to 1 MHz, while the repetition rate of the pulsed laser was set to 80 MHz. The temperature decay with depth is shown when the heat flux is (a) CW and (b) pulsed and observed at $t = 100 \text{ ps}$.

pulse absorption for the pulsed case. Figure 3.10 clearly demonstrates this, showing calculations of temperature rise as a function of depth for a (a) CW and (b) pulsed source. For a CW source, the temperature profile with depth at $r = 0$ (representing FDTR when $r_1 \ll r_0$) shows that when considering the magnitude of temperature decay, Eq. (3.73) exactly predicts the calculated TPD for bulk a-SiO₂. However, when a pulsed response of equivalent power is observed at 100 ps, the TPD is clearly not accurately predicted by Eq. (3.73). Thus, the TPD varies with time in the pulsed case, making its use as a metric of measurement volume unreliable in many situations. Of course, it can be argued that since temperature deviations in pulsed vs. CW solutions occur only near-surface for high repetition rate pulsed sources (note, as per our previous discussion, this is not the case with low repetition rate sources), the experimental volume as a whole can still be reasonably predicted using the CW solution. Nonetheless, it is clear that Eq. (3.73) has limitations, such that its use can result in inaccurate predictions of TPD for certain experimental conditions. As it turns out, such conditions are well within the norm of those typically used in TDTR and FDTR experiments. Two such examples include: (i) the modulation frequency is on the order of the radially averaged thermal diffusivity ($\omega_0 \lesssim D/r_0^2$) and (2) layers and interfaces become significant to thermal transport.

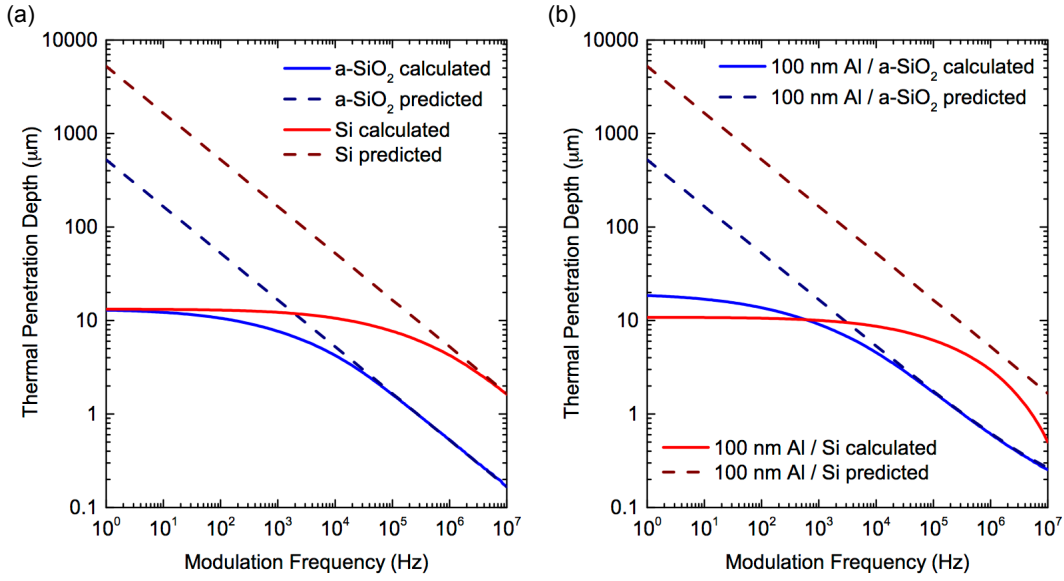


Figure 3.11: Thermal penetration depth vs. modulation frequency for (a) bulk a-SiO₂ and Si and (b) 100 nm Al on a-SiO₂ and Si as determined computationally using the approach described in this manuscript compared to that predicted via Eq. (3.73). In all cases, the heat flux is provided by a CW source with power $\alpha_0 A_0 = 1$ mW and $1/e^2$ gaussian radius of 15 μm and the TPD is given for the depth-dependent temperature decay along the $r = 0$ profile.

We consider both cases below.

The unmodulated temperature response suggests a physical limit to the thermal penetration depth obtainable by a modulated source; that is, the thermal penetration depth resulting from a modulated heat flux can never be greater than that resulting from an unmodulated heat flux with all other parameters staying equal. Thus, Eq. (3.73) clearly breaks down at low modulation frequencies. Figure 3.11(a) displays the thermal penetration depth vs. modulation frequency as predicted via Eq. (3.73) and that calculated using the full solution discussed in the analysis above for both Si and a-SiO₂ (homogeneous semi-infinite substrates) using a pump beam radius of 15 μm . For bulk a-SiO₂, the thermal penetration depth predicted is reasonably accurate for the frequencies greater than ~ 100 kHz, proving to be an effective predictor of TPD in the range of typical modulation frequencies used in TDTR and FDTR. However, for Si, the prediction of TPD via Eq. (3.73) is not accurate until ~ 10 MHz using the thermal properties listed in Table 3.1. We note that manipulating the pump radius can change the accuracy of Eq. (3.73) relative to the calculated results. Smaller pump radii lead to a decrease in the upper limit to the attainable TPD as calculated in the unmod-

ulated case. As a result, the onset of disagreement between prediction and calculation occurs at higher modulation frequencies for smaller pump radii. To get a better idea of where this discrepancy begins, the TPD is normalized to determine the ratio of TPD/r_0 as a function of modulation frequency. Doing so reveals that the breakdown of calculation and theory, as implied by Si and a-SiO₂ examples, occurs when this ratio reaches approximately 0.2.

More importantly, however, note that in a typical TDTR or FDTR experiment, a metal transducer (typically on the order of 100 nm) is deposited onto a bulk substrate. The addition of this thin film (and more importantly for high-thermal diffusivity materials, the interface between the thin film and substrate) serves to completely change the temperature decay profile such that for Si, the predicted TPD is never in agreement with the calculated TPD and can be off by orders of magnitude at modulation frequency extremes on both the high and low end. This is observed in Fig. 3.11(b), where the calculated TPD represents that within the Si or a-SiO₂ substrate after subtracting the 100 nm Al thickness. a-SiO₂, on the other hand, shows similar agreement to the predicted model as in the bulk case since the thermal resistance from the Al and Al/SiO₂ interface is negligible compared to that of the a-SiO₂.

From these observations, two generalizations can be made. First, low-thermal diffusivity materials are less prone to the breakdown of Eq. (3.73) within typical experimental conditions of TDTR and FDTR. Second, for high-thermal diffusivity materials, interfaces and layered structures completely change the thermal decay profile such that simple analytical expressions can no longer be used to accurately predict TPD. Thus, to obtain accurate estimations, the full solution to the temperature decay profile with depth, radius, and time must be solved.

3.6 Steady-State Temperature Rise

In any optical pump-probe technique, the pump induces a steady-state temperature rise associated with the average power absorbed during laser heating. In such experiments, an estimation of this temperature rise can be crucial since thermal properties can vary significantly with temperature. Because fitting procedures to extract thermal properties can be highly sensitive to these

temperature-dependent input parameters, neglecting the temperature rise can result in large errors of fitted parameters. This is particularly important at low temperatures where heat capacities and thermal conductivities are highly temperature-dependent [2]. Moreover, appropriate modeling of the temperature rise is needed in many cases for determining critical temperatures like phase transition temperatures and damage thresholds. For example, many polymers have glass transition temperatures well within the range of temperature excursions reached in typical TDTR and FDTR experiments [145, 146], while the same is true for the denaturing temperature of proteins [147, 148]. Whether the goal is to avoid such temperatures or investigate material properties at those temperatures, the calculation of the steady-state temperature rise due to laser heating is necessary.

In this section, the previously derived equations are used to understand steady-state temperature rise in pump-probe experiments in order to determine its practical implications on the experiments. In particular, the effects that various thermal length scales have on the steady-state temperature rise are revealed and all results are generalized where appropriate. For a modulated heating event, these length scales include the the $1/e^2$ pump radius (r_0), $1/e^2$ probe radius (r_1), and the thermal penetration depth. In the previous section, it was shown that the temperature rise resulting from a modulated heating event in TDTR and FDTR could be decoupled into a modulated and steady-state temperature response. As such, there are two thermal penetration depths to consider: the modulated thermal penetration depth (δ_m), which defines the $1/e$ decay in depth relative to the magnitude of the modulated component to temperature rise at the sample surface, and the steady-state thermal penetration depth (δ_s), which defines the $1/e$ decay in depth relative to the steady-state surface temperature rise.

From these calculations, several key findings are found based on typical experimental conditions used in TDTR and FDTR. First, conductive thin film transducer layers, such as aluminum (Al) and gold (Au) films ubiquitous in TDTR and FDTR, can significantly reduce the temperature rise by providing radial heat dissipation, leading to reductions in temperature rise of (in some cases) orders of magnitude compared to the same temperature rise without a transducer. Second, when sampling thin films, conductive substrates can likewise reduce this temperature by acting

as heat sinks. However, their effectiveness as heat sinks is entirely dependent on the length of $\delta_s (\approx r_0)$ with respect to the film thickness. Finally, the effect of optical penetration depth on the steady-state temperature rise is quantified to reveal that large ζ can reduce the steady-state temperature rise, but is only significant when it approaches the important thermal length scales such that $\zeta \approx \delta_s \approx r_0$. Taken together, this study emphasizes the need to decouple the modulated heating event from the steady-state heating event when considering laser heating and the importance of accurately determining the steady-state temperature rise for layered structures.

In the case of a pulsed laser heat source, the steady-state response is taken as the accumulated temperature rise resulting from a summation over all pulses absorbed by the sample. For high repetition-rate lasers typically used in TDTR, the temperature rise associated with a single pulse is small compared to the accumulated temperature rise for low thermal conductivity materials where steady-state heating is of concern [120]. Additionally, the pulsed solution to steady-state heating, for the time scales of interest in TDTR (100's of ps to several ns), can be approximated as a CW solution without significant loss of accuracy [120]. Thus, in this section, we generalize all results to hold true for both high-repetition rate pulsed and CW sources, but solve all temperature profiles assuming the heating event is from a CW source. Doing so has two advantages: (i) it is far more computationally efficient since one does not need to sum over all pulses, and (ii) it eliminates any time dependence (however small) to the temperature profile between pulse absorption.

Although the temperature rise can be decoupled into two terms for the modulated laser heating event, the steady-state temperature rise dominates the temperature profile of any system, such that for practical applications this temperature rise is the only one that needs to be considered. The modulated temperature rise oscillates about this steady-state temperature such that when time-averaged over several periods it is zero. Moreover, for typical modulation frequencies used in TDTR and FDTR, the amplitude of the modulated temperature rise can be orders of magnitude lower than steady-state temperature rise. For example, Fig. 3.12 shows the steady-state and modulated temperature profiles associated with a representative 100 nm aluminum (Al) film on an amorphous silicon dioxide ($a\text{-SiO}_2$) substrate subjected to laser irradiation modulated at 10 MHz and absorbed at the Al surface. The average absorbed power is 1 mW and the beam has a Gaussian radial profile

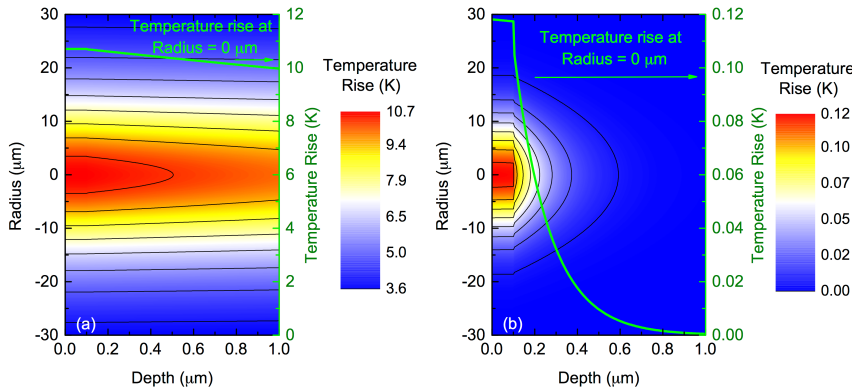


Figure 3.12: Temperature profile as a function of radius and depth for a 100 nm Al / a-SiO₂ sample subjected to a radially symmetric gaussian surface heating event with $1/e^2$ radius of 15 μm and an average absorbed power of 1 mW. The heating event is modulated sinusoidally at 10 MHz; the temperature profile is decoupled to display the (a) constant component from the unmodulated (steady-state) response and (b) the magnitude of temperature from the modulated component.

with a $1/e^2$ heater radius, $r_0 = 15 \mu\text{m}$. Figure 3.12(a) shows that the maximum temperature rise of the steady-state component is over 10 K. In contrast, Fig. 3.12(b) shows that the magnitude (amplitude of the temperature oscillation in time) of the modulated component of the temperature rise is two orders of magnitude lower than the steady-state component. The material-dependent thermal parameters used for all calculations in this chapter are listed in Table 3.1. Although this section is focused on interpreting temperature profiles associated with TDTR and FDTR, most of the results presented in this study can be generalized to interpret temperature profiles associated with other experiments having radially symmetric heating at comparable length scales to those presented in this study.

The condition that $\delta_m \ll \delta_s$ is beneficial for determining thermal properties at a specific temperature in TDTR and FDTR. Since the depth of the experimental volume is typically assumed as δ_m [115, 116], the condition of $\delta_m \ll \delta_s$ implies that one can assume a single temperature approximation within the experimental depth to avoid complications with spatially varying thermal properties. This approximation is important because, in order to extract thermal parameters via a heat diffusion model, fixed input parameters need to be defined; these parameters are generally temperature dependent. A single temperature approximation allows one to assign fixed, spatially independent values to these fixed parameters. In Fig. 3.12, δ_m is limited to under 300 nm for the

Al / SiO₂ sample (including the 100 nm Al film thickness). The 99% temperature decay depth is in this case is roughly 850 nm. Across the same depth, the temperature decay of the steady-state temperature is less than 10%, validating the assumption that the steady-state temperature rise is constant across the experimental depth. Increasing the modulation frequency or increasing the heater radius can further reduce the ratio of δ_m/δ_s , ensuring a single temperature approximation holds in depth.

The radial temperature decay lengths at the sample surface, on the other hand, are similar in the modulated and steady-state cases. To determine the conditions for which a single temperature approximation is valid in the radial direction, it is necessary to discuss the probe detection, turning back to Eq. (3.45). When considering a bulk, homogenous material, this expression can be solved analytically for an unmodulated CW source to become

$$T = \frac{\alpha_0 A_0}{\sqrt{2\pi\kappa_r\kappa_z(r_0^2 + r_1^2)}}. \quad (3.74)$$

For an isotropic material with thermal conductivity κ and when $r_1 = r_0$, this becomes [94]

$$T = \frac{\alpha_0 A_0}{2\sqrt{\pi}r_0\kappa}. \quad (3.75)$$

This expression is often employed as an estimation of temperature when pump and probe radii are similar, as it provides a simple analytical expression for calculating the temperature rise from laser heating. However, there are two assumptions inherent in Eq. (3.75) that complicate its use for TDTR and FDTR experiments when experimental conditions deviate from these assumptions.

The first assumption is that the radial distribution of temperature is accurately approximated by a single temperature coming from T_{PA} when $r_0 = r_1$. T_{PA} is a Gaussian average of the radial temperature distribution over the probe radius, providing a single temperature to estimate the radial decay of temperature for a sample. This means that in the case of large radial temperature gradients, Eq. (3.75) will significantly underestimate the maximum temperature of the system and the use of a single temperature approximation within the experimental volume of TDTR and FDTR may not be valid. For example, Fig. 3.13(a) shows the surface steady-state temperature profile

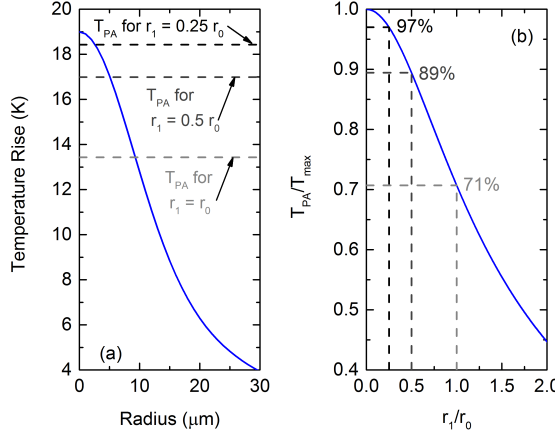


Figure 3.13: (a) Temperature rise due to pump beam heating as a function of radius. T_{PA} is the probe-averaged temperature rise, shown for the cases when the probe radius is equal to pump radius, half the pump radius, and a quarter of the pump radius. (b) Normalized temperature (defined as probe averaged temperature rise divided by maximum temperature rise from pump heating) as a function of normalized probe radius (defined as the ratio of probe to pump radii).

induced by a pump beam with $r_0 = 15 \mu\text{m}$ and $\alpha_0 A_0 = 1 \text{ mW}$ for a bulk a-SiO₂ sample assuming a surface heating event. When $r_1 = r_0$, the calculated temperature rise (T_{PA}), which agrees perfectly with Eq. (3.75), is only capturing the temperature rise associated with a fraction of the radial temperature gradient. When r_1 is reduced relative to r_0 , T_{PA} changes significantly, as depicted in Fig. 3.13(a), approaching the peak temperature as $r_1 \rightarrow 0 \mu\text{m}$. While this simple example shows temperature deviations of only a few Kelvin, higher heat fluxes or lower thermal conductivity materials can greatly increase the steady-state temperature rise; we explore the latter case below. Before doing so, Fig. 3.13(b) generalizes these results to show the normalized temperature, defined as the ratio of maximum temperature of the radial surface temperature profile (T_{max}) to T_{PA} , as a function of normalized probe radius (r_1/r_0). When the normalized radius is 1, T_{PA} gives a temperature of 71% of the maximum temperature, while lowering the normalized radius to 0.5 and 0.25 increases the normalized temperature rise to 89% and 97% respectively. These results are independent of laser power and material properties for this bulk, homogeneous case, allowing for a generalized understanding of the conditions needed ensure a single temperature approximation in the radial direction. Since the radial component to the measurement volume is dictated by the probe, it is beneficial to reduce the probe radius relative to pump size to ensure a single-temperature

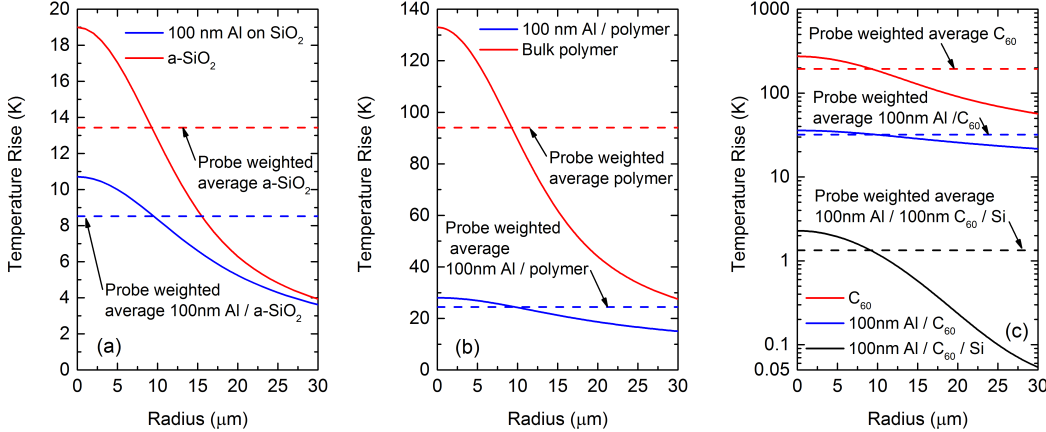


Figure 3.14: Steady-state temperature rise as a function of radius for (a) bulk amorphous SiO_2 , (b) bulk polymer and a 100 nm Al film on a polymer substrate, and (c) bulk disordered C_{60} , a 100 nm Al film on a C_{60} substrate, and a 100 nm Al film on a 100 nm C_{60} film on a Si substrate

approximation in the radial direction.

The second assumption in Eq. 3.75 is that the sample is bulk and homogeneous, such that it is not valid when layers and interfaces are considered. Since TDTR and FDTR experiments almost always require a thin-film metal transducer layer, Eq. 3.75 becomes invalid. To show this, in Fig. 3.14 we consider the steady-state surface temperature profiles for three representative low-thermal conductivity materials, (a) a- SiO_2 , (b) polymer, and (c) disordered C_{60} . In all cases, a surface heating event with $r_0 = 15 \mu\text{m}$ and $\alpha_0 A_0 = 1 \text{ mW}$ is used and all temperature profiles are shown with and without a 100 nm Al transducer layer (typical thickness used in TDTR and FDTR). Additionally, T_{PA} is shown to demonstrate the equivalence of Eq. 3.75 and T_{PA} when $r_1 = r_0$ and no transducer layer is included. The addition of the transducer layer completely changes the steady-state temperature profile. For a- SiO_2 , T_{max} is reduced by 44% with the addition of the transducer layer, while the difference is compounded in the case of polymers and C_{60} , reducing the peak temperature by 79% and 87%, respectively.

This strong temperature reduction occurs because the transducer acts as a heat sink in the radial direction. This radial heat sink effect is shown in Fig. 3.15 through the comparison of the heat flux vector field (which includes heat flux components in the depth and radial directions) for

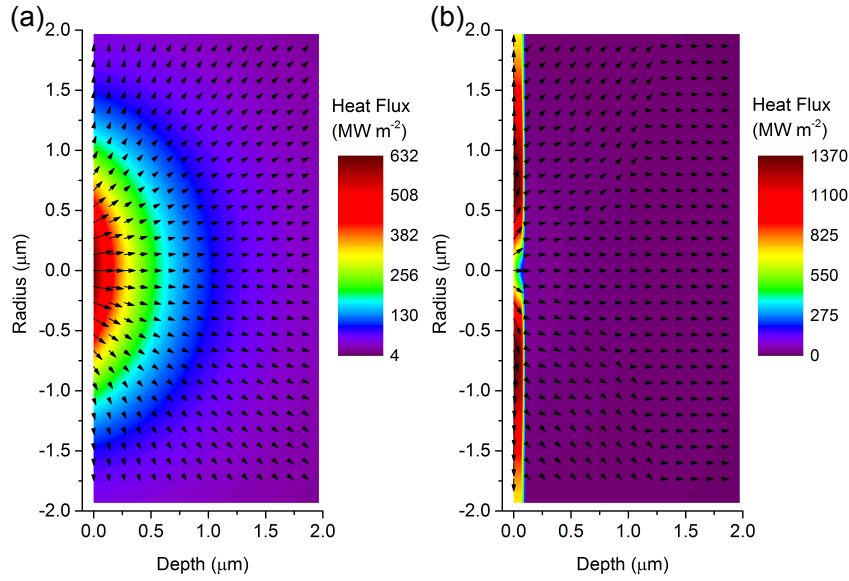


Figure 3.15: Heat flux vector field resulting from steady-state heating in (a) bulk a-SiO₂ and (b) 100 nm Al on a-SiO₂ when $r_0 = 1 \mu\text{m}$ and $\alpha_0 A_0 = 1 \text{ mW}$.

(a) bulk a-SiO₂ and (b) 100 nm Al on a-SiO₂. In these examples, $r_0 = 1 \mu\text{m}$ to be comparable to the transducer thickness for better visualization of the heat flux in the Al layer. For bulk a-SiO₂, the heat flux is dissipated throughout the depth and radial directions with similar magnitudes. However, when a 100 nm Al layer is added, the radial heat flux in the Al layer is much greater than any magnitude of heat flux in the a-SiO₂ layer. In order to sustain the similar radial temperature profiles in both the Al layer and a-SiO₂ (see Fig. 3.12), the radial heat flux in the Al must be much greater than that in the a-SiO₂ to compensate for the difference in thermal conductivities.

This heat sink effect is generally not a factor in the modulated temperature rise, emphasizing the need to decouple the steady-state and modulated temperature profiles that occur simultaneously with a modulated laser heating event. Whereas the latter can typically be assumed one-dimensional so that radial thermal transport is negligible, the former is highly dependent on radial transport. We quantify this further in an experimental case study on a thin Au film deposited on a-SiO₂ in the following section. Although the steady-state heating is partially mitigated by the transducer layer, adding a substrate can further reduce the heating, as shown in Fig. 3.14(c), where the steady-state temperature rise is calculated for 100 nm Al on a C₆₀ thin film with thickness $d = 100 \text{ nm}$ (a thickness achievable for spin-coated thin films) on a bulk Si substrate. In this case, the temperature

rise, compared to bulk C₆₀ alone, is reduced by two orders of magnitude.

3.6.1 Experimental Case Study: Au on a-SiO₂

To validate the calculations of steady-state heating, provide an example of when properly estimating temperature rise is important, and develop an iterative approach to determining temperature-dependent thermal properties, we study the case of a-SiO₂ with a 65 nm gold (Au) transducer layer using TDTR, the details and analyses for which are described elsewhere [94, 96, 97]. Gold was chosen as the transducer because of its high absorbance at our pump wavelength of 400 nm, which allows for large steady-state temperature rises. Additionally, Au has low absorbance at the probe wavelength of 800 nm, so we can ignore any contribution from the probe when calculating the steady-state temperature rise. An a-SiO₂ substrate was chosen because of its well-established thermal conductivity as a function of temperature, making it a good choice for proof of concept. We measure the ratio of the in-phase to out-of-phase voltage of the probe response recorded by a lock-in amplifier as a function of probe delay time. The 1/e² radii for the pump and probe are 16.5 and 6.5 μm , respectively. The pump pulses are modulated with a 10 MHz sinusoidally varying envelope. Using a high modulation frequency and small probe radius relative to the pump ensure the single temperature approximation will be reasonably accurate for our experimental volume, as discussed previously. Using a multilayer, radially symmetric thermal model [94, 97], we fit for the thermal boundary conductance between the Au transducer and the a-SiO₂ ($G_{\text{Au/a-SiO}_2}$) and the a-SiO₂ thermal conductivity ($\kappa_{\text{a-SiO}_2}$). We assume bulk values for the heat capacities [61, 127] for the Au transducer and a-SiO₂ and adjust these with temperature as appropriate. The radial component to thermal conductivity of the Au transducer is determined using the Wiedemann-Franz law based on 4-point probe resistivity measurements.

To elucidate the importance of the thermal parameters that determine the temperature rise (both modulated and steady-state), we can quantify the sensitivity of the surface temperature response function to each parameter of interest as described by [149]

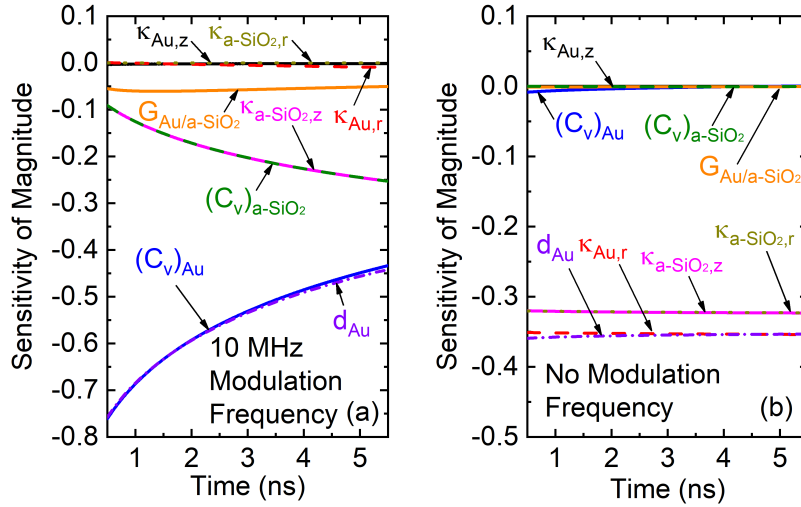


Figure 3.16: Sensitivity of the magnitude of surface temperature rise to thermal parameters as determined by Eq. (4.3) for the (a) 10 MHz modulated frequency response and (b) steady-state unmodulated response for a 65 nm Au on a-SiO₂ sample. Thermal parameters considered include in-plane and cross-plane thermal conductivities (κ_r and κ_z , respectively) for both the Au and a-SiO₂ layers, volumetric heat capacities (C_v) for both layers, and thermal boundary conductance across the Au/a-SiO₂ interface ($G_{\text{Au/a-SiO}_2}$)

$$S_p = \frac{\partial \ln(V)}{\partial \ln(p)} \quad (3.76)$$

where V is response function of interest, in this case the magnitude of the in-phase and out-of-phase temperature response, and p is the parameter of interest. Although we fit for the ratio of in-phase to out-of-phase signals to improve the signal-to-noise ratio, to theoretically compare the modulated and steady-state responses, the magnitude is used since the steady-state response has no out-of-phase component. Figure 3.16(a) shows the sensitivity of the 10 MHz modulated component of temperature rise, while (b) shows the sensitivity of the steady-state component. In both cases, higher absolute value of sensitivity indicates greater importance of a parameter to the temperature response function. Comparison of the two suggests that in the modulated case, the influence of both in-plane and cross-plane thermal conductivities of the Au layer ($\kappa_{\text{Au},r}$ and $\kappa_{\text{Au},z}$, respectively) are negligible to the magnitude of the temperature response. In contrast, the heat capacity ($C_{v,\text{Au}}$), and by extension, the thickness of the Au film (d_{Au}), play critical roles in determining this response. As expected, the radial component to thermal conductivity of a-SiO₂ ($\kappa_{\text{a-SiO}_2,r}$) has negligible sen-

sitivity to the temperature rise since the decay length in depth is much smaller than that radially, such that heat flow is essentially one-dimensional. Because at typical TDTR modulation frequencies, the thermal effusivity dominates the modulated temperature response from the a-SiO₂ [150], the heat capacity ($C_{v,a-\text{SiO}_2}$) and cross-plane thermal conductivity ($\kappa_{a-\text{SiO}_2,z}$) are indistinguishable and share the same sensitivity. Finally, the thermal boundary conductance between Au and a-SiO₂ ($G_{\text{Au}/a-\text{SiO}_2}$) has a significant contribution to the modulated temperature response due to the relatively low measured value of $\sim 50 \text{ W m}^{-2} \text{ K}^{-1}$, which could be due to poor adhesion between the substrate and metal film [151, 152]. Taken together, the important parameters determining the modulated temperature response function are temperature dependent. In particular, $C_{v,\text{Au}}$ is crucial to accurately determining the modulated temperature response. In analyzing TDTR data with the thermal model, we fit for $\kappa_{a-\text{SiO}_2,z}$ and $G_{\text{Au}/a-\text{SiO}_2}$. However it is essential to input appropriate estimates for $C_{v,\text{Au}}$ and $C_{v,a-\text{SiO}_2}$ based on steady-state temperature rise calculations to accurately determine the thermal properties of interest. Thus, we need to understand the sensitivity of the steady-state temperature response to these parameters.

The steady-state temperature response sensitivity to the same parameters is shown in Fig. 3.16(b). In contrast to the modulated sensitivities, the heat capacities and thermal boundary conductance are negligible, whereas the thermal conductivities (apart from $\kappa_{\text{Au},z}$) dictate the temperature rise. The sensitivity to $\kappa_{\text{Au},z}$ is negligible due to the limited thickness of the Au layer relative to the thermal penetration depth of the steady-state temperature profile. Therefore, as previously alluded to, the length and time scales of the temperature decay dictate the importance of the thermal parameters to the temperature response at the surface. In TDTR, this means that estimating the temperature rise governing the thermal parameters involves an appropriate estimation of the steady-state temperature rise. However, this temperature rise is governed by the thermal conductivity of the material of interest, which is often the desired property to be measured in TDTR experiments.

To overcome this conflict and demonstrate a practical approach to employ temperature rise calculations in conjunction with TDTR, we simultaneously estimate the steady-state temperature rise and fit the a-SiO₂ thermal conductivity iteratively via the process described in the inset of Fig. 3.17. The laser power was measured and the Au absorbance was assumed to be 0.606 [154].

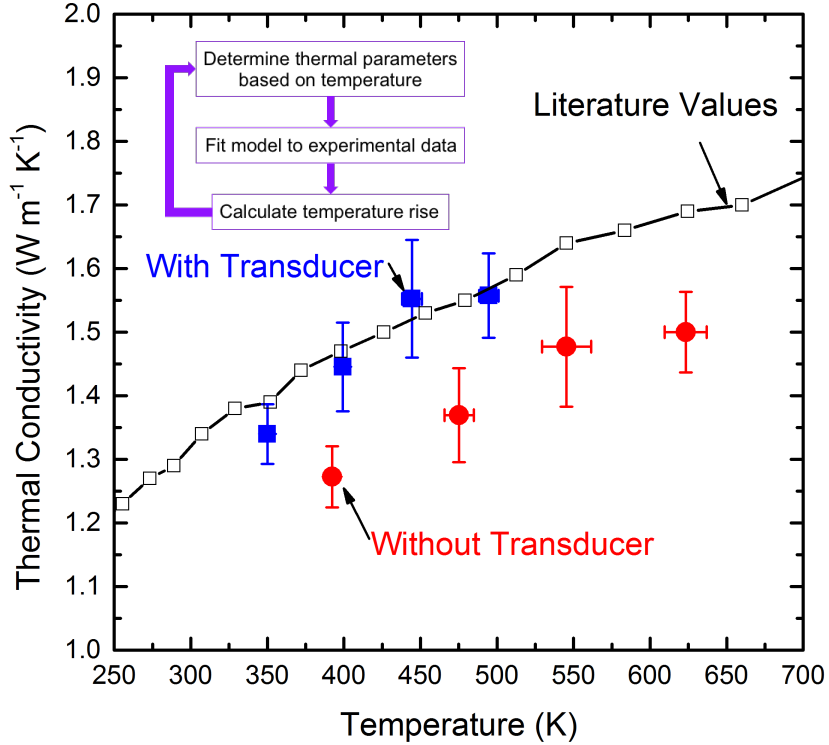


Figure 3.17: Experimentally determined thermal conductivities of a-SiO₂ measured with TDTR when a 65 nm Au transducer layer is used. Blue squares denote the fitted values with temperatures based on calculations that include the Au transducer layer, while red circles denote the fitted values using temperature rise calculations without including the Au transducer. In both cases, an iterative method was used as described by the inset whereby input thermal parameters were chosen based on the steady-state temperature rise calculated, the TDTR data was used to fit the a-SiO₂ thermal conductivity and the Au/a-SiO₂ thermal boundary conductance, and all thermal parameters were then used to recalculate the steady-state temperature rise. This process is repeated until convergence is reached. Literature values are taken from Ref. [153].

Starting with the phase-corrected TDTR ratio data, we (1) input thermal parameters based on a lookup table of thermal properties vs. temperature, interpolating where necessary. We then (2) fit the thermal model governing the modulated surface temperature response to the TDTR data to extract $\kappa_{\text{a-SiO}_2,z}$ and $G_{\text{Au/a-SiO}_2}$. These values, along with the other thermal parameters, are then used to (3) calculate the steady-state temperature rise based on the full solution to the heat diffusion equation for a layered sample. We then return to step (1) to repeat the process until a convergence of temperature is reached. In this case, it took only 5 iterations on average to reach a convergence. To emphasize the importance of the transducer layer to the steady-state temperature

rise calculation, we perform this iterative method in two ways: calculating temperature rise with and without the transducer layer. Note that the fit always includes the transducer layer and only the steady-state temperature rise calculation is altered.

Figure 3.17 shows the resulting converged temperature rises and fitted thermal conductivities for both cases of including and not including the transducer when calculating the steady-state temperature rises. Uncertainties correspond to statistical variations between measurements as well as uncertainty in Au film thickness (measured via mechanical profilometry as 63 - 65 nm). The latter, because it is coupled to the heat capacity through the thermal mass of the film, such that they share similar sensitivities, is the largest contribution to the uncertainty. A comparison of the measured values of thermal conductivities to literature values [153] shows that the measured values, when performing the appropriate temperature rise calculations, agree well with literature values. In contrast, not accounting for the transducer results in an over-prediction of the temperature rise so that C_{v,SiO_2} is overestimated; due to the coupling of $C_{v,a-\text{SiO}_2}$ and $\kappa_{a-\text{SiO}_2,z}$ in this thermal effusivity regime, $\kappa_{a-\text{SiO}_2,z}$ is underpredicted, resulting in a disagreement with literature values.

3.6.2 Consideration of Optical Absorption Depth

Recent works have demonstrated the ability to use TDTR/FDTR to measure materials without the use of a thin-film transducer layer [121, 155]. For this purpose, the effects of optical absorption and depth-dependent laser excitation must be considered. The solution to this was derived already in section 3.4.1, where ζ_0 defines the optical penetration depth (OPD) of the absorbing layer. Using this approach, we calculate the steady-state temperature rise and heat flux profiles for a bulk amorphous Si (a-Si) sample with OPD of 300 nm [121] for the pump wavelength in FDTR. To understand the effect of this parameter on the temperature profile, we also vary the OPD from 0 to 15 μm (the pump spot size) and calculate the variation in maximum temperature. The results are summarized in Fig. 3.18, where the (a) steady-state temperature and (b) heat flux profiles are shown for a-Si irradiated by a pump laser with $r_0 = 15 \mu\text{m}$ and $\alpha_0 A_0 = 1 \text{ mW}$. In this case, because the insulated boundary condition is invoked, there is no depth component to heat flux at the surface, which results in a shifted distribution of heat flux compared to the surface heat flux considered in

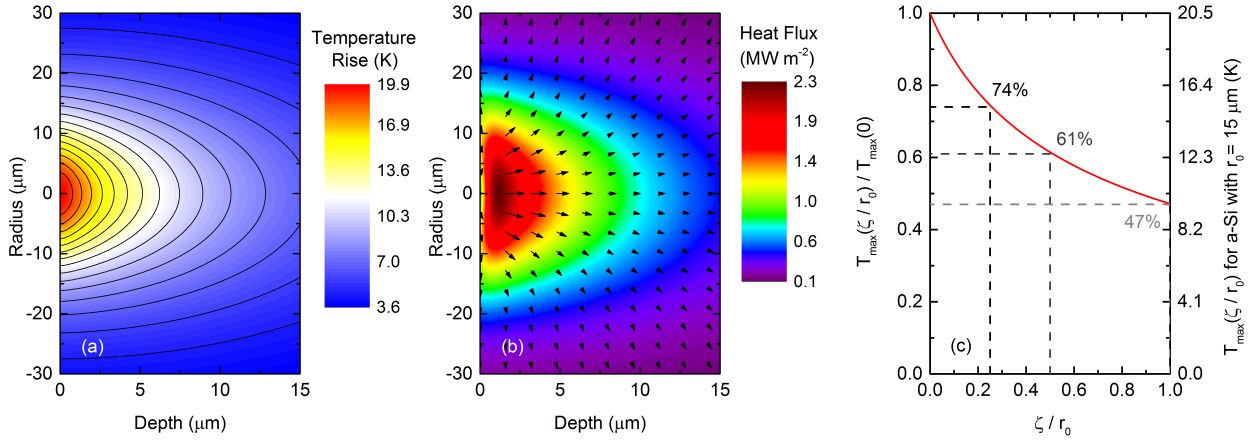


Figure 3.18: Effect of optical penetration depth on the heating of bulk materials: (a) and (b) depict the steady-state temperature profile and heat flux for a bulk a-Si film when $r_0 = 15 \mu\text{m}$ and $\alpha_0 A_0 = 1 \text{ mW}$ and the optical penetration depth is 300 nm. (c) Maximum temperature rise for the same sample. The normalized temperature, defined as the ratio of maximum temperature with a finite optical absorption depth to the maximum temperature assuming all optical absorption occurs at the surface, is also plotted as a function of normalized optical penetration depth, defined as the ratio of optical penetration depth to pump radius.

the previous sections. However, the temperature is still maximum at the surface; the influence of optical absorption is to reduce this maximum temperature by distributing the heat flux into the depth of the sample. A comparison of this temperature distribution to the same surface heating event ($\zeta = 0$) reveals little difference between them. The maximum temperature is reduced in the former case by less than 3%, a clear reduction but not likely to be of consequence to pump-probe experiments when estimating the steady-state temperature rise.

As with all previous discussion on the steady-state temperature rise, we emphasize the importance of length scales when generalizing these results. Although the influence of a 300 nm optical penetration depth has a negligible effect on the steady-state temperature profile of the bulk a-Si when a 15 μm pump radius is used, as ζ is increased (or equivalently, r_0 is reduced), the role of ζ becomes more influential in determining the temperature rise. To quantify this, we show in Fig. 3.18(c) the difference in maximum temperature when ζ is varied from 0 to 15 μm. Moreover, we generalize these results, which for isotropic bulk materials prove to be independent of material properties and absorbed power when normalizing the temperature rise. We define the normalized maximum temperature as the ratio of maximum temperature when an optical penetration depth of

ζ is used to the maximum temperature when all the laser power is absorbed at the surface, such that $\zeta = 0$. The normalized OPD is defined by the ratio ζ/r_0 . Thus, we have incorporated the important length scale of radius to demonstrate that when ζ/r_0 is small, the steady-state temperature rise can be calculated using a surface heating event without significant loss of accuracy. This also means that when considering the probe averaged temperature rise, Eq. (3.75) becomes a good estimation for the temperature rise when the pump and probe spot sizes are similar.

An important final note is that this discussion has been focused on the steady-state, rather than modulated, temperature rise. The 300 nm OPD proved to negligibly affect the steady-state temperature rise in the a-Si example above due to the length scale of temperature decay in both radius and depth being two orders of magnitude greater than this OPD. This is not the case for a modulated heating event detected in TDTR/FDTR, which typically has a thermal penetration depth on the order of 10's to 100's of nm for low thermal conductivity materials. As a result, the OPD plays a crucial role in the temperature response of the modulated heating event, as shown by Wang *et al.* [155] and Yang *et al.* [121]. In summary, when the optical penetration depth becomes on the order of the defining length scales of temperature decay, large deviations in temperature distributions can exist relative to the surface heating case.

3.7 Model Limitations

There are several limitations to the methodology employed to calculate temperature rise. One such limitation is that this model is only valid in the diffusive and continuum limit to heat transfer. Thus, at length scales when Fourier's law breaks down due to heat carrier length scales exceeding the experimental volume, this approach will not capture the temperature rise accurately within that volume [129, 156] without adjusting the thermal properties to become “effective” properties rather than intrinsic. For such cases, other approaches such as solving the full Boltzmann transport equation may prove more appropriate. However, in most pump-probe techniques having beam radii on the order of $>1 \mu\text{m}$, steady-state heating is typically only a concern for materials with low thermal conductivities resulting from relatively short mean-free-path vibrations. Therefore,

for most practical applications, a diffusive heat equation is valid for calculating the steady-state temperature rise. A similar complication can arise with the use of the exponential decay of heat flux described in Eq. (3.46). This term implicitly assumes that the heat carriers absorbing the optical energy thermalize to obtain the same exponential decay in depth. This is not the case for materials with weak electron-phonon coupling (e.g., Au or Ag) or long carrier relaxation times.

When determining the steady-state temperature rise, we discuss the heating imposed by a pump beam in pump-probe techniques but have neglected the temperature rise associated with the heating due to the probe beam. Accounting for the temperature rise associated with the probe beam is necessary when the absorbed power density of the probe becomes significant compared to the pump. Doing so is no different than the calculation of temperature rise from the pump, and the total temperature rise is simply the addition of both pump and probe temperature rises, due to the property of superposition [96]. However, in typical experimental conditions, the probe contribution to temperature rise is often negligible due to the high reflectivity at probe wavelengths needed for thermoreflectance measurements and the low power needed to establish a measurable signal. For example, the probe power used in the experimental case study was only 3 mW while the pump is varied from 10 mW to 40 mW. To compound this discrepancy, we used a gold transducer layer such that the absorbance is about 0.6 for the 400 nm pump but less than 0.03 for the 800 nm probe. Thus, the absorbed powers are roughly 6 - 24 mW for the pump and only \sim 0.1 mW for the probe. In this case, it is clear that the probe plays a negligible role compared to the pump. However, given other transducers such as aluminum or platinum, or different wavelengths used for pump and probe, the probe may have a larger influence on the steady-state temperature rise.

Finally, there are limitations to the heat diffusion equation when large spatial steady-state temperature gradients exist. Since the thermal properties that determine these gradients are temperature-dependent, the thermal properties can vary spatially, such that nonlinear spatial temperature derivative terms arise in the heat diffusion equation. In many cases, such as for amorphous materials whose thermal conductivities vary negligibly around and above their Debye temperatures, these nonlinear terms can be ignored such that the heat diffusion model used here is valid for determining the steady-state temperature rise. When this is not the case, one must account for the

temperature-dependent properties throughout all spatial gradients, which significantly complicates the analysis. For such applications, finite difference methods or more rigorous analyses based on solving the Boltzmann transport equation may be more appropriate.

3.8 Summary

In this chapter, I presented the key concepts and mathematical details governing TDTR and FDTR. I derived the general set of equations necessary to not only interpret TDTR and FDTR data, but understand the important length and time scales associated with experiments. One area I focused heavily on was quantifying the thermal penetration depth. There has been immense interest spectrally resolving the contribution from individual phonons to thermal conductivity, i.e., mean free path spectroscopy [117]. Despite the complexity of the experiments, the basis for estimating the experimental length scale has been a simple analytical expression, Eq. 3.73 [115, 128–132]. Here, I show that under realistic experimental conditions, this simple expression breaks down. In the same vain, I show that the steady-state temperature rise estimation based on the commonly used simple expression, Eq. 3.75, similarly breaks down in realistic conditions. Taken together, this chapter emphasizes the need to accurately model the spatial temperature profile to properly interpret experimental results.

Chapter 4

Steady-State Thermoreflectance

In this chapter, I will present a new optical pump-probe technique to measure the thermal conductivity of materials, steady-state thermoreflectance. This technique relies on using a continuous wave laser to heat a material long enough to induce a steady-state temperature rise. A secondary continuous wave laser is used to probe the resulting temperature rise. By varying the pump power and monitoring the resulting temperature rise, Fourier's law is used to determine a material's thermal conductivity. Below I present all experimental details and analysis describing the technique.

4.1 Background

Measurement techniques used to characterize the thermal conductivity of materials can be broadly categorized into steady-state and transient techniques. The former, based on Fourier's law, allow for direct measurements of thermal conductivity, whereas the latter rely on the heat diffusion equation such that volumetric heat capacity and thermal conductivity are coupled through the thermal effusivity or thermal diffusivity, depending on the time and length scales of the measurement. Some examples of transient techniques include transient hot-wire [157], transient plane source [158], the 3ω method [153], and non-contact pump-probe techniques such as laser flash [159], time-domain thermoreflectance (TDTR) [90] and frequency-domain thermoreflectance (FDTR) [101]. The 3ω method, TDTR, and FDTR have proven to be robust techniques capable of mea-

suring thermal properties of both bulk and thin film materials. TDTR and FDTR, as discussed in detail in the previous chapter, have the advantage of being non-contact techniques requiring a very small experimental surface area to heat and probe. However, these techniques can be expensive and difficult to operate, as they generally require detection of the phase shift of a signal that needs to be separated from instrument electronic phase shifts, along with additional knowledge of the heat capacity of the material under study.

Steady-state techniques include the absolute technique, comparative cut bar technique, radial heat flow method, and the parallel thermal conductance technique. Zhao *et al.* provide an extensive review of these techniques [160]. While these techniques are straightforward and require only variations of Fourier's law to analyze experimental data, they have practical limitations that make them undesirable compared to the aforementioned transient techniques. For example, all of these techniques are designed for bulk materials, so they require relatively large experimental volumes and heater/sensor areas. This makes them highly susceptible to radiative and convective losses, often necessitating vacuum conditions during measurements [161]. Moreover, techniques requiring contact between a sensor and sample generally include the undesired artifact of contact thermal resistance that can obscure the measurement of intrinsic thermal conductivity. Additionally, they can require waiting times up to several hours to reach steady-state temperatures. Finally, these techniques fundamentally measure the thermal conductance across a bulk specimen, rather than within a locally probed area as has been shown in FTDR [162, 163] and TDTR [164, 165]. Given the benefits inherent in transient pump-probe techniques and the simplicity of steady-state techniques, we develop a steady-state thermoreflectance (SSTR) technique based on a continuous wave (CW) laser pump and probe. We show that SSTR is robust, capable of measuring materials having thermal conductivities ranging from 1 to $> 2000 \text{ W m}^{-1}\text{K}^{-1}$, showing excellent agreement with literature values.

SSTR has several key benefits over conventional steady-state techniques. First, because transient temperature rise times can be on the order of tens of microseconds, SSTR is capable of high throughput measurements, limited only by the electronics and sampling periods used. Typical measurement times in this study vary from about ten seconds to five minutes per scan depend-

ing on the resolution needed. Second, SSTR is non-contact, requiring no attached thermocouple. Akin to TDTR and FDTR, SSTR as presented in this work is facilitated with the deposition of a thin metal film transducer. However, because the time scales associated with SSTR measurements (i.e., $>$ tens of microseconds) can be much longer than lifetimes of photoexcited carriers that can also contribute to changes in reflectivity, an additional transducer may not be needed [121, 155]. Third, steady-state techniques generally require large thermal resistances for accurate measurements, so that the minimum sample volume needed scales with the sample's thermal conductivity. By contrast, the thermal penetration depth in SSTR is governed solely by the pump radius, since this radius determines the thermal penetration depth in steady-state laser heating [120]. As such, the measurement volume of SSTR is independent of the thermal properties of the material under study; we show this later by measuring 300 μm thick wafers of diamond. Furthermore, because the thermal length scales are governed by the pump radius, the spatial resolution in SSTR is limited only by the ability to focus the pump and probe; in our experiments we can obtain pump/probe $1/e^2$ radii as low as $\sim 1 \mu\text{m}$. This allows us to probe local thermal conductivities to avoid, for example, damaged regions of a bulk specimen that could otherwise obscure the intrinsic thermal conductivity. Additionally, this allows for measurements of moderately thick films ranging from tens to hundreds of microns without significant influence of any underlying substrate.

Comparing SSTR to transient thermoreflectance techniques, SSTR has a few distinct advantages. First, TDTR and FDTR generally have shallow thermal penetration depths ($< 1 \mu\text{m}$ for most materials), so they are typically mostly sensitive to cross-plane thermal conductivity. By comparison, SSTR is fundamentally sensitive to the determinant of the total thermal conductivity tensor, analogous to the 3ω method [166]. Second, when a thin film transducer is used, generally, the large thermal penetration depth makes the temperature rise at the sample surface more sensitive to the thermal properties of the sample rather than the transducer properties or interface resistances. Third, since there is no time dependence after the transient rise time, the steady-state temperature profile is solely dependent on thermal conductivity. From a practical point of view, this greatly simplifies the experiment and analysis.

4.2 Principles of Operation

Detection of reflectivity (R) changes due to an induced temperature (T) rise is limited by the very small relative change in reflectivity of a material with temperature. For typical metals used as transducers in thermoreflectance experiments, $|dR/dT|$ is on the order of 10^{-5} or 10^{-4} K^{-1} [91–93]. There are two ways by which this limitation can be overcome. Using a periodic heat source, lock-in amplification (LIA) techniques overcome this limitation through amplification and electronic filtering, discussed in Chapter 3. Similarly, a periodic waveform analyzer (PWA) with a boxcar averager can be used with a large enough sampling time to extract a periodic signal. Since the steady-state signal has no frequency component, we seemingly cannot use these techniques to measure the $|dR/dT|$ associated with the “DC” temperature rise. Generally, in steady-state techniques, a constant heat flux is used to induce a transient temperature rise followed by a steady-state temperature rise. The transient portion of the temperature rise, which can persist for hours in bulk techniques [160], is ignored and measurements are taken only in the steady-state regime. In SSTR, obtaining a fast transient temperature rise followed by a long-lived steady-state temperature rise allows us to cyclically turn the steady-state temperature rise on and off, enabling use of the aforementioned signal detection schemes.

Thus, the concept of SSTR is to modulate the pump beam with a square wave at a low enough frequency to enable an “on” state and an “off” state for the steady-state temperature rise to be reached. By varying the power (\propto heat flux) of the pump beam, we can vary the temperature rise of the “on” state. Measuring the corresponding change in reflectivity (\propto temperature), we can apply Fourier’s law to determine thermal conductivity based on the linear relation between heat flux and temperature. This concept is fundamentally different from FDTR in that our controlled variable is pump power and we rely on measuring the magnitude of the reflectance signal, which is directly proportional to the temperature rise induced by the pump under steady-state temperature rise conditions. As such, there is no need to separate electronic phase from the overall signal phase, as is necessary in both TDTR and FDTR.

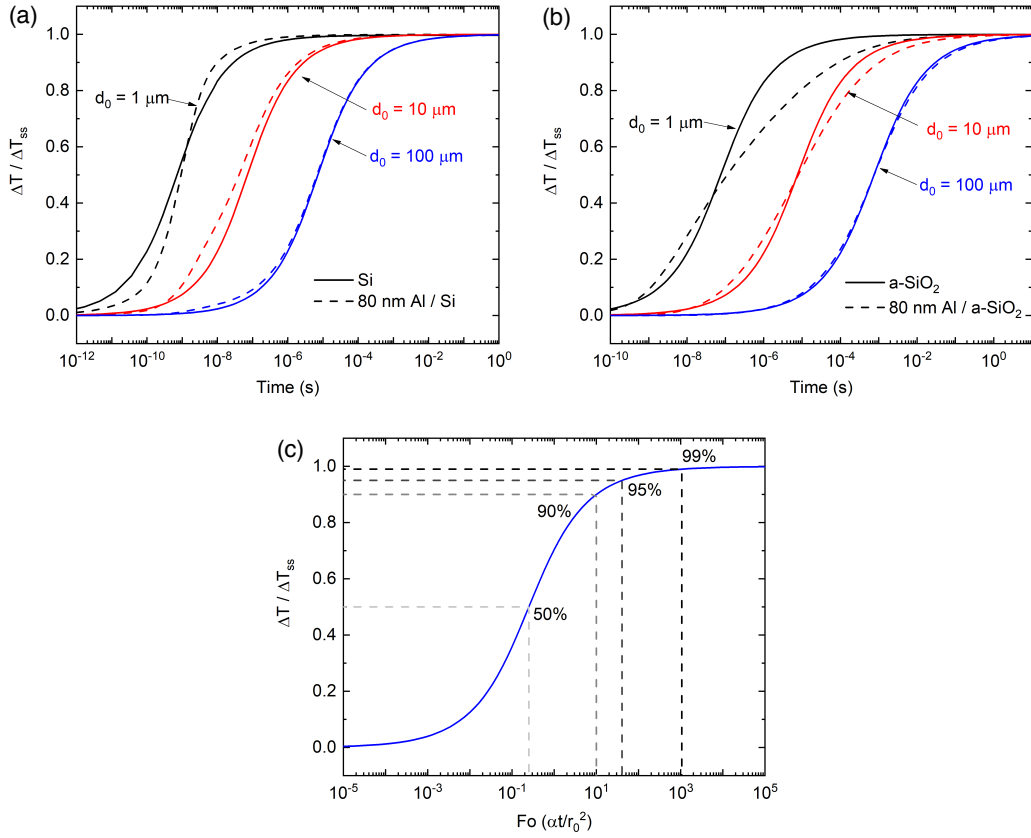


Figure 4.1: Normalized surface temperature rise ($\Delta T / \Delta T_{ss}$) vs. time for (a) Si and (b) a-SiO₂ for CW laser surface heating with $1/e^2$ diameters (d_0) of $1 \mu\text{m}$, $10 \mu\text{m}$, and $100 \mu\text{m}$. Solid lines indicate no transducer while dashed lines show the case with an 80 nm Al transducer. (c) $\Delta T / \Delta T_{ss}$ vs. Fourier number in the case of no transducer. Thermal parameters used in model include those for a-SiO₂ ($C_v = 1.66 \text{ MJ m}^{-3} \text{ K}^{-1}$, $\kappa = 1.4 \text{ W m}^{-1} \text{ K}^{-1}$), Si ($C_v = 1.60 \text{ MJ m}^{-3} \text{ K}^{-1}$, $\kappa = 140 \text{ W m}^{-1} \text{ K}^{-1}$), and Al ($C_v = 2.42 \text{ MJ m}^{-3} \text{ K}^{-1}$, $\kappa = 130 \text{ W m}^{-1} \text{ K}^{-1}$). Thermal boundary conductance between Al and substrate was modeled to be $200 \text{ MW m}^{-2} \text{ K}^{-1}$.

4.3 Theory

4.3.1 Transient Temperature Rise

We now establish the criteria needed to establish a steady-state temperature rise “on” state. To do this, we solve the heat diffusion equation in the time domain to determine the time needed for the temperature rise to reach steady-state. Using the radially symmetric heat diffusion equation, a material at an initial temperature rise of zero degrees at time $t = 0$ is subjected to a temporally constant, spatially gaussian heat flux at the sample surface to simulate CW laser heating. A semi-

infinite boundary condition is applied in all spatial dimensions. The derivation for this solution is provided in Appendix A. We find that two experimental parameters can be balanced to determine the operating conditions needed to achieve steady-state: the pump/probe radius and the modulation frequency of the pump. This can be seen in two common examples used as calibrations in TDTR and FDTR, silicon (Si, $\kappa \approx 140 \text{ W m}^{-1} \text{ K}^{-1}$) and amorphous silicon dioxide (a-SiO₂, $\kappa \approx 1.4 \text{ W m}^{-1} \text{ K}^{-1}$). For simplicity, these thermal conductivities were approximated to be exactly $100\times$ different from one another. Three $1/e^2$ pump/probe diameters spanning three orders of magnitude are considered: 1, 10 and 100 μm . Pump and probe sizes are equal in all example cases. Figure 4.1 shows the normalized temperature rise, $\Delta T / \Delta T_{\text{SS}}$, where $\Delta T_{\text{SS}} = \Delta T(t \rightarrow \infty)$ is the steady-state temperature rise, shown for (a) Si and (b) a-SiO₂. Since thin metal transducers are typically used in experiments, we apply the solution both with and without an 80 nm aluminum (Al) layer.

Strictly speaking, the temperature rise asymptotes to the steady state temperature rise, but we can define a threshold for $\Delta T / \Delta T_{\text{SS}}$ based on a desired measurement tolerance. For example if a ratio of 95% is used, we can select a modulation frequency that has a period longer than the 95% rise time of the temperature rise. For Si, the 95% rise times for a $1/e^2$ pump diameter of 1, 10, and 100 μm are $\sim 10^{-7}$, 10^{-5} , and 10^{-3} seconds, respectively. Similarly, for a-SiO₂, the 95% rise time for a pump radius of 1, 10, and 100 μm are $\sim 10^{-5}$, 10^{-3} , and 10^{-1} seconds, respectively. It is instructive to compare Si to a-SiO₂, which differ in thermal diffusivity by almost exactly two orders of magnitude. We see that for the same pump diameter, the rise time of a-SiO₂ is two orders of magnitude longer than for Si. Furthermore, for both Si and a-SiO₂, increasing the pump diameter by one order of magnitude increases the rise time by exactly two orders of magnitude. These two correlations suggest we can use the nondimensional Fourier number, $Fo = \alpha t / r_0^2$, where α is the thermal diffusivity, t is time, and r_0 is the pump radius, to generalize these results for a universal criterion to determine the rise times for any material. Figure 4.1(c) shows the relation between $\Delta T / \Delta T_{\text{SS}}$ and Fo, which holds true for any material having the previously defined boundary conditions.

As previously mentioned, thermoreflectance experiments generally require use of a thin metal transducer. In addition to having significant impact on the steady-state temperature rise itself [167],

we find that it can have significant impact on the rise time of the transient temperature rise. For example, for 80 nm Al/ Si, the rise time is lower than it is without the transducer layer for all laser spot sizes, allowing for higher modulation frequencies to be used to obtain a steady-state temperature rise. Conversely, the addition of an 80 nm Al layer to a-SiO₂ leads to longer 95% rise times than without the transducer layer. However, in both cases, the degree to which the rise time differs from the predictable case without this transducer is entirely dependent on the pump spot size, relative mismatch in thermal properties between the transducer layer and substrate, and, to a lesser extent, the thermal boundary conductance between the transducer and substrate. In particular, as laser spot size decreases, the influence of the transducer on the rise time becomes more substantial. Still, we find that in most cases, the nondimensional relation found in Fig. 4.1(c) is a useful guide to select the maximum modulation frequency given the pump radius and a rough idea of the thermal diffusivity of a sample. Of course, in practice, one can simply select a modulation frequency as low as possible to ensure the steady-state temperature rise is reached; the advantage of using higher modulation frequencies, if possible, is to reduce 1/f noise and expedite testing times.

4.3.2 Quasi Steady-State via a Sine Wave Heat Source

While the theoretical discussion thus far has been based on the idea of inducing an on/off state of the steady-state temperature rise (i.e., square wave modulation), many lock-in amplifiers use a pure sinusoid as a reference mixer, such that higher harmonics are not captured in detection. In this case, the lock-in only captures the magnitude of the probe signal at the fundamental frequency of the square wave. This does not pose an experimental problem, however, as we can still obtain a regime of quasi steady-state temperature rise. To illustrate this point, we examine the frequency-domain solution to the heat equation subjected to CW laser heating with a sinusoidal amplitude modulation [101]. The normalized temperature rise, $\Delta T / \Delta T_{SS}$, is shown in Fig. 4.2 for a-SiO₂, crystalline sapphire (Al₂O₃), Si, and diamond with 80 nm Al transducers. The solutions are shown for 1/e² pump and probe diameters of 1 μm, 10 μm, and 100 μm in Fig. 4.2(a), (b), and (c), respectively. The temperature rise ΔT is the modulated temperature rise that varies sinusoidally at

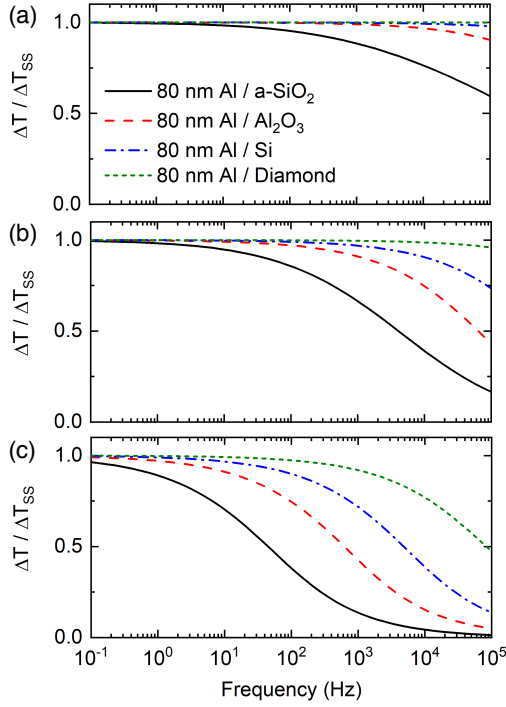


Figure 4.2: Normalized surface temperature rise ($\Delta T / \Delta T_{ss}$) vs. modulation frequency for CW laser heating with an amplitude modulated sinusoidal profile. The samples modeled include a-SiO₂ ($C_v = 1.66 \text{ MJ m}^{-3} \text{ K}^{-1}$, $\kappa = 1.4 \text{ W m}^{-1} \text{ K}^{-1}$), Al₂O₃ ($C_v = 3.06 \text{ MJ m}^{-3} \text{ K}^{-1}$, $\kappa = 35 \text{ W m}^{-1} \text{ K}^{-1}$), Si ($C_v = 1.60 \text{ MJ m}^{-3} \text{ K}^{-1}$, $\kappa = 140 \text{ W m}^{-1} \text{ K}^{-1}$), and diamond ($C_v = 1.78 \text{ MJ m}^{-3} \text{ K}^{-1}$, $\kappa = 2000 \text{ W m}^{-1} \text{ K}^{-1}$), shown for pump and probe 1/e² diameters of (a) 1 μm , (b) 10 μm , and (c) 100 μm . Al was modeled to have $C_v = 2.42 \text{ MJ m}^{-3} \text{ K}^{-1}$ and $\kappa = 130 \text{ W m}^{-1} \text{ K}^{-1}$, while Al/substrate thermal boundary conductance was modeled as 200 MW m⁻² K⁻¹ in all cases.

the same frequency as the laser heat source, but its magnitude asymptotes to a constant value, that of the steady-state temperature rise, as the modulation frequency approaches zero. Similar to the transient temperature rise case discussed previously, we see that smaller laser spot sizes allow for a quasi steady-state temperature rise to be reached at higher modulation frequencies. We can exploit this fact by running experiments at higher modulation frequencies and smaller spot sizes to reduce 1/f noise at low frequencies.

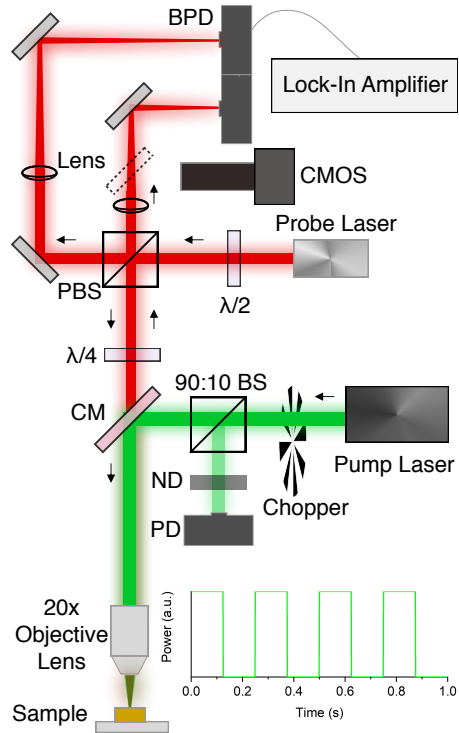


Figure 4.3: Schematic of the Steady-State Thermoreflectance (SSTR) experiment. PBS: polarizing beam splitter, $\lambda/2$, $\lambda/4$: half- and quarter-wave plates, respectively, 90:10 BS: 90% transmission / 10% reflection beamsplitter, PD: photodetector, BPD: balanced photodetector, ND: neutral density filter. Inset shows a representative pump waveform vs. time.

4.4 Experimental Details

Our experimental setup, shown in Fig. 4.3, consists of a CW diode probe laser (Coherent Cube), having a wavelength of 786 nm and output power up to 30 mW, and a CW pump laser (Spectra-Physics Millenia Vs) with a wavelength of 532 nm and output power up to 5 W. In practice, the pump power is limited to <200 mW except in the case of the most conductive materials studied here, where output powers up to 1 W proved sufficient for the pump radii used in this study. Likewise, the probe output is limited to < 1 mW to avoid any additional heating of the sample. A mechanical chopper (Thorlabs MC2000B) is used to modulate the pump. Identical experiments were performed using an electro-optic modulator (Thorlabs EO-AM-NR-C4) with excellent agreement found between the two modulation sources. Ultimately, the chopper is preferred because it is simple to use, inexpensive, allows for fully on/off square waves, and has a damage threshold far

exceeding the operating powers of the pump. Internal modulation of a pump laser offers a further step toward simplicity and cost reduction of the SSTR system. The pump waveform and power are monitored by a photodetector (Thorlabs DET10A) by picking off 10% of the beam using a 90:10 beamsplitter. Although a power meter is sufficient for this purpose and was used in our original implementation of SSTR, a photodetector is preferable because it allows us to send the signal to a second oscillator in the lock-in amplifier to measure the pump power amplitude in the same way we do the probe, i.e., with LIA or PWA detection. A neutral density (ND) filter is placed before the pump photodetector to avoid saturation of the detector. The transmitted power is then reflected by a cold mirror and sent through an objective lens to focus onto the sample.

The probe is split into two paths using a polarizing beam splitter. A half-wave plate is used to control the power of each path. The transmitted portion is used as a reference while the reflected portion passes through a quarter-wave plate that is adjusted to allow for maximum transmission of the back-reflected probe from the sample. The probe is transmitted through the cold mirror and is focused coaxially with the pump onto the sample using an objective lens. The focused pump and probe diameters were adjusted with lenses to be equivalent sizes. Using a 20 \times and 10 \times objective lens, the 1/e² diameters are 11 μm and 20 μm , respectively, as measured via a scanning slit beam profiler (Thorlabs BP209-VIS). The probe is back-reflected to a balanced photodetector (Thorlabs PDB410A) along with the path-matched reference beam to minimize common noise in the probe. The powers of the reference and sample beams going into the photodetector are adjusted to be equivalent via the half-wave plate to minimize noise. Samples tested in this study include two types of a-SiO₂, a plain glass microscope slide (Fisherbrand) and a 3 mm thick Borosilicate Glass (BK7) optical window (Thorlabs WG10530); a 1 mm thick quartz wafer (Precision Micro Optics); two types of Al₂O₃, a 300 μm thick wafer (UniversityWafer) and a 3 mm thick window (Thorlabs WG30530); two types of Si, a 300 μm thick wafer (UniversityWafer) and a 3 mm thick window (Thorlabs WG80530); a 300 μm thick nitrogen-doped, n-type 4H-silicon carbide (4H-SiC) wafer (MTI Corporation); and a 300 μm thick polycrystalline diamond wafer (Element Six TM200).

When using the 10 \times objective lens, we typically use a higher order ND filter to further reduce power going into the pump photodetector. This is done to compensate for the increased power

needed to heat the sample to similar temperatures to those achieved with the $20\times$ objective. Using a lock-in amplifier (Zurich Instruments UHFLI) synced to the chopper frequency, the magnitude (ΔV) of the probe signal divided by the DC probe signal (V) is recorded simultaneously with the lock-in magnitude of the pump photodetector (ΔP). ΔP as determined by the LIA is proportional to the amplitude of the sinusoidal component of the pump waveform. Likewise, ΔV corresponds to only the sinusoidal component of the probe waveform. LIA detection thus allows for modulation of the pump with an arbitrary periodic waveform (square, sine, triangle, etc.) and with any offset power to obtain the same relation between the lock-in pump power and lock-in probe magnitude. The pump power is increased linearly so that a linear relation between $\Delta V/V$ with pump power is obtained. The slope of this relation, after determining the appropriate proportionality constant, is used to determine thermal conductivity by comparing it to the expected temperature rise (Eq. 3.45 as calculated for a modulated CW source) per unit power. Alternatively, a PWA with boxcar averager is used to record both the pump and probe waveforms over several periods of temperature oscillation by again syncing to the chopper frequency. Using this approach, we can visualize the sample temperature rise vs. time to determine the steady-state regime of the temperature rise.

Comparing the two detection schemes, the LIA approach allows for faster data acquisition, allows for full automation of both data acquisition and analysis, and is independent of the waveform used, as only the sinusoidal component is recorded. However, because sinusoidal modulation can only achieve a quasi steady-state, for accurate determination of low-diffusivity materials, (i) the modulation frequency must be lower compared with the PWA case or (ii) the thermal model must include the modulation frequency as an input parameter. The PWA approach, on the other hand, extracts the total waveform of the probe reflectivity vs. time. As such, the square wave reflectivity waveform that results from a square wave pump input can be deduced. Furthermore, data analysis is done by manually choosing the time range in which the “on” and “off” state occur, ensuring we can pick the true steady-state temperature rise for determining thermal conductivity.

4.5 Signal Analysis

The probe reflectivity response measured by the photodetector, $\Delta V/V$, is proportional to the normalized change in reflectivity, $\Delta R/R$, which is related to the change in temperature of the sample surface by the thermoreflectance coefficient β , as described by Eq. (3.1). In general, β is temperature dependent. For Al, β is $1.14 \times 10^{-4} \text{ K}^{-1}$ and varies at a rate of 0.22×10^{-4} per 100 K [168] near our probe wavelength of 786 nm. Keeping temperature rises below 50 K ensures β varies less than 10%; estimated temperature rises [167] for our experiments are < 20 K. Using the thermoreflectance coefficient and an additional conversion of $\Delta V/V$ to $\Delta R/R$, we can obtain ΔT . Next, by measuring the power of the pump and the reflectance of the sample at the pump wavelength, we can in principle calculate the heat flux absorbed by the sample. These two quantities allow for the determination of thermal conductivity through Fourier's law applied to a semi-infinite substrate. Thus, accurate determination of heat flux and temperature would allow for an absolute technique to directly measure thermal conductivity. Since we measure $\Delta V/V$ and the pump photodetector response, $\Delta P \propto$ pump power, we seemingly have two proportionality constants to consider, one relating $\Delta V/V$ to ΔT and one relating ΔP to the heat flux magnitude $\Delta|Q|$. We eliminate one of these proportionality constants by determining $\Delta V/(V \Delta P)$, so that

$$\left(\frac{\Delta V}{V \Delta P} \right) = \gamma \left(\frac{\Delta T(\kappa)}{\Delta|Q|} \right), \quad (4.1)$$

where $\Delta T/\Delta|Q|$ is the modeled temperature rise per unit power. Next, we use a calibration with a known thermal conductivity to determine γ ,

$$\gamma = \left(\frac{\Delta T(\kappa_{\text{cal}})}{\Delta|Q|} \right)^{-1}_{\text{cal}} \left(\frac{\Delta V}{V \Delta P} \right)_{\text{cal}}. \quad (4.2)$$

The calibration used to determine γ is a single-crystal sapphire (Al_2O_3) wafer, measured to have a net thermal conductivity ($\sqrt{\kappa_r \kappa_z}$) of $35 \pm 2 \text{ W m}^{-1} \text{ K}^{-1}$ using both time-domain thermoreflectance and a hot-disk transient plane source technique (Hot Disk AB - TPS 3500). We determine γ by comparing the measured $\Delta V/(V \Delta P)$ to the ΔT predicted using the thermal model. We note that γ is different for different objective lenses used because (i) power loss may not be the same within

the two objectives and (ii) we use a stronger neutral density filter to reduce power detected with the pump photodetector when moving from the $20\times$ to $10\times$ objective to avoid saturation of the detector. Additionally, γ will differ between the LIA and the PWA approaches.

With γ defined by a calibration, measurement of $\Delta V/(V \Delta P)$ for any sample can be related to the sample's thermal conductivity by relating it to a thermal model predicting $\Delta T(\kappa)/\Delta|Q|$. The thermal conductivity input to the model is adjusted to obtain the best fit to the experimental data using a global minimization algorithm to search for the smallest absolute difference between model and data. The fundamental assumption using this approach is that the proportionality constant γ , which encompasses the thermoreflectance coefficient and conversion factor of change in reflectance to change in photodetector voltage, is equivalent between calibration and sample. To ensure this, we evaporate an 80 nm Al transducer layer on all samples under the same deposition to ensure the thermoreflectance coefficient is the same from sample to sample. As a general rule, we adjust the input power of the pump to induce approximately the same magnitude of $\Delta V/V$ for each sample. This ensures that any nonlinear responses, whether from physical parameters such as the thermoreflectance coefficient or from the photodetector response, however small, are offset since they are encompassed in γ .

4.5.1 Periodic Waveform Analyzer / Boxcar Averager

We first collect data using the PWA via a digital boxcar averager while modulating the pump beam with a chopper at 100 Hz. Using two independent oscillators, we simultaneously record the pump and probe waveforms over a phase space divided into 1024 bins. The reference frequency is provided by the chopper. The resulting waveforms, which have been converted from phase space to time, are shown for the pump in Fig. 4.4, while those of the probe are shown in Fig. 4.5. The six samples shown include (a) an a-SiO₂ glass slide, (b) z-cut quartz, (c) Al₂O₃, (d) Si, (e) 4H-SiC and (f) diamond. The modulation frequency was kept at 100 Hz in all cases and a $20\times$ objective lens was used, corresponding to $1/e^2$ pump/probe diameters of 11 μm . Each waveform was generated by averaging over 5 minutes of real time data acquisition.

As expected, the pump waveform shows a perfect on/off square wave. Note that the magnitude

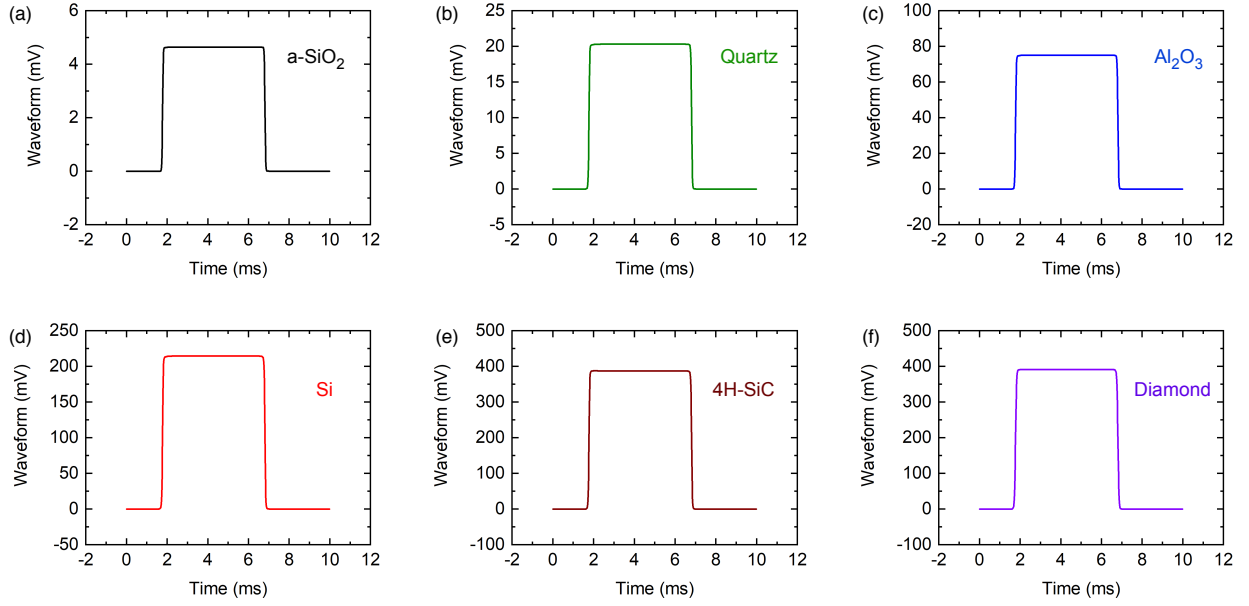


Figure 4.4: Pump waveforms obtained using a periodic waveform analyzer, shown for (a) a-SiO₂, (b) quartz, (c) Al₂O₃, (d) Si, (e) 4H-SiC, and (f) diamond. The difference between the upper and lower regimes of the waveform magnitude, ΔP (proportional to heat flux), is used to determine thermal conductivity in each case.

is increased when moving to higher thermal conductivity materials to allow for the probe waveform to reach approximately the same magnitude in each sample. The probe waveforms reveal that for all samples except a-SiO₂, a clear steady-state temperature rise is obtained as indicated by the near-square waveform. By comparison, a-SiO₂ has a relatively long-lived transient temperature rise, but reaches our steady-state threshold by the end of the waveform. The advantage of PWA analysis is that the signal difference between “on” and “off” state (ΔV) is chosen manually, so that we can neglect the transient portions of the temperature rise (however small) and only extract the steady-state regime. This is achieved through a MATLAB script in which we pick the range of time to extract signal in the “on” state and “off” state and subtract the mean signal of each state. The difference corresponds to ΔV . The mean “on” and “off” signals chosen for each case are displayed as dashed lines in Fig. 4.5. We repeat the same process for the pump waveform, where the difference between high and low waveform states corresponds to ΔP . With γ defined using a calibration, this is all the information we need to determine thermal conductivity via a purely

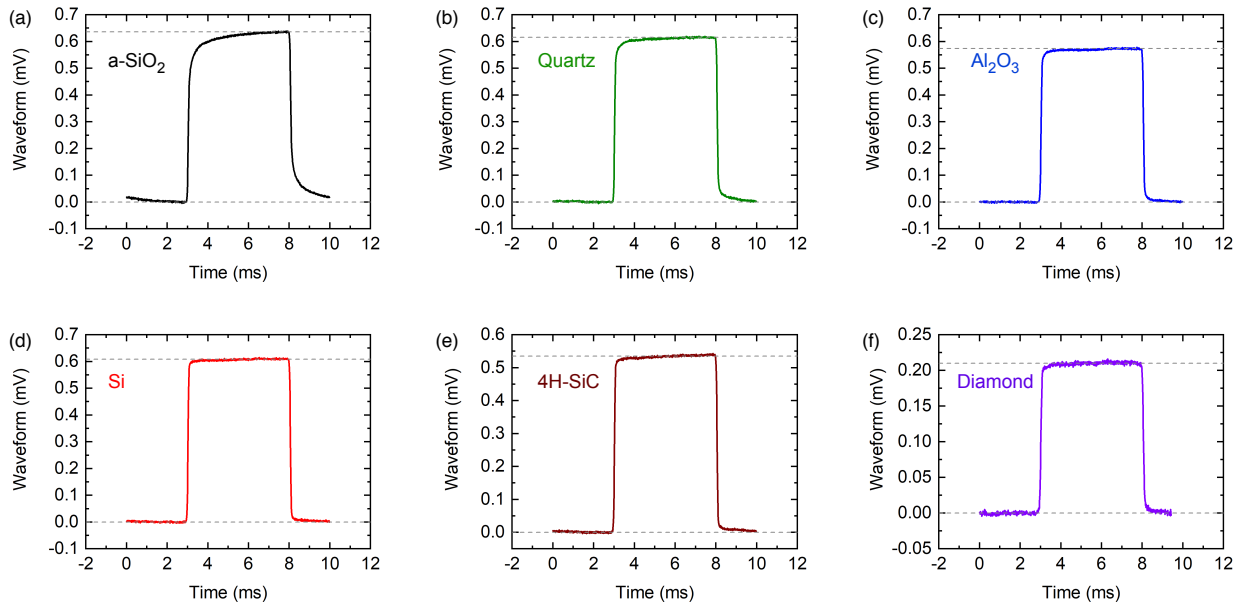


Figure 4.5: Probe waveforms obtained using a periodic waveform analyzer, shown for (a) a-SiO₂, (b) quartz, (c) Al₂O₃, (d) Si, (e) 4H-SiC, and (f) diamond. The difference between the upper and lower dashed lines indicate the ΔV (proportional to temperature rise) used to determine thermal conductivity in each case.

steady-state model (i.e., modulation frequency = 0 in the model).

4.5.2 Lock-in Amplifier

Next, we collect data via the LIA. To do so, we use the chopper reference frequency to lock into the periodic signal produced by the reflected probe. Using an automated program to control the pump power via serial command, we capture the magnitude of probe lock-in voltage as a function of 10 powers. Figure 4.6 shows the resulting relationship between $\Delta V/V$ and proportional pump power (ΔP) for two objective lenses, 10× and 20×. The lock-in time constant used was 400 ms and each datapoint represents the average over \sim 10 seconds of acquisition. The data shown include those from 3 to 5 spots on each sample, which is the primary reason for any visible scatter in the data. Each 10-data point scan takes about 2 to 3 minutes to run; this time is primarily dictated by the wait time allowed to adjust the pump power. However, in principle, after characterizing the noise floor, only a single data point is needed to establish a slope, suggesting the data acquisition

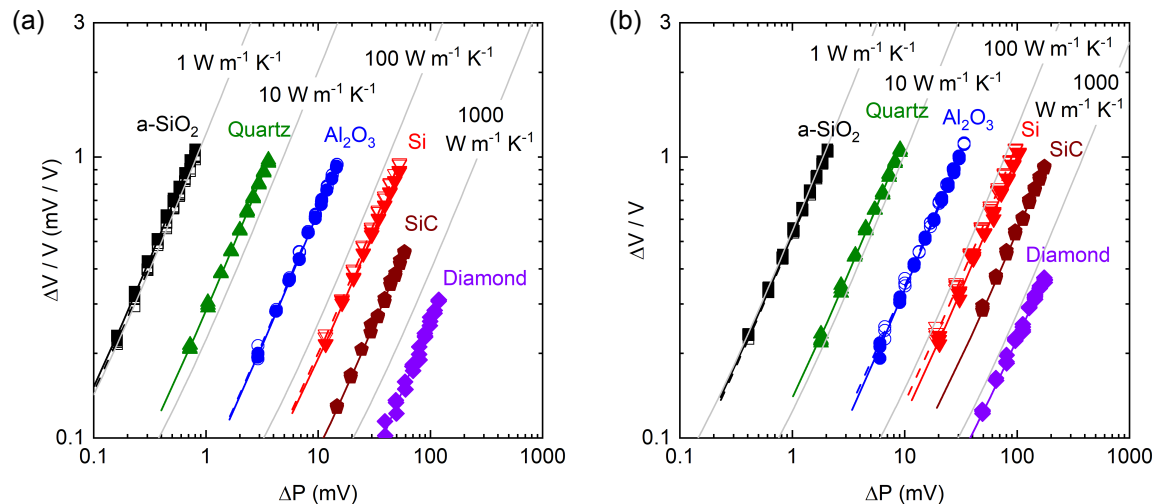


Figure 4.6: Measured $\Delta V / V$ vs. ΔP (\propto pump power) shown for (a) 10 \times objective lens (pump and probe $1/e^2$ diameters of 20 μm) and (b) 20 \times objective lens (pump and probe $1/e^2$ diameters of 11 μm). Measured samples include glass slide (squares), BK7 glass (open squares), quartz (triangles), sapphire wafer (circles), sapphire window (open circles), silicon wafer (inverted triangles), silicon window (open inverted triangles), 4H-SiC (pentagons), and diamond (diamonds). Gray lines show the predicted slopes for materials having thermal conductivities 1, 10, 100, and 1000 $\text{W m}^{-1} \text{K}^{-1}$. A different neutral density filter was used to filter pump power detected when the objective lens changed from 10 \times to 20 \times , so the x-axes are not comparable between (a) and (b).

time is limited only by the time to reach a steady lock-in magnitude.

A linear fit is performed on each dataset to determine the slope, $\Delta V / (V \Delta P)$. From this, the thermal conductivity can be determined by comparing this slope to the thermal model after dividing by γ . Figure 4.6 shows the expected slopes for a material having thermal conductivity of 1, 10, 100, and 1000 $\text{W m}^{-1} \text{K}^{-1}$. Comparing these lines with our experimental data, we see that our samples' slopes fall in line with what is expected for each substrate. For these models, we assumed an Al transducer thermal conductivity that is descriptive of what we measure via four point probe resistivity measurements, $\sim 100 \text{ W m}^{-1} \text{K}^{-1}$, a constant thermal boundary conductance of 200 $\text{MW m}^{-2} \text{K}^{-1}$ and modulation frequency of 100 Hz. To determine the impact of these assumptions, we need to determine sensitivity to our model parameters, described below.

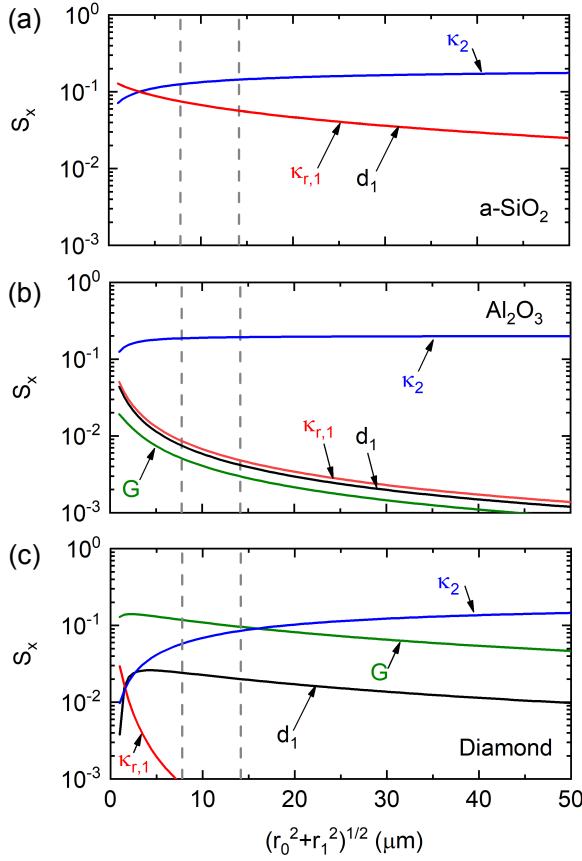


Figure 4.7: Sensitivity, S_x , to parameter x vs. effective radius, defined as $\sqrt{r_0^2 + r_1^2}$, where r_0 and r_1 are the pump and probe radii, respectively, shown for (a) a-SiO₂, (b) Al₂O₃, and (c) diamond. S_x is defined by Eq. (4.3) and the parameters varied include the sample thermal conductivity, κ_2 ; the transducer in-plane thermal conductivity, $\kappa_{r,1}$; transducer thickness, d_1 ; and the thermal boundary conductance, G , between the sample and transducer. κ_2 is defined as the geometric mean of the cross- and in-plane thermal conductivities, $\sqrt{\kappa_z \kappa_r}$.

4.5.3 Parameter Sensitivity

We quantify the sensitivity, S_x , of the thermal model to parameter x using a similar approach to that defined by Yang *et al.* [162] by varying x plus or minus 10%. Since we measure magnitude instead of phase, we add an additional division term to allow for fair comparison of sensitivities between samples. Thus,

$$S_x = \frac{|\Delta T_{1.1x}(r_{01}) - \Delta T_{0.9x}(r_{01})|}{\Delta T_x(r_{01})}, \quad (4.3)$$

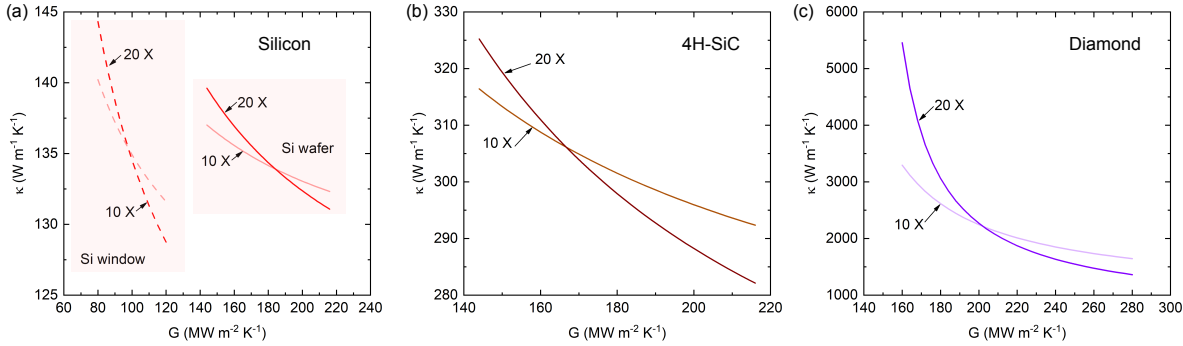


Figure 4.8: Thermal conductivity, κ vs. thermal boundary conductance, G , between the Al transducer and (a) silicon, (b) 4H-SiC, and (c) diamond. Two silicon samples were measured, a silicon wafer and silicon window, to show that the same thermal conductivity is obtained despite a large disparity in thermal boundary conductance between the two.

where ΔT_x is the temperature rise calculated for input parameter x and $r_{01} = \sqrt{r_0^2 + r_1^2}$, where r_0 and r_1 are the pump and probe radii, respectively. We define sensitivity as a function of r_{01} to show that we gain sensitivity to different parameters by utilizing multiple pump/probe diameters. Figure 4.7 shows the sensitivity as a function of r_{01} for four parameters, in-plane transducer thermal conductivity ($\kappa_{r,1}$), transducer thickness (d_1), sample thermal conductivity ($\kappa_2 \equiv \sqrt{\kappa_{r,2}\kappa_{z,2}}$), and thermal boundary conductance (G) between the transducer and substrate. The r_{01} used in our experiments are shown as dashed lines. Three samples are considered: (a) a-SiO₂, (b) Al₂O₃, and (c) diamond. Amorphous silica and diamond were chosen to display because they represent the lower and upper extremes of thermal conductivity measured in this study. For Al₂O₃, sensitivity of the thermal model is overwhelmingly dictated by κ_2 , demonstrating why Al₂O₃ is a great calibration sample to determine γ . For a-SiO₂, κ_2 again is the most sensitive parameter to our thermal model for the r_{01} used in experiment. However, we see that sensitivity to $\kappa_{r,1}$ and d_1 are still somewhat significant. These two quantities (and their corresponding uncertainties) were measured via four point probe resistivity measurements and mechanical profilometry, respectively. Sensitivity to G (not shown) was not significant at all in this case.

For diamond, we see that for the r_{01} used in experiment, we are highly sensitive to G . Therefore, in order to determine diamond's thermal conductivity, we need an accurate measurement for G . To obtain this quantity, we exploit the different sensitivities to κ_2 and G at different r_{01} values

Table 4.1: Best fit thermal conductivities for all samples tested using signal analysis by both the periodic waveform analyzer (PWA) and lock-in amplifier (LIA). For anisotropic materials, e.g. quartz and 4H-SiC, $\kappa \equiv \sqrt{\kappa_r \kappa_z}$.

Sample	κ (W m ⁻¹ K ⁻¹)			
	SSTR (PWA)	SSTR (LIA)	TDTR	literature
a-SiO ₂ glass slide	1.13 ± 0.08	1.06 ± 0.08	1.37 ± 0.13	1.3, ref. [153]
a-SiO ₂ BK7 window	1.12 ± 0.08	1.07 ± 0.09	1.18 ± 0.10	1.06, ref. [170]
z-cut Quartz	8.63 ± 0.36	8.63 ± 0.36	8.66 ± 0.61	8.6, ref. [171]
Al ₂ O ₃ wafer	35.0 ± 1.4	35.2 ± 1.4	34.9 ± 1.6	34, ref. [156]
Al ₂ O ₃ window	35.1 ± 1.4	34.8 ± 1.4	35.1 ± 1.8	34, ref. [156]
Silicon wafer	133 ± 6	136 ± 7	128 ± 9	133, ref. [156]
Silicon window	135 ± 10	136 ± 11	131 ± 9	133, ref. [156]
4H-SiC	310 ± 23	335 ± 28	324 ± 48	364, ref. [172]
Diamond	1760 ± 390	2010 ± 460	1950 ± 240	1900, ref. [93]

to determine both κ_2 and G . This procedure is performed for silicon (both the thin wafer and the thick window), 4H-SiC, and diamond. After determining $\Delta V/(V \Delta P)$ and converting to $\Delta T/\Delta|Q|$ via γ , we adjust G in the thermal model and determine the best fit κ_2 . Repeating this procedure for two objective lenses results in two distinct curves describing κ_2 vs G ; the intersection of these curves represents the true values of κ_2 and G . This approach is similar to that described by Liu *et al.* [150] to extract both thermal conductivity and heat capacity in TDTR by using multiple modulation frequencies. The results are shown in Fig. 4.8 for (a) silicon, (b) 4H-SiC, and (c) diamond. For silicon, the thermal boundary conductances are different between the wafer and the window. This may be due to extrinsic effects such as roughness, surface finish, or variations in native oxide thickness [169]. Nonetheless, the thermal conductivity is found to be equivalent in both samples, at ~ 135 W m⁻¹ K⁻¹, in agreement with literature values [156]. Likewise, for 4H-SiC and diamond, we determine G and κ_2 based on the intersection of the curves for the 10× and 20× objectives. Note, this approach can be avoided by running experiments at larger pump/probe spot sizes to become insensitive to G entirely. This approach was not needed for any other samples studied, since those measurements were not sensitive to thermal boundary conductance.

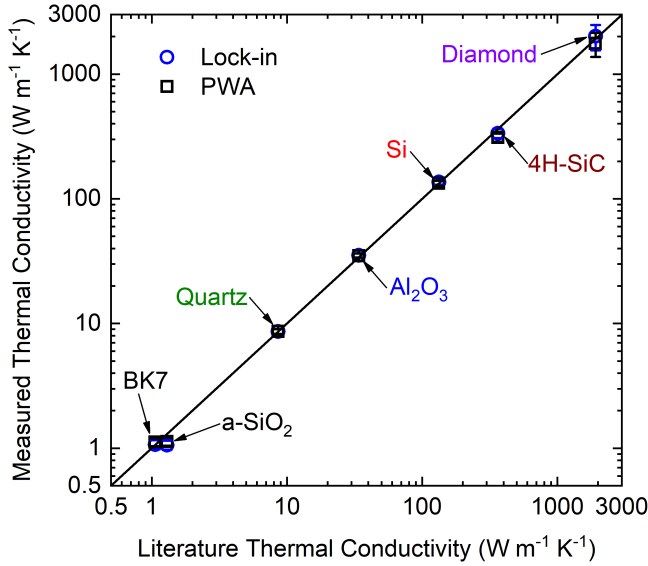


Figure 4.9: Measured thermal conductivity vs. literature thermal conductivity. Results are shown for all samples using both the lock-in amplifier analysis (open circles) and periodic waveform analysis (open squares) methods. References are listed in Table 4.1.

4.6 Results and Discussion

The measured thermal conductivities for all samples tested are listed in Table 4.1. Results are shown for SSTR using both the PWA/Boxcar and LIA signal analysis approaches to reveal that the two approaches agree with one other. To confirm the accuracy of these measurements, Table 4.1 also shows the thermal conductivities for the same samples obtained using TDTR, as well as reported thermal conductivities in the literature. Figure 4.9 shows the measured thermal conductivities vs. literature thermal conductivities spanning over three orders of magnitude. Overall, we observe excellent agreement between literature values and our measured thermal conductivities using both SSTR and TDTR. Because SSTR fundamentally measures $\sqrt{\kappa_z \kappa_r}$, for the case of anisotropic materials, the reported values for κ are equivalent to $\sqrt{\kappa_z \kappa_r}$. To obtain κ_z and κ_r independently in TDTR, for 4H-SiC we followed the methodology outlined by Qian *et al.* [172], using a relatively large pump diameter of $\sim 20 \mu\text{m}$ and high modulation frequency of 8.4 MHz to determine κ_z , followed by a smaller pump diameter of $\sim 10 \mu\text{m}$ and low modulation frequency of 1.0 MHz to determine κ_r . Using this approach, we find that $\kappa_z = 299 \pm 33 \text{ W m}^{-1} \text{ K}^{-1}$ and

$\kappa_r = 350 \pm 64 \text{ W m}^{-1} \text{ K}^{-1}$. Noting that the 4H-SiC sample measured in this study is N-doped at a level somewhere between 10^{18} and 10^{19} cm^{-3} , this measured κ_z agrees almost perfectly to that reported by Qian *et al.* [172], whereas our measured κ_r is roughly 25% lower than their reported value. This difference could be due to the sample-specific attributes such as doping level or defects. Nonetheless, the measured κ for TDTR agrees well with that of SSTR. For quartz, the thermal diffusivity is too low to enable sensitivity to κ_r ; instead, we determined κ with TDTR using two samples: z-cut and y-cut quartz. We find that for z-cut quartz, $\kappa_z = 11.63 \pm 0.80 \text{ W m}^{-1} \text{ K}^{-1}$, while $\kappa_z = 6.45 \pm 0.46 \text{ W m}^{-1} \text{ K}^{-1}$ for y-cut quartz (equal to κ_r for z-cut quartz), both in agreement with values reported by Feser *et al.* [171]. Thus, κ is equal to 8.66 ± 0.61 as determined by TDTR, in excellent agreement with that determined by SSTR.

One possible discrepancy between SSTR and literature is observed in the case of a-SiO₂. Although we reference a commonly accepted literature thermal conductivity for glass of $1.3 \text{ W m}^{-1} \text{ K}^{-1}$, we note that reported values range from 1 to $1.4 \text{ W m}^{-1} \text{ K}^{-1}$ for glass depending on the chemistry and density; in our case we measure a negligible difference between our glass microscope slide and our BK7 window. In TDTR, we measure $1.37 \text{ W m}^{-1} \text{ K}^{-1}$ for a-SiO₂, but because TDTR requires a known heat capacity to determine thermal conductivity, any discrepancy between our assumed value for volumetric heat capacity ($1.66 \text{ MJ m}^{-3} \text{ K}^{-1}$) and the actual value (which is density-dependent) could explain the difference in values obtained between the two techniques. To prove this point, TDTR and SSTR provide a similar thermal conductivity for BK7, but BK7 has a higher volumetric heat capacity than a-SiO₂ [170].

Finally, we note that the thermal conductivity of diamond has relatively large uncertainty. This is in part due to the limited temperature rise achievable in the material, resulting in a relatively low signal-to noise ratio. However, by taking multiple measurements at the same spot on the sample, we determine that this alone would only account for ~5-10% of the uncertainty. Uncertainty in thermal boundary conductance adds another significant contribution, as revealed in Fig. 4.8. Finally, we note that there is significant variation between different spots on the sample; measured thermal conductivities varied as much as ~25% from the mean. This variation could be due to local thermal conductivity reduction from grain boundaries. Sood *et al* [165]. showed that local

thermal conductivities in CVD-grown boron-doped polycrystalline diamond (average grain size of $23\ \mu\text{m}$) can decrease κ by nearly 60% near grain boundaries. Because grain sizes in the diamond measured in this study range from 10 to $100\ \mu\text{m}$, we do not expect to see the same extent of variation observed by Sood *et al.*

4.7 Sources of Uncertainty

Because SSTR relies on the proportionality constant, γ , it is highly important to characterize γ and its uncertainty with accuracy. To determine uncertainty in γ , we use a Monte Carlo approach to randomly vary input parameters to the thermal model based on their corresponding uncertainties. These parameters include the transducer thickness, d_1 ($80 \pm 3\ \text{nm}$); transducer thermal conductivity, $\kappa_{r,1}$ ($100 \pm 5\ \text{W m}^{-1}\ \text{K}^{-1}$); substrate thermal conductivity, κ_2 (for Al_2O_3 , $35 \pm 2\ \text{W m}^{-1}\ \text{K}^{-1}$); transducer / substrate thermal boundary conductance, G (for Al / Al_2O_3 , $250 \pm 30\ \text{MW m}^{-2}\ \text{K}^{-1}$); and effective radius, r_{01} (assumed 5% uncertainty). Additionally, we include experimental uncertainty in determining $(\Delta V/V \Delta P)$. For the LIA analysis, this was determined by the standard deviation of the best fit slope to experimental data, while in the PWA case it was determined by the standard deviation of the signal in both the “on” and “off” states. Iterating over 10^5 simulations, we obtain a standard deviation of $< 5\%$ of the mean. The same approach was used to characterize uncertainties of the samples tested in this study. Assuming the independence of parameters simplifies the uncertainty analysis, so that the uncertainty is $\Delta \approx \sqrt{\sum_i \Delta_i^2}$, where Δ_i is the uncertainty in κ resulting from uncertainty in parameter i . The reported uncertainties are listed in Table 4.1.

Signal noise comes primarily from $1/f$ noise. Using low probe powers, high pump powers, and longer averaging and/or lock-in times can help to overcome this noise, but ultimately there is a lower limit to the frequency that can be detected with a sufficient signal-to-noise ratio. We used a digital oscilloscope to observe, in the frequency domain, the magnitude of ΔV compared to the noise floor. For the highest pump powers used in each case, the signal-to-noise ratio was anywhere from 10 to 100. Lock-in amplification and/or boxcar averaging further facilitated signal extraction.

For uncertainty resulting from model parameters, sensitivity to these parameters dictates the

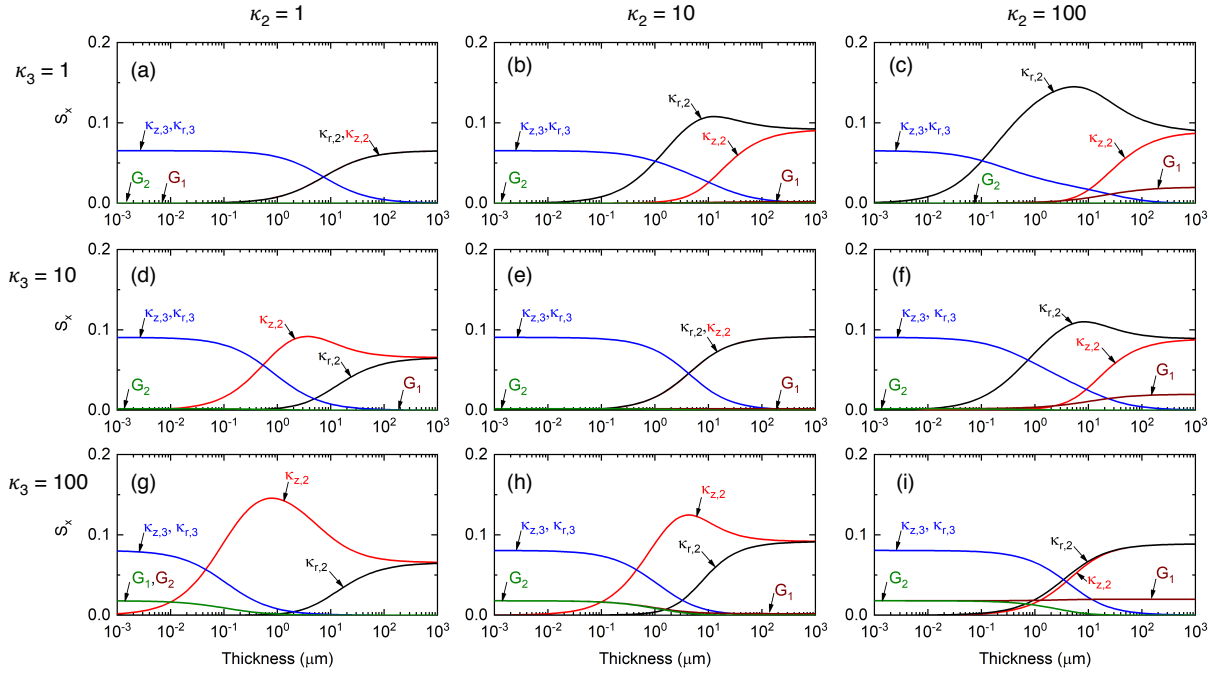


Figure 4.10: Sensitivity to thermal parameters of a three-layer model (1: 80 nm transducer / 2: film / 3: substrate) vs. layer 2 film thickness. The nine cases considered include (a) $\kappa_2 = 1$, $\kappa_3 = 1$, (b) $\kappa_2 = 10$, $\kappa_3 = 1$, (c) $\kappa_2 = 100$, $\kappa_3 = 1$, (d) $\kappa_2 = 1$, $\kappa_3 = 10$, (e) $\kappa_2 = 10$, $\kappa_3 = 10$, (f) $\kappa_2 = 100$, $\kappa_3 = 10$, (g) $\kappa_2 = 1$, $\kappa_3 = 100$, (h) $\kappa_2 = 10$, $\kappa_3 = 100$, and (i) $\kappa_2 = 100$, $\kappa_3 = 100 \text{ W m}^{-1} \text{ K}^{-1}$. In all cases, the transducer thermal conductivity is set to $100 \text{ W m}^{-1} \text{ K}^{-1}$, while the transducer/film and film/substrate thermal boundary conductances (G_1 and G_2 , respectively) are set to $100 \text{ MW m}^{-2} \text{ K}^{-1}$.

magnitude of their contributions to total uncertainty. For low thermal conductivity materials, transducer thickness and thermal conductivity can be relatively significant, while for higher thermal conductivity materials the interface conductance can be significant.

4.8 Thin Film Measurement Sensitivity

While the discussion and experimental results have been focused on the measurement of bulk substrates, we note that thin film thermal conductivities can be measured under the right conditions. In Fig. 4.10 we show the relative sensitivities to thermal parameters of a three-layer model (layer 1: 80 nm transducer / layer 2: film / layer 3: substrate) as a function of layer 2 film thickness, assuming a $10\times$ objective lens is used so that the pump and probe diameters are 20 μm (radii

are $10 \mu\text{m}$). Due to the sensitivity of SSTR measurements being highly dependent on the relative properties of film and substrate, κ_2 and κ_3 are varied in combinations of 1, 10, and $100 \text{ W m}^{-1} \text{ K}^{-1}$ for a total of nine cases. Sensitivities are shown for both in-plane (r) and cross-plane (z) directions, as well as for transducer/film and film/substrate thermal boundary conductances (G_1 and G_2 , respectively).

Quantifying the thickness at which SSTR can measure κ_2 as the thickness at which sensitivity to this parameter surpassing κ_3 , we find that highly dissimilar κ_2 and κ_3 allow for such measurement as low as $< 100 \text{ nm}$, two orders of magnitude below the measurement characteristic length scale defined by the pump radius. Interestingly, whereas for bulk materials SSTR maintains the same sensitivity to $\kappa_{r,2}$ and $\kappa_{z,2}$, for thin films this is not the case. For a thermally conductive film on an insulating substrate, SSTR becomes highly sensitive to $\kappa_{r,2}$, whereas for a thermally insulating film on conductive substrate, $\kappa_{z,2}$ becomes the dominant thermal parameter in the model. At the other extreme, when film and substrate κ are highly similar, sensitivity to κ_2 does not surpass κ_3 until close to $10 \mu\text{m}$, i.e., the pump radius. In this case, symmetry in the temperature profile between the z and r directions is preserved so that sensitivity to κ_2 and κ_3 are equivalent, barring minor influence from G_2 . Clearly, measurement of thin films is facilitated by strong differences in film and substrate κ . Still, even in the worst-case scenario in which these thermal conductivities are equal, the critical film thickness that can be measured, as we define it, is about equal to the pump radius. Consequently, reducing the pump/probe radii via higher objective lenses becomes an option for improving sensitivity to thin film thermal conductivities.

4.9 Summary

A steady-state thermoreflectance method has been presented for measuring the thermal conductivity of materials. This method relies on square-wave modulation of a continuous wave pump laser to induce a steady-state temperature rise within a sample that is modulated continuously between “on” and “off” states. Using both a lock-in amplifier and periodic waveform analyzer with a boxcar averager, we measure the change in reflectivity of a sample via a continuous wave probe

(proportional to temperature change) together with the change in power of the pump (proportional to heat flux). Using SSTR, we measure samples having thermal conductivities ranging from 1 to $>2000 \text{ W m}^{-1}\text{K}^{-1}$.

Chapter 5

Entropy-Stabilized Oxides

One of the goals of this dissertation is to understand the mechanisms that enable crystalline materials to behave, from a thermal transport perspective, as if they were amorphous. As discussed in Chapter 2, introducing large disorder into a crystal through alloying is an approach to understand this phenomena. In this chapter, I will investigate the effect of high configurational disorder on the thermal properties of crystals by studying a new class of material: entropy-stabilized oxides.

5.1 Motivation

High-entropy alloys (HEAs), consisting of five or more approximately equimolar compositions of elements [173, 174], have proven to exhibit unique physical properties such as high hardness [175], thermal stability [176], structural stability [177], as well as corrosion, oxidation, and wear resistance [178–180]. While microstructure and mechanical properties have been extensively studied, thermal properties, such as heat capacity and thermal conductivity, have been given far less attention [181–183]. Although the random distribution of atomic configurations in HEAs are appealing for understanding the role of configurational disorder on thermal transport, insight is limited by the significant electronic contribution that arises from the metallic nature of most HEAs, which can obscure insight into the lattice thermal conductivity. When nonmetal constituents comprise a disordered solid solution, the dynamics of thermal transport becomes dominated by phonons. However,

only recently was the concept of entropy stabilization realized in ceramics [184], allowing for an ideal platform to study the role of mass and interatomic force disorder beyond what has been previously accessible. Since the conception of these ceramics, high-entropy oxides have demonstrated the capability for superionic mobility [185] and thermochemical water splitting [186]. Furthermore, high configurational entropy can be highly beneficial to the development of thermoelectric properties [187]. Understanding the general implications of extreme configurational entropy on the lattice thermal conductivity would greatly benefit the design of high-entropy materials for use in such applications.

To this end, we study the thermal properties of a new class of mixed oxides analogous to their HEA metallic counterparts, entropy-stabilized oxides (ESOs), characterized by their high configurational entropy that leads to structural and chemical stabilization through a local minimization of Gibbs free energy [184]. Each ESO forms a single phase, single crystal rocksalt structure having a fixed oxygen anion sublattice; between each oxygen atom pair sits a cation randomly selected among the equiprobable distribution of 5 or 6 unique elements. The ESOs (see Table 5.1) include J14 ($\text{Mg}_x\text{Ni}_x\text{Cu}_x\text{Co}_x\text{Zn}_x\text{O}$, $x = 0.2$), and five 6-cation oxides made up of the J14 composition plus an additional cation to include Sc (J30), Sb (J31), Sn (J34), Cr (J35), and Ge (J36). We show that ESOs possess amorphous-like thermal conductivities that, in contrast to analytical theory, drop by a factor of two when adding an additional cation species to a 5-cation crystal, regardless of the mass added. Using extended X-ray absorption fine structure, we isolate the mechanism of this reduction to atomic level disorder resulting from charge differences among the ions. This local atomic disorder manifests itself in an observable distortion of the oxygen sublattice while preserving long range crystallographic order measured with X-ray diffraction. This finding is further corroborated by molecular dynamics simulations that account for differences among interatomic forces through electrostatic interactions based on Bader charges taken from density functional theory calculations [188].

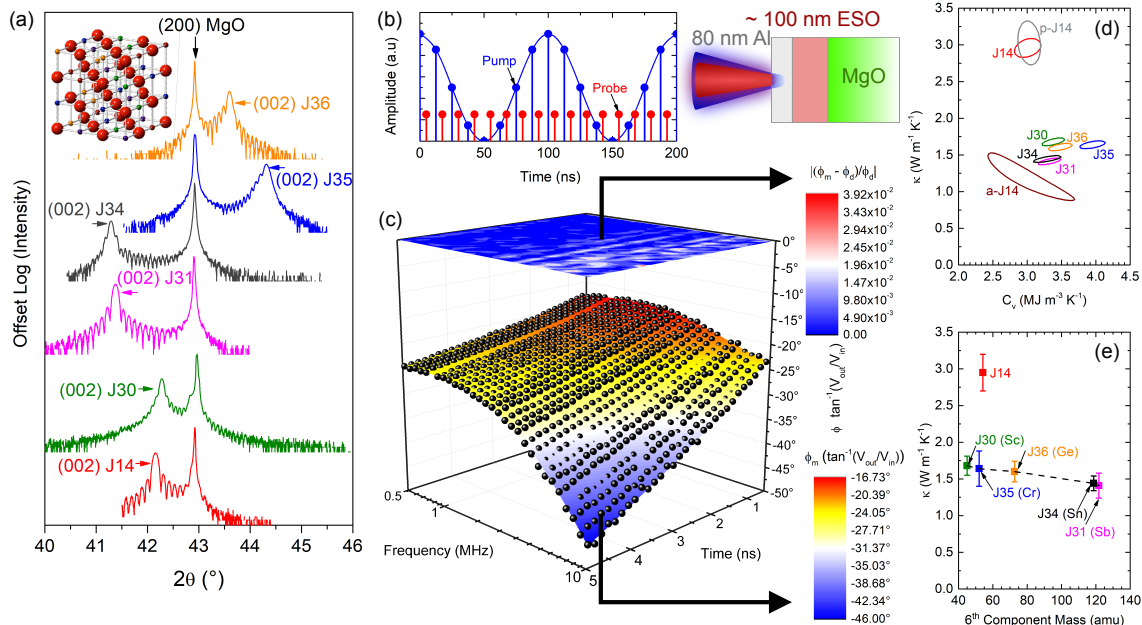


Figure 5.1: (a) 2θ - ω X-ray diffraction scan around the (200) MgO substrate peak. Inset shows J14 crystal structure with red anions representing oxygen and cation sites occupied by a random distribution of five distinct elements. (b) Schematic for TDTR/FDTR experiment: sample is 80 nm Aluminum on a \sim 100 nm ESO film grown on an MgO substrate. Laser heating by a modulated pulsed pump is detected by a probe by locking into the pump modulation frequency; the modulation frequency is varied and the probe is delayed in time relative to the pump, creating a time and frequency space to which to fit a thermal model. (c) Combined TDTR/FDTR experimental phase data ($\phi = \tan^{-1}(V_{out}/V_{in})$) and surface fit for J14 at room temperature (symbols), together with the best-fit thermal model and resulting normalized residuals $|(\phi_m - \phi_d)/\phi_d|$. (d) Contour of deviation sum as functions of κ and C_v for all thin film samples, as determined by the 95% confidence interval in the normalized residuals. Sample compositions are provided in Table 5.1. (e) κ vs. 6th-cation atomic mass for 6-cation ESOs. For reference, κ of J14 is also shown at its average cation mass.

5.2 Experimental Details

ESO thin films were grown epitaxially on MgO substrates using pulsed laser deposition. Because the ESOs are pinned in-plane to the MgO substrate, their in-plane lattice parameters match that of MgO at 4.21 Å, whereas the out-of-plane lattice parameters vary slightly based on composition. Crystal structures were characterized using X-ray diffraction (XRD). Figure 5.1(a) shows the 2θ - ω XRD scan around the (200) MgO substrate peak. Lower (higher) 2θ indicates larger (smaller) out-of-plane lattice parameters. Thermal characterization was performed using a combined time- and frequency-domain thermoreflectance technique to simultaneously measure the

thermal conductivity (κ) and volumetric heat capacity (C_v) of the thin-film ESO samples. This approach is based on the concept of varying the modulation frequency of the heating event to change the measurement property from thermal effusivity to thermal diffusivity, thereby decoupling thermal conductivity from volumetric heat capacity, allowing for a unique measurement of both quantities [101, 150, 164].

We extend the approach by Wei *et al.* [164] to incorporate TDTR phase data over a range of frequencies sufficient for FDTR, so as to combine the benefits of multifrequency TDTR and FDTR for thermal property measurement. This development provides a robust approach for measuring both the heat capacity and thermal conductivity of thin films. In brief, by collecting data as a function of both time and frequency, we use a surface fitting method to minimize the residuals between a time- and frequency-dependent thermal model with experimental data by varying three thermal parameters: ESO volumetric heat capacity, ESO thermal conductivity, and Al/ESO thermal boundary conductance ($G_{\text{Al}/\text{ESO}}$). The ESO/MgO thermal boundary conductance ($G_{\text{ESO}/\text{MgO}}$) can in principle be set as a fitting parameter as well. However, in practice we are generally insensitive to this parameter, such that doing so gives us no additional benefit or physically meaningful information. Further details on the combined TDTR/FDTR approach and its comparison to the alternative methods to simultaneously measure C_v and κ can be found in the supporting information of Ref. [167]. A schematic of the experiment and the sample geometry is shown in Fig. 5.1(b). The resulting best-fit surface model and data are shown in Fig. 5.1(c) for J14, along with the normalized residuals, for the phase as a function of delay time and modulation frequency. From this, we follow the procedure outlined by Wang *et al.* [51] to determine the 95% confidence interval of fitted thermal conductivity and heat capacity based on the 2 standard deviation difference from the minimum normalized residual. Figure 5.1(d) shows the results for J14 and all 6-component ESOs, where contour lines indicate the combinations of κ and C_v corresponding to a 95% confidence interval.

Table 5.1: Thermal and physical properties of ESOs at room temperature. Compositions and measured properties include film thickness (d), thermal conductivity (κ), volumetric heat capacity (C_v), and elastic modulus (E).

Name	Composition	d (nm)	κ ($\frac{\text{W}}{\text{mK}}$)	C_v ($\frac{\text{MJ}}{\text{m}^3\text{K}}$)	E (GPa)
J14	$\text{Mg}_x\text{Ni}_x\text{Cu}_x\text{Co}_x\text{Zn}_x\text{O}$, $x = 0.2$	114 ± 2	2.95 ± 0.25	3.01 ± 0.49	152.0 ± 10.6
J30	$\text{Mg}_x\text{Ni}_x\text{Cu}_x\text{Co}_x\text{Zn}_x\text{Sc}_x\text{O}$, $x = 0.167$	149 ± 4	1.68 ± 0.13	3.37 ± 0.42	236.7 ± 15.9
J31	$\text{Mg}_x\text{Ni}_x\text{Cu}_x\text{Co}_x\text{Zn}_x\text{Sb}_x\text{O}$, $x = 0.167$	117 ± 6	1.41 ± 0.17	3.29 ± 0.54	158.4 ± 10.9
J34	$\text{Mg}_x\text{Ni}_x\text{Cu}_x\text{Co}_x\text{Zn}_x\text{Sn}_x\text{O}$, $x = 0.167$	118 ± 2	1.44 ± 0.10	3.29 ± 0.44	180.8 ± 17.9
J35	$\text{Mg}_x\text{Ni}_x\text{Cu}_x\text{Co}_x\text{Zn}_x\text{Cr}_x\text{O}$, $x = 0.167$	109 ± 8	1.64 ± 0.24	3.96 ± 0.75	151.0 ± 9.2
J36	$\text{Mg}_x\text{Ni}_x\text{Cu}_x\text{Co}_x\text{Zn}_x\text{Ge}_x\text{O}$, $x = 0.167$	109 ± 3	1.60 ± 0.14	3.55 ± 0.48	229.9 ± 21.2

5.3 Results and Discussion

There is a strong reduction in thermal conductivity between J14 and all 6-cation oxides; variation in κ among the latter are within 20% of one another and follow an expected decreasing trend with heavier average cation mass, as shown in Fig. 5.1(e). Accounting for uncertainties arising from film thicknesses and thermal properties does not explain this reduction from 5- to 6-cations. This finding suggests that there is an enhanced level of phonon scattering intrinsic to the 6-cation oxides compared to J14 that is dictating the observed reduction in thermal conductivity. Furthermore, a 105 nm polycrystalline J14 sample (p-J14) was fabricated on an amorphous SiO_2 (a- SiO_2) substrate; grain sizes were on the order of 50-100 nm as determined by atomic force microscopy (AFM). Grain boundaries typically scatter phonons on the order of the grain size [112, 113], which would reduce the thermal conductivity of p-J14 relative to single crystal J14. Because the substrate is a- SiO_2 in this case, heat capacity and thermal conductivity cannot be decoupled. However, if we assume that the heat capacity is that of J14, the thermal conductivity is, within uncertainty, equal to that of J14. This indicates that phonon scattering at grain boundaries negligibly affects the thermal conductivity, suggesting that the phonons contributing most strongly to thermal transport in J14 have mean free paths smaller than this average grain size. Moreover, this result indicates that even with additional external scattering mechanisms, the thermal conductivity of J14 does not reduce to those of the 6-cation oxides. To understand the significance of this reduction in thermal conductivity, we measure a 78 nm amorphous J14 (a-J14) film grown on a- SiO_2 . Again assuming the same heat capacity as J14, the thermal conductivity of a-J14 is 1.16 ± 0.16 , almost a third that

of J14, and within 20% of the thermal conductivity of J31. This amorphous thermal conductivity is typically assumed to be the minimum limit to the intrinsic thermal conductivity of a solid [80].

Reduced crystalline thermal conductivity approaching the amorphous limit is an attractive property to several applications, including thermoelectric power generation [25] and thermal barrier coatings [37], where crystalline materials allow for the desirable electronic properties and temperature stability necessary for extreme environments. Such reduction is often achieved via nanostructuring with defects and/or interfaces, the latter of which resulted in the lowest thermal conductivity measured in a fully dense solid at $0.05 \text{ W m}^{-1} \text{ K}^{-1}$ for WSe_2 in the cross-plane direction [103], a $30\times$ reduction over the c-axis thermal conductivity of single-crystal WSe_2 . For macroscale applications in which films inevitably become large enough that grains of varying orientations form, thermal conductivity reduction in one crystallographic direction does not have significant benefit. Thus, for isotropic crystals, such reduction is typically achieved via increasing compositional disorder [13], which can lead to mass mismatch, atomic radii mismatch, and local atomic strain that results in additional phonon scattering. For example, mixed crystals with controlled disorder were shown to have thermal conductivities that approach their minimum limit [80]. Similarly, unary and binary compound superatomic crystals were shown to have amorphous-like thermal conductivities when orientational disorder is present [189]. On the other hand, complex crystals such as the cubic I-VI₂ semiconductor AgSbTe_2 have intrinsically glass-like thermal conductivities [190] attributed to the spontaneous formation of nanoscale domains with different orderings on the cation sublattice [191].

Regardless of the mechanism, a thermal conductivity reduction generally comes at the expense of a crystal's stiffness, as determined by its elastic modulus. This is shown in Fig. 5.2(a), where thermal conductivity is plotted as a function of elastic modulus for a wide array of isotropic crystals. Whereas metals can maintain a relatively high thermal conductivity due to contribution from electron transport, phonons are the dominant heat carriers in nonmetals; reduction of elastic modulus is indicative of a reduction in phonon group velocity and energies, resulting in a lowered thermal conductivity. As shown in Fig. 5.2(a), the regime of simultaneously stiff and insulative crystals is unpopulated, despite the need in practical applications such as thermal barrier coatings. We show

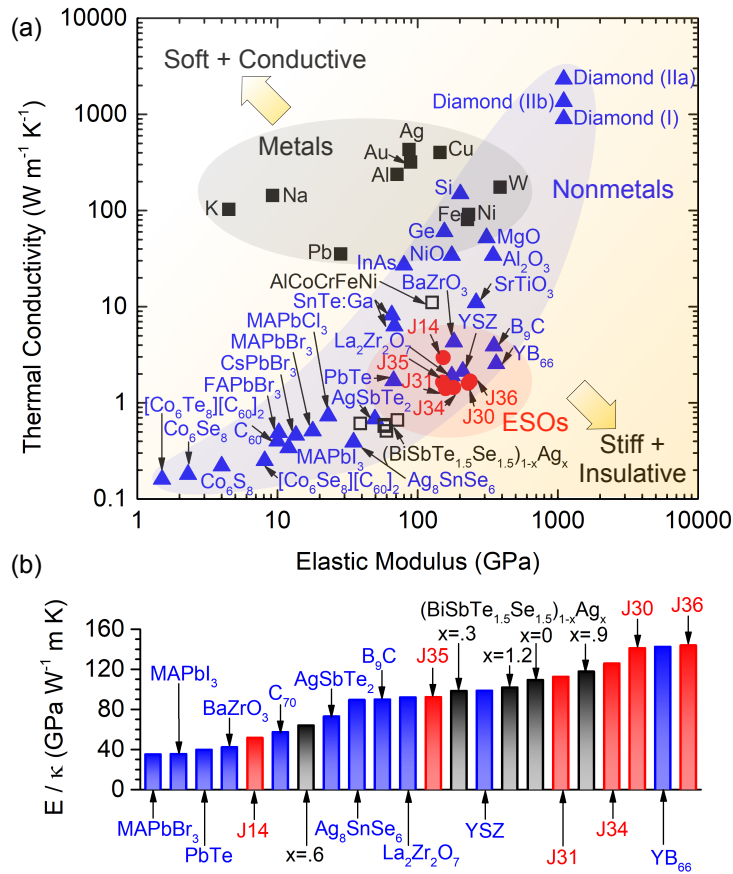


Figure 5.2: (a) Thermal conductivity (κ) vs. elastic modulus (E) for a wide range of isotropic crystals at room temperature. Materials are grouped into metals (squares) and nonmetals (triangles), the former having the subset of high-entropy alloys (open squares) and the latter having the subset of ESOs (circles). (b) Ratio of E to κ for the highest-ratio crystals from (a). A table of data and references can be found in the Supporting Information.

that ESOs, whose elastic moduli are measured with contact resonance atomic force microscopy (CR-AFM), represent a step towards filling this void. In fact, in Fig. 5.2(b) we quantify the ratio of elastic modulus to thermal conductivity (E/κ) to show that ESOs fall in line with the highest E/κ crystals at room temperature, surpassing prominent thermal barrier coating materials such as zirconates BaZrO₃, and La₂Zr₂O₇ and the most commonly used Y₂O₃-stabilized ZrO₂ (YSZ) [40]. By comparison, HEAs have elastic moduli falling anywhere from 20 to 180 GPa [192], while thermal conductivities generally exceed $10 \text{ W m}^{-1} \text{ K}^{-1}$ [192]. The general metallic nature of most HEAs means that they will have relatively large contributions from electrons to thermal conductivity. However, recent developments in HEAs for use in thermoelectric applications [183, 193] have

demonstrated that HEAs can have thermal conductivities as low as $0.5 \text{ W m}^{-1} \text{ K}^{-1}$ at room temperature [183]. Because $E/\kappa (\propto 1/C\tau)$, where C is heat capacity and τ is phonon scattering time) is indicative of the phonon scattering rate, the high ratios observed for ESOs demonstrate the use of entropy stabilization with multiple components to reduce phonon scattering times rather than velocities, which opens the door to unique combinations of properties, in this case simultaneously high elastic modulus and near-minimum thermal conductivity.

To better understand this reduction in thermal conductivity from 5- to 6-cations, we measure the thermal conductivities of J14 and J35 over a temperature range of 78 – 450 K, presented in Fig. 5.3(a). J14 and J35 have nearly identical average mass, thickness, and sound speed, making the two ideal candidates to compare. A similar reduction in thermal conductivity is observed in J35 compared to J14 at all temperatures tested. Unlike typical crystalline materials' thermal conductivity trends with temperature, both J14 and J35 display trends indicative of amorphous materials, having increasing thermal conductivities with temperature. To put this into perspective, we measure the thermal conductivity of a-J14 to show this characteristic amorphous thermal conductivity relation with temperature, revealing that J35 shows similar magnitudes of thermal conductivity to those of a-J14 at comparable temperatures. Furthermore, we measure 2-cation oxides of $\text{Cu}_{0.2}\text{Ni}_{0.8}\text{O}$, $\text{Zn}_{0.4}\text{Mg}_{0.6}\text{O}$, $\text{Co}_{0.25}\text{Ni}_{0.75}\text{O}$ at 230 – 450 K to show the characteristic Umklapp scattering trend ($\propto 1/T$) expected in crystalline materials and enhanced thermal conductivity relative to J14/J35. Qualitatively, the addition of cations results in greater deviation from a perfect crystal, which reduces thermal conductivity through increased phonon scattering. We model this phonon scattering to estimate the thermal conductivity as a function of temperature using the virtual crystal approximation (VCA) [12], based on the kinetic theory model presented in Ch. 2.

Under the VCA, all cations are assumed to have the same mass equal to the average cation mass such that mass differences in Eq. (2.22) are with respect to this average mass. Additionally, the differences in stiffness constants and atomic radii are with respect to those average quantities of all cations. In this case, the B and C used in Eq. (2.18) will take the form of the average B and C for each oxide constituent. However, we estimate these values based on the average of only two such components, MgO and NiO, due to the lack of rigorous temperature dependent thermal

Table 5.2: Model parameters for VCA under a Debye approximation: γ is the Grüneisen parameter, Γ_f is the strain portion of Γ , B and C are Umklapp scattering parameters.

Sample	B (s K $^{-1}$)	C (K)	No fit		Best fit	
			Γ_f	γ	Γ_f	γ
J14	1.081×10^{-18}	114	0	1.6 ± 0.4	0.496	0
J35	1.081×10^{-18}	114	0	1.6 ± 0.4	1.39	0
$\text{Cu}_{0.2}\text{Ni}_{0.8}\text{O}$	1.24×10^{-18}	81.6	0	1.6 ± 0.4	0.0015	1.43
$\text{Zn}_{0.4}\text{Mg}_{0.6}\text{O}$	0.92×10^{-18}	146.3	0	1.6 ± 0.4	0	0.84
$\text{Co}_{0.25}\text{Ni}_{0.75}\text{O}$	1.24×10^{-18}	81.6	0	1.6 ± 0.4	0.11	1.34

conductivity data for single crystal forms of the other constituents. Nonetheless, we find that this approximation B and C is relatively unimportant because the other scattering terms dominate the total scattering time of the system. We use the VCA with the relaxation time described by Eq. (2.24) to calculate the models. We begin with no fitting parameters, ignoring Γ_f in Eq 2.22 and assuming the Grüneisen parameter is that of MgO. Uncertainty in the VCA is primarily from uncertainty in this Grüneisen parameter controlling the normal scattering rate, which we vary from 1.2 to 2.0 based on the constituent oxide values. We then fit for Γ_f and γ . All model parameters are listed in Table 5.2.

Assessing the VCA as a predictive model, Fig. 5.3 shows that it accurately describes the thermal conductivity relation with temperature for both (b) $\text{Cu}_{0.2}\text{Ni}_{0.8}\text{O}$ and (c) $\text{Zn}_{0.4}\text{Mg}_{0.6}\text{O}$ when considering only mass disorder as the phonon-defect scattering process. The VCA, while capturing the Umklapp scattering temperature trend observed experimentally, does not accurately predict the magnitude of thermal conductivity for (d) $\text{Co}_{0.25}\text{Ni}_{0.75}\text{O}$, owing to the nearly identical mass of Co and Ni, suggesting the need to include additional phonon scattering due to variations in the interatomic force constants (IFCs). For the purposes of the VCA analytical model, we treat the IFC scattering rate coefficient and the Grüneisen parameter, which affects normal scattering rates, as fitting parameters. With these adjustable parameters, the VCA can accurately capture the measured thermal conductivity, as depicted in Fig. 5.3(d). Addition of these fitting terms proves to make a negligible difference for (b) $\text{Cu}_{0.2}\text{Ni}_{0.8}\text{O}$ and (c) $\text{Zn}_{0.4}\text{Mg}_{0.6}\text{O}$. Overall, the VCA captures the thermal conductivity of these 2-cation oxides with reasonable agreement to experiment.

When applied to 5- and 6-component ESOs, the VCA lacks predictive capability in both mag-

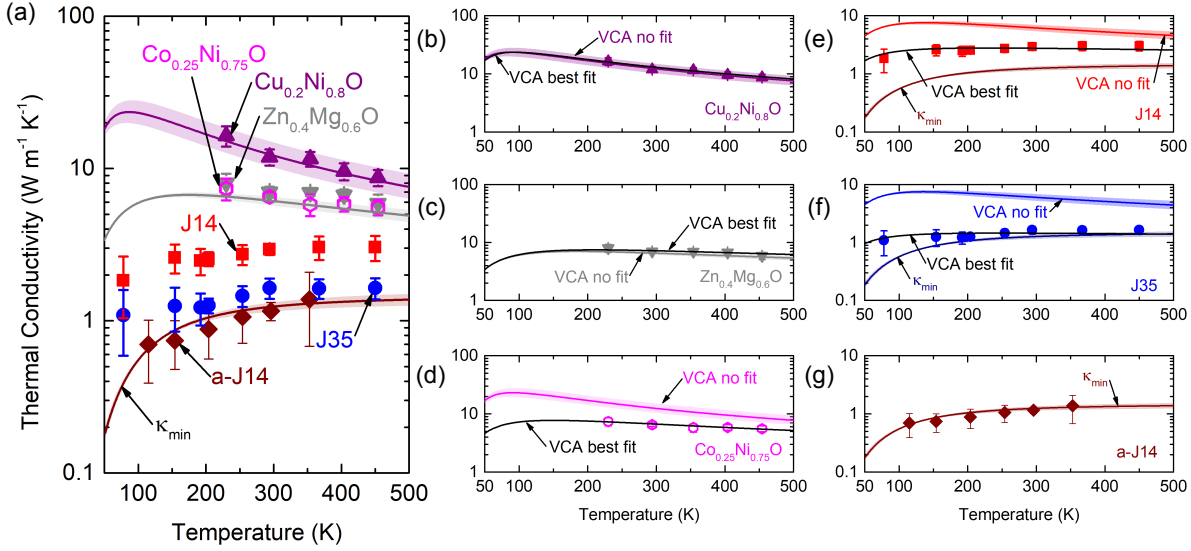


Figure 5.3: (a) Thermal conductivity vs. temperature. Purple and gray lines depict VCA models without fitting parameters for Cu_{0.2}Ni_{0.8}O and Zn_{0.4}Mg_{0.6}O, while maroon line is the minimum thermal conductivity model for J14 (κ_{\min}); shaded regions indicate uncertainties in the model. Thermal conductivity data is shown together with VCA models with and without adjustable parameters for (b) Cu_{0.2}Ni_{0.8}O, (c) Zn_{0.4}Mg_{0.6}O, (d) Co_{0.25}Ni_{0.75}O, (e) J14 (f) J35, and (g) a-J14.

nitude and temperature trend; this is shown in Fig. 5.3(e) and (f) for J14 and J35, respectively. In fact, the VCA predicts that J14 and J35 should have higher thermal conductivities than both Zn_{0.4}Mg_{0.6}O and Co_{0.25}Ni_{0.75}O due their virtual crystal's average mass having a smaller weighted difference with constituent masses than do the 2-cation oxides. Indeed, a saturation of phonon scattering from mass disorder limits the thermal conductivity reduction achievable with an increasing number of components [194]. A similar argument can be made regarding additional terms describing disorder scattering in the VCA, which are likewise defined by the difference between average and constituent properties. While fitting parameters allow for better agreement between the VCA and experimental thermal conductivities, no combination of Grüneisen parameter and IFC scattering rate can capture the amorphous-like temperature trend. However, this amorphous-like trend has been observed in a variety of complex crystalline systems [13]. In such cases, the minimum thermal conductivity (κ_{\min}) model [80] that was defined in Eq (2.30) can be invoked to lend insight into experimental findings. We show in Fig. 5.3(g) that κ_{\min} , as defined for J14 based on sound speed derived from CR-AFM, agrees well with experimental thermal conductivities for a-J14 and

reasonably captures J35's thermal conductivity.

That the VCA fails to capture the trend in thermal conductivity of J14 and J35 may be interpreted by recent developments by Seyf *et al.* [75], who hypothesize that non-propagating modes (diffusons) can comprise the majority of vibrational modes contributing to thermal conductivity when disorder becomes large. This manifests itself in amorphous-like thermal conductivity trends with temperature. Moreover, we do not observe any statistically significant size effects in thermal conductivity for the samples tested here (see supporting information of Ref. [167]), further supporting the idea that either diffusons or short mean-free-path phonons/propagons dominate thermal transport in these systems. An alternative interpretation, however, is that if the VCA is valid, the temperature-independent Rayleigh scattering may be large enough to overwhelm Umklapp scattering. Indeed, if we remove Umklapp scattering from the VCA model, we can reasonably emulate the thermal conductivity as a function of temperature, suggesting that Rayleigh scattering is the dominant phonon scattering mechanism dictating thermal conductivity. Finally, although strong anharmonic phonon scattering has been shown to arise due to large mass disorder [76], the thermal expansion coefficient for the ESOs are measured via temperature-dependent XRD to be $\sim 1.2 - 1.4 \times 10^{-5}/^{\circ}\text{C}$, in agreement with constituent oxides MgO [195] and NiO [62], suggesting anharmonic scattering is not abnormally strong in the ESOs. Therefore, the temperature-independent nature of the mechanism causing reduction in thermal conductivity in ESOs, in particular that driving down 5- to 6-cation thermal conductivities, suggests strong Rayleigh scattering resulting from IFC disorder. The best-fit VCA models reveal that IFC disorder-induced scattering must be $\sim 2.8 \times$ higher in J35 than in J14 to account for the difference in thermal conductivities between the two. We emphasize that J14 and J35 have approximately the same average mass. Additionally, we systematically increase mass disorder among 6-component oxides via increasing 6th-cation mass (Fig. 5.1(e)) to conclude that while this increase leads to a reduction in thermal conductivity, the variation is less than 20%, far from the level of reduction needed to explain the difference from that of J14. Therefore, we hypothesize that there is a strong IFC disorder induced by local ionic charge disorder that is driving the enhanced reduction in thermal conductivity. Such a mechanism should be observable via differences in the local structure within the unit cell of J14 and J35.

Table 5.3: Resulting parameter values from EXAFS analysis. All uncertainties are propagated through Artemis. S_0^2 is the amplitude reduction factor, E_0 is the inner potential energy shift, R is the half scattering path distance, and σ^2 is the EXAFS Debye-Waller factor.

Parameter	J14	J35
S_0^2	1.0	0.85
E_0	3.0 ± 1.0	2.0 ± 1.0
R	2.10 ± 0.02	1.96 ± 0.08
σ^2	0.0073 ± 0.0005	0.006 ± 0.002
R	2.15 ± 0.04	1.93 ± 0.04
σ^2	0.0073 ± 0.0005	0.006 ± 0.002
R	3.00 ± 0.01	2.86 ± 0.02
σ^2	0.0073 ± 0.0005	0.006 ± 0.002
R	-	2.97 ± 0.02
σ^2	-	0.006 ± 0.002

To test this hypothesis, we use extended X-ray absorption fine structure (EXAFS) [196–199] to observe changes in the local coordination environment about Co absorbers in J14 and J35. EXAFS spectra were collected at beamline 10-BM-B at the Advanced Photon Source, Argonne National Laboratory (Lemont, IL). The Co K-edge was measured in fluorescence mode using a 4-element Vortex detector, elevated 30° above the sample. Measurement parameters varied by region of interest, determined by signal at higher k values up to ~ 12 Å, as described elsewhere [200]. Individual scattering paths from Co absorbers are generated in J14 and J35 using FEFF6 [201], and fit to $\chi(R)$ using Artemis [202]. All EXAFS related uncertainty values were generated though the least squares output from fitting results. Quantitatively, we obtain local structural information of the first and second nearest neighbors by fitting a theoretical model to the uncorrected $\chi(R)$ between $\sim 1\text{--}3.1$ Å using a Kaiser-Bessel window, including all scattering path lengths that fall within this range. The structural model used for fits is based on information obtained though X-ray diffraction, shown in Fig. 5.1(a), exhibiting a single phase, tetragonally strained rocksalt structure pinned in-plane to the MgO substrate. Each fit generally contains four fitting parameters: amplitude reduction factor S_0^2 , inner potential energy shift E_0 , half scattering path distance R , and EXAFS Debye-Waller factor σ^2 . The resulting best-fit values for which are listed in Table 5.3.

While XRD revealed crystallographic order, EXAFS allows for an atomic-level probe of the local crystal structure needed for determination of any observable quantity that would reveal such

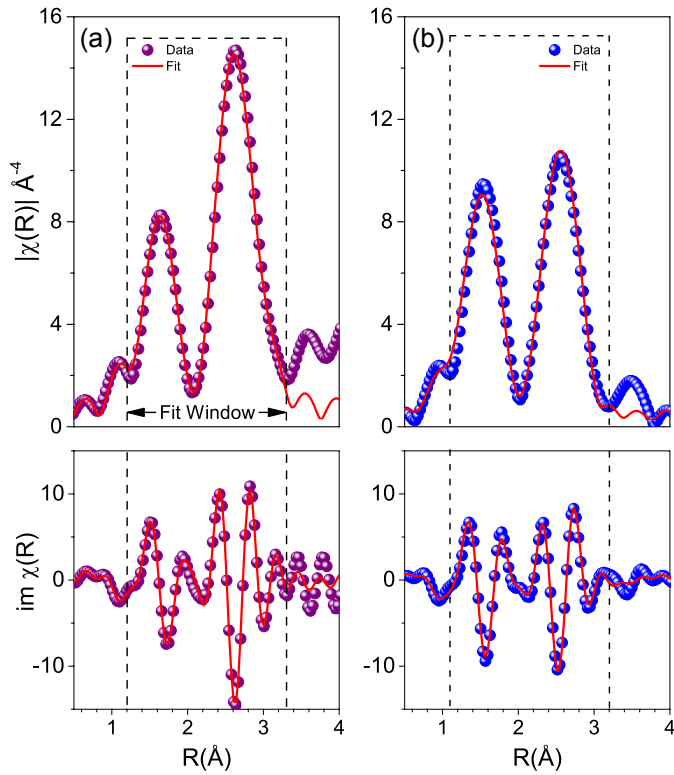


Figure 5.4: Extended X-ray absorption fine structure data and models about cobalt for (a) J14 and (b) J35. Model and best fit model are shown for the magnitude (top) and imaginary portion of the real space function $\chi(R)$ as a function of radius away from the cobalt absorber (R).

IFC disorder. Figure 5.4 shows fits to the phase-uncorrected, self-absorption corrected magnitude and imaginary part of the real space function $\chi(R)$ for (a) J14 and (b) J35, obtained by taking the Fourier transform of the EXAFS spectra, $k^2\chi(k)$, using a Keiser-Bessel window in the range of $3.75 - 10 \text{ \AA}^{-1}$. Each $\chi(R)$ is consistent with a typical metal-oxide system, where the first and second peaks correspond to scattering between the absorber and atoms in the first and second coordination shells, respectively. Figure 5.5 illustrates the modified unit cell for both (a) J14 and (b) J35 compositions extracted by EXAFS. For J14, we find an expected distortion of the Co octahedra that coincides with the observed lattice parameters of the tetragonal unit cell, $a = 4.21 \text{ \AA}$ and $c = 4.29 \text{ \AA}$. By the second coordination shell, or absorber-metal scattering paths, we find that the half-path length agrees with observed lattice parameters within less than 1%. The addition of a 6th component, as is the case in J35, appears to dramatically change the absorber octahedra such that a geometric extension no longer aligns to the lattice parameters. J35 exhibits a tetragonally

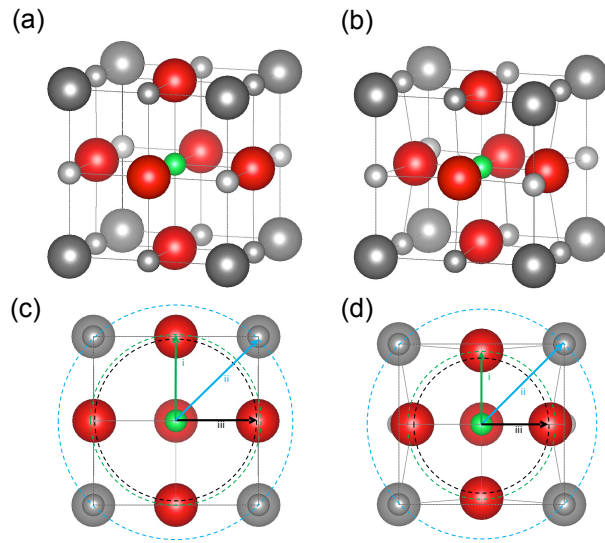


Figure 5.5: Illustration depicting local structural changes about the cobalt species in (a) J14 and (b) J35. A comparison of the changes as a result of adding the 6th cation can be viewed by unit cell cross section along the (200) plane, as shown in (c) and (d) for J14 and J35 respectively. The lowercase roman numerals mark the coordination shell radius for i. nearest neighbor anion, ii. next nearest neighbor anion, and iii. nearest neighbor cation. In both cases, the nearest neighbor cation shell radius corresponds to one-half the face diagonal of the unit cell parameters, as determined through XRD.

compressed unit cell, with $a = 4.21 \text{ \AA}$ and $c = 4.08 \text{ \AA}$. Half scattering path lengths between the Co absorber and the six nearest neighboring oxygen atoms suggest a highly compressed octahedra with 4 planar oxygens at 1.93 \AA and 2 axial oxygens at 1.96 \AA . Again, comparing the half scattering path length of the next nearest neighbors agrees with observed lattice parameters to within 1%. These EXAFS results largely align with our hypothesis from the thermal measurements in that a large strain is present in the 6-component ESOs such that the oxygen atoms are displaced from their ideal coordination positions. Such strong oxygen sublattice distortion is the indicator that IFC disorder is greatly enhanced in J35 relative to J14. This strong IFC disorder is promoted by charge compensation among cations to preserve charge neutrality when a 6th cation is added [203].

The attribution of thermal conductivity reduction in ESOs to IFC disorder is further supported by molecular dynamics simulations in which IFC disorder is modeled by electrostatic point charges in the interatomic potential based on Bader charges from density functional theory calculations [188]. These simulations reveal that accounting for differences in interatomic forces through ad-

justment of average properties, analogous to the VCA, cannot capture magnitude or trend in thermal conductivity, whereas integration of randomly distributed mass and charge disorder accurately captures the reduction in thermal conductivity observed between J14 and 6-cation oxides, reducing the thermal conductivity by a factor of almost two, in agreement with experiment. Moreover, in these simulations, mass and charge disorder are decoupled to show that the latter is responsible for the strong reduction in thermal conductivity. Taken together, the experiment and simulation reveal that ESOs can possess a uniquely low thermal conductivity while maintaining a relatively high elastic modulus, made possible through highly disordered interatomic forces resulting from charge disorder among ionic bonds. These results provide an example of the broader aspect of entropy stabilization as a means to create materials with unique thermophysical properties that could be highly beneficial to thermoelectric and thermal barrier coating applications.

5.4 Summary

In this chapter, we studied the role of increasing compositional disorder on the thermal conductivity of crystalline oxide thin films. From a thermal transport perspective, large differences between elemental properties such as mass and interatomic force can reduce the rate at which phonons carry heat and thus reduce the thermal conductivity. Measuring the structural, mechanical, and thermal properties of single-crystal ESOs, we showed that local ionic charge disorder can effectively reduce thermal conductivity without compromising mechanical stiffness. These materials demonstrate similar thermal conductivities to their amorphous counterparts, in agreement with the theoretical minimum limit, resulting in this class of material possessing the highest ratio of elastic modulus to thermal conductivity of any isotropic crystal. Towards the goal of this dissertation, we now understand that the mechanism dictating the reduction of thermal conductivity in highly configurationally disordered oxides is the local charge disorder. This charge disorder is strong enough to induce an observable structural distortion of the oxygen sublattice. In this respect, configurational disorder and structural disorder are coupled and the distinction between the two, from a phonon scattering perspective, becomes ambiguous.

Chapter 6

High-Entropy Ceramics

In the previous chapter, the effects of increasing configurational disorder on thermal conductivity were studied using thin-film entropy-stabilized oxides. These single-crystal, epitaxially grown films were ideal for isolating the effects of large compositional disorder on phonon scattering to reduce thermal conductivity. Many applications where high-entropy materials are of interest require bulk samples having thicknesses on the order of tens of microns to meters. In bulk material synthesis, it is far more difficult to obtain the same level of control over unwanted defect formation. As a result, the microstructure of these bulk materials can have features that make interpretation of thermal conductivity more challenging; these include multiple phases, polycrystallinity, and porosity, to name just a few. Additionally, while oxides were studied in the previous chapter, the application space for high-entropy ceramics motivates the use of additional base sublattice elements, namely borides, carbides, and silicides. Therefore, in this chapter, I will experimentally study the thermal conductivity of high-entropy oxides, carbides, borides, and silicides to understand the combined effects of configurational disorder and microstructure on the thermal conductivity in these bulk materials.

6.1 Motivation

In aerospace applications operating at very high temperatures ($> 2000^{\circ}\text{C}$), such as hypersonic flight or rocket propulsion systems, there is a critical need for the development of materials which can survive such extreme temperatures. To this end, ultra-high temperature ceramics (UHTCs) have proven to be at the forefront of research [204, 205], as they are of interest to thermal protection systems, coatings, and heating elements. While early development of UHTCs were focused on SiC and Si_3N_4 , currently there is a strong interest in transition metal diborides such as hafnium diboride (HfB_2) and zirconium diboride (ZrB_2) as well as carbides such as hafnium carbide (HfC), tantalum carbide (TaC), and alloys thereof; in fact, an alloy of HfC and TaC was recently predicted by *ab initio* molecular dynamics simulations to possess the highest melting point of any material [206].

While melting temperature is a significant metric used to determine a materials effectiveness as a UHTC, in real engineering applications failure typically occurs from other means such as oxidation [207], thermal shock [204], or other thermomechanical or thermochemical-based processes [208]. Thus, UHTCs are generally desired to possess a high oxidation resistance, high thermal shock resistance, high hardness and elastic modulus, and high thermal conductivity. A high thermal conductivity can be especially important to distribute heat effectively away from a high load heat source, such as wing leading edges and nosetips. On the other hand, low thermal conductivity can be desired for other applications such as thermal barrier coatings to protect essential device components by maintaining a strong temperature difference within the coating when a heat source is present [37]. Thus, understanding thermal conductivity in UHTCs will greatly benefit the advance of these materials for engineering applications. To this point, most research efforts have been limited to binary diborides and carbides such as the ones previously discussed. However, as detailed in Chapter 5, great advances in physical properties of metals ensued with the advent of high-entropy alloys. In the nascent field of high-entropy ceramics, there is a critical need to characterize and understand physical properties such as thermal conductivity. Thus, the goal of this chapter is to experimentally measure the thermal conductivity of bulk high-entropy ceramics containing up to five metal components in order to understand how high-entropy ceramics differ

from constituent binary ceramics and how microstructure plays a role. To do so, the sample space studied includes high-entropy fluorite oxides, high-entropy carbides, and high-entropy borides, and high-entropy silicides.

6.2 High-Entropy Fluorite Oxides

The fabrication of entropy-stabilized oxides was the first demonstration of extending the concept of high-entropy alloys to ceramics with ionic bonds [184]. These and similar oxides have been shown to possess unique material properties to include superionic mobility [185], enhanced dielectric constants [209], and capability for thermochemical water splitting [186]. As a result, there is tremendous interest in developing new high-entropy oxides to explore the capabilities of their physical properties. Current developments include single-phase high-entropy perovskite oxides [210] and multicomponent rare earth oxides [211].

In this section, we study a new class of such oxides, high-entropy fluorite oxides (HEFOs). Fluorite oxides are of interest because of their use as solid ionic conductors [212], high temperature barrier coatings [213], and solid electrolyte materials for solid oxide fuel cells [214]. In all such applications, the thermal conductivity is an important factor as the device's operating temperature, often dictated by the oxide layer's properties, can significantly affect performance. The most widely used fluorite oxides (ZrO_2 , HfO_2 and CeO_2) generally possess high oxygen conductivities, low thermal conductivities, high hardnesses, and high melting temperatures. Note that this low thermal conductivity in rare-earth oxides is in contrast to that observed for typical constituent oxides of the ESOs studied in the previous chapter. For example, monoclinic ZrO_2 has a room temperature κ of about $5 \text{ W m}^{-1} \text{ K}^{-1}$ [33], whereas MgO exceeds $50 \text{ W m}^{-1} \text{ K}^{-1}$ [73]. These intrinsically low thermal conductivities make rare-earth oxides exceptional candidates for insulating applications such as thermal barrier coatings. Given the strong reduction in thermal conductivity observed in ESOs compared to constituent oxides, the use of heavy rare earth metals used in the development of high-entropy fluorite oxides motivates the study of thermal conductivity in these systems.

Table 6.1: Thermal conductivity (κ) and hardness of HEFOs at room temperature. Thermal conductivity was measured using TDTR, and hardness was measured in Ref. [215] using a Vickers diamond indenter.

Name	Composition	κ ($\frac{\text{W}}{\text{mK}}$)	Hardness (GPa)
HEFO1	(Hf _{0.25} Zr _{0.25} Ce _{0.25} Y _{0.25})O _{2-δ}	1.74 ± 0.15	13.6 ± 0.5
HEFO4A	(Hf _{0.25} Zr _{0.25} Ce _{0.25})(Y _{0.125} Yb _{0.125})O _{2-δ}	1.55 ± 0.20	12.7 ± 0.7
HEFO7B	(Hf _{0.2} Zr _{0.2} Ce _{0.2})(Y _{0.2} Gd _{0.2})O _{2-δ}	1.61 ± 0.13	13.1 ± 0.5
HEFO8A	(Hf _{0.25} Zr _{0.25} Ce _{0.25})(Yb _{0.125} Gd _{0.125})O _{2-δ}	1.81 ± 0.14	12.6 ± 0.5
HEFO8B	(Hf _{0.2} Zr _{0.2} Ce _{0.2})(Yb _{0.2} Gd _{0.2})O _{2-δ}	1.62 ± 0.13	12.3 ± 0.7
8YSZ	8 mol% Y ₂ O ₃ Fully Stabilized ZrO ₂	2.02 ± 0.17	13.2 ± 0.4

The samples studied in this section include five single-phase HEFOs as well as 8YSZ (8 mol% Y₂O₃ Fully Stabilized ZrO₂) for comparison. The compositions of these HEFOs are listed in Table 6.1; they include the elements Hf, Zr, Ce, Y, Yb, and Gd in various combinations and compositions. Although other HEFOs were synthesized and detailed in Ref. [215], the five considered here were all single-phase, synthesized at the same time, and tested at the same time, making them the best to compare as part of a single controlled study.

Thermal conductivities were measured using TDTR. To do so, a ~90 nm Al film (measured using picosecond acoustics) was thermally evaporated onto each sample to act as a transducer to convert the optical energy to thermal energy. Using TDTR, the pump was modulated at a frequency of 9.8 MHz. The pump and probe beams were focused with a 5× objective lens to 35 μm and 15 μm 1/e² diameters, respectively. Since in the previous chapter, we found that ESOs had heat capacities that generally agreed with the rule of mixtures, the heat capacity was assumed in this case to be 3 MJ m⁻³ K⁻¹; thus, the fitting parameters include only the HEFO thermal conductivity and Al/HEFO thermal boundary conductance. The ratio of in-phase to out-of-phase data was used to fit for these parameters.

Figure 6.1(a) shows the TDTR ratio (-X/Y) data obtained for all samples. Although the fitting time window was from 300 to 5500 ps, Fig. 6.1(a) shows the data down to 10 ps to display the picosecond acoustic echos used to determine the Al film thickness. The best-fit thermal conductivities are shown in Fig. 6.1(b), and are listed in Table 6.1. For 8YSZ, κ was measured to be 2.02 ± 0.17 W m⁻¹ K⁻¹, which agrees well with literature for fully-dense, polycrystalline 8YSZ [39].

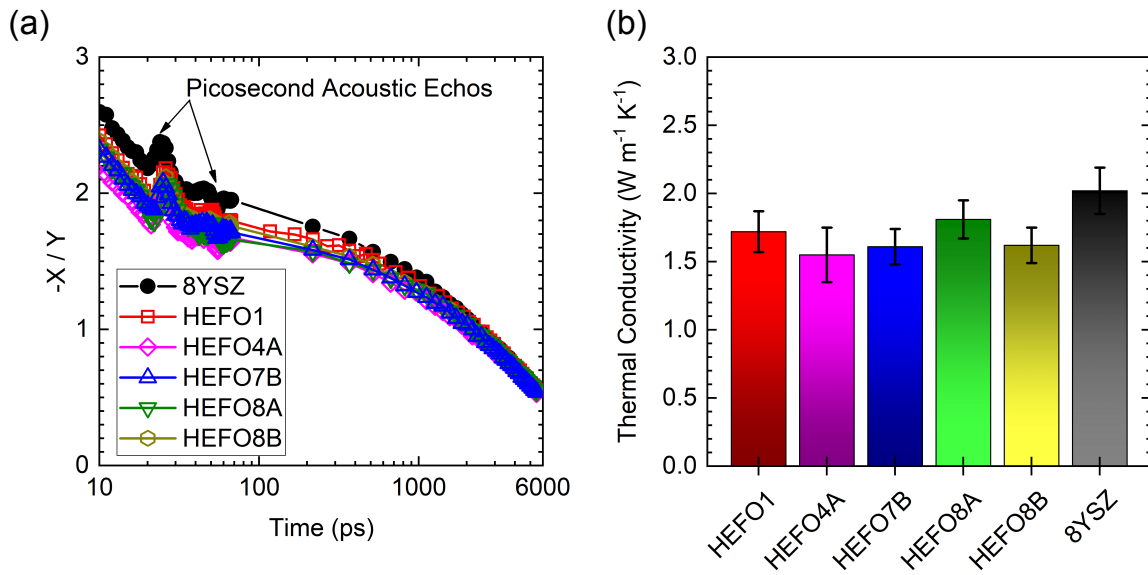


Figure 6.1: (a) TDTR ratio ($-X/Y$) data taken for five HEFO samples and 8YSZ. (b) Thermal conductivities determined from TDTR.

This low thermal conductivity of 8YSZ is a large reason for its ubiquitous use as a thermal barrier coating. In general, κ is dependent on extrinsic properties such as porosity, doping concentration, and microstructure variation resulting from differences sample preparation. Thus, the agreement between literature and measured values for 8YSZ, together with the fact that HEFO and 8YSZ samples were fabricated in the same way, allows for a fair comparison of thermal conductivities between all samples.

Comparing the measured κ of HEFO samples to 8YSZ, we observe a small reduction for all HEFOs, with HEFO4A having a 23% lower κ . Similar to the results observed in ESOs, the effects of having 5 components in the oxide reduces the thermal conductivity. As a note, Vickers hardness measurements were performed on all single-phase high-entropy oxides and 8YSZ (results are shown in Table 6.1) to reveal that there is generally no significant difference between samples. While hardness is not directly related to intrinsic bond strength as was the case with the elastic modulus measured for the ESOs, hardness is still generally indicative of elastic modulus and thus phonon group velocity. Therefore, given the similarity in heat capacities, any differences in thermal conductivity can be attributed to differences in phonon scattering times. That said, there is little variation in κ between samples. Even HEFO1, which has only four metal components, does

not show a significant difference in thermal conductivity compared to the others having five components. This suggests that the saturation of reduction, which was observed in ESO samples only when six metal components were introduced, is reached with fewer components in this case. This could be due to the heavier atomic masses and already intrinsically lower thermal conductivities of constituent oxides. Taken as a whole, the concept of high-entropy engineering shows promise for fabricating materials with low thermal conductivities; however, there is a lower limit to this reduction. As is typical in engineering YSZ for thermal insulation applications, introduction of porosity can provide an additional tool to reduce thermal conductivity on a macro scale.

6.3 High-Entropy Carbides

The next class of high-entropy ceramic studied is the high-entropy carbide (HEC). Transition-metal carbides are of major interest to UHTC applications because of their potential for extremely high melting temperatures that exceed those of the current state-of-the art refractory borides [204]. For example, tantalum carbide and hafnium carbide have two of the highest melting temperatures of any known materials at 3980 °C and 3928 °C, respectively [204]. These carbides also possess high hardnesses and elastic modulii that are favorable to UHTC applications. The primary issue with carbides is that they are highly susceptible to oxidation [204]. As high-entropy alloys have shown, fabrication of multi-component materials with high-entropy can lead to enhanced properties to include resistance to corrosion, oxidation, and wear at elevated temperatures [178–180]. However, from a thermal conductivity perspective, as revealed by the previously studied oxides, the large variations in masses and interatomic forces resulting from the lattice containing multiple components can result in increased phonon scattering to reduce thermal conductivity. In contrast to oxides, however, carbides are electrically conductive, meaning they can also have a significant electronic contribution to thermal conductivity. For instance, in near-stoichiometric single crystal TiC, electrons can comprise 25% of the total thermal conductivity [216]. Therefore, in this subsection, we will study the thermal conductivity of a series HECs to determine how thermal conductivity is affected by valence electron concentration to reveal the importance of the electronic contribution

Table 6.2: Thermal properties of HECs at room temperature. The thermal conductivity (κ) for each composition was measured with SSTR using the both the LIA and PWA, while volumetric heat capacity (C_v) was determined using TDTR.

Name	Composition	$\kappa \left(\frac{W}{mK} \right)$, LIA	$\kappa \left(\frac{W}{mK} \right)$, PWA	$C_v \left(\frac{MJ}{m^3 K} \right)$, TDTR
HEC1	Hf _{0.2} Nb _{0.2} Ta _{0.2} Ti _{0.2} V _{0.2} C	9.16 ± 0.45	9.07 ± 0.40	2.76 ± 0.25
HEC2	Hf _{0.2} Nb _{0.2} Ta _{0.2} Ti _{0.2} W _{0.2} C	8.78 ± 0.43	8.80 ± 0.39	2.71 ± 0.29
HEC3	Hf _{0.2} Nb _{0.2} Ta _{0.2} Ti _{0.2} Zr _{0.2} C	13.6 ± 0.6	13.6 ± 0.6	2.99 ± 0.28
HEC4	Nb _{0.2} Ta _{0.2} Ti _{0.2} V _{0.2} W _{0.2} C	8.70 ± 0.43	8.64 ± 0.39	3.15 ± 0.28
HEC5	Hf _{0.2} Ta _{0.2} Ti _{0.2} W _{0.2} Zr _{0.2} C	9.81 ± 0.49	9.57 ± 0.42	2.85 ± 0.26
HEC6	V _{0.2} Nb _{0.2} Ta _{0.2} Mo _{0.2} W _{0.2} C	8.26 ± 0.42	8.19 ± 0.37	3.16 ± 0.28
TiC	TiC	30.4 ± 1.3	29.8 ± 1.3	2.70 ± 0.23
TaC	TaC	36.2 ± 1.5	36.3 ± 1.4	2.85 ± 0.25
HfC	HfC	20.1 ± 0.9	20.1 ± 0.8	2.42 ± 0.21

to thermal conductivity.

The samples studied include six HECs comprised of nominally 50 mol % carbon and a 50 mol % mixture of five distinct transition metal elements with equal composition. HECs possess a single-phase, rocksalt crystal structure comprised of a fixed carbon sublattice and cation sublattice containing equimolar, randomly distributed metal elements. For comparison, we also study three binary carbides: TaC, TiC, and HfC. The names and compositions for all samples are listed in Table 6.2. Details on fabrication and characterization of these samples can be found in Refs. [217] and [218]. In brief, samples were fabricated using high energy ball milling in argon atmosphere by mixing powders of each of the individual carbide compounds (TiC, ZrC, HfC, VC_{0.88}, NbC, TaC, Mo₂C, W₂C). The milled powders were consolidated in batches via spark plasma sintering at 2473 K under a uniaxial load of 30 MPa in vacuum environment.

To measure the thermal conductivity, we use two techniques: TDTR and SSTR. When measuring κ using TDTR, the heat capacity is an input parameter to the thermal model used to fit to experimental data. Just as in Chapter 5, we do not know the heat capacities of these new materials. While we can estimate this quantity using the rule of mixtures, a more rigorous approach would involve measuring it independently. Unlike in the thin film case of ESOs, we cannot use a multi-frequency TDTR approach to determine both C_v and κ simultaneously due to the sensitivity of the two being coupled within the experimental frequency range of our TDTR capabilities [150]. This motivates the use of SSTR, which is insensitive to heat capacity. Using SSTR, we measure κ for

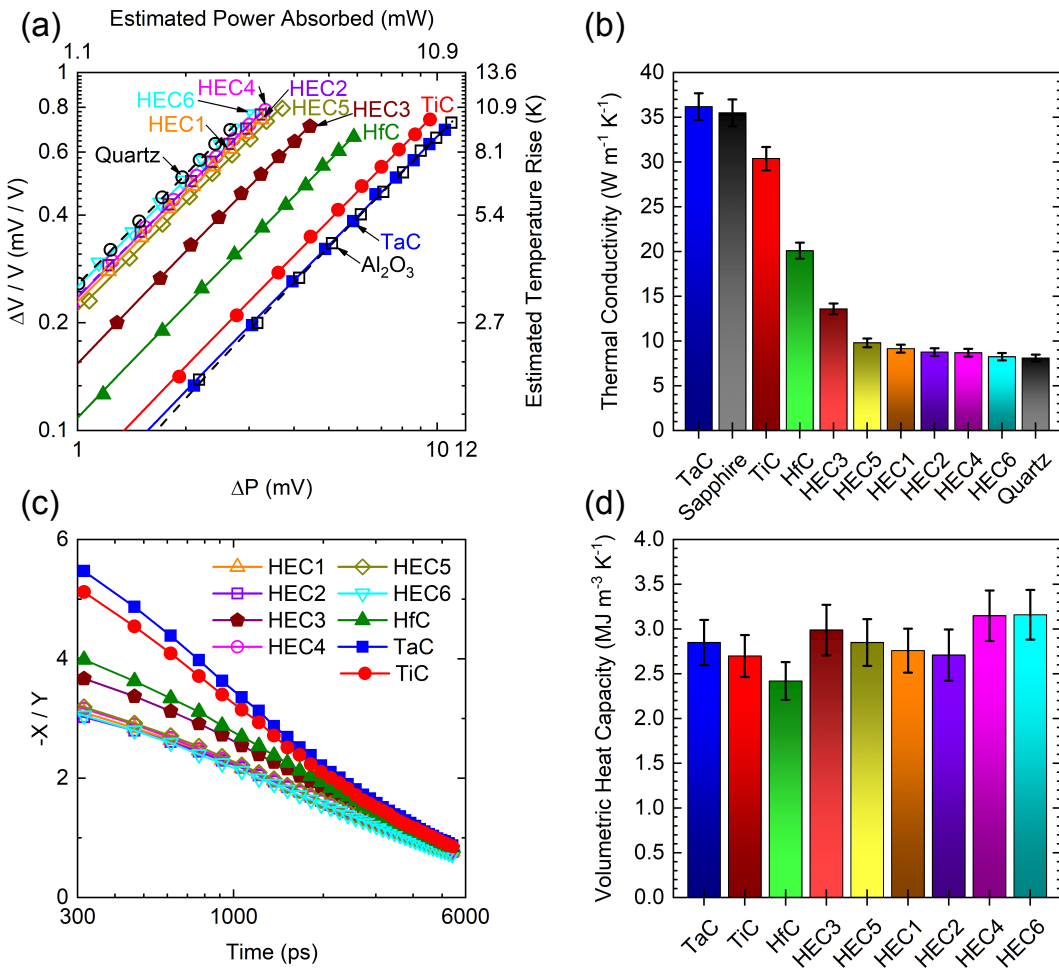


Figure 6.2: (a) SSTR data taken for six HEC samples, TaC, TiC, HfC, Sapphire (Al_2O_3) and z-cut Quartz. (b) Thermal conductivities determined from SSTR. (c) TDTR ratio data ($-X/Y$) vs. time for six HEC samples, TaC, TiC, and HfC. (d) Volumetric heat capacities determined from TDTR.

HEC samples; using TDTR, we can then determine C_v independently.

SSTR measurements are conducted using both the PWA and LIA approaches discussed in Chapter 4 with a $10\times$ objective lens resulting in pump and probe $1/e^2$ diameters of 19.5 and 18.5 μm , respectively. Before doing so, an 80 nm Al transducer (thickness confirmed with picosecond acoustics) was deposited onto each sample. A sapphire wafer, with Al deposited under the same deposition, was used as a calibration. After calibrating, all HEC and binary carbide samples were tested and the resulting thermal conductivities are listed in Table 6.2. Figure 6.2(a) shows the SSTR data obtained for all samples, including the Al_2O_3 calibration and a z-cut quartz reference,

included to show that the tested samples have thermal conductivities that are effectively bounded by quartz on the low end and sapphire on the high end. The y-axis is shown as both the measured probe signal and estimated temperature rise, while the x-axis is shown for both the measured pump signal and estimated absorbed power of by the sample. The resulting thermal conductivities are shown in Fig. 6.2(b) and listed in Table 6.2.

TDTR was also used to measure the thermal properties of these samples; a high modulation frequency of 8.4 MHz and relatively large $1/e^2$ pump/probe radii of 20/13 μm ensure the temperature decay is one-dimensional and the extracted property is thermal effusivity [150]. Since κ is known from SSTR, we can then determine C_v via TDTR independently. This also serves as a check for SSTR measurements, since the heat capacity of TiC, TaC, and HfC are known to be 2.76, 2.72, and 2.39 $\text{MJ m}^{-3} \text{K}^{-1}$, respectively [61]. TDTR ratio data is shown in Fig. 6.2(c). In general, the higher ratios observed are indicative of higher thermal effusivities. Given the expected similarity in C_v among all samples, the ratio is therefore also indicative of κ ; the same qualitative trend is observed for samples in TDTR and SSTR. The heat capacities extracted are shown in Fig. 6.2(d) and given in Table 6.2. As a check, the binary carbide heat capacities all fall within about 3% of the aforementioned literature heat capacities.

For thermal conductivity, SSTR reveals that TiC has a κ of $\sim 30 \text{ W m}^{-1} \text{ K}^{-1}$. Literature reveals that κ can vary heavily, with reports from ~ 18 to $34 \text{ W m}^{-1} \text{ K}^{-1}$ near room temperature [219]. It is well known that in transition metal carbides, carbon vacancies can scatter phonons to significantly reduce κ [220]. The relatively high κ obtained for this TiC suggests that carbon vacancies are not as significant in this sample compared with other literature values. Similarly, TaC exhibits the highest κ of the samples tested at $\sim 36 \text{ W m}^{-1} \text{ K}^{-1}$, significantly higher than the often quoted $22 \text{ W m}^{-1} \text{ K}^{-1}$ [220]. Again this may be indicative of fewer carbon vacancies and/or closer to stoichiometric composition of our tested TaC. On the other hand, HfC exhibits a κ of $20 \text{ W m}^{-1} \text{ K}^{-1}$, in agreement with prior studies on stoichiometric HfC [220, 221].

In comparison to the binary carbides, HECs have reduced thermal conductivities that generally fall between 8 and $10 \text{ W m}^{-1} \text{ K}^{-1}$, with one outlier (HEC3) having a thermal conductivity of $13.6 \text{ W m}^{-1} \text{ K}^{-1}$. There is not a large difference in mechanical properties within the set of HECs;

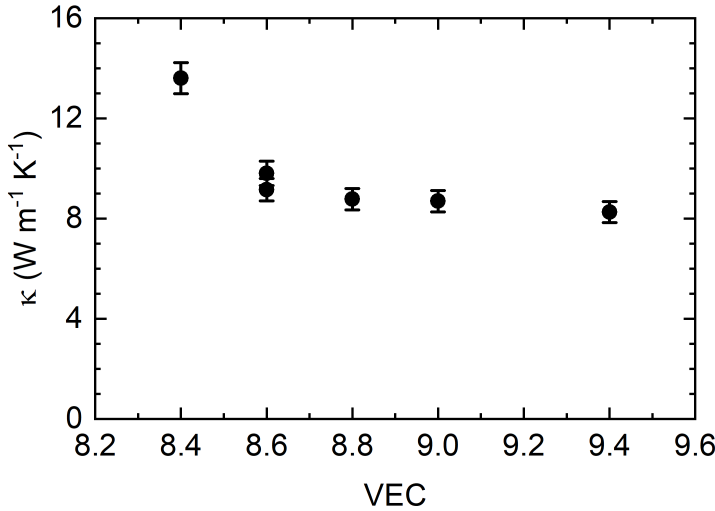


Figure 6.3: Thermal conductivity (κ) vs. valence electron concentration (VEC) for HECs.

elastic modulii of all samples range from 443 to 533 GPa [218], while hardness is between 27 to 33 GPa [218]. Based on the previous studies on entropy-stabilized and high-entropy oxides, we expect that phonon scattering is significantly enhanced in these HECs as compared to the binary carbides. However, unlike the oxides, there is an electronic contribution to thermal conductivity that could still be significant. That the thermal conductivity remains relatively high is perhaps indicative of this significance. In order to confirm this, we show that thermal conductivity is increased as valence electron concentration (VEC) decreases (i.e., as the HEC becomes more metallic). Indeed, Fig 6.3 shows that thermal conductivity monotonically decreases with increasing VEC.

As mentioned previously, one of the goals of this chapter is to understand the effect of microstructure on thermal conductivity. To do so, we determine κ as a function of real space in two dimensions to extract a thermal conductivity map (or image). Thermal property mapping, or sometimes referred to as thermal microscopy when a frequency component is added to change the depth of the image [162], is a recently established technique that has evolved in frequency-domain thermoreflectance [162, 163], time-domain thermoreflectance [165], and CCD-based full-field thermal imaging [222–224]. In this work, we use the time-domain variation, which has the major advantage of allowing adjustment of the probe beam delay time to ensure the measurement is insensitive to thermal boundary conductance between the transducer and the sample [165]. At a fixed delay

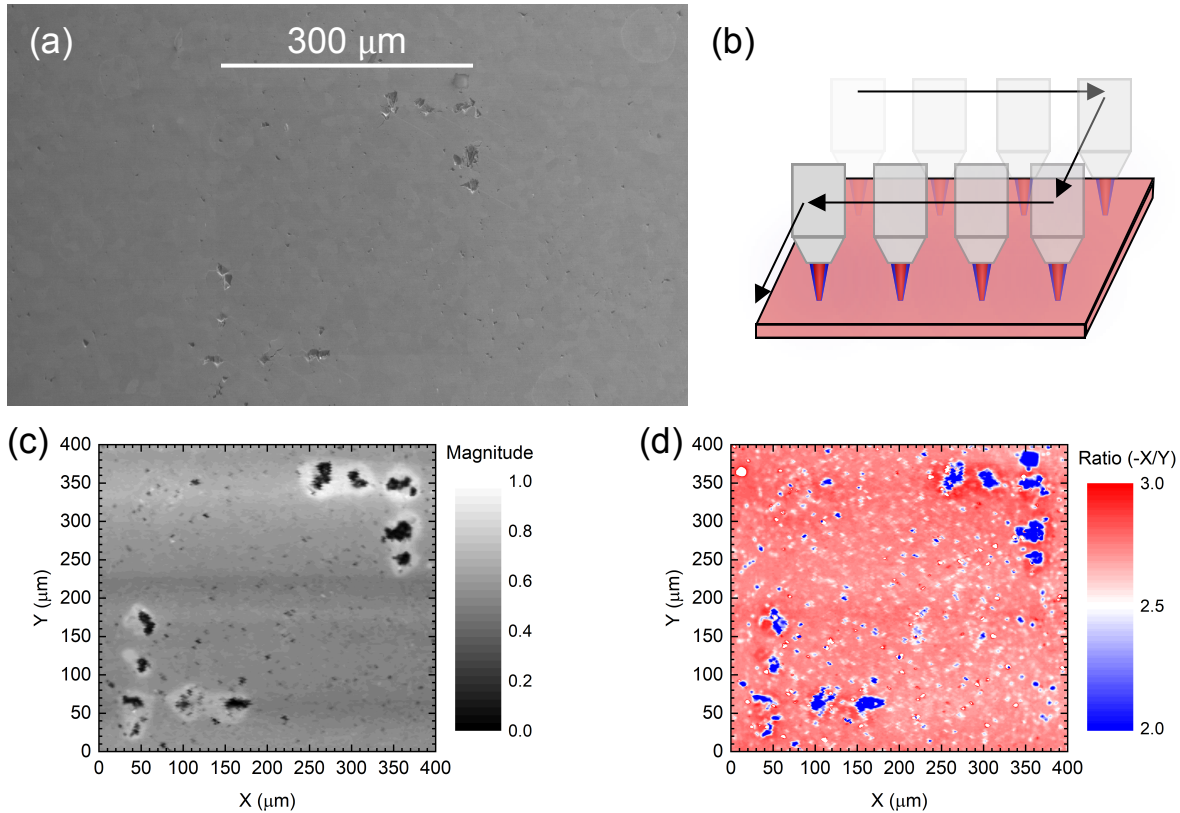


Figure 6.4: (a) SEM image of HEC3 around the $\sim 300 \mu\text{m} \times 300 \mu\text{m}$ region that is mapped with TDTR. (b) Depiction of mapping procedure: the sample is rastered in two dimensions with respect to the focused pump/probe spot. (c) Normalized magnitude image of the probe recorded for a $20\times$ objective lens magnification at a delay time of 1 ns. (d) The ratio data for the same conditions as (c).

time, the phase-corrected ratio and magnitude of the thermoreflectance signal is recorded at discrete points on the sample to make up pixels to be used to create an image. Comparing the ratio value of each pixel to the thermal model discussed in Chapter 3, κ is determined for each pixel to create a thermal conductivity image.

In practice, this process is achieved by mounting the sample on a 3-axis stage with motors having a bidirectional repeatability of $< 1.5 \mu\text{m}$ and a closed-loop piezo motor controlling the focal plane of the sample. The sample is oriented so that movements along the sample surface result in no appreciable changes in focus. The position of the sample is rastered about two dimensions relative to the pump/probe focused spot in steps of as small as 1 micron; in this case, a step size of $4 \mu\text{m}$ is used for a $10\times$ objective lens (pump and probe $1/e^2$ diameters of 20.5 and $12.0 \mu\text{m}$,

respectively) and a step size of $2 \mu\text{m}$ is used for the $20\times$ objective lens (pump and probe $1/\text{e}^2$ diameters of 10.5 and $7.5 \mu\text{m}$, respectively).

The TDTR mapping is performed on HEC3 over a $\sim 300 \mu\text{m} \times 300 \mu\text{m}$ square area whose corners were indented with a diamond indenter. Figure 6.4(a) shows an SEM image of the sample area before an 80 nm Al transducer was deposited. To obtain an image, the sample is rastered in 2 dimensions as depicted conceptually in Fig. 6.4(b); the magnitude of the probe signal and the ratio ($-X/Y$) are recorded at a probe delay time of 1 ns . This delay time was chosen to reduce sensitivity to the thermal boundary conductance between the aluminum and HEC in order to maximize the relative sensitivity to HEC3's thermal conductivity. Using the magnitude and ratio data, images can be obtained by stitching together the data recorded at each pixel. The corresponding normalized magnitude and ratio images are shown in Fig. 6.4(c) and (d), respectively, using a $20\times$ objective lens, a step size of $2 \mu\text{m}$, and a dimension size of $\sim 400 \mu\text{m} \times 400 \mu\text{m}$ for a total of 40,401 pixels. Comparison of the magnitude (Fig. 6.4(c)) image to the SEM image (Fig. 6.4(a)) reveals that the many microscale features appear well, if not better, in the former image. The clear appearance of the indented corners ensure that the orientation of the TDTR images match that of the SEM. Next, the ratio image (Fig. 6.4(d)) again shows large contrast between the indented areas and elsewhere, but shows a relatively uniform ratio otherwise.

To convert the ratio image to a thermal conductivity image, the TDTR model is calculated for a range of κ to create a dataset of κ and their corresponding ratios. The ratio image is then converted to a thermal conductivity image by comparing to this dataset and interpolating where necessary. The resulting thermal conductivity images are shown in Fig. 6.5(a) and (c) for a $10\times$ and $20\times$ objective lens, respectively. The $10\times$ case used a step size of $4 \mu\text{m}$ in each direction, whereas the $20\times$ case used a step size of $2 \mu\text{m}$. Comparison of the two reveals that features, including the indented corners, become sharper in the latter case thanks to the improved resolution. Sampling κ within the area enclosed by dashed lines, the statistical average of the κ distribution is equivalent in each case. This κ distribution is shown for the $10\times$ case and $20\times$ case in Fig. 6.5(b) and(d), respectively. The mean is 14.0 ± 1.0 in the $10\times$ case and $14.1 \pm 1.2 \text{ W m}^{-1} \text{ K}^{-1}$ in the $20\times$ case, both within uncertainty of the previously measure value using SSTR.

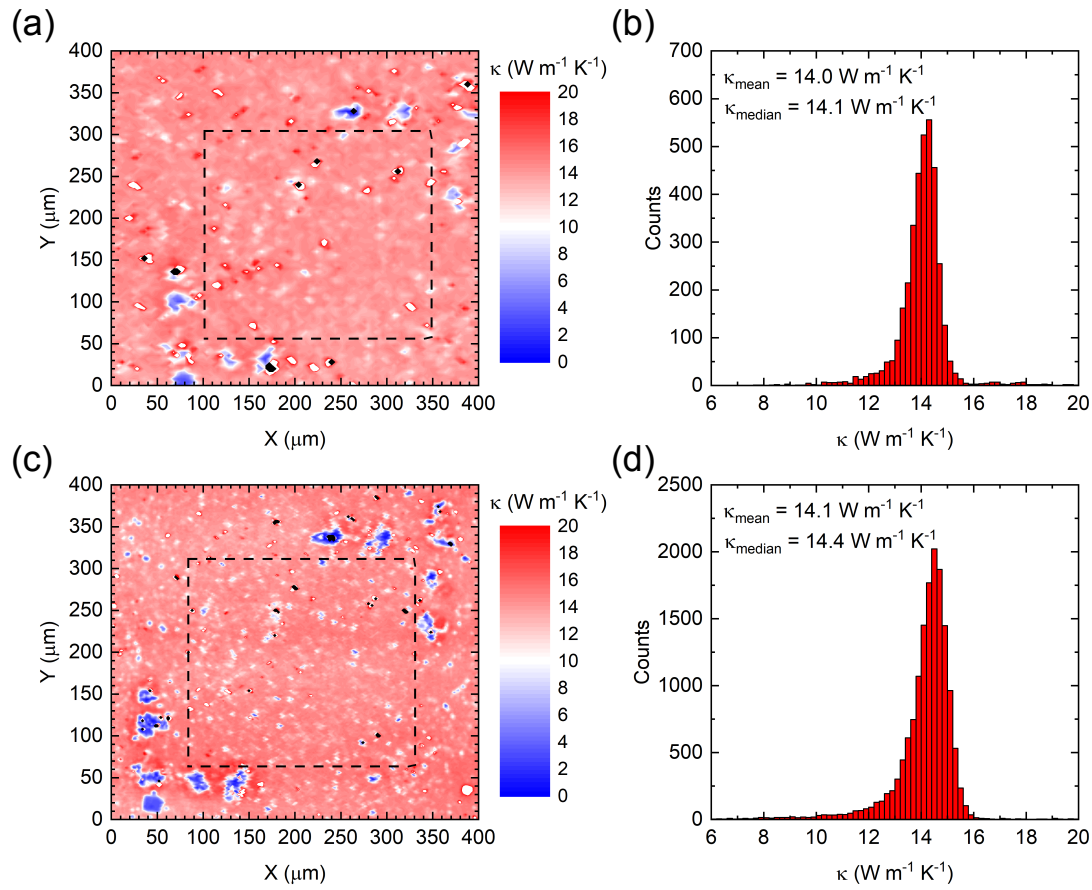


Figure 6.5: (a) Thermal conductivity map obtained using a 10× objective lens with pump and probe $1/e^2$ diameters of 20.5 and 12.0 microns, respectively. (b) Histogram of thermal conductivity values for the region enclosed by the dashed lines in (a); the mean and median thermal conductivities are 14.0 and $14.1 \text{ W m}^{-1} \text{ K}^{-1}$. (c) Thermal conductivity map obtained using a 20× objective lens with pump and probe $1/e^2$ diameters of 10.5 and 7.5 microns, respectively. (d) Histogram of thermal conductivity values for the region enclosed by the dashed lines in (c); the mean and median thermal conductivities are 14.1 and $14.4 \text{ W m}^{-1} \text{ K}^{-1}$.

Fundamentally, the conditions used in TDTR ensure that the temperature profile is effectively one-dimensional, so that thermal conductivity in the cross-plane direction is being measured. So, although the grain orientations are random within this area, the cubic crystal structure of HECs implies that the thermal conductivity is isotropic and therefore should not vary with grain orientation. Therefore, any differences in thermal conductivity can be attributed to microstructural features. While a few such features can be observed, appearing as black pixels in the image, thermal conductivity is relatively uniform throughout the sampled area, indicating that potential microstructure scattering mechanisms such as grain boundaries are having little effect on the thermal conductivity.

6.4 High-Entropy Borides

The next class of high-entropy ceramic studied is the high-entropy boride (HEB). Because of the aforementioned appealing attributes of refractory metal diborides, namely ZrB_2 and HfB_2 , the extension of high-entropy engineering to borides is a logical step beyond oxides. In this section, we study the local κ of HEB1, which has the composition $(\text{Hf}_{0.2}\text{Zr}_{0.2}\text{Ta}_{0.2}\text{Nb}_{0.2}\text{Ti}_{0.2})\text{B}_2$, to reveal how microstructure can influence thermal conductivity. To do so, we use the same TDTR mapping procedure discussed in the previous section. HEB1 is unique from all high-entropy ceramics prior to it in that it possesses a layered hexagonal crystal structure with alternating rigid two-dimensional boron nets and high-entropy two-dimensional layers of metal cations [225]. The samples were fabricated using high energy ball milling to mix the five constituent diboride powders, followed by densification via spark plasma sintering. XRD, SEM, and EDX were used to characterize the sample to confirm the compositions were largely uniform, albeit with the presence of uniformly-distributed minor secondary $(\text{Zr}, \text{Hf})\text{O}_2$ phases. Extensive details on the fabrication and characterization of HEB1 can be found in Ref. [225].

TDTR mapping is performed on HEB1 over a $180 \mu\text{m} \times 180 \mu\text{m}$ square area to capture the full $\sim 70 \mu\text{m} \times 120 \mu\text{m}$ region of the sample that was captured in SEM and EBSD. The SEM image of this region is shown in Fig. 6.6(a); this region's corners were marked using a focused ion beam (FIB) in order to easily match the TDTR image with the SEM image. The darker regions of the image include the secondary $(\text{Zr}, \text{Hf})\text{O}_2$ phases. Fig. 6.6(b) shows the same image rotated to match the orientation that was captured with TDTR. The magnitude of the probe signal and the ratio were recorded at a probe delay time of 4.5 ns, chosen as such to reduce sensitivity to the thermal boundary conductance between the aluminum and HEB in order to maximize the relative sensitivity to HEB1's thermal conductivity. The normalized magnitude and ratio images are shown in Figs. 6.6(c) and (d), respectively, using a $20\times$ objective lens, a step size of $2 \mu\text{m}$, and a dimension size of $\sim 180 \mu\text{m} \times 180 \mu\text{m}$ for a total of 8281 pixels. Both the magnitude and the ratio images show there is a distinct difference in signal between the area within the FIB markings and the area outside of these markings. Because EBSD was performed in this area over

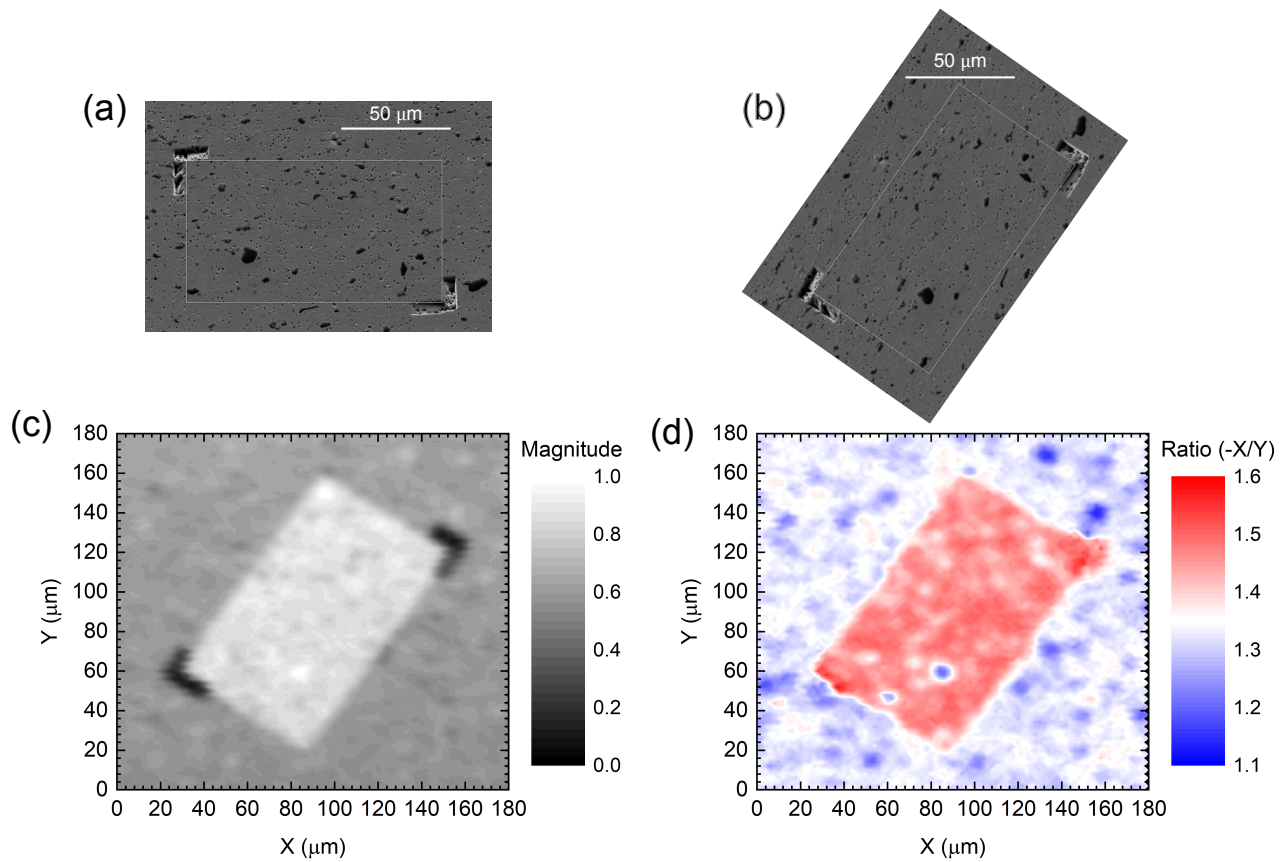


Figure 6.6: (a) SEM image of HEB around the $\sim 60 \mu\text{m} \times 120 \mu\text{m}$ region that is mapped with TDTR. (b) Rotated image of SEM to match orientation of TDTR images. (c) Normalized magnitude image of the probe recorded for a $20\times$ objective lens magnification at a delay time of 4.5 ns. (d) The ratio data for the same conditions as (c).

a long period of time (~ 8 hours), a thin carbon layer is formed, adding an additional thermal resistance that affects the TDTR signal. Because this carbon layer is estimated to be on the order of nanometers, it only affects the thermal boundary conductance between the Al and HEB1, rather than the HEB1 thermal conductivity. This is confirmed by performing full TDTR scans within the region and outside the region. On average, κ is equivalent within and outside the region at $\sim 25 \text{ W m}^{-1} \text{ K}^{-1}$, whereas the thermal boundary conductance was $37 \text{ MW m}^{-2} \text{ K}^{-1}$ inside the region and $72 \text{ MW m}^{-2} \text{ K}^{-1}$ outside the region.

Next, the ratio image is converted to a thermal conductivity image. Figure 6.7(a) and (c) show the thermal conductivity images using a $10\times$ and $20\times$ objective lens, respectively. Like the ratio image, there is a large contrast due to the difference in thermal boundary conductances within

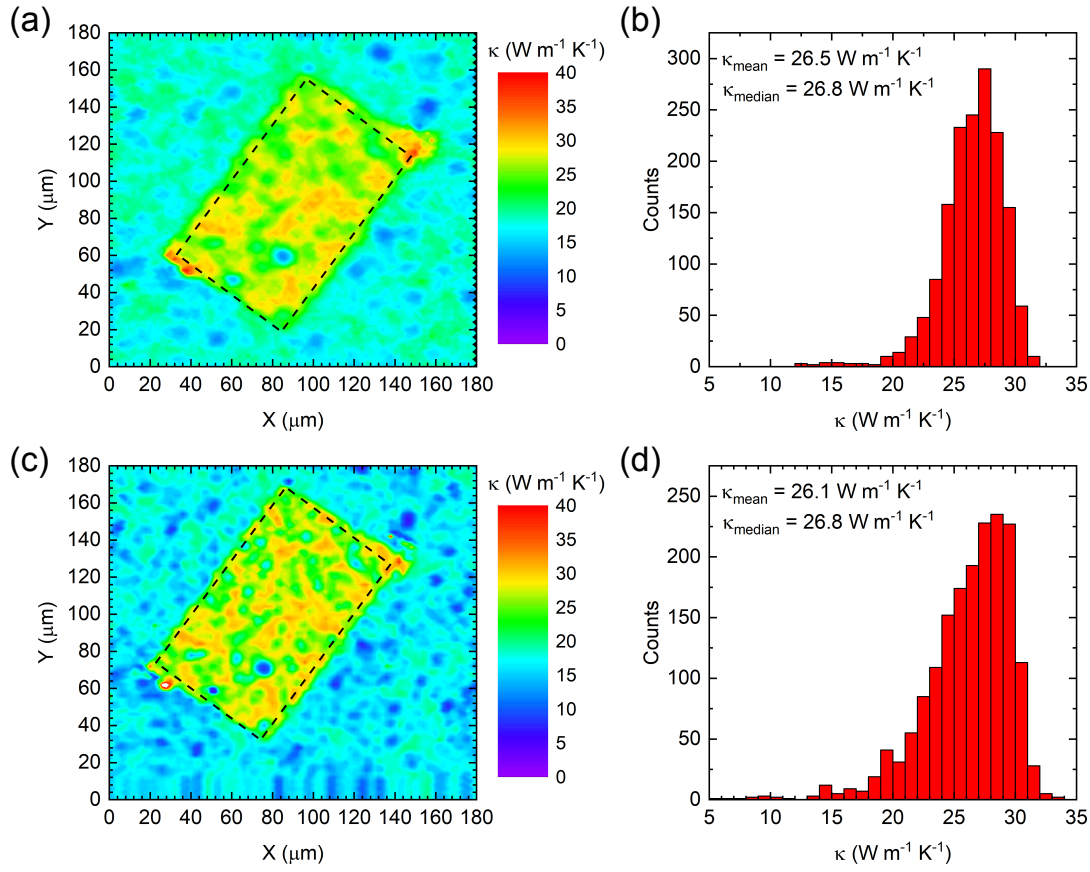


Figure 6.7: (a) Thermal conductivity map obtained using a $10\times$ objective lens with pump and probe $1/e^2$ diameters of 20.5 and 12.0 microns, respectively. (b) Histogram of thermal conductivity values for the region enclosed by the dashed lines in (a); the mean and median thermal conductivities are 26.5 and $26.8 \text{ W m}^{-1} \text{K}^{-1}$. (c) Thermal conductivity map obtained using a $20\times$ objective lens with pump and probe $1/e^2$ diameters of 10.5 and 7.5 microns, respectively. (d) Histogram of thermal conductivity values for the region enclosed by the dashed lines in (c); the mean and median thermal conductivities are 26.1 and $26.8 \text{ W m}^{-1} \text{K}^{-1}$.

the region enclosed by dashed lines and outside this region. The values for κ shown in the map are only valid for the enclosed region. A distribution of thermal conductivities within this area is shown for the $10\times$ case and $20\times$ case in Fig. 6.7(b) and (d), respectively. The mean κ is 26.5 ± 2.6 in the $10\times$ case and $26.1 \pm 3.6 \text{ W m}^{-1} \text{K}^{-1}$ in the $20\times$ case. There are two noteworthy points of comparison between the $10\times$ and $20\times$ cases: first, the influence of microscale features such as secondary $(\text{Zr}, \text{Hf})\text{O}_2$ phases become stronger in the latter case, which can be explained by the fact that when a larger pump and probe are used, the sampled area encompasses more variation over which an average thermal conductivity is extracted; when the pump/probe become

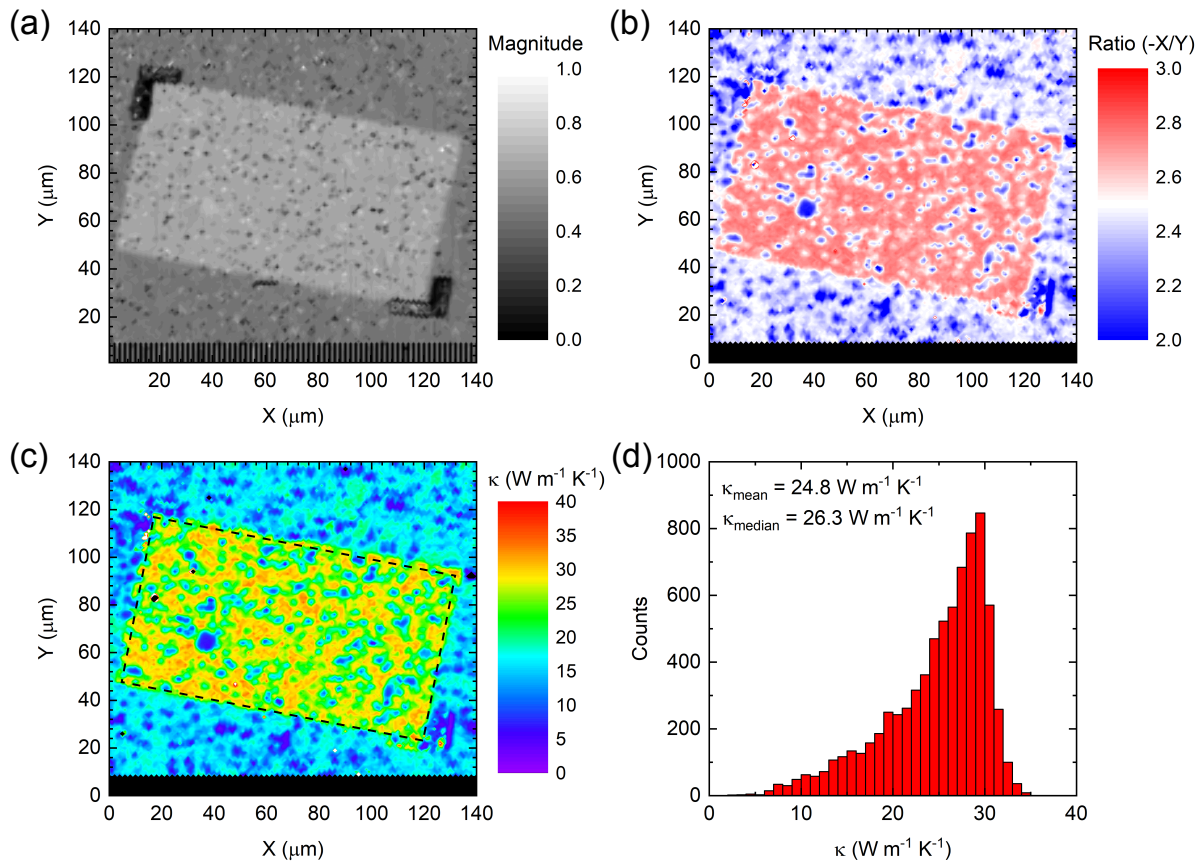


Figure 6.8: (a) TDTR normalized magnitude, (b) ratio, and (c) thermal conductivity image of HEB1 using a $50\times$ objective lens with pump and probe $1/e^2$ diameters of 3.5 and 3.25 microns, respectively. (d) Histogram of thermal conductivity values for the region enclosed by the dashed lines in (c); the mean and median thermal conductivities are 25.8 and $27.7 \text{ W m}^{-1} \text{ K}^{-1}$.

small enough, grains and phases can be sampled individually. Second, the distribution of thermal conductivities becomes larger and skewed towards lower values in the $20\times$ case, evidenced by the higher standard deviation. Interestingly, though, the average thermal conductivity remains the same (within uncertainty) in both cases.

Next, TDTR mapping is repeated using a $50\times$ objective lens, allowing for pump and probe $1/e^2$ diameters of 3.5 and $3.25 \mu\text{m}$, respectively. In this case, the delay time is 2.8 ns, the step size is $1 \mu\text{m}$, and the total size is $140 \mu\text{m} \times 140 \mu\text{m}$. The TDTR magnitude and ratio images are shown Fig. 6.8(a) and(b), respectively. The corresponding thermal conductivity image is shown in Fig. 6.8(c) and resulting distribution from the enclosed region within the dashed lines is shown in Fig. 6.8(d). The higher resolution of the $50\times$ image allows for finer details to be seen, including

the appearance of regions of low thermal conductivity ($< 15 \text{ W m}^{-1} \text{ K}^{-1}$). The distribution shows that the mean thermal conductivity is $24.8 \pm 5.6 \text{ W m}^{-1} \text{ K}^{-1}$; the higher standard deviation in this case is consistent with the previous findings. Furthermore, the skewed distribution towards lower values is evident, indicative of sampling more independent grains and/or secondary phases having lower thermal conductivities.

The wide distribution in thermal conductivity observed demonstrates that microstructure is influencing thermal conductivity. Given the anisotropic nature of HEB1, there is reason to believe this variation is due to grain orientation. To test this, we compare the EBSD grain orientation image to the thermal conductivity image to extract the thermal conductivity corresponding to each grain orientation. Figure 6.9(a) shows the EBSD micrograph, where grain orientations are depicted by a colormap. The 0001 crystallographic direction is represented by red, the $\bar{1}\bar{2}\bar{1}0$ direction by blue, and the $02\bar{1}0$ direction by green. The black regions represent the secondary $(\text{Zr}, \text{Hf})\text{O}_2$ phases. In order to determine the thermal conductivity of each orientation, we first apply a filter to determine the regions of each orientation. To do so, the filter criteria is defined such that for each orientation the RGB threshold is set to >100 for one of the three colors and <100 for the others, where the RGB scale ranges from 0 to 255. Filtering for each orientation results in the filtered EBSD micrographs shown in Fig. 6.9 for the (b) 0001 direction, (c) $\bar{1}\bar{2}\bar{1}0$ direction, and (d) $02\bar{1}0$ direction. For each filter, the coordinates are recorded and the thermal conductivity map is interpolated over these coordinates to extract a distribution of thermal conductivities corresponding to each orientation. Figure 6.9(f) shows the resulting distributions for (red) the 0001 direction, (blue) the $\bar{1}\bar{2}\bar{1}0$ direction, (green) the $02\bar{1}0$ direction, and (black) secondary phases. These histograms reveal that although HEB1 has an anisotropic crystal structure, its thermal conductivity in each orientation is on average equivalent under the present experimental conditions at $\sim 25 \text{ W m}^{-1} \text{ K}^{-1}$. In contrast, the secondary $(\text{Zr}, \text{Hf})\text{O}_2$ phases show a wide κ distribution with a significantly lower average of $18.4 \text{ W m}^{-1} \text{ K}^{-1}$.

To further elucidate the roll of this secondary oxide phase, we next compare the EBSD phase image to the thermal conductivity image. Figure 6.9(g) shows the EBSD phase image, where green represents the HEB1 composition and black represents secondary $(\text{Zr}, \text{Hf})\text{O}_2$ phases as well

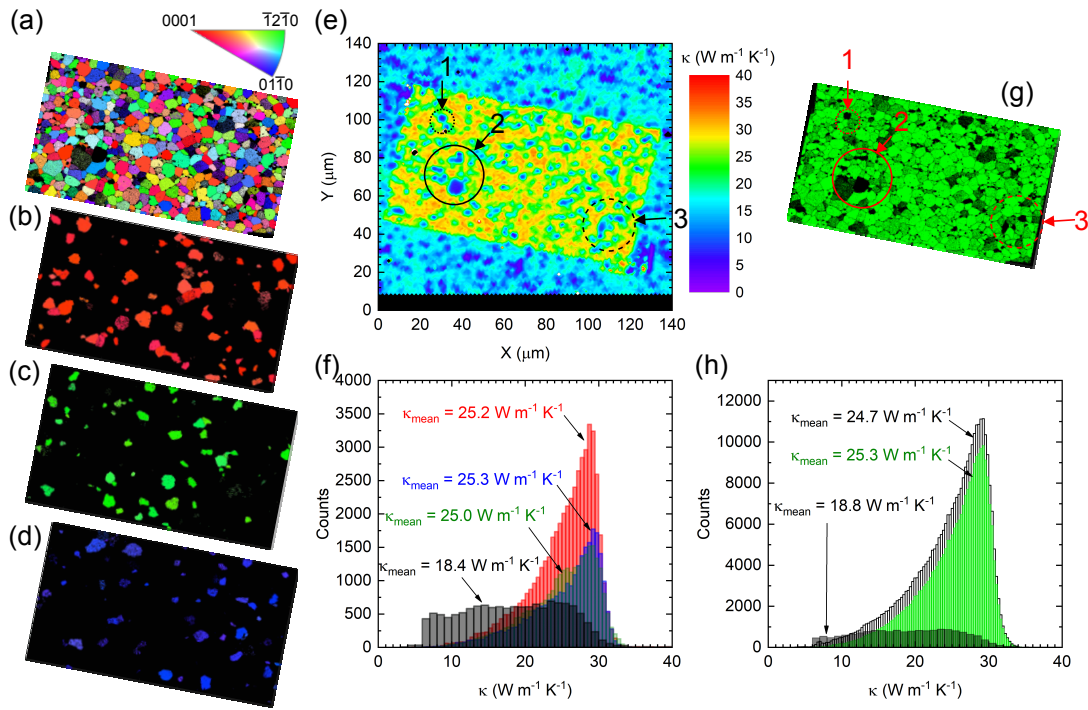


Figure 6.9: (a) EBSD micrograph showing grains and corresponding orientations; the image is rotated to match the thermal conductivity image determined by TDTR mapping. Filtered EBSD micrograph for the (b) 0001 direction, (c) 1̄2̄1̄0 direction, and (d) 02̄1̄0 direction. (e) thermal conductivity image of HEB1 using a 50× objective lens with pump and probe 1/e² diameters of 3.5 and 3.25 μm , respectively. The three circles, represented by 1,2, and 3, indicate secondary phases to be compared to the phase image. (f) Histograms of thermal conductivities for each of the three filtered grain orientations; the red corresponds to the 0001 direction, blue to the 1̄2̄1̄0 direction, green to the 02̄1̄0 direction, and black to regions of black in (a), corresponding to secondary phases. (g) Phase identification via EBSD: green is the HEB1 composition and black shows the secondary (Zr, Hf)O₂ phases. (h) Thermal conductivity histograms for (black) (Zr, Hf)O₂ phases, (green) HEB1 phase, and (hollow) all phases. The same circles shown in (e) are included for comparison.

as grain boundaries. Comparing Fig. 6.9(g) to (e), it is evident that the relatively low regions of thermal conductivity correspond to the oxide phase regions of the phase image. This is made clear by the three circles labeled 1, 2 and 3 in both (e) and (g), where relatively large oxide phases give rise to local regions of reduced thermal conductivity. Furthermore, using RGB filtering to determine the locations of black pixels, the thermal conductivity image is interpolated to extract a distribution shown in Fig. 6.9(h). In agreement with the orientation results, using the phase image reveals the secondary oxides possess a wide thermal conductivity range with an average of 18.8 $\text{W m}^{-1} \text{K}^{-1}$. This wide distribution could be due to variation in structure within (Zr, Hf)O₂, but also

due to the fact that there is overlap in the measured area between $(\text{Zr}, \text{Hf})\text{O}_2$ and HEB1 phases, such that some thermal conductivities encompass a weighted average of the two. By comparison, the HEB1 phase has an average of $25.3 \text{ W m}^{-1} \text{ K}^{-1}$, and the total average for all phases is $24.7 \text{ W m}^{-1} \text{ K}^{-1}$. Thus, while the $(\text{Zr}, \text{Hf})\text{O}_2$ phases have reduced thermal conductivities relative to the HEB1 phase, their presence is minor enough to not significantly alter the total average. Nonetheless, it is clear that *local* thermal conductivity can vary widely and be heavily influenced by the presence of secondary phases.

6.5 High-Entropy Silicides

The final high-entropy ceramic studied is the high-entropy silicide (HES). Refractory disilicides, particularly those of group IV, V, and VI elements, are promising for high-temperature applications due to their relatively high melting temperatures, which can exceed 2000°C [226], and oxidation resistance at elevated temperatures with the formation of a protective SiO_2 native oxide layer [227, 228]. Until now, the scope of high-entropy ceramics has been limited to oxides, carbides, borides, and nitrides. Here, we examine the thermal conductivity and volumetric heat capacity of the HES, $(\text{Mo}_{0.2}\text{Nb}_{0.2}\text{Ta}_{0.2}\text{Ti}_{0.2}\text{W}_{0.2})\text{Si}_2$. This HES is unique in that it possesses a CrSi_2 -type hexagonal C40 structure with the ABC stacking sequence [229]. This is significant because, to date, all known HECs, with the exception of HEBs discussed in the previous section, have cubic symmetries. Even the diborides possess a relatively simple hexagonal (AlB_2) crystal structure with comparatively high symmetry [225].

Extensive details on the structural properties and fabrication procedures can be found in Ref. [229]. In brief, high-energy ball milling was used to mix starting powders of MoSi_2 , NbSi_2 , TaSi_2 , TiSi_2 , and WSi_2 , and densification was achieved via spark-plasma sintering in vacuum environment with an argon backfill to minimize any oxidation. XRD, SEM, EDX, and EBSD confirm the presence of a single high-entropy solid-solution phase with some additional oxide contaminations. Finally, nanoindentation was used to characterize the hardness at $16.7 \pm 1.9 \text{ GPa}$ and elastic modulus of $421 \pm 19 \text{ GPa}$, comparable to those for constituent disilicides MoSi_2 and WSi_2 [230].

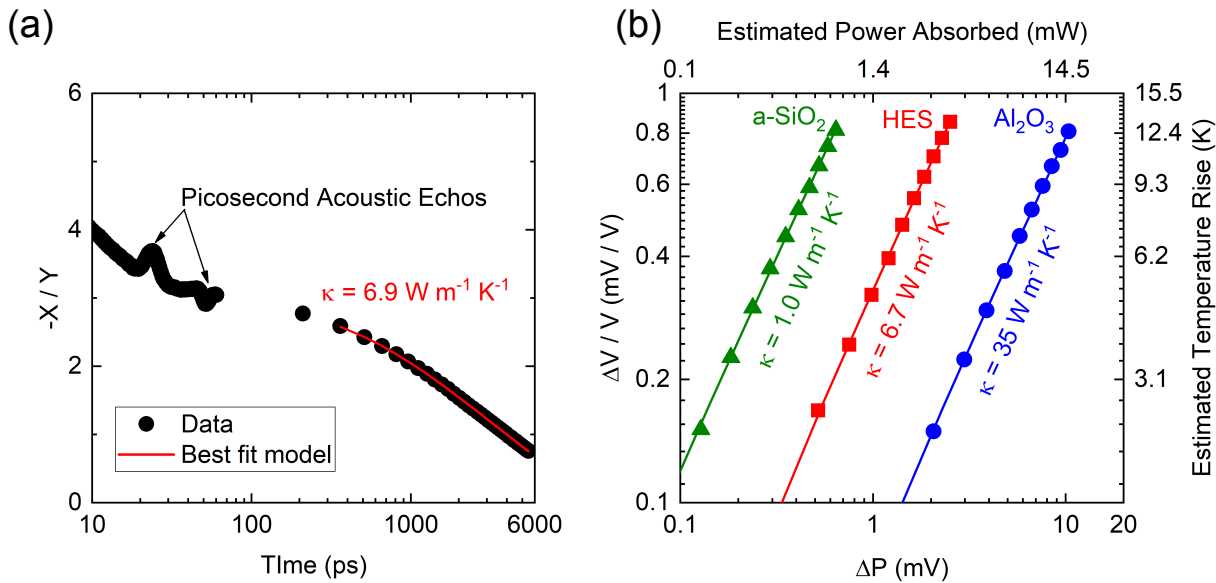


Figure 6.10: (a) TDTR ratio ($-X/Y$) data vs. probe delay time for HES. (b) SSTR probe lock-in magnitude vs. pump lock-in magnitude for HES, Al_2O_3 , Quartz, and glass.

Thermal conductivity was measured using both TDTR and SSTR. To do so, a thin Al transducer ($84 \pm 4 \text{ nm}$ measured using picosecond acoustics) was electron-beam evaporated onto the sample. The TDTR ratio data is shown in Fig. 6.10(a), with the best fit model corresponding to $\kappa = 6.9 \text{ W m}^{-1} \text{ K}^{-1}$. For TDTR, the pump was modulated at 8.4 MHz to heat the sample. The pump and probe $1/e^2$ diameters were 15 and 9 μm , respectively. These two conditions ensure a one-dimensional heating event in the cross-plane direction and an effective measurement of thermal effusivity [150]. To determine the thermal conductivity, the volumetric heat capacity was estimated to be $2.5 \pm 0.3 \text{ MJ m}^{-3} \text{ K}^{-1}$ based on the rule of mixtures average of constituent heat capacities [61]. Fitting a multilayer heat diffusion model to experimental ratio data, the best-fit thermal conductivity is determined to be $6.9 \pm 1.1 \text{ W m}^{-1} \text{ K}^{-1}$. Uncertainty in thermal conductivity results from variation from multiple measurements, uncertainty in Al thickness, and uncertainty in heat capacity.

As confirmed in the HEC study, SSTR provides an independent means for determining thermal conductivity without the need for estimating a heat capacity. The SSTR data shown in Fig. 6.10(b) for HES as well as two reference samples, an a-SiO₂ glass slide and a Al_2O_3 wafer, both deposited with Al at the same time as the HEC. The thermal conductivities of a-SiO₂ and Al_2O_3 were 1.0 and

$35 \text{ W m}^{-1} \text{ K}^{-1}$, respectively, in agreement with those measured in Ch. 4. The thermal conductivity of the HES is determined to be $6.7 \pm 0.5 \text{ W m}^{-1} \text{ K}^{-1}$, in agreement with TDTR. If we return to the TDTR data and now fit for heat capacity using the SSTR-determined thermal conductivity as an input, we determine that the heat capacity for HES is $2.6 \pm 0.3 \text{ MJ m}^{-1} \text{ K}^{-1}$, in close agreement with the rule of mixtures assumption.

6.6 Summary

In this chapter, we studied the role of compositional disorder on the thermal conductivity of bulk high-entropy ceramics. Beginning with high-entropy fluorite oxides, we determined that the thermal conductivity was $< 2 \text{ W m}^{-1} \text{ K}^{-1}$, on par with the 6-cation entropy-stabilized oxides from Ch. 5. Next, we studied cubic high-entropy carbides to show that the thermal conductivity in these materials is largely dictated by electrons, as evidenced by the increasing thermal conductivity with reduced valence electron concentration. This large electronic contribution allows carbides to have thermal conductivities significantly higher than the oxides, ranging from ~ 8 to $14 \text{ W m}^{-1} \text{ K}^{-1}$. Using TDTR mapping, we determined that the thermal conductivity of HEC3 was largely uniform, indicating little to no influence from microstructure, grain orientation, or any secondary phases. Next, we studied the high entropy boride to show that the thermal conductivity is even higher, at $\sim 25 \text{ W m}^{-1} \text{ K}^{-1}$. This HEB sample, having a layered hexagonal crystal structure, showed a wider variation in local thermal conductivity extracted from TDTR mapping. Comparison of thermal conductivity images to EBSD micrographs revealed that the thermal conductivity for each grain orientation was on average equivalent. However, local reductions in thermal conductivity were attributed to secondary $(\text{Zr}, \text{Hf})\text{O}_2$ phases. Finally, we studied the high-entropy silicide to show that the thermal conductivity was lower than the HECs and HEBs, at $\sim 7 \text{ W m}^{-1} \text{ K}^{-1}$. In all cases, thermal conductivities are reduced up to an order of magnitude from constituent elements, attributed to a reduction in phonon thermal conductivity from mass and strain disorder. However, the electronic contribution to thermal conductivity can still be significant, allowing carbides and borides to maintain relatively high thermal conductivities.

Chapter 7

Amorphous Thin Films

Having established the role of increasing configurational and compositional disorder on the thermal conductivity of crystalline materials, I now turn to amorphous materials. I first investigate the role of size effects on the thermal conductivity of amorphous silicon to reveal that long-wavelength propagating vibrational modes can contribute significantly to thermal conductivity, in direct opposition to the traditional outlook that thermal transport in amorphous materials is governed by diffusive vibrational modes limited to length scales on the order of the average interatomic spacing. I then investigate the role of composition on the thermal conductivity of amorphous hydrogenated silicon nitride ($a\text{-SiN}_x\text{:H}$). After establishing an understanding of thermal transport in $a\text{-Si}$, $a\text{-SiN}_x\text{:H}$ enables us to understand how the introduction of compositional disorder through new atomic species can change the underlying bond network and the resulting thermal conductivity.

7.1 Amorphous Silicon: Size Effects on Thermal Conductivity

7.1.1 Background

The influence of size effects on the phonon thermal conductivity of crystalline thin films has been the topic of a wide array of studies [2, 10, 11, 231] that have shaped the direction of fields rooted in nanoscale heat transfer and applications reliant on nanotechnology. It is well known

that for films with thicknesses less than the length scale of their phonon mean free paths, thermal conductivity can be reduced due to incoherent boundary scattering of phonons ballistically traversing the film. By comparison, the role of size effects on the thermal conductivity of disordered or fully amorphous solids has been examined to a lesser extent. Unlike crystalline solids, in which a well defined spectrum of phonons exists in a periodically repeating lattice, the vibrational modes in disordered solids are described using a different taxonomy due to the lack of atomic periodicity [84]. In these systems, the vibrational modes can be classified as propagating, delocalized (phonon-like) modes called “propagons”; non-propagating, delocalized modes called “diffusons”; and non-propagating, localized modes called “locons” [21, 84, 232, 233]. Previous studies have demonstrated that propagating modes in disordered and amorphous systems can contribute significantly to the thermal conductivity of certain materials, such as amorphous silicon nitride [234] and disordered silicon-germanium alloys [109, 115]. This implies that in highly disordered or amorphous thin films, size effects in the vibrational thermal conductivity can exist depending on the degree to which propagating modes contribute to the thermal conductivity. However, in other amorphous thin films, namely SiO_2 and Al_2O_3 , size effects in the thermal conductivity have not been observed [21, 88].

Taken together, the impact of size effects on thermal conductivity in amorphous solids remains underdeveloped. The study of heat carrier mean free path contributions to thermal conductivity has evolved significantly over the past decade [130] through analytical methods like the thermal conductivity accumulation function [235] and through experimental methods like TDTR [94] and Broadband FDTR (BB-FDTR) [116]. In the approach taken here, we use TDTR to measure the thermal conductivity of amorphous silicon films of varying thicknesses, an approach that Zhang *et al.* [231] analytically demonstrated can provide information regarding the spectral dependence of the phonon thermal conductivity in nanosystems. While our results provide similar insight into the role of long mean free path propagons to the thermal conductivity of amorphous silicon as that reported by Liu *et al.* [132], our approach is fundamentally different. Liu *et al.*’s approach relied on varying the modulation frequency, and hence the thermal penetration depth and resulting measurement volume beneath the surface in order to isolate the role of propagons with mean free paths

larger than the measurement volume on the thermal conductivity measurement. Our approach of varying the amorphous silicon film thickness in a regime in which we sample a substantial portion of the thickness leads our measurements to be independent of modulation frequency. This allows us to report an intrinsic value of thermal conductivity of our samples, gives direct insight into the role boundary scattering of propagons on the thermal conductivity in the amorphous silicon, and avoids any potential complications or misconceptions regarding the interpretation of modulation frequency dependent TDTR data that otherwise could cloud our results [116, 236–238].

Examining the vibrational taxonomy discussed above, if the amorphous solid's thermal conductivity contains a significant contribution from propagons compared to non-propagating modes, then size effects should play a role in thermal conduction. That is, increasing film thickness will reduce propagon-boundary scattering as films approach the length scales of propagon mean free paths, allowing these propagons to contribute to thermal conductivity. Amorphous silicon (a-Si) serves as a suitable candidate to study this hypothesis given the well established literature both experimentally [116, 131, 132, 239–244] and computationally [21, 84, 245]. These computational studies suggest that propagons can contribute significantly to thermal conductivity when not restricted by forced scattering (e.g., by boundaries). Thus, clear size effects on the measured thermal conductivity of a-Si films should be observable, driven by propagon-boundary scattering. Figure 7.1 summarizes the literature data on experimentally measured values of a-Si thermal conductivity as a function of film thickness. While a general trend of increasing thermal conductivity with film thickness is observed, the lack of uniform growth conditions among samples hinders any insight into discerning intrinsic properties from byproducts of fabrication or measurement technique. It is clear that in order to study the nature of long-wavelength heat carriers and the role of film thickness on a-Si thermal conductivity, a systematic study with samples prepared under identical growth conditions is necessary.

To this end, we measure the thermal conductivity of a series of amorphous silicon thin films ranging in thickness from 3 – 1636 nm. Our results not only demonstrate size effects in the thermal conductivity, which remain pronounced up to the thickest films, but also show evidence of a crossover from a constant thermal conductivity to an increasing thermal conductivity. We an-

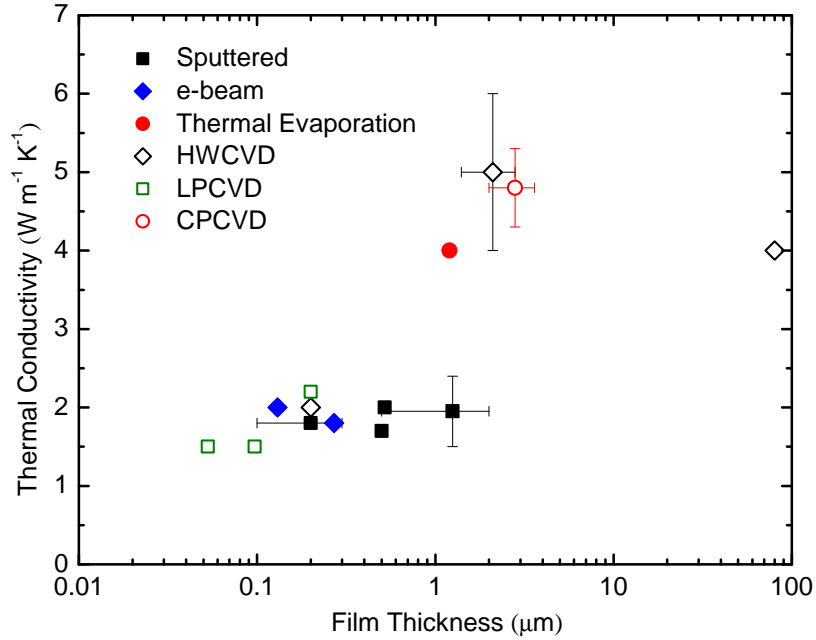


Figure 7.1: Literature data for thermal conductivity of amorphous silicon as a function of film thickness: solid squares represent samples prepared via sputter deposition [116, 240–242], solid diamonds represents samples prepared via e-beam evaporation [244], open diamonds represent samples prepared via hot-wire chemical vapor deposition (HWCVD) [131, 132], open squares represent sample prepared via low-pressure chemical vapor deposition (LPCVD) [243], and closed and open circles represent samples prepared via thermal evaporation and cyclic plasma chemical vapor deposition (CPCVD), respectively [239].

alytically study this trend under the hypothesis that it is driven by an increasing contribution from propagons with increasing a-Si thickness [21]. Using a kinetic theory approach to modeling the thickness dependent thermal conductivity, we empirically determine a propagon/diffuson crossover frequency in our a-Si samples, which is in excellent agreement with previous theory and molecular dynamic simulations [21, 84]. Our results provide experimental support to the propagon/diffuson/locon taxonomy describing the underlying vibrational thermophysics driving the thermal conductivity of a-Si, while also highlighting the shortcomings of the minimum thermal conductivity model for describing the thermal conductivity of thick a-Si films [80].

7.1.2 Experimental Details

We fabricated a-Si films on native oxide/silicon substrates using RF sputter deposition. Nominal 80 \pm 3 nm of Al was deposited on top of the a-Si samples by electron-beam evaporation to act as an opto-thermal transducer during our thermal conductivity measurements; we verified the thickness of the Al film on each sample using mechanical profilometry and picosecond acoustics [246, 247]. As detailed in the supplemental material of Ref. [22], we characterize the a-Si films with X-ray photoemission spectroscopy to quantify the chemical composition and Raman spectroscopy to confirm the amorphous nature of the films.

We measured the thermal conductivity of the a-Si using TDTR, the details and analyses for which are described in Chapter 3. We measure the ratio of the in-phase to out-of-phase voltage of the probe response as a function of pump-probe delay time using pump and probe $1/e^2$ spot sizes (diameters) of 55 and 13 μm , respectively, while the pump pulses are modulated with a $f = 12.2$ MHz sinusoidally varying envelope. Using a multilayer, radially symmetric thermal model [94, 97], we fit for the thermal boundary conductance between the Al transducer and the a-Si film ($G_{\text{Al/a-Si}}$) and the a-Si thermal conductivity ($\kappa_{\text{a-Si}}$). We assume bulk values for the heat capacities of the Al transducer, a-Si film, and Si substrate [61, 127]. Using a modulation frequency of 12.2 MHz, the thermal penetration depth is relatively shallow (roughly 140 – 180 nm using an approximation for thermal penetration depth as $\delta \approx \sqrt{\kappa_{\text{a-Si}}/\pi f C_{\text{v,a-Si}}}$, where C_{v} is the volumetric heat capacity). As a result, for the samples having thicknesses greater than δ , we can measure $G_{\text{Al/a-Si}}$ and $\kappa_{\text{a-Si}}$ without knowledge of the thermal boundary conductance across the a-Si/native oxide/Si substrate interface, and for thicknesses greater than approximately $\delta/0.47$, we can assume the a-Si film as semi-infinite compared to the modulated pump-induced thermal wave [150]. While this semi-infinite assumption simplifies the analysis, we note that to ensure our results are independent of thermal penetration depth, we repeat measurements over modulation frequencies ranging from 1.0 to 12.2 MHz (corresponding to thermal penetration depths between \sim 150 to 600 nm) and confirm consistency among results.

It is important to realize that as the film thickness decreases to thicknesses less than the Al transducer thickness, TDTR measurements become more sensitive to the thermal conductance of

the film ($\kappa_{\text{a-Si}}/d$), where d is the film thickness, and lose sensitivity to the thermal mass of the film ($C_v d$). In this thin-film regime, the intrinsic thermal conduction of the film must be separated from the thermal boundary conductance across the a-Si/native oxide/Si interface ($G_{\text{a-Si/c-Si}}$), especially when $G_{\text{a-Si/c-Si}} \approx \kappa_{\text{a-Si}}/d$ and the thermal penetration depth during TDTR experiments is on the order of, or greater than, the film thickness. In general, this thin-film regime can be loosely defined as having a thickness less than the thermal penetration depth. To appropriately quantify this regime, we apply sensitivity analyses in which we perturb several parameters in our TDTR analysis to determine the magnitude of influence for these parameters on the results. We find that the thermal conductivity measured for samples with thicknesses less than ~ 150 nm includes an additional thermal resistance due to the substrate interface that masks its intrinsic value.

7.1.3 Thin Film Analysis

Analysis of samples within this thin-film regime ($d < 150$ nm) can be difficult. Lee and Cahill [248] showed that if the intrinsic thermal conductivity is independent of film thickness, a series resistor model can be used to account for the presence of the interface resistance being measured during TDTR. In parallel with molecular dynamics described in detail in the supplemental material of Ref. [22], we systematically study this with the initial assumption that the series resistor model is valid for all film thicknesses in the thin-film regime. To model intrinsic thermal conductivity, we use the following:

$$\frac{1}{G_m} = \frac{1}{G_{\text{total}}} + \frac{d}{\kappa_i}, \quad (7.1)$$

where G_m is the total measured thermal conductance across the Al/a-Si interface, a-Si layer, and a-Si/c-Si interface, κ_i is the intrinsic thermal conductivity, and G_{total} accounts for the both $G_{\text{Al/a-Si}}$ and $G_{\text{a-Si/c-Si}}$ in series using a thermal circuit model. Defining $\kappa_{\text{eff}} = G_m d$, we rearrange Eq. (7.1) to become:

$$\kappa_i = \frac{\kappa_{\text{eff}}}{1 - \frac{\kappa_{\text{eff}}}{G_{\text{total}} d}}. \quad (7.2)$$

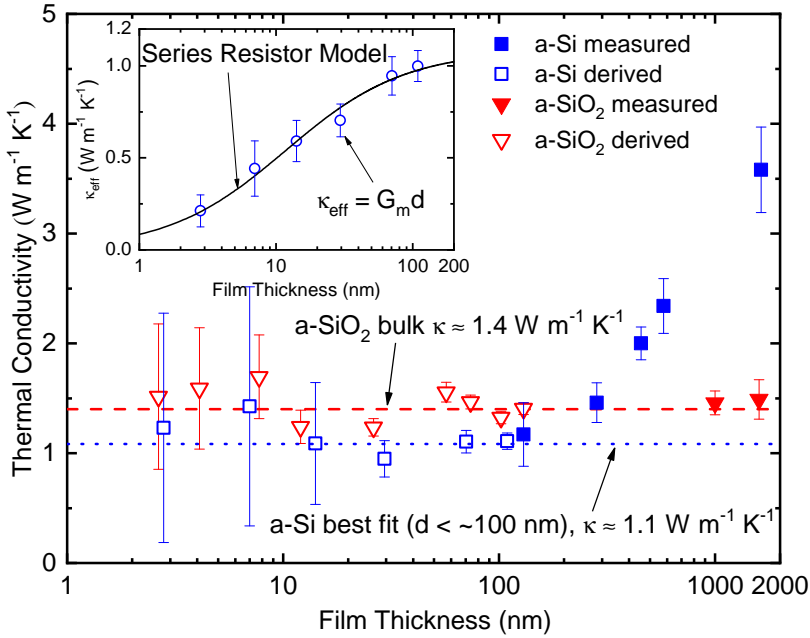


Figure 7.2: Thermal conductivity of amorphous silicon (amorphous silica) samples: filled squares (filled triangles) represent thermal conductivity as measured without influence of $G_{a\text{-Si}/c\text{-Si}}$ ($G_{a\text{-SiO}_2/\text{Si}}$), while open squares (open triangles) denote the derived thermal conductivity as determined using Eq. (7.2). The dashed line at $\kappa = 1.4 \text{ W m}^{-1} \text{ K}^{-1}$ represents the literature bulk value of SiO_2 thermal conductivity [249], while the dotted line at $\kappa \approx 1.1 \text{ W m}^{-1} \text{ K}^{-1}$ represents the fitted value for the thermal conductivity of our a-Si thin films using Eq. (7.2). Shown in the inset is a plot of effective thermal conductivity of a-Si thin-films vs. film thickness and the model using Eq. (7.2) with best fit values for κ_i and G_{total} .

Using Eq. (7.2), we fit κ_i and G_{total} to our experimental data (6 data points classified by the thin-film regime) using a nonlinear least-squares fit. If the aforementioned assumptions are correct, we should observe a good fit to our data. Indeed, this is the case, as shown in the inset to Fig. 7.2. The best fit value for κ_i is $1.1 (\pm 0.15) \text{ W m}^{-1} \text{ K}^{-1}$ while the best fit value for G_{total} is $92 (\pm 30) \text{ MW m}^{-2} \text{ K}^{-1}$, where uncertainty is based on 95% confidence bounds. To further validate these results, we repeat this procedure using all subsets of data points within the set of films used in this initial calculation; we find a remarkable consistency among all combinations, indicating that this procedure gives an acceptable average for the thermal conductivity for films in the thin-film regime. Moreover, it demonstrates that any film size effects on thermal conductivity are relatively insignificant, such that we proceed under the conclusion that thermal conductivity for films less

than ~ 100 nm is constant.

To understand the sensitivity of this data to the fitted value for G_{total} , we use this value (92 ± 30 MW m $^{-2}$ K $^{-1}$) and corresponding uncertainty to calculate κ_i values for each film thickness via Eq. (7.2); we denote these values as “derived” thermal conductivities to distinguish them from measured values. Both derived and measured thermal conductivity values are shown as a function of thickness in Fig. 7.2. Uncertainty in the data includes contribution from uncertainty in Al and a-Si film thickness as well as uncertainty in fitting. Sensitivity to G_{total} becomes more prominent with decreasing film thickness, hence the large uncertainty associated with the estimated thermal conductivity of the thinnest films. Note that the 150 nm film, not analyzed with this thin-film procedure, still shows near-negligible film size dependence on its thermal conductivity.

To confirm the validity of this analysis technique, we follow the same procedure with a-SiO₂ thin films grown via dry oxidation. We find that the best fit value for κ_i is 1.4 ± 0.13 W m $^{-1}$ K $^{-1}$ while the best fit value for G_{total} is 180 ± 55 MW m $^{-2}$ K $^{-1}$, where again uncertainties are based on 95% confidence bounds. This fitted value of 1.4 W m $^{-1}$ K $^{-1}$ is in agreement with the bulk value for thermal conductivity of amorphous silica [249]. Moreover, these findings suggest that any size dependence observed in our a-Si data are not a result of partial oxidation of the films.

7.1.4 Results and Discussion

We move forward in our analysis with the assertion that the intrinsic thermal conductivities of our a-Si films below ~ 100 nm are relatively constant ($\kappa_i = 1.1$ W m $^{-1}$ K $^{-1}$) with changes in film thickness. Figure 7.2 depicts the thermal conductivity over the entire range of thicknesses measured in this study; a clear increasing thermal conductivity trend is observed with increasing film thickness beyond ~ 100 nm. Given that the thermal conductivity of these films is determined to be intrinsic to the a-Si layer and that films with thicknesses greater than the thermal penetration depth have near negligible sensitivity to the a-Si/substrate interface, we hypothesize that our measurements are sensitive to the increasing thermal effusivity of the a-Si due to the increased contribution of propagon modes to thermal transport. In other words, for films with thicknesses less than the mean free path of propagons, these propagons are traversing the thickness of the a-Si

ballistically and scattering at the a-Si/c-Si interface, leading to a reduction in the thermal conductivity. Thus, size effects in these long wavelength modes become less pronounced as the film thickness is increased, leading to an increase in thermal conductivity, an experimental result that has been demonstrated in crystalline solids [2, 11] and disordered alloys [109]. As the limit of this contribution to thermal conductivity by propagons approaches zero, we are left with only contribution by diffusons; we therefore attribute the constant thermal conductivity we derive above to diffuson thermal conductivity. This experimentally observed conclusion is consistent with Larkin and McGaughey's [21] recent molecular dynamics simulations, which predicted a diffusion thermal conductivity in a-Si of $1.2 (\pm 0.1) \text{ W m}^{-1} \text{ K}^{-1}$ and attributed size effects in a-Si to be driven by propagon-boundary scattering.

We compare this derived value for diffuson thermal conductivity to the prediction from the minimum thermal conductivity (κ_{\min}) model, given by Cahill *et al.* [80]. For amorphous silicon, κ_{\min} as calculated by this model is $\sim 1 \text{ W m}^{-1} \text{ K}^{-1}$, in close agreement with what we observe in our results. This model treats atomic vibrations as harmonic oscillators that scatter at distances on the order of the average interatomic spacing. This κ_{\min} model captures the nature of diffusons given the small length scales over which diffusons scatter ($< 10 \text{ nm}$) [245]. However, the model fails to capture the nature of propagon contribution to thermal conductivity, as evidenced by our data in Fig. 7.2. Thus, an improved model is needed to describe the thermal conductivity of all heat carriers in a-Si.

Our data suggest two regimes of thermal conductivity in a-Si films: the regime of relatively constant thermal conductivity that is dominated by diffuson transport ($d < 100 \text{ nm}$, $\kappa_{\text{diffuson}} = 1.1 \text{ W m}^{-1} \text{ K}^{-1}$) and a regime of increasing thermal conductivity dominated by propagon transport ($d > 100 \text{ nm}$). Based on these regimes, the rate of increase in thermal conductivity of films in the “propagon-dominated” regime can be directly linked to the propagon/diffuson crossover frequency, so that the propagon contribution to the thermal conductivity of a-Si can be analytically modeled via:

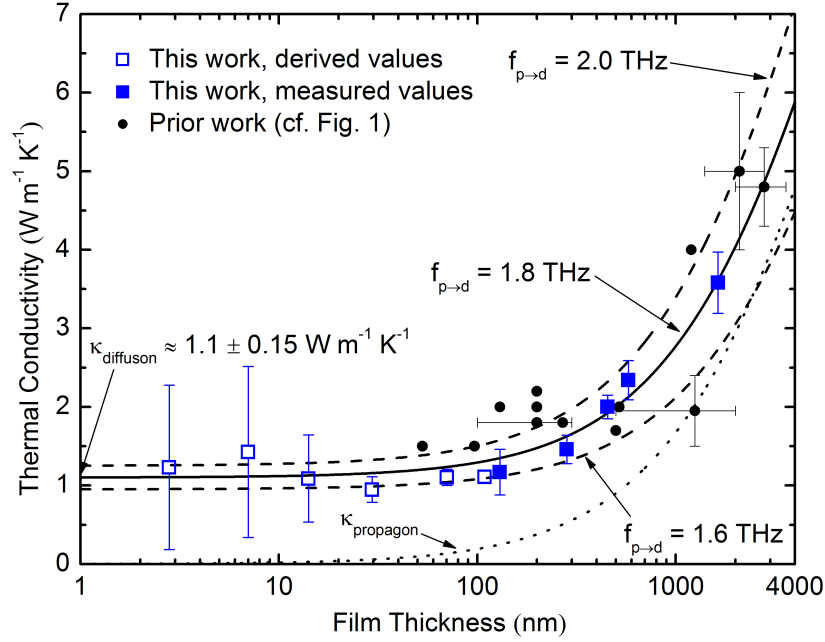


Figure 7.3: Thermal conductivity of our a-Si thin films. Open squares denote derived thermal conductivity using Eq. (7.2), while filled squares denote the thermal conductivity as directly measured. Our thermal conductivity model ($\kappa = \kappa_{\text{diffuson}} + \kappa_{\text{propagon}}$) is plotted with its best fit value for $f_{p \rightarrow d}$ of 1.8 THz (solid curve) as well as the individual contribution of κ_{propagon} as calculated using Eq. (7.3) (dotted curve). Also shown are the calculated curves for the same model using values for $f_{p \rightarrow d}$ of 1.6 THz with $\kappa_d = 0.95 \text{ W m}^{-1} \text{ K}^{-1}$ and 2.0 THz with $\kappa_d = 1.25 \text{ W m}^{-1} \text{ K}^{-1}$ (dashed curves). Finally, shown in solid circles is the literature data presented in Fig. 7.1 up to a film thickness of 4 μm to demonstrate agreement between our model and this data.

$$\kappa_{\text{propagon}} = \frac{1}{3} \sum_j \int_0^{\omega_{p \rightarrow d, j}} \hbar \omega D_j(\omega) \frac{\partial f}{\partial T} v_j^2 \tau_j d\omega \quad (7.3)$$

where j is an index that refers to the polarization (longitudinal or transverse), $\omega_{p \rightarrow d}$ is the crossover angular frequency (from propagon regime to diffuson regime), \hbar is the reduced Planck's constant, ω is the propagon angular frequency, D is the propagon density of states, f is the propagon equilibrium distribution function (assumed to be a Bose-Einstein distribution), v is the sound speed, and τ is the propagon relaxation time. Due to the long-wavelength nature of propagons, we model the density of states using a Debye model based on the sound speeds and atomic density of a-Si [80].

We also assume that relaxation times of propagons can be modeled similarly to Umklapp scattering and impurity scattering of long-wavelength phonons in silicon; we use values for these relaxation times based on a three-phonon scattering model of the form $\tau^{-1} = A\omega^4 + BT\omega^2 \exp(-C/T)$ [64, 66, 68–70]. Fitting to bulk literature thermal conductivity data for crystalline silicon sampled over 100 – 700 K using a Debye approximation, we find that $A = 1.82 \times 10^{-45}$ s³, $B = 2.8 \times 10^{-19}$ s K⁻¹, and $C = 182$ K. We include a boundary scattering time for the propagons given by $\tau_b = d/(2\nu_j)$ [21, 250]. Finally, we assume $\omega_{p \rightarrow d,T} = \omega_{p \rightarrow d,LV_T}/v_L$, where “L” and “T” denote the longitudinal and transverse propagon modes, respectively.

Figure 7.3 shows the intrinsic thermal conductivity as a function of film thickness for all a-Si films in this study as well as our model for propagon contribution to thermal conductivity for film thicknesses up to 4 μm. The total thermal conductivity is the sum of thermal conductivity contributions from diffusons (κ_{diffuson}) and propagons (κ_{propagon}). Treating $\omega_{p \rightarrow d}$ as a free parameter, we use a least-squares method to fit this model to our experimental data. The best fit value for this propagon-diffuson crossover frequency, $f_{p \rightarrow d} = \omega_{p \rightarrow d,L}/2\pi$ is ~ 1.82 (± 0.2) THz, indicating that vibrational frequencies describing a-Si’s dispersion relation beyond this value do not behave as propagons. One notes the sensitivity of this curve to the fitting parameter; while negligible at smaller film thicknesses, choice of $\omega_{p \rightarrow d}$ becomes significant in the propagon-dominated, large film thickness regime. For comparison, we include the literature values of a-Si thermal conductivity as a function of film thickness first presented in Fig. 7.1. Although simple, our model aligns with both our experimental observations and literature data up to thicknesses of 4 μm. Additionally, our propagon-diffuson crossover frequency agrees well with our molecular dynamics calculation of 2.0 THz as well as that of Larkin and McGaughey, 1.8 THz [21].

In conclusion, we presented evidence for size effects in the measured thermal conductivity of amorphous silicon thin films. We showed that size effects can be attributed to the nature of the long-wavelength vibrations. Based on our experimental observations, only propagons with mean free paths greater than ~ 100 nm contribute significantly to thermal conductivity. For films with thicknesses less than ~ 100 nm, the thermal conductivity is dominated by diffusons, which do not show a significant, observable film thickness dependence for the films measured in this study.

Towards the goal of this dissertation, this section shows that fully amorphous materials can possess thermal properties normally attributed to crystalline materials, arising from long-wavelength propagating modes. Thus, the conventional notion of κ_{\min} defining the thermal conductivity of amorphous materials is only appropriate in diffuson-limited thermal transport.

7.2 Amorphous Hydrogenated Silicon Nitride: Composition Effects on Thermal Conductivity

7.2.1 Background

Hydrogenated amorphous thin films synthesized by plasma-enhanced chemical vapor deposition (PECVD) are widely used in the semiconductor industry for a variety of electronic, optoelectronic, photovoltaic, thermal, mechanical, microelectromechanical, and biological applications [251, 252]. Amorphous hydrogenated silicon nitride ($a\text{-SiN}_x\text{:H}$) films, in particular, are widely used for both surface and bulk passivation of silicon and as anti-reflective coatings to improve solar cell efficiency [253–259]. The higher refractive indices achievable in these films and tunability thereof based on stoichiometry makes $a\text{-SiN:H}$ highly appealing for selective anti-reflective coatings compared with alternative thermal oxide layers [255]. Beyond solar cell applications, $a\text{-SiN}_x\text{:H}$ films also find use as gate dielectrics for insulation in amorphous hydrogenated silicon ($a\text{-Si:H}$)-based and organic thin-film transistors [260, 261], heterojunction bipolar transistor technology [262], as well as liquid-crystal display (LCD) and other newly emerging display technologies [252].

Despite its ubiquity in these application areas, a thorough investigation of the thermal properties of $a\text{-SiN}_x\text{:H}$ has remained unexplored. In particular, because stoichiometry and hydrogen composition control the physical properties of this material [263], a systematic study of the role of Si, N, and H composition on the thermal conductivity of $a\text{-SiN}_x\text{:H}$ thin films would greatly benefit the prediction and modeling of heat transfer in devices reliant on $a\text{-SiN}_x\text{:H}$ films. Considering the aforementioned application space, the thicknesses of $a\text{-SiN}_x\text{:H}$ films can vary between a few

nanometers to several microns. Thus, in this section, we investigate the role of film thickness, composition, and hydrogenation on the thermal conductivity of PECVD-grown a-SiN_x:H films to show how thermal conductivity can be systematically reduced through hydrogen content; in fact, no matter the ratio of Si and N, the thermal conductivity is primarily dictated by the atomic percentage (at.%) H. In general, we find that deposition through PECVD restricts the lower-bound of achievable hydrogen content. In order to further reduce the at.% H in these materials, we anneal the samples at four temperatures ranging from 650 °C to 1000 °C to induce chemical dissociation of the hydrogen out of the films [264].

Towards the goal of this dissertation, a-SiN_x:H serves as a sample system to understand the role of compositional disorder on the thermal conductivity of amorphous materials through systematic variation of the underlying stoichiometry. As will be discussed in detail soon, the thermal conductivity of a-SiN_x has been suggested to have strong contribution from propagons at room temperature [16], but verification of this as a general rule has remained elusive. Thus, to selectively study the role of hydrogen on propagon thermal transport, we additionally measure the thermal conductivity of hydrogenated amorphous silicon (a-Si:H) as a function of film thickness. As was determined in the first half of this chapter, a-Si can have a large fraction of its thermal conductivity comprised of propagons, giving rise to thickness-dependent thermal conductivity. The addition of hydrogen to both a-Si and a-SiN_x adds the additional complexity of bond termination. Beyond simply mass variation alone, the addition of hydrogen fundamentally reduces the coordination number, which we previously showed to have significant influence on the thermal conductivity of 200 nm films of amorphous hydrogenated silicon oxycarbide (a-Si[O/C]:H) [265].

Because of the limited nature of thermal characterization of a-SiN_x:H, we begin by turning to the more widely studied a-SiN_x, representing the limit of the composition space for a-SiN_x:H when H → 0. a-SiN_x has been extensively studied due to its application in thermal isolation, surface passivation, etch masking, and as structural or optical layers for various micro-electromechanical systems (MEMS) [282, 283]. A review of literature, summarized in Fig. 7.4, reveals a wide variation in reported κ for a-SiN_x as a function of film thickness, ranging from ∼0.5 to 13 W m⁻¹ K⁻¹ at room temperature. While conventional wisdom suggests the thermal conductivity of amorphous

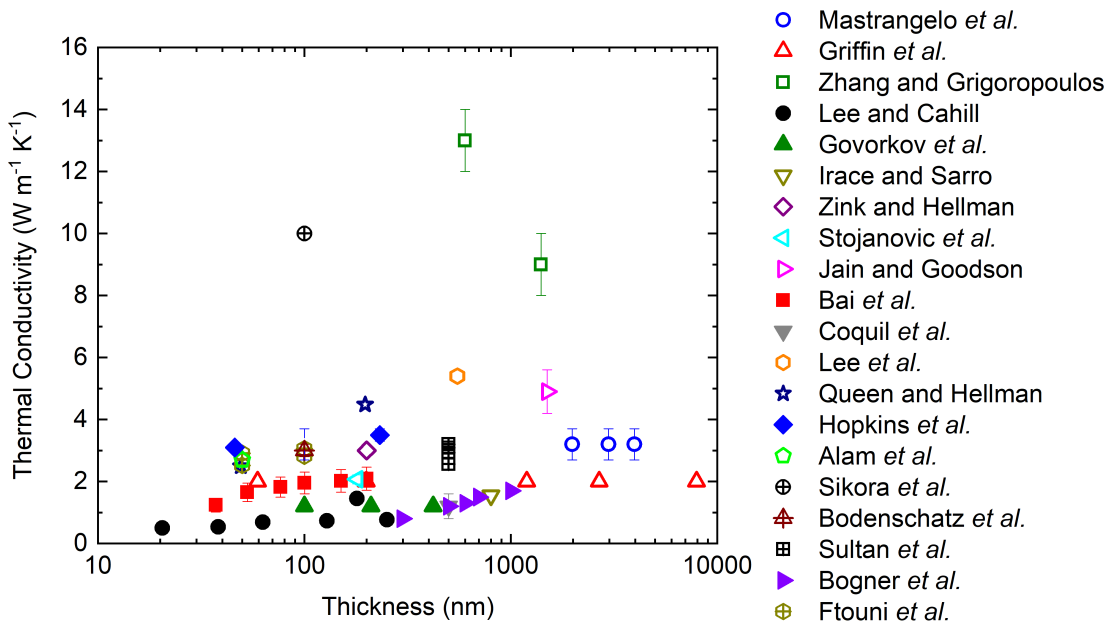


Figure 7.4: Literature thermal conductivity (κ) vs. film thickness for amorphous silicon nitride. The thermal conductivity is shown for References [97, 234, 248, 266–281]. Closed symbols represent cross-plane thermal conductivity measurements, while all others represent in-plane thermal conductivity measurements.

materials is isotropic, Kwon *et al.* [23] used a-Si to show that this isn't always the case. Therefore, it is important to emphasize the direction of κ reported (in-plane, κ_r , which is perpendicular to the limiting dimension, or cross-plane, κ_z , which is parallel to the direction of limiting dimension). The majority of reported measurements of thermal conductivity have been for suspended films and membranes, such that κ_r is fundamentally measured. Mastrangelo *et al.* [266] first measured κ_r of low stress, low pressure chemical vapor deposition (LPCVD) grown Si_{1.0}N_{1.1} microbridges ranging in thickness from 2 to 4 μm to be 3.2 W m⁻¹ K⁻¹, with no dependence on thickness. Griffin *et al.* [267] later measured κ_r for CVD-grown Si₃N₄ using a steady-state technique to be \sim 2 W m⁻¹ K⁻¹ and independent of thickness for films ranging in thicknesses from 0.06 to 8 μm . Zhang and Grigoropoulos [273] used three experimental methods – the phase-shift method, the amplitude method, and the heat-pulse method – to determine κ_r for an a-Si-rich SiN_x film (66.8% Si and 33.2% N in atomic weight) deposited via LPVCD; they found κ_r to be 9 and 13 W m⁻¹ K⁻¹ for the 1.4 μm and 0.6 μm film, respectively, where the reduced thermal conductivity of the thicker film was postulated to be due to a higher density of voids. Irace and Sarro [276] used a resistor

heating and thermocouple-based technique to measure κ_r of a 800 nm thick, low stress LPCVD-grown SiN_x membrane to be $1.55 \text{ W m}^{-1} \text{ K}^{-1}$, the lowest value of κ_r yet reported. However, Zink and Hellman [268] later used a membrane-based microcalorimeter technique to measure κ_r of a LPCVD grown 200 nm thick low-stress amorphous SiN_x membrane to be $\sim 3 \text{ W m}^{-1} \text{ K}^{-1}$ at room temperature, in agreement with the measurement by Mastrangelo *et al.* despite an order of magnitude reduction in thickness. Stojoanovic *et al.* [278] used a resistive heater and resistance-based temperature detector to determine κ_r of a plasma-enhanced chemical vapor deposition (PECVD)-grown, 180 nm thick SiN_x membrane to be $\sim 2 \text{ W m}^{-1} \text{ K}^{-1}$. Shortly after, Jain and Goodson [269] used the 3ω method to determine κ_r for a LPCVD-grown, freestanding $1.5 \mu\text{m}$ thick SiN_x film to be $\sim 5 \text{ W m}^{-1} \text{ K}^{-1}$. Around the same time, Lee *et al.* [274] used a similar in-plane 3ω method to measure κ_r for a 550 nm thick, LPCVD-grown SiN_x film to be $5.4 \text{ W m}^{-1} \text{ K}^{-1}$, in agreement with the $3\times$ thicker film measured by Jain and Goodson. Queen and Hellman used a membrane-based nanocalorimeter approach find that κ_r of 50 and 200 nm thick suspended $\text{SiN}_{1.15}$ membranes were ~ 2.5 and $\sim 4.5 \text{ W m}^{-1} \text{ K}^{-1}$, respectively; the reduced value of the former was attributed to boundary scattering, possibly evidence for strong propagon contribution to κ . Alam *et al.* [284] used a MEMS-based experiment to measure the strain dependent κ_r of a 50 nm thick, LPCVD grown, stoichiometric Si_3N_4 suspended film; the unstrained κ_r was $2.7 \text{ W m}^{-1} \text{ K}^{-1}$ but reduced to $0.34 \text{ W m}^{-1} \text{ K}^{-1}$ when tensile strain was increased to 2.4%. In contrast, Ftouni *et al.* [271] used the reported stress-independent κ_r of 50 and 100 nm thick membranes to be $\sim 2.5 - 3 \text{ W m}^{-1} \text{ K}^{-1}$ for the four samples tested, with modest thickness dependence in thermal conductivity. Sikora *et al.* [272] used the 3ω -Völklein method to measure κ_r of a LPCVD-grown, low stress a- SiN_x , 100 nm thick membrane to be $10 \text{ W m}^{-1} \text{ K}^{-1}$, in agreement with the seemingly outlier values determined by Zhang and Grigoropoulos. Bodenschatz *et al.* [275] measured κ_r of a 100 nm thick SiN_x membrane to be $3 \text{ W m}^{-1} \text{ K}^{-1}$. Finally, Sultan *et al.* [234] used a MEMS-based micromachined suspended platform structure to measure κ_r for 500 nm thick, LPCVD-grown SiN_x microbridges to be ~ 2.5 to $3.2 \text{ W m}^{-1} \text{ K}^{-1}$ at room temperature, a wider range but still in agreement with previous measurements from the same group [285]. Taken as a whole, there is a wide variation in reported κ_r ranging from 1.2 to $13 \text{ W m}^{-1} \text{ K}^{-1}$ and no clear evidence for film thickness systematically

affecting κ_r .

Cross-plane thermal conductivity measurements are more limited. Lee and Cahill [248] first used the 3ω technique to measure the thickness dependence of κ_z in PECVD grown $\text{Si}_{1.0}\text{N}_{1.1}$ having thicknesses from 20 nm to 300 nm to reveal an increase in κ_z from ~ 0.5 to $\sim 0.8 \text{ W m}^{-1} \text{ K}^{-1}$ over this thickness range; however, they ascribe this trend to interfacial thermal resistance. On the other hand, a 180 nm sample grown with atmospheric pressure CVD had a thermal conductivity of $\sim 1.5 \text{ W m}^{-1} \text{ K}^{-1}$, revealing that differences in deposition process can have much larger influences on thermal conductivity than film size. Govorkov *et al.* [281] used a differential photoacoustic method to measure κ of sputter-deposited Si_3N_4 to be $1.2 \text{ W m}^{-1} \text{ K}^{-1}$ for 100 nm, 210 nm, and 420 nm films. Bai *et al.* [277] used transient thermoreflectance to measure κ_z of LPCVD-grown Si_3N_4 films ranging in thickness from 37 to 200 nm; they found an increasing κ_z with thickness, increasing from 1.24 to $2.09 \text{ W m}^{-1} \text{ K}^{-1}$. Coquil *et al.* [279] used the 3ω method to determine κ_z for a 500 nm thick, PECVD-grown SiN_x film to be $1.2 \pm 0.4 \text{ W m}^{-1} \text{ K}^{-1}$. Hopkins *et al.* [97] used TDTR to measure κ_z to be 3.1 and $3.5 \text{ W m}^{-1} \text{ K}^{-1}$ for a 46 nm and 232 nm thick sample, respectively. Finally, Bogner *et al.* [280] used a differential 3ω method to determine that κ_z of Si_3N_4 increased from 0.8 to $1.7 \text{ W m}^{-1} \text{ K}^{-1}$ when film thickness increased from 298 to 1001 nm. For κ_z , the individual studies revealing a thickness-dependence in κ_z makes a stronger case for significant propagon thermal transport. However, like the case for κ_r , when taken as a whole there is no obvious trend indicating this is the case, particularly when compared with the evidence provided for amorphous Si [22]. Furthermore, in addition to differences in deposition conditions, it is important also to note that stoichiometries of the SiN_x in Fig. 7.4 varied significantly; reported nitrogen content varied from 33 to 57 atomic percentage.

7.2.2 Experimental Details

The samples measured in this study include seven sets of a-SiN:H samples having varying stoichiometries, each set having six samples varying in thickness from nominally 50 nm up to $2 \mu\text{m}$, two sets of a-Si:H samples varying in thickness from nominally 50 nm up to $2 \mu\text{m}$, and two sets of stoichiometric Si_3N_4 films. The Si_3N_4 films include four samples grown via LPCVD and having

film thicknesses ranging from nominally 50 nm to 500 nm and an additional sample grown via high-temperature CVD (HTCVD); all were grown on (100) Si substrates. The a-SiN:H samples were grown on (100) Si substrates via PECVD, while a-Si:H samples were grown via PECVD on (100) Si with an intermediate 49 nm a-SiO₂ layer between the film and substrate; this a-SiO₂ layer is necessary as a-Si:H alone does not adhere to the Si substrate. To systematically control the ratio of N to Si within the a-SiN:H samples, seven sets of samples were grown, each using a constant SiH₄ flow rate of 600 sccm but having a NH₃ flow rate ranging from 1500 sccm to 18000 sccm. The deposition temperature was 400 °C. The set compositions and densities were characterized using a combined nuclear reaction analysis and Rutherford backscattering (NRA-RBS) measurement performed at the University of Albany Dynamitron Accelerator Laboratory, while fourier-transform infrared spectroscopy (FTIR) was used as an auxiliary technique to compliment composition characterization and quantify bond states. Film thicknesses for all a-SiN_x:H and a-Si:H samples were characterized by ellipsometry using a combination of both transparent and absorbing models.

Thermal conductivities were measured using TDTR after depositing an 80 nm Al film onto the samples to serve as a transducer of optical energy to thermal energy. Pump and probe diameters were 36 μm and 17 μm, respectively, and the pump modulation frequency was 8.4 MHz; these two conditions ensure measurement sensitivity is limited to κ_z rather than κ_r . In order to avoid estimation of heat capacity, which could potentially vary based on density and stoichiometry, a combined TDTR and FDTR method was used, as discussed in Chapter 5, to simultaneously measure the thermal conductivity and volumetric heat capacity of ~200 nm thin-film samples for each set of a-SiN:H samples. For the set of films having ~200 nm thicknesses, we use multiple modulation frequencies to decouple thermal conductivity from volumetric heat capacity, thereby measuring of both quantities [101, 150, 164, 286]. In this case, the modulation frequencies used were 8.4 MHz, 4.8 MHz, and 1.3 MHz. Using this approach, the heat capacity is determined to range from ~1.8 to 2 MJ m⁻³ K⁻¹ for all a-SiN_x:H samples, in agreement with Chen *et al.*'s measurement of a-SiN_x:H (19.3 at.% H). As a further check, this procedure was performed on all LPCVD-grown Si₃N₄ samples; the measured heat capacities fell within 2.0 ± 0.2 MJ m⁻³ K⁻¹, which equates to 0.71 ± 0.07 J g⁻¹ K⁻¹, in agreement with prior studies on a-SiN_x.[266, 270, 271, 284]

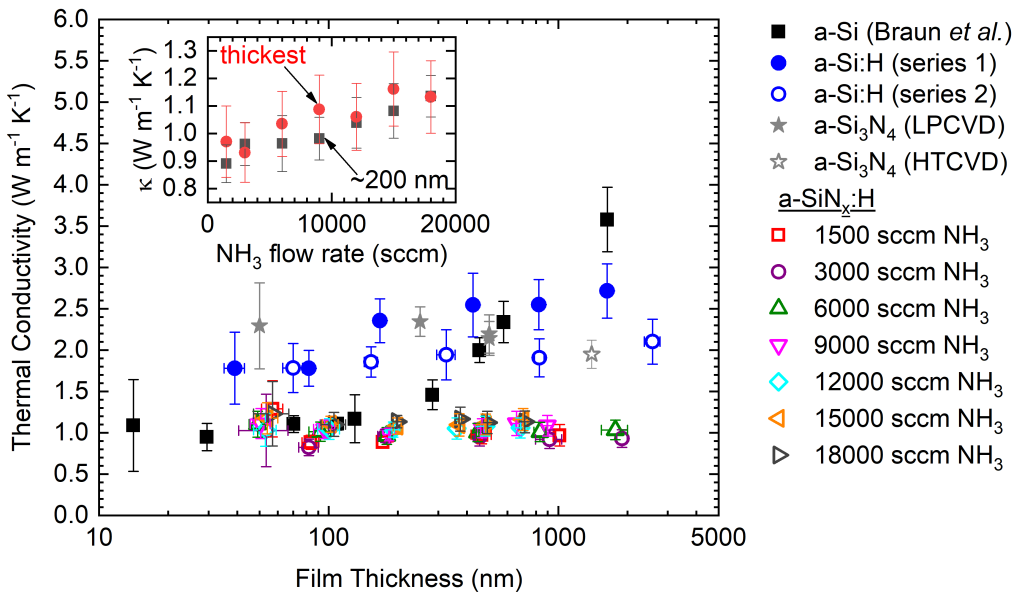


Figure 7.5: Measured thermal conductivity (κ) vs. film thickness for all samples under study: two sets of a-Si:H samples, seven sets of a-SiN:H samples grown with varying NH_3 flow rates (1500 sccm, 3000 sccm, 6000 sccm, 9000 sccm, 12000 sccm, 15000 sccm, and 18000 sccm), and CVD-grown Si_3N_4 samples. For comparison, also included are the results for a-Si obtained in the previous section. Inset shows thermal conductivity vs. NH_3 flow rate for the ~ 200 nm sample and thickest (~ 1 to $2 \mu\text{m}$) sample of each set.

7.2.3 Results and Discussion

Figure 7.5 shows the thermal conductivity vs. film thickness for all measured samples; included for reference is the measured thermal conductivity of a-Si determined in the previous section. Beginning with the stoichiometric a- Si_3N_4 samples, the measured κ for a 50 nm, 250 nm, and two 500 nm films grown via LPCVD were all approximately equivalent at $\sim 2.1 - 2.3 \text{ W m}^{-1} \text{ K}^{-1}$ with no clear thickness dependence. However, the Si_3N_4 sample grown with HTCVD was measured to have a κ of $1.95 \text{ W m}^{-1} \text{ K}^{-1}$. Next, for the a-SiN:H samples we observe that all sets possess a thickness-independent thermal conductivity of $\sim 1 \text{ W m}^{-1} \text{ K}^{-1}$. There is a minor dependence on thermal conductivity with NH_3 flow rate, showing that samples fabricated with higher NH_3 flow rates generally possess higher thermal conductivities by as much as 25%. This is shown in the inset to Fig. 7.5, where the thermal conductivity relation with NH_3 flow rate is plotted for the 200 nm and thickest sample (nominally 1 to 2 μm) for each set. No matter the thickness, a general

increasing relation between κ and increasing NH_3 flow rate is observed. Nevertheless, for each individual series there is no observable increase in κ with increasing film thickness. This finding is in contrast to the a-Si:H samples, which show an increasing κ with increasing film thickness. The size effects observed for a-Si:H are less pronounced than the a-Si samples, suggesting that the addition of hydrogen is restricting the propagon thermal transport to some extent. This idea is in conceptual agreement with the findings of Liu *et al.* [132], who note that for an 80 μm thick, a-Si:H sample having 1 at.% H, the thermal conductivity measured with TDTR is modulation-frequency dependent and at low frequencies agrees with 3ω measurements of $\kappa = 4.5 \text{ W m}^{-1} \text{ K}^{-1}$ at room temperature; their TDTR results indicate that propagons having mean free paths between 162 and 612 nm contribute $\sim 40\%$ of κ [132]. On the other hand, the thinnest a-Si:H films measured in this study fall within the expected diffuson-dominated thickness regime established for a-Si. Interestingly, these samples possess a higher thermal conductivity than the a-Si, suggesting hydrogenation is enhancing the diffuson contribution to κ in a-Si:H. Note that this is common to both sample sets, despite deviation in κ at larger film thicknesses between the sets. The a-Si:H results indicate that, while hydrogen can affect the ability of propagons to contribute to thermal conductivity, it does not eliminate them completely. Therefore, we cannot attribute the lack of size effects observed in the case of a-SiN:H to hydrogen alone.

In order to further understand the role of hydrogen on the thermal conductivity of a-Si_x:H, we thermally annealed the samples to remove hydrogen. Three sets of a-Si_x:H were chosen to anneal: the 1500 sccm NH_3 series, the 9000 sccm NH_3 series, and the 18000 sccm NH_3 series, representing the low, median, and high NH_3 flow rate conditions used in deposition. Samples were annealed in an argon-filled tube furnace for 4 hours at four different annealing temperatures: 650 °C, 775 °C, 900 °C, and 1000 °C. The samples were then characterized for composition via NRA-RBS and FTIR. Additionally, for the nominally 200 nm thick samples in each NH_3 flow rate series, FTIR and ellipsometry via IR-VASE were used to determine the film thickness. Finally, TDTR was used to measure the thermal conductivity of each sample. Table 7.1 shows the resulting compositions, thicknesses, and thermal conductivities for the nominally 200 nm thick samples of each series as deposited and at each annealing temperature. Note that upon annealing, the

Table 7.1: Properties of annealed a-SiN_x:H samples. RBS was used to measure at. % N, at. % Si, at. % H, and coordination number, $\langle r \rangle$. Thickness (d) was measured in two ways, FTIR and ellipsometry via IR-VASE. Thermal conductivity was measured via TDTR.

Anneal Temperature (°C)	% N	% Si	% H	$\langle r \rangle$	d (nm), FTIR	d (nm), IR-VASE	κ (W m ⁻¹ K ⁻¹)
1500 sccm NH₃ series							
as deposited	28.5	51.4	20.1	3.11	194	190	0.89 ± 0.09
650	30.2	67.6	2.2	3.63	171	146	1.46 ± 0.16
775	33.2	66.6	0.2	3.66	161	-	1.88 ± 0.22
900	32.7	67.1	0.2	3.67	158	-	1.90 ± 0.22
1000	34.0	66.0	0.0	3.66	147	138	2.63 ± 0.39
9000 sccm NH₃ series							
as deposited	37.7	36.4	26.0	2.84	171	175	0.98 ± 0.08
650	44.4	45.8	9.8	3.26	168	171	1.41 ± 0.12
775	49.5	44.3	6.2	3.32	144	-	1.41 ± 0.15
900	50.4	48.4	1.2	3.46	132	-	1.58 ± 0.18
1000	48.8	51.2	0.0	3.51	131	139	2.25 ± 0.29
18000 sccm NH₃ series							
as deposited	43.4	30.8	25.8	2.79	176	191	1.14 ± 0.08
650	52.3	38.2	9.6	3.19	157	181	1.42 ± 0.12
775	50.2	42.1	7.7	3.27	142	-	1.50 ± 0.14
900	54.8	42.5	2.7	3.37	137	-	1.88 ± 0.19
1000	55.0	45.0	0.0	3.45	143	168	2.13 ± 0.24

films shrink significantly in size to compensate for the loss of hydrogen. This observation is in agreement with that of previous studies on annealed a-SiN_x:H films [287, 288]. Figure 7.6 shows the resulting thermal conductivity as a function of annealing temperature for these samples to reveal a systematic increase in thermal conductivity with annealing temperature; at the highest annealing temperature of 1000 °C, κ increases by 200 to 250 % from the as-deposited samples. Furthermore, for all annealed samples, the measured thermal conductivities showed no observable thickness dependence.

To understand the relationship between κ and annealing temperature, we turn to the compositional analysis of the post-annealed samples. NRA-RBS reveals that the as-deposited samples possess significant differences in stoichiometry stemming from the deposition with varying NH₃ flow rates. The 1500 sccm NH₃ flow rate case proved to be Si-rich with 51.4 at.% Si and 28.5 at.% N, while the 18000 sccm NH₃ case proved to be N-rich with 30.8 at.% Si and 43.4 at.% N. However, the hydrogen content did not vary as heavily; in fact, the 9000 sccm NH₃ and 18000

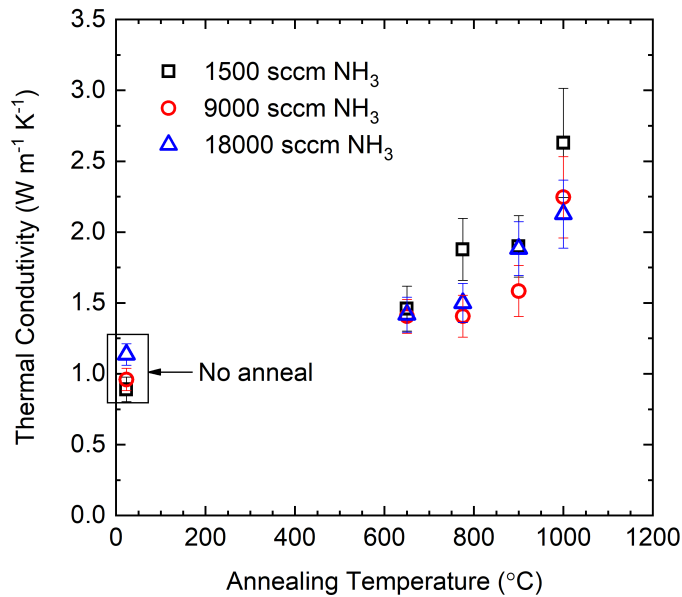


Figure 7.6: Measured thermal conductivity (κ) vs. annealing temperature for a-SiN:H samples for three sample sets: the high and low sccm NH₃ cases (1500 and 18000 sccm, respectively) and one in between (9000 sccm).

sccm NH₃ cases show nearly identical H content of ~ 26 at.%, suggesting a limit to the hydrogen content achievable through this deposition procedure. At the low end, the 1500 sccm NH₃ series has a hydrogen composition of only ~ 20 at.%. Upon annealing, however, the hydrogen content can be further reduced. Beginning with the 1500 sccm NH₃ case, annealing at 650 °C significantly reduces the hydrogen, from 20.1 to just 2.2 at.%. The corresponding change in thermal conductivity is 0.89 to 1.46 W m⁻¹ K⁻¹. While a substantial increase, this is still a relatively low thermal conductivity compared to the next annealed cases; at 775°C and 900°C annealing temperatures, the hydrogen is reduced to just 0.2 at.% and the corresponding thermal conductivities measured are 1.88 and 1.90 W m⁻¹ K⁻¹, respectively. Annealing out the final, seemingly insignificant, 0.2 at.% H at 1000°C proves to have a significant effect on thermal conductivity, increasing it to 2.63. This final composition is a Si-heavy Si_{0.66}N_{0.34} stoichiometry. For the 9000 sccm NH₃ case, annealing at 650 °C, 775 °C, 900 °C, and 1000 °C diminishes the hydrogen percentage from 26.0 to 9.8, 6.2, 1.2, and 0 at.%, increasing the thermal conductivity from 0.98 to 1.41, 1.41, 1.58, and 2.25 W m⁻¹ K⁻¹, respectively. The final composition in this case is a nearly equal ratio of Si and

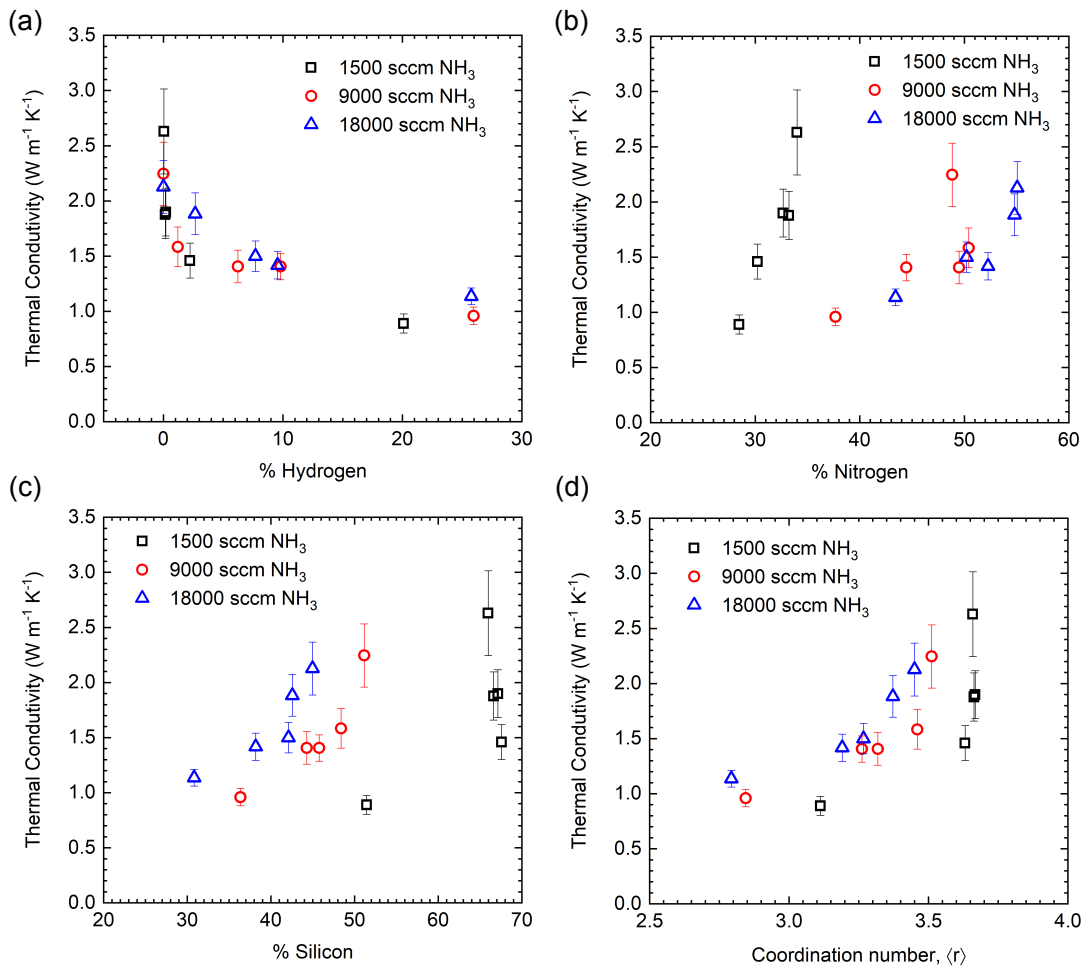


Figure 7.7: Measured thermal conductivity (κ) vs. (a) atomic % Hydrogen, (b) atomic % Nitrogen, (c) atomic % Silicon, and (d) coordination number for the same samples shown in Fig. 7.6.

$\text{N}, \text{Si}_{0.51}\text{N}_{0.49}$. Finally, for the 18000 sccm NH_3 case, annealing at 650 °C, 775 °C, 900 °C, and 1000 °C diminishes the hydrogen percentage from 25.8 to 9.6, 7.7, 2.7, and 0 at.%, increasing the thermal conductivity from 1.14 to 1.42, 1.50, 1.88, and 2.13 $\text{W m}^{-1} \text{K}^{-1}$, respectively. The final composition in this case is a close to stoichiometric ratio of Si and N, $\text{Si}_{0.45}\text{N}_{0.55}$. Stoichiometry proves to have a significant impact on the thermal conductivity of SiN_x , increasing with Si concentration.

Recasting the thermal conductivity as a function of composition, Fig. 7.7 shows κ vs. (a) at.% H, (b) at.% N, (c) at.% Si, and (d) coordination number, $\langle r \rangle$. Hydrogen content proves to be a good predictor of the thermal conductivity for all samples regardless of Si and N stoichiometry,

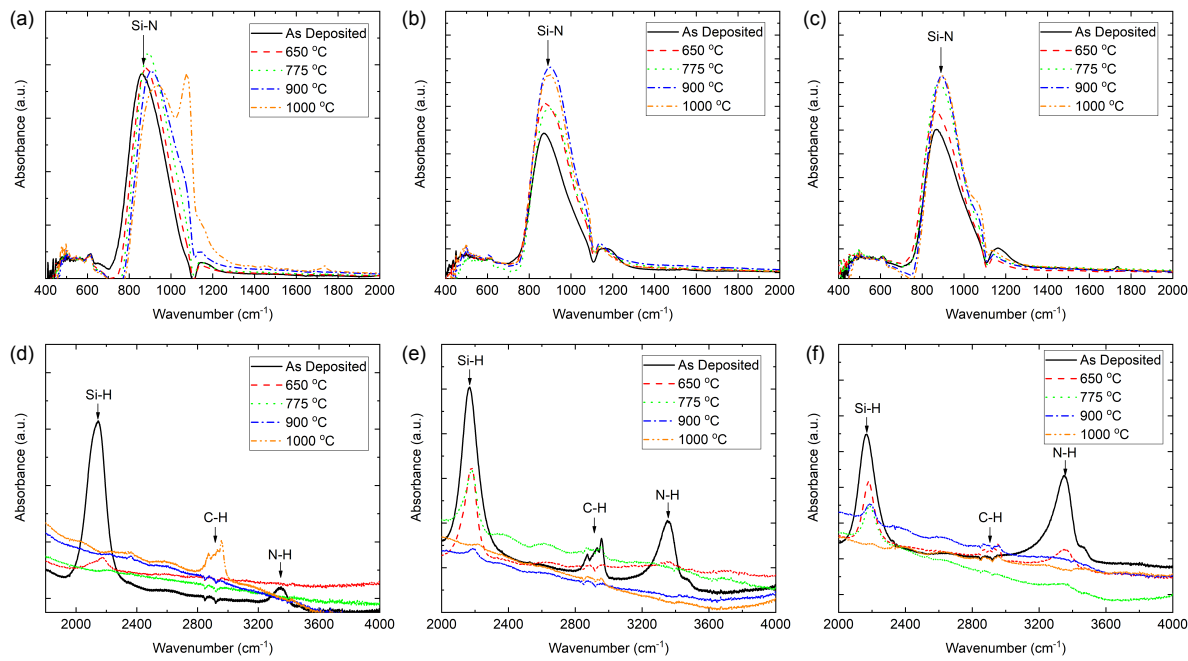


Figure 7.8: FTIR spectrum for a-SiN:H samples annealed from 650 to 1000 °C for the (a/d) 1500 sccm NH₃ series, (b/e) 9000 sccm NH₃ series, and (c/f) 18000 sccm NH₃ series.

showing a decreasing trend with increasing hydrogen content. As a function of nitrogen composition, κ generally increases with increasing at.% N. Similarly, as a function of silicon composition, κ increases monotonically with increasing at.% Si for the 9000 sccm NH₃ and 18000 sccm NH₃ cases. On the other hand, the 1500 sccm NH₃ case does not show this trend. Annealing beyond 650 °C in this case results in an increase in at.% N while the at.% Si remains nearly constant. Finally, for each set, within uncertainty κ increases monotonically with increasing coordination number, in agreement with what has been observed for a-Si[O/C]:H [265] and amorphous fluorocarbons [289]. Conceptually, the increase in coordination number is indicative of increasing the covalently bonded Si-N network, which is directly indicative of elastic properties and sound speeds of the system [289]. Beyond the direct contribution of improved elastic properties to thermal conductivity, the aforementioned a-Si[O/C]:H samples showed that increases in coordination number lead to higher vibrational mean free paths through a longer network for heat to traverse [265].

While RBS gives a direct measurement of the composition of each sample, FTIR is used to further quantify the hydrogen reduction to show the specific bonds being dissociated during an-

nealing. Figure 7.8 shows the FTIR spectra obtained for samples listed in Table 7.1 over the range of (a)-(c) 400 to 2000 cm⁻¹ and (d)-(f) 2000 to 4000 cm⁻¹, separated as such to rescale the magnitude to emphasize the relevant peaks corresponding to particular bonds. Specifically, Fig. 7.8(a) and (d) show the absorption spectra for the 1500 sccm NH₃ sample as-deposited and annealed at 650 °C, 775 °C, 900 °C, and 1000 °C, Fig. 7.8(b) and (e) show the same information for the 9000 sccm NH₃ case, and Fig. 7.8(b) and (e) show this for the 18000 sccm NH₃ case. Referring first to the 400 to 2000 cm⁻¹ window, a strongly IR-sensitive Si-N stretching mode [290] is observed around 830 - 890 cm⁻¹. Secondary peaks above 1000 cm⁻¹ result from substrate effects, likely due to SiO stretching modes [290] within the underlying Si substrate. Although the peak near 1200 cm⁻¹ has been observed in previous studies of a-SiN:H films [291] and attributed to a bending mode in the Si-NH-Si group [292], the presence of this peak in the 1000 °C annealed cases, where RBS confirms no hydrogen presence, indicates this is not the case. Within the 2000 to 4000 cm⁻¹ window, an SiH stretching mode [290] is observed around 2100 - 2200 cm⁻¹. In particular, absorption near 2150 cm⁻¹ and 2300 cm⁻¹ has been attributed to the stretching modes of Si-H₂ and/or (Si-H₂)_n chains (n ≥ 2), and Si-H₃ [291, 293], so the wide spectra around this peak observed in the as-deposited cases likely stem from a combination of these bonds. An additional NH stretching mode [290] is observed near 3350 cm⁻¹ for all as-deposited samples. Finally, there is also a C-H peak labeled that we attribute to minor surface contamination. Upon annealing to 650 °C, both the Si-H and N-H peaks are significantly reduced in magnitude relative to the Si-N peak, supporting the conclusion obtained from RBS that hydrogen is leaving the film and additional Si-N bonds are being formed to increase coordination number. For all samples, each subsequent anneal leads to a further decrease in Si-H and Ni-H bond peak intensities. The Ni-H bond appears to dissociate more readily than the Si-H bond, as evidenced by the lower annealing temperature necessary to reduce this peak to background noise. This is in agreement with predictions from Yin and Smith [294] based on a free energy model, as well as observation by Chen *et al.* [251] on similar a-SiN:H films. We find that the N-H peak is reduced to the level of background noise at annealing temperature of 650 °C, 775°C, and 900 °C for the 1500 sccm NH₃, 9000 sccm NH₃, and 18000 sccm NH₃ cases, respectively, while the Si-H peak is not reduced to noise level until 775°C for the

1500 sccm NH₃ case and 1000 °C for the other two cases. Overall, the FTIR spectra reveal that hydrogen bonding is, within measurement sensitivity, nonexistent when annealed to 1000 °C for all samples, corroborating RBS conclusions.

No significant size effects were observed on the thermal conductivity of a-SiN:H samples either before or after annealing, in agreement with results for the stoichiometric a-Si₃N₄ samples measured in this study. As mentioned previously, several prior studies present evidence for size-dependent thermal conductivities in a-SiN_x samples. Lee and Cahill [248] used a 3ω measurement to report *effective* thermal conductivities that increase with thickness, but argue against intrinsic size effects in the thermal conductivity of the films by accounting for thermal boundary resistance between both the heater/film and film substrate. Indeed, Lee and Cahill also observed size effects in the effective thermal conductivity of a-SiO₂ thin films, which we showed in the previous section to lack when considering interface resistances. Bogner *et al.* [280] also observed thickness-dependent thermal conductivities for a-Si₃N₄ films measured by differential 3ω, which could be due to the same thermal boundary resistance argument. On the other hand, Bai *et al.* [277] used a transient thermoreflectance to measure a thickness-dependent thermal conductivity of a-Si₃N₄ films and account for the interface resistance between the transducer and sample in their model. The authors suggest that microstructure could be a factor in the observed thickness dependence, noting that the density of their films was relatively low at 2.2 g cm⁻³; for comparison, the LPCVD Si₃N₄ films measured here had a density of 2.8 g cm⁻³.

One potential effect on thermal conductivity to consider is the internal stress of the films, as the thicker films showed cracked regions on the order of hundreds of microns to millimeters after annealing. As-deposited a-SiN:H films have an estimated stress of <0.4 GPa. The coefficient of thermal expansion mismatch between the a-SiN_x:H film and Si substrate is ~2 ppm/°C. Multiplying this by the maximum anneal temperature of 1000 °C and the elastic modulus (~200 GPa) provides an estimated stress increase of 0.4 GPa, resulting in a total estimated stress of ~0.8 GPa. This falls within the range (0.2 - 0.85 GPa) that Ftouni *et al.* [271] showed resulted in a stress-independent thermal conductivity for a-SiN_x membranes. However, Alam *et al.* [284] showed that an applied mechanical strain can significantly reduce the thermal conductivity of a-SiN_x membranes. The

estimated strain in our films, as determined by the internal stress divided by elastic modulus, is at most $\sim 0.4\%$ without accounting for potential strain relaxation upon cracking, which falls in line with that of reported a-SiN_x films fabricated with PECVD. [248, 278] and LPCVD [268, 277]. Alam *et al.*'s results indicate that a strain of this amount could result in a decrease in thermal conductivity by as much as 20%, in contrast to what Ftouni *et al.* described. Nonetheless, the a-Si:H films, having similar levels of internal stresses (as deposited stress is ~ 0.45 GPa), prove that strain will not diminish potential size effects on thermal conductivity. Taken together, the lack of size effects observed for samples in this study suggest the thermal conductivities are diffuson-limited with no significant contribution from propagons.

In summary, in this section we showed that the thermal conductivity of a-SiN:H is highly dependent on stoichiometry and hydrogen composition. It is well known that PECVD growth of a-SiN_x films lead to high hydrogen concentrations [295]. As we determined in this section, no matter the flow rate of NH₃ used in deposition (1500 to 18000 sccm NH₃ was used in this study), the resulting films having hydrogen compositions ranging from 20 to 26 at.% possess a thermal conductivity of ~ 1 W m⁻¹ K⁻¹. However, thermally annealing the films proves to reduce hydrogen content to increase coordination number, resulting in increased thermal conductivities of 2.6 W m⁻¹ K⁻¹ for Si-rich Si_{0.66}N_{0.34} and 2.1 W m⁻¹ K⁻¹ for near-stoichiometric Si_{0.45}N_{0.55}. This points to a clear methodology for manipulating the thermal conductivity within this range based on the use of hydrogenation and thermal annealing.

7.3 Summary

In this chapter, I studied the role of size and composition on the thermal conductivity of amorphous thin films. I first investigated thickness-limited size effects on the thermal conductivity of amorphous silicon thin films ranging from 3 – 1636 nm grown via sputter deposition. While exhibiting a constant value up to ~ 100 nm, the thermal conductivity increases with film thickness thereafter. This trend is in stark contrast with previous thermal conductivity measurements of amorphous systems, which have shown thickness-independent thermal conductivities. The thick-

ness dependence demonstrated is ascribed to boundary scattering of long wavelength vibrations and an interplay between the energy transfer associated with propagating modes (propagons) and non-propagating modes (diffusons). A crossover from propagon to diffuson modes is deduced to occur at a frequency of ~ 1.8 THz via simple analytical arguments. These results provide empirical evidence of size effects on the thermal conductivity of amorphous silicon and systematic experimental insight into the nature of vibrational thermal transport in amorphous solids. Next, I investigated the role of stoichiometry and hydrogen concentration on the thermal conductivity of amorphous hydrogenated silicon nitride thin films to show that in heavily hydrogenated samples (>20 at.% H), the thermal conductivity is limited to ~ 1 W m $^{-1}$ K $^{-1}$. Thermally annealing the samples induces chemical dissociation of hydrogen bonds to effuse hydrogen out of the sample, in turn increasing the coordination number and thermal conductivity. Upon full annealing to 0 at.% H, the thermal conductivity is higher for Si-rich Si $_{0.66}$ N $_{0.34}$ samples at 2.6 W m $^{-1}$ K $^{-1}$, while near-stoichiometric Si $_{0.45}$ N $_{0.55}$ has a size-independent thermal conductivity of 2.1 W m $^{-1}$ K $^{-1}$.

Chapter 8

Summary and Future Projects

The continuing progress in modern technologies has been fueled by device miniaturization and the engineering of material properties through compositional and configurational disorder. Understanding the fundamental behavior of heat carriers and how they are affected in the presence of such disorder is pivotal for the thermal management of a wide array of applications ranging from microelectronics to hypersonic aircraft design. This dissertation presented three studies outlining the effects of configurational and compositional disorder on the thermal conductivity of crystalline and amorphous materials. It was shown that extreme disorder leads to amorphous-like thermal conductivities in crystalline, entropy-stabilized oxides. Bulk high-entropy ceramics – including oxides, carbides, borides, and silicides – proved to have significantly reduced thermal conductivities relative to constituent components that can be further affected by microstructure. In amorphous materials, it was shown that amorphous silicon could possess significant contribution to thermal conductivity from propagating modes typically attributed to crystalline solids. On the other hand, when compositional disorder is introduced as investigated through hydrogenated amorphous silicon nitride, the thermal conductivity is heavily dependent on hydrogen content and the coordination number; thermal annealing provides a means to systematically reduce hydrogen content to increase thermal conductivity.

8.1 Summary

In Chapter 2, the core concepts and mathematical equations governing heat conduction were reviewed. The macroscale picture of heat diffusion based on Fourier’s law of heat conduction, to be applied in depth in Chapters 3 and 4 for interpreting experimental data, was first introduced. Thereafter, a simple derivation of a kinetic theory model for a microscale description of thermal conductivity was outlined. Applying this kinetic theory model to crystalline solids, the various phonon scattering mechanisms to be applied in Chapters 5 – 7 were reviewed. Next, a review of thermal transport in amorphous materials was considered and the “minimum limit” to thermal conductivity was derived. Furthermore, a review of the vibrational mode characterization in amorphous materials was used to introduce the concept of locons, diffusons, and propagons in order to motivate the study of amorphous solids presented in Chapter 7.

Chapter 3 provided a detailed overview of time- and frequency-domain thermoreflectance (TDTR and FDTR). The experimental details of the combined TDTR/FDTR apparatus used throughout this work was presented. Thereafter, the core concepts of TDTR and FDTR were outlined, followed by a detailed derivation of the physical temperature rises and lock-in amplifier responses that occur during experiment. An emphasis was placed on the thermal penetration depth and steady-state temperature rise that occurs during realistic experimental conditions. The generalization of the derivations provided ensures that solutions can be obtained for arbitrary pump and probe temporal and spatial functions.

In Chapter 4, a new experiment, steady-state thermoreflectance (SSTR), was proposed and implemented. The experiment is based on applying long exposure to a constant laser heat flux so that a steady-state temperature rise is obtained; a probe laser is used to measure the resulting temperature rise in the material based on the resulting change in reflectivity. The experimental details of the apparatus were provided and all mathematical details were derived in Appendix A. Using SSTR, samples having thermal conductivities ranging from 1 to $>2000 \text{ W m}^{-1}\text{K}^{-1}$ were measured and shown to have excellent agreement with literature values and measurements by TDTR. This technique was applied to the bulk materials studied in Chapter 6.

Chapter 5 introduced the first study of how extreme configurational disorder affects phonon thermal conductivity of entropy-stabilized oxides (ESOs). Manipulating a crystalline material's configurational entropy through the introduction of unique atomic species can produce novel materials with desirable mechanical and electrical properties. From a thermal transport perspective, however, large differences between elemental properties such as mass and interatomic force can reduce the rate at which phonons carry heat and thus reduce the thermal conductivity. Measuring the structural, mechanical, and thermal properties of single-crystal ESOs, Chapter 5 revealed that local ionic charge disorder can effectively reduce thermal conductivity without compromising mechanical stiffness. These materials demonstrate similar thermal conductivities to their amorphous counterparts, in agreement with the theoretical minimum limit, resulting in this class of material possessing the highest ratio of elastic modulus to thermal conductivity of any isotropic crystal.

In Chapter 6, the thermal conductivities of four classes of novel bulk high-entropy ceramics – high-entropy fluorite oxides, borides, carbides, and silicides – were reported to build on the understanding of how configurational disorder effects thermal transport. Specifically, the role of microstructure, including grain orientation and phase segregation, on the thermal conductivity was quantified using TDTR-based thermal conductivity imaging. It was found that 4- and 5-cation fluorite oxides possessed low thermal conductivities on the order the ESOs from Chapter 5, 1 to 2 W m⁻¹ K⁻¹. High-entropy carbides exhibited reduced thermal conductivities relative to their binary constituent carbides, but maintained relatively high thermal conductivities at \sim 10 W m⁻¹ K⁻¹ that showed only a minor dependence on microstructure. The high-entropy boride studied was able to maintain an even higher thermal conductivity of \sim 25 W m⁻¹ K⁻¹, although still significantly reduced relative to constituent diborides. There was found to be large variation in local thermal conductivity attributed primarily to residual oxide phases. Finally the high-entropy silicide studied showed a moderate thermal conductivity of \sim 7 W m⁻¹ K⁻¹, again reduced relative to constituent disilicides. Taken together, this chapter further emphasized the effect of configurational disorder on reducing the thermal conductivity of high-entropy ceramics, while revealing that microstructure can further reduce the local thermal conductivity in these systems.

In Chapter 7, the role of size and composition on the thermal conductivity of amorphous ma-

terials was investigated. Amorphous silicon thin films ranging from 3 – 1636 nm were determined to have a constant thermal conductivity up to ~ 100 nm and an increasing the thermal conductivity with film thickness thereafter. This trend contrasts with previous thermal conductivity measurements of amorphous systems, which have shown thickness-independent thermal conductivities. The thickness dependence we demonstrate is ascribed to boundary scattering of long wavelength vibrations and an interplay between the energy transfer associated with propagating modes (propagons) and non-propagating modes (diffusons). A crossover from propagon to diffuson modes is deduced to occur at a frequency of ~ 1.8 THz via simple analytical arguments. Next, the role of stoichiometry and hydrogen concentration on the thermal conductivity of amorphous hydrogenated silicon nitride thin films was investigated. It was found that in heavily hydrogenated samples ($> 20\%$), the thermal conductivity is limited to $\sim 1 \text{ W m}^{-1} \text{ K}^{-1}$ and size-independent. Thermally annealing the samples thermal conductivity up to $2.6 \text{ W m}^{-1} \text{ K}^{-1}$. This increase is attributed to an increase in coordination number resulting from chemical dissociation of hydrogen bonds to effuse hydrogen out of the sample.

8.2 Opportunities for Future Investigation

- **Thermal diffusivity measurements using SSTR** - In Chapter 4, I discussed the SSTR technique as a new tool to measure thermal conductivity of bulk materials. The technique relies on modulating the pump at a low enough frequency to induce a long-lived steady-state temperature rise. In this steady-state regime, only thermal conductivity dictates the temperature rise of the material; thus, we ignore the transient temperature rise that comes before the steady-state is reached. However, there is useful information contained in this transient regime – namely, the thermal diffusivity. Analogous to the laser flash method, one can use this transient rise time to determine a material’s thermal diffusivity. The periodic waveform analyzer makes this transient regime possible to capture as a function of time. Furthermore, to ensure this rise time is slow enough to capture for highly diffusive materials, one can increase the pump diameter and lower the frequency, both of which increase the time to reach

steady-state.

- **Exploring the composition space of a-SiO_x** - In Chapter 7, I discussed how size and composition can both influence thermal conductivity of a-Si and a-SiN_x:H to reveal the influence of propagons on thermal transport. In this study, we could not vary the nitrogen content enough to explore the full bounds of composition space between a-Si and stoichiometric a-Si₃N₄. Perhaps a better candidate for this study is a-SiO_x, where x varies from 0 to 2. At room temperature, a-Si shows an unambiguous increase in thermal conductivity with film thickness, whereas a-SiO₂ shows unambiguous constant thermal conductivity with thickness. The obvious question then is, at what concentration of O does this lack of size effects occur? Answering this question could advance our understanding of propagon thermal transport.
- **Size effects on the thermal conductivity of amorphous multilayers** - As an additional follow on to Chapter 7, it would be very interesting to understand of how interfaces affect the thermal conductivity of multilayers of amorphous materials that support propagons. For example, if a-Si is grown in layers with a-SiO₂, do propagons scatter with the a-SiO₂ so that no size effects in thermal conductivity are observed? Is there a critical thickness of SiO₂ necessary for this to occur? Can amorphous multilayers show evidence for coherent (wave-like) to incoherent propagon (particle-like) regime akin to what has been shown in crystalline superlattices? Answering these questions would further the current understanding of vibrational modes and thermal transport in amorphous materials.

Appendix A

Transient Temperature Rise in SSTR

In Chapter 3 we derived an expression to describe the surface temperature induced by a heating event with an arbitrary time-dependence. The temperature of the top surface as a function of radius and time is given by Eq. 3.36. The same procedure is used to determine the solution to the transient response, but to do so we must modify the laser heat flux function to start at time $t = 0$. Therefore, we apply the Heaviside step function, $u(t)$, so that the source term for a CW source becomes

$$G(t) = A_0 u(t), \quad (\text{A.1})$$

where A_0 is the absorbed power. The Fourier transform is

$$\tilde{G}(\omega) = A_0 \pi \left(\frac{1}{i\pi\omega} + \delta(\omega) \right). \quad (\text{A.2})$$

Substituting Eq. (A.2) into Eq. (3.36), the surface temperature becomes

$$\begin{aligned} T_{\text{top}}(r, t) &= \frac{A_0}{2} \int_{-\infty}^{\infty} \tilde{L}(r, \omega) \left(\frac{1}{i\pi\omega} + \delta(\omega) \right) e^{i\omega t} d\omega \\ &= \frac{A_0}{2} \int_{-\infty}^{\infty} \frac{\tilde{L}(r, \omega) e^{i\omega t}}{i\pi\omega} d\omega + \frac{A_0}{2} \int_{-\infty}^{\infty} \tilde{L}(r, \omega) \delta(\omega) e^{i\omega t} d\omega \\ &= \frac{A_0}{2} \int_{-\infty}^{\infty} \frac{\tilde{L}(r, \omega) e^{i\omega t}}{i\pi\omega} d\omega + \frac{A_0}{2} \tilde{L}(r, 0). \end{aligned} \quad (\text{A.3})$$

Integration is done numerically. In order to simplify the integration procedure, we expand $\tilde{L}(r, \omega)$ so that the first term in Eq. (A.3) becomes

$$\begin{aligned} \frac{A_0}{2} \int_{-\infty}^{\infty} \frac{\tilde{L}(r, \omega) e^{i\omega t}}{i\pi\omega} d\omega &= \frac{-A_0}{4\pi} \int_{-\infty}^{\infty} \left(\int_0^{\infty} \left(\frac{\tilde{D}(k, \omega)}{\tilde{C}(k, \omega)} \right) \exp\left(-\frac{k^2 r_0^2}{8}\right) J_0(kr) k dk \right) \frac{e^{i\omega t}}{i\pi\omega} d\omega \\ &= \frac{-A_0}{4\pi} \int_0^{\infty} \left(\int_{-\infty}^{\infty} \left(\frac{\tilde{D}(k, \omega)}{\tilde{C}(k, \omega)} \right) \frac{e^{i\omega t}}{i\pi\omega} d\omega \right) \exp\left(-\frac{k^2 r_0^2}{8}\right) J_0(kr) k dk \\ &= \frac{A_0}{4\pi} \int_0^{\infty} \underline{P}_t(k, t) \exp\left(-\frac{k^2 r_0^2}{8}\right) J_0(kr) k dk, \end{aligned} \quad (\text{A.4})$$

where \underline{P}_t is a time-dependent function defined by

$$\underline{P}_t(k, t) = - \int_{-\infty}^{\infty} \left(\frac{\tilde{D}(k, \omega)}{\tilde{C}(k, \omega)} \right) \frac{e^{i\omega t}}{i\pi\omega} d\omega. \quad (\text{A.5})$$

The final term in Eq. (A.3) can be shown to take a similar form so that

$$\frac{A_0}{2} \tilde{L}(r, 0) = \frac{A_0}{4\pi} \int_0^{\infty} \underline{P}_0(k) \exp\left(-\frac{k^2 r_0^2}{8}\right) J_0(kr) k dk \quad (\text{A.6})$$

where $\underline{P}_0(k)$ is a time-independent function defined by

$$\underline{P}_0(k) = - \int_{-\infty}^{\infty} \left(\frac{\tilde{D}(k, \omega)}{\tilde{C}(k, \omega)} \right) e^{i\omega t} \delta(\omega) d\omega = - \frac{\tilde{D}(k, 0)}{\tilde{C}(k, 0)} \quad (\text{A.7})$$

The probe-averaged change in reflectance is the integration over the gaussian intensity in real space. This probe averaged temperature rise, T_{PA} is given by

$$T_{PA}(t) = \frac{4}{r_1^2} \int_0^\infty T_{top}(r, t) \exp\left(\frac{-2r^2}{r_1^2}\right) r dr. \quad (A.8)$$

This expression can then be simplified to

$$\begin{aligned} T_{PA}(t) &= \frac{4}{r_1^2} \int_0^\infty \left[\frac{A_0}{4\pi} \int_0^\infty (P_t(k, t) + P_0(k, t)) \exp\left(-\frac{k^2 r_0^2}{8}\right) J_0(kr) k dk \right] \exp\left(\frac{-2r^2}{r_1^2}\right) r dr \\ &= \frac{A_0}{2} \int_0^\infty (P_t(k, t) + P_0(k, t)) \exp\left(-\frac{k^2 r_0^2}{8}\right) \left[\frac{2}{\pi r_1^2} \int_0^\infty J_0(kr) \exp\left(\frac{-2r^2}{r_1^2}\right) r dr \right] k dk \\ &= \frac{A_0}{2} \int_0^\infty (P_t(k, t) + P_0(k, t)) \exp\left(-\frac{k^2 r_0^2}{8}\right) \left[\frac{1}{2\pi} \exp\left(-\frac{k^2 r_1^2}{8}\right) \right] k dk \\ &= \frac{A_0}{4\pi} \int_0^\infty (P_t(k, t) + P_0(k, t)) \exp\left(-\frac{k^2(r_0^2 + r_1^2)}{8}\right) k dk. \end{aligned} \quad (A.9)$$

With P_0 and P_t defined above, it is straightforward to numerically integrate this expression to obtain the transient temperature rise.

Appendix B

Published Work

As part of my dissertation research, I have published six first-author journal publications [22, 120, 167, 265, 286, 296] and contributed to nineteen other journal publications [93, 113, 114, 155, 194, 215, 297–307]. Below, I list all works and bold the works that have been discussed in this dissertation, either through modeling and experimental advances or through physical insight into how disorder effects thermal transport. In reverse-chronological order, these include

25. **J. Gild, J. Braun, K. Kaufmann, E. Marin, T. Harrington, P. Hopkins, K. Vecchio, and J. Luo,** “A high-entropy silicide:(mo0.2nb0.2ta0.2ti0.2w0.2) si2,” *arXiv preprint arXiv:1902.01033*, 2019
24. **J. L. Braun, D. H. Olson, J. T. Gaskins, and P. E. Hopkins,** “A steady-state thermoreflectance method to measure thermal conductivity,” *Review of Scientific Instruments*, vol. 90, no. 2, p. 024905, 2019
23. M. Lim, Z. Rak, J. L. Braun, C. M. Rost, G. N. Kotsonis, P. E. Hopkins, J.-P. Maria, and D. W. Brenner, “Influence of mass and charge disorder on the phonon thermal conductivity of entropy stabilized oxides determined by molecular dynamics simulations,” *Journal of Applied Physics*, vol. 125, no. 5, p. 055105, 2019
22. D. H. Olson, C. M. Rost, J. T. Gaskins, C. J. Szwedkowski, J. L. Braun, and P. E. Hopkins, “Size effects on the cross-plane thermal conductivity of transparent conducting indium tin oxide and fluorine tin oxide thin films,” *IEEE Transactions on Components, Packaging and Manufacturing Technology*, vol. 9, pp. 51–57, Jan 2019
21. A. Giri, J. L. Braun, D. M. Shima, S. Addamane, G. Balakrishnan, and P. E. Hopkins, “Experimental evidence of suppression of subterahertz phonons and thermal conductivity in gaas/als superlattices due to extrinsic scattering processes,” *The Journal of Physical Chemistry C*, vol. 122, no. 51, pp. 29577–29585, 2018
20. **J. L. Braun, C. M. Rost, M. Lim, A. Giri, D. H. Olson, G. N. Kotsonis, G. Stan, D. W. Brenner, J.-P. Maria, and P. E. Hopkins,** “Charge-induced disorder controls the thermal conductivity of entropy-stabilized oxides,” *Advanced Materials*, vol. 30, no. 51, p. 1805004, 2018

19. E. L. Radue, J. A. Tomko, A. Giri, J. L. Braun, X. Zhou, O. V. Prezhdo, E. L. Runnerstrom, J.-P. Maria, and P. E. Hopkins, “Hot electron thermorelectance coefficient of gold during electron–phonon nonequilibrium,” *ACS Photonics*, vol. 5, no. 12, pp. 4880–4887, 2018
18. A. Giri, S. W. King, W. A. Lanford, A. B. Mei, D. Merrill, L. Li, R. Oviedo, J. Richards, D. H. Olson, J. L. Braun, J. T. Gaskins, F. Deangelis, A. Henry, and P. E. Hopkins, “Interfacial defect vibrations enhance thermal transport in amorphous multilayers with ultrahigh thermal boundary conductance,” *Advanced Materials*, vol. 30, no. 44, p. 1804097, 2018
17. S. Alaie, M. G. Baboly, Y.-B. Jiang, S. Rempe, D. H. Anjum, S. Chaieb, B. F. Donovan, A. Giri, C. J. Szwejkowski, J. T. Gaskins, M. M. M. Elahi, D. F. Goettler, J. Braun, P. E. Hopkins, and Z. C. Leseman, “Reduction and increase in thermal conductivity of si irradiated with ga+ via focused ion beam,” *ACS Applied Materials & Interfaces*, vol. 10, no. 43, pp. 37679–37684, 2018. PMID: 30280889
16. J. Gild, M. Samiee, J. L. Braun, T. Harrington, H. Vega, P. E. Hopkins, K. Vecchio, and J. Luo, “High-entropy fluorite oxides,” *Journal of the European Ceramic Society*, vol. 38, no. 10, pp. 3578–3584, 2018
15. **J. L. Braun, C. J. Szwejkowski, A. Giri, and P. E. Hopkins, “On the steady-state temperature rise during laser heating of multilayer thin films in optical pump–probe techniques,” *Journal of Heat Transfer*, vol. 140, pp. 052801–052801–10, 02 2018**
14. J. A. Tomko, D. H. Olson, J. L. Braun, A. P. Kelliher, B. Kaehr, and P. E. Hopkins, “Substrate thermal conductivity controls the ability to manufacture microstructures via laser-induced direct write,” *Applied Physics Letters*, vol. 112, p. 051906, 2018/04/25 2018
13. A. Giri, J. L. Braun, and P. E. Hopkins, “Reduced dependence of thermal conductivity on temperature and pressure of multi-atom component crystalline solid solutions,” *Journal of Applied Physics*, vol. 123, p. 015106, 2018/01/17 2018
12. C. M. Rost, J. Braun, K. Ferri, L. Backman, A. Giri, E. J. Opila, J.-P. Maria, and P. E. Hopkins, “Hafnium nitride films for thermorelectance transducers at high temperatures: Potential based on heating from laser absorption,” *Applied Physics Letters*, vol. 111, p. 151902, 2018/04/25 2017
11. L. Chen, J. L. Braun, B. F. Donovan, P. E. Hopkins, and S. J. Poon, “Ballistic transport of long wavelength phonons and thermal conductivity accumulation in nanograined silicon-germanium alloys,” *Applied Physics Letters*, vol. 111, p. 131902, 2017/09/27 2017
10. A. Giri, J. L. Braun, C. Rost-Barber, and P. E. Hopkins, “On the minimum limit to thermal conductivity of multi-atom component crystalline solid solutions based on impurity mass scattering,” *Scripta Materialia*, vol. 138, pp. 134–138, 09 2017
9. A. Giri, J. L. Braun, J. A. Tomko, and P. E. Hopkins, “Reducing the thermal conductivity of chemically ordered binary alloys below the alloy limit via the alteration of phonon dispersion relations,” *Applied Physics Letters*, vol. 110, p. 233112, 2018/04/25 2017

8. **J. L. Braun and P. E. Hopkins**, “Upper limit to the thermal penetration depth during modulated heating of multilayer thin films with pulsed and continuous wave lasers: A numerical study,” *Journal of Applied Physics*, vol. 121, no. 17, p. 175107, 2017
7. B. F. Donovan, J. A. Tomko, A. Giri, D. H. Olson, J. L. Braun, J. T. Gaskins, and P. E. Hopkins, “Localized thin film damage sourced and monitored via pump-probe modulated thermorelectance,” *Review of Scientific Instruments*, vol. 88, p. 054903, 2018/04/25 2017
6. K. E. Meyer, R. Cheaito, E. Paisley, C. T. Shelton, J. L. Braun, J.-P. Maria, J. F. Ihlefeld, and P. E. Hopkins, “Crystalline coherence length effects on the thermal conductivity of mgo thin films,” *Journal of Materials Science*, vol. 51, no. 23, pp. 10408–10417, 2016
5. J. L. Braun, S. W. King, A. Giri, J. T. Gaskins, M. Sato, T. Fujiseki, H. Fujiwara, and P. E. Hopkins, “Breaking network connectivity leads to ultralow thermal conductivities in fully dense amorphous solids,” *Applied Physics Letters*, vol. 109, no. 19, p. 191905, 2016
4. A. Giri, J. L. Braun, and P. E. Hopkins, “Implications of interfacial bond strength on the spectral contributions to thermal boundary conductance across solid, liquid, and gas interfaces: A molecular dynamics study,” *The Journal of Physical Chemistry C*, vol. 120, pp. 24847–24856, 11 2016
3. L. Wang, R. Cheaito, J. L. Braun, A. Giri, and P. E. Hopkins, “Thermal conductivity measurements of non-metals via combined time- and frequency-domain thermorelectance without a metal film transducer,” *Review of Scientific Instruments*, vol. 87, no. 9, p. 094902, 2016
2. A. Giri, J. L. Braun, and P. E. Hopkins, “Effect of crystalline/amorphous interfaces on thermal transport across confined thin films and superlattices,” *Journal of Applied Physics*, vol. 119, no. 23, p. 235305, 2016
1. **J. L. Braun, C. H. Baker, A. Giri, M. Elahi, K. Artyushkova, T. E. Beechem, P. M. Norris, Z. C. Leseman, J. T. Gaskins, and P. E. Hopkins**, “Size effects on the thermal conductivity of amorphous silicon thin films,” *Phys. Rev. B*, vol. 93, p. 140201, Apr 2016

Bibliography

- [1] L. Shi, C. Dames, J. R. Lukes, P. Reddy, J. Duda, D. G. Cahill, J. Lee, A. Marconnet, K. E. Goodson, J.-H. Bahk, A. Shakouri, R. S. Prasher, J. Felts, W. P. King, B. Han, and J. C. Bischof, “Evaluating broader impacts of nanoscale thermal transport research,” *Nanoscale and Microscale Thermophysical Engineering*, vol. 19, no. 2, pp. 127–165, 2015.
- [2] G. Chen, *Nanoscale Energy Transport and Conversion: A Parallel Treatment of Electrons, Molecules, Phonons, and Photons*. Oxford University Press, USA, 2005.
- [3] E. Pop, “Energy dissipation and transport in nanoscale devices,” *Nano Research*, vol. 3, pp. 147–169, 2010.
- [4] J. Carrete, B. Vermeersch, A. Katre, A. van Roekhem, T. Wang, G. K. H. Madsen, and N. Mingo, “almabte : A solver of the space–time dependent boltzmann transport equation for phonons in structured materials,” *Computer Physics Communications*, vol. 220, no. Supplement C, pp. 351–362, 2017.
- [5] K. Esfarjani, G. Chen, and H. T. Stokes, “Heat transport in silicon from first-principles calculations,” *Physical Review B*, vol. 84, pp. 085204–, 08 2011.
- [6] W. de Haas and T. Biermasz, “The thermal conductivity of quartz at low temperatures,” *Physica*, vol. 2, no. 1, pp. 673 – 682, 1935.
- [7] W. D. Haas and T. Biermasz, “The thermal conductivity of kbr, kcl and sio₂ at low temperatures,” *Physica*, vol. 4, no. 8, pp. 752 – 756, 1937.
- [8] H. Casimir, “Note on the conduction of heat in crystals,” *Physica*, vol. 5, no. 6, pp. 495 – 500, 1938.
- [9] J. Cuffe, J. K. Eliason, A. A. Maznev, K. C. Collins, J. A. Johnson, A. Shchepetov, M. Prunnila, J. Ahopelto, C. M. Sotomayor Torres, G. Chen, and K. A. Nelson, “Reconstructing phonon mean-free-path contributions to thermal conductivity using nanoscale membranes,” *Physical Review B*, vol. 91, pp. 245423–, 06 2015.
- [10] D. Li, Y. Wu, P. Kim, L. Shi, P. Yang, and A. Majumdar, “Thermal conductivity of individual silicon nanowires,” *Applied Physics Letters*, vol. 83, no. 14, pp. 2934–2936, 2003.
- [11] A. M. Marconnet, M. Asheghi, and K. E. Goodson, “From the casimir limit to phononic crystals: 20 years of phonon transport studies using silicon-on-insulator technology,” *Journal of Heat Transfer*, vol. 135, pp. 061601–061601, 05 2013.
- [12] B. Abeles, “Lattice thermal conductivity of disordered semiconductor alloys at high temperatures,” *Physical Review*, vol. 131, pp. 1906–1911, Sep 1963.
- [13] M. Beekman and D. G. Cahill, “Inorganic crystals with glass-like and ultralow thermal conductivities,” *Crystal Research and Technology*, vol. 52, no. 10, pp. 1700114–n/a, 2017.
- [14] J. Mort, “Applications of amorphous materials,” *Physics in Technology*, vol. 11, no. 4, p. 134, 1980.
- [15] T. Meydan, “Application of amorphous materials to sensors,” *Journal of Magnetism and Magnetic Materials*, vol. 133, no. 1, pp. 525–532, 1994.

- [16] M. C. Wingert, J. Zheng, S. Kwon, and R. Chen, "Thermal transport in amorphous materials: a review," *Semiconductor Science and Technology*, vol. 31, no. 11, p. 113003, 2016.
- [17] J. J. Freeman and A. C. Anderson, "Thermal conductivity of amorphous solids," *Phys. Rev. B*, vol. 34, pp. 5684–5690, Oct 1986.
- [18] D. G. Cahill and R. Pohl, "Lattice vibrations and heat transport in crystals and glasses," *Annual Review of Physical Chemistry*, vol. 39, no. 1, pp. 93–121, 1988.
- [19] G. A. Slack, "The thermal conductivity of nonmetallic crystals," in *Solid State Physics* (H. Ehrenreich, F. Seitz, and D. Turnbull, eds.), vol. 34 of *Solid State Physics*, pp. 1 – 71, Academic Press, 1979.
- [20] D. G. Cahill and R. O. Pohl, "Heat flow and lattice vibrations in glasses," *Solid State Communications*, vol. 70, no. 10, pp. 927–930, 1989.
- [21] J. M. Larkin and A. J. H. McGaughey, "Thermal conductivity accumulation in amorphous silica and amorphous silicon," *Phys. Rev. B*, vol. 89, p. 144303, Apr 2014.
- [22] J. L. Braun, C. H. Baker, A. Giri, M. Elahi, K. Artyushkova, T. E. Beechem, P. M. Norris, Z. C. Leseman, J. T. Gaskins, and P. E. Hopkins, "Size effects on the thermal conductivity of amorphous silicon thin films," *Phys. Rev. B*, vol. 93, p. 140201, Apr 2016.
- [23] S. Kwon, J. Zheng, M. C. Wingert, S. Cui, and R. Chen, "Unusually high and anisotropic thermal conductivity in amorphous silicon nanostructures," *ACS Nano*, vol. 11, pp. 2470–2476, 03 2017.
- [24] J. Moon, B. Latour, and A. J. Minnich, "Propagating elastic vibrations dominate thermal conduction in amorphous silicon," *Physical Review B*, vol. 97, pp. 024201–, 01 2018.
- [25] F. J. DiSalvo, "Thermoelectric cooling and power generation," *Science*, vol. 285, p. 703, 07 1999.
- [26] H. J. Goldsmid, *Electronic refrigeration*. Pion, 1986.
- [27] G. Chen, "Diffusion–transmission interface condition for electron and phonon transport," *Applied Physics Letters*, vol. 82, February 2003.
- [28] G. D. Mahan and J. O. Sofo, "The best thermoelectric," *Proceedings of the National Academy of Sciences*, vol. 93, no. 15, pp. 7436–7439, 1996.
- [29] H. J. Goldsmid and R. W. Douglas, "The use of semiconductors in thermoelectric refrigeration," *British Journal of Applied Physics*, vol. 5, pp. 386–390, nov 1954.
- [30] D. A. WRIGHT, "Thermoelectric properties of bismuth telluride and its alloys," *Nature*, vol. 181, no. 4612, pp. 834–834, 1958.
- [31] G. D. Mahan and H. B. Lyon, "Thermoelectric devices using semiconductor quantum wells," *Journal of Applied Physics*, vol. 76, no. 3, pp. 1899–1901, 1994.
- [32] R. Venkatasubramanian, E. Siivola, T. Colpitts, and B. O'Quinn, "Thin-film thermoelectric devices with high room-temperature figures of merit," *Nature*, vol. 413, pp. 597 EP –, 10 2001.
- [33] D. R. Clarke and S. R. Phillipot, "Thermal barrier coating materials," *Materials Today*, vol. 8, no. 6, pp. 22 – 29, 2005.
- [34] N. R. Council *et al.*, *Coatings for high-temperature structural materials: trends and opportunities*. National Academies Press, 1996.
- [35] S. M. Meier, D. K. Gupta, and K. D. Sheffler, "Ceramic thermal barrier coatings for commercial gas turbine engines," *JOM*, vol. 43, pp. 50–53, Mar 1991.

- [36] R. Novak, A. Matarese, R. Huston, A. Scharman, and T. Yonushonis, "Development of thick thermal barrier coatings for diesel applications," *Materials and Manufacturing Processes*, vol. 7, no. 1, pp. 15–30, 1992.
- [37] N. P. Padture, M. Gell, and E. H. Jordan, "Thermal barrier coatings for gas-turbine engine applications," *Science*, vol. 296, p. 280, 04 2002.
- [38] L. W. Hobbs, *Science and Technology of Zirconia: Proceedings of the 1a International Conference on the Science and Technology of Zirconia: Held at the Case Institute of Technology, Case Western Reserve University, Cleveland, Ohio, June 16-18, 1980*. American Ceramic Society, 1981.
- [39] K. W. Schlichting, N. P. Padture, and P. G. Klemens, "Thermal conductivity of dense and porous yttria-stabilized zirconia," *Journal of Materials Science*, vol. 36, pp. 3003–3010, Jun 2001.
- [40] R. Vassen, X. Cao, F. Tietz, D. Basu, and D. Stöver, "Zirconates as new materials for thermal barrier coatings," *Journal of the American Ceramic Society*, vol. 83, no. 8, pp. 2023–2028, 2000.
- [41] P. K. Schelling and S. R. Phillpot, "Mechanism of thermal transport in zirconia and yttria-stabilized zirconia by molecular-dynamics simulation," *Journal of the American Ceramic Society*, vol. 84, no. 12, pp. 2997–3007, 2001.
- [42] G. E. Moore, "Cramming more components onto integrated circuits, reprinted from electronics, volume 38, number 8, april 19, 1965, pp.114 ff.," *IEEE Solid-State Circuits Society Newsletter*, vol. 11, pp. 33–35, Sep. 2006.
- [43] M. K. Qureshi, V. Srinivasan, and J. A. Rivers, "Scalable high performance main memory system using phase-change memory technology," *ACM SIGARCH Computer Architecture News*, vol. 37, no. 3, pp. 24–33, 2009.
- [44] H. . P. Wong, S. Raoux, S. Kim, J. Liang, J. P. Reifenberg, B. Rajendran, M. Asheghi, and K. E. Goodson, "Phase change memory," *Proceedings of the IEEE*, vol. 98, pp. 2201–2227, Dec 2010.
- [45] S. Raoux, G. W. Burr, M. J. Breitwisch, C. T. Rettner, Y. . Chen, R. M. Shelby, M. Salinga, D. Krebs, S. . Chen, H. . Lung, and C. H. Lam, "Phase-change random access memory: A scalable technology," *IBM Journal of Research and Development*, vol. 52, pp. 465–479, July 2008.
- [46] G. W. Burr, M. J. Breitwisch, M. Franceschini, D. Garetto, K. Gopalakrishnan, B. Jackson, B. Kurdi, C. Lam, L. A. Lastras, A. Padilla, B. Rajendran, S. Raoux, and R. S. Shenoy, "Phase change memory technology," *Journal of Vacuum Science & Technology B*, vol. 28, no. 2, pp. 223–262, 2010.
- [47] S. R. Ovshinsky, "Reversible electrical switching phenomena in disordered structures," *Phys. Rev. Lett.*, vol. 21, pp. 1450–1453, Nov 1968.
- [48] N. Yamada, E. Ohno, K. Nishiuchi, N. Akahira, and M. Takao, "Rapidphase transitions of getesb2te3 pseudobinary amorphous thin films for an optical disk memory," *Journal of Applied Physics*, vol. 69, no. 5, pp. 2849–2856, 1991.
- [49] T. N. Narasimhan, "Fourier's heat conduction equation: History, influence, and connections," *Proceedings of the Indian Academy of Sciences - Earth and Planetary Sciences*, vol. 108, pp. 117–148, Sep 1999.
- [50] J. B. J. Fourier, *Théorie Analytique de la Chaleur*. Cambridge Library Collection - Mathematics, Cambridge University Press, 2009.
- [51] X. Wang, C. D. Liman, N. D. Treat, M. L. Chabinyc, and D. G. Cahill, "Ultralow thermal conductivity of fullerene derivatives," *Physical Review B*, vol. 88, pp. 075310–, 08 2013.
- [52] C. Y. Ho, R. W. Powell, and P. E. Liley, "Thermal conductivity of the elements," *Journal of Physical and Chemical Reference Data*, vol. 1, no. 2, pp. 279–421, 1972.

- [53] T. M. Tritt, *Thermal conductivity: theory, properties, and applications*. Springer Science & Business Media, 2005.
- [54] W. G. Vincenti and C. H. Kruger, *Introduction to physical gas dynamics*, vol. 246. Wiley New York, 1965.
- [55] M. Kaviany, *Heat Transfer Physics*. Cambridge University Press, 2 ed., 2014.
- [56] G. P. Srivastava, *The physics of phonons*. CRC press, 1990.
- [57] A. Furrer, T. StrÃ, et al., *Neutron scattering in condensed matter physics*. World Scientific Publishing Company, 2009.
- [58] C. Kittel, P. McEuen, and P. McEuen, *Introduction to solid state physics*, vol. 8. Wiley New York, 1996.
- [59] K. Parlinski, J. Łazewski, and Y. Kawazoe, “Ab initio studies of phonons in mgo by the direct method including {LO} mode,” *Journal of Physics and Chemistry of Solids*, vol. 61, no. 1, pp. 87 – 90, 2000.
- [60] R. Coy, C. Tompson, and E. Gürmen, “Phonon dispersion in nio,” *Solid State Communications*, vol. 18, no. 7, pp. 845 – 847, 1976.
- [61] Y. S. Touloukian, R. W. Powell, C. Y. Ho, and P. G. Klemens, *Thermophysical Properties of Matter - Specific Heat: Non-metallic Solids*, vol. 5. New York, IFI/Plenum, 1970.
- [62] J. Keem and J. Honig, “Selected electrical and thermal properties of undoped nickel oxide,” tech. rep., DTIC Document, 1978.
- [63] J. De Heer, “Thermodynamics, an advanced treatment for chemists and physicists. third edition (guggenheim, e.a.),” *Journal of Chemical Education*, vol. 34, no. 11, p. A556, 1957.
- [64] P. Klemens, “The thermal conductivity of dielectric solids at low temperatures (theoretical),” in *Proceedings of the Royal Society of London A: Mathematical, Physical and Engineering Sciences*, vol. 208, pp. 108–133, The Royal Society, 1951.
- [65] J. M. Ziman, “The general variational principle of transport theory,” *Canadian Journal of Physics*, vol. 34, pp. 1256–1273, 2017/09/27 1956.
- [66] J. Callaway, “Model for lattice thermal conductivity at low temperatures,” *Physical Review*, vol. 113, pp. 1046–1051, Feb 1959.
- [67] P. G. Klemens, “Thermal resistance due to point defects at high temperatures,” *Physical Review*, vol. 119, pp. 507–509, 07 1960.
- [68] C. Herring, “Role of low-energy phonons in thermal conduction,” *Phys. Rev.*, vol. 95, pp. 954–965, Aug 1954.
- [69] M. G. Holland, “Analysis of lattice thermal conductivity,” *Phys. Rev.*, vol. 132, pp. 2461–2471, Dec 1963.
- [70] G. A. Slack and S. Galginaitis, “Thermal conductivity and phonon scattering by magnetic impurities in cdte,” *Phys. Rev.*, vol. 133, pp. A253–A268, Jan 1964.
- [71] T. Feng, L. Lindsay, and X. Ruan, “Four-phonon scattering significantly reduces intrinsic thermal conductivity of solids,” *Phys. Rev. B*, vol. 96, p. 161201, Oct 2017.
- [72] P. G. Klemens, “The scattering of low-frequency lattice waves by static imperfections,” *Proceedings of the Physical Society. Section A*, vol. 68, no. 12, p. 1113, 1955.
- [73] D. G. Cahill, “Thermal conductivity data.” <http://users.mrl.illinois.edu/cahill/tcdata/tcdata.html>.

- [74] F. B. Lewis and N. H. Saunders, “The thermal conductivity of nio and coo at the neel temperature,” *Journal of Physics C: Solid State Physics*, vol. 6, no. 15, p. 2525, 1973.
- [75] H. R. Seyf, L. Yates, T. L. Bouger, S. Graham, B. A. Cola, T. Detchprohm, M.-H. Ji, J. Kim, R. Dupuis, W. Lv, and A. Henry, “Rethinking phonons: The issue of disorder,” *npj Computational Materials*, vol. 3, no. 1, p. 49, 2017.
- [76] J. Garg, N. Bonini, B. Kozinsky, and N. Marzari, “Role of disorder and anharmonicity in the thermal conductivity of silicon-germanium alloys: A first-principles study,” *Physical Review Letters*, vol. 106, p. 045901, Jan 2011.
- [77] D. G. Cahill, F. Watanabe, A. Rockett, and C. B. Vining, “Thermal conductivity of epitaxial layers of dilute sige alloys,” *Phys. Rev. B*, vol. 71, p. 235202, Jun 2005.
- [78] T. Tong, D. Fu, A. X. Levander, W. J. Schaff, B. N. Pantha, N. Lu, B. Liu, I. Ferguson, R. Zhang, J. Y. Lin, H. X. Jiang, J. Wu, and D. G. Cahill, “Suppression of thermal conductivity in inxga1xn alloys by nanometer-scale disorder,” *Applied Physics Letters*, vol. 102, p. 121906, 2017/10/23 2013.
- [79] Y. Touloukian, P. Liley, and S. Saxena, “Thermophysical properties of matter-the tprc data series. volume 3. thermal conductivity-nonmetallic liquids and gases,” tech. rep., DTIC Document, 1970.
- [80] D. G. Cahill, S. K. Watson, and R. O. Pohl, “Lower limit to the thermal conductivity of disordered crystals,” *Phys. Rev. B*, vol. 46, pp. 6131–6140, Sep 1992.
- [81] A. F. Birch and H. Clark, “The thermal conductivity of rocks and its dependence upon temperature and composition,” *American Journal of Science*, vol. 238, no. 8, pp. 529–558, 1940.
- [82] A. Einstein, “Elementare betrachtungen über die thermische molekularbewegung in festen körpern,” *Annalen der Physik*, vol. 340, no. 9, pp. 679–694, 1911.
- [83] W. Lv and A. Henry, “Examining the validity of the phonon gas model in amorphous materials,” *Scientific Reports*, vol. 6, pp. 37675 EP –, 12 2016.
- [84] P. B. Allen, J. L. Feldman, J. Fabian, and F. Wooten, “Diffusons, locons, propagons: Character of atomic vibrations in amorphous si,” *Philosophical Magazine B*, vol. 79, p. 1715, 1999.
- [85] M. T. Agne, R. Hanus, and G. J. Snyder, “Minimum thermal conductivity in the context of diffuson-mediated thermal transport,” *Energy Environ. Sci.*, vol. 11, pp. 609–616, 2018.
- [86] A. Ioffe and A. Regel, “Non-crystalline, amorphous and liquid electronic semiconductors,” *Prog. Semicond.*, vol. 4, no. 237, p. 89, 1960.
- [87] P. B. Allen and J. Kelner, “Evolution of a vibrational wave packet on a disordered chain,” *American Journal of Physics*, vol. 66, no. 6, pp. 497–506, 1998.
- [88] S. Shenogin, A. Bodapati, P. Kebinski, and A. J. H. McGaughey, “Predicting the thermal conductivity of inorganic and polymeric glasses: The role of anharmonicity,” *Journal of Applied Physics*, vol. 105, no. 3, pp. –, 2009.
- [89] L. Yang, Q. Zhang, Z. Cui, M. Gerboth, Y. Zhao, T. T. Xu, D. G. Walker, and D. Li, “Ballistic phonon penetration depth in amorphous silicon dioxide,” *Nano Letters*, vol. 17, pp. 7218–7225, 12 2017.
- [90] C. A. Paddock and G. L. Eesley, “Transient thermoreflectance from thin metal films,” *Journal of Applied Physics*, vol. 60, pp. 285–290, 2018/06/21 1986.
- [91] Y. Wang, J. Y. Park, Y. K. Koh, and D. G. Cahill, “Thermoreflectance of metal transducers for time-domain thermoreflectance,” *Journal of Applied Physics*, vol. 108, p. 043507, 2017/10/05 2010.

- [92] R. B. Wilson, B. A. Apgar, L. W. Martin, and D. G. Cahill, "Thermoreflectance of metal transducers for optical pump-probe studies of thermal properties," *Optics Express*, vol. 20, no. 27, pp. 28829–28838, 2012.
- [93] C. M. Rost, J. Braun, K. Ferri, L. Backman, A. Giri, E. J. Opila, J.-P. Maria, and P. E. Hopkins, "Hafnium nitride films for thermoreflectance transducers at high temperatures: Potential based on heating from laser absorption," *Applied Physics Letters*, vol. 111, p. 151902, 2018/04/25 2017.
- [94] D. G. Cahill, "Analysis of heat flow in layered structures for time-domain thermoreflectance," *Review of Scientific Instruments*, vol. 75, p. 5119, 2004.
- [95] A. J. Schmidt, X. Chen, and G. Chen, "Pulse accumulation, radial heat conduction, and anisotropic thermal conductivity in pump-probe transient thermoreflectance," *Review of Scientific Instruments*, vol. 79, no. 11, p. 114902, 2008.
- [96] A. J. Schmidt, "Pump-probe thermoreflectance," *Annual Review of Heat Transfer*, vol. 16, p. 159, 2013.
- [97] P. E. Hopkins, J. R. Serrano, L. M. Phinney, S. P. Kearney, T. W. Grassner, and C. T. Harris, "Criteria for cross-plane dominated thermal transport in multilayer thin film systems during modulated laser heating," *Journal of Heat Transfer*, vol. 132, pp. 081302–081302, 05 2010.
- [98] Y. K. Koh, S. L. Singer, W. Kim, J. M. O. Zide, H. Lu, D. G. Cahill, A. Majumdar, and A. C. Gossard, "Comparison of the 3method and time-domain thermoreflectance for measurements of the cross-plane thermal conductivity of epitaxial semiconductors," *Journal of Applied Physics*, vol. 105, p. 054303, 2017/09/13 2009.
- [99] J. Opsal, A. Rosencwaig, and D. L. Willenborg, "Thermal-wave detection and thin-film thickness measurements with laser beam deflection," *Appl. Opt.*, vol. 22, pp. 3169–3176, Oct 1983.
- [100] A. Rosencwaig, J. Opsal, W. L. Smith, and D. L. Willenborg, "Detection of thermal waves through optical reflectance," *Applied Physics Letters*, vol. 46, no. 11, pp. 1013–1015, 1985.
- [101] A. J. Schmidt, R. Cheaito, and M. Chiesa, "A frequency-domain thermoreflectance method for the characterization of thermal properties," *Review of Scientific Instruments*, vol. 80, no. 9, pp. –, 2009.
- [102] J. A. Malen, K. Baheti, T. Tong, Y. Zhao, J. A. Hudgings, and A. Majumdar, "Optical measurement of thermal conductivity using fiber aligned frequency domain thermoreflectance," *Journal of Heat Transfer*, vol. 133, pp. 081601–081601–7, 05 2011.
- [103] C. Chiritescu, D. G. Cahill, N. Nguyen, D. Johnson, A. Bodapati, P. Kebinski, and P. Zschack, "Ultralow thermal conductivity in disordered, layered wse₂ crystals," *Science*, vol. 315, no. 5810, pp. 351–353, 2007.
- [104] J. C. Duda, P. E. Hopkins, Y. Shen, and M. C. Gupta, "Exceptionally low thermal conductivities of films of the fullerene derivative pcbm," *Physical Review Letters*, vol. 110, pp. 015902–, 01 2013.
- [105] J. S. Kang, M. Li, H. Wu, H. Nguyen, and Y. Hu, "Experimental observation of high thermal conductivity in boron arsenide," *Science*, 07 2018.
- [106] S. Li, Q. Zheng, Y. Lv, X. Liu, X. Wang, P. Y. Huang, D. G. Cahill, and B. Lv, "High thermal conductivity in cubic boron arsenide crystals," *Science*, 07 2018.
- [107] F. Tian, B. Song, X. Chen, N. K. Ravichandran, Y. Lv, K. Chen, S. Sullivan, J. Kim, Y. Zhou, T.-H. Liu, M. Goni, Z. Ding, J. Sun, G. A. G. U. Gamage, H. Sun, H. Ziyae, S. Huyan, L. Deng, J. Zhou, A. J. Schmidt, S. Chen, C.-W. Chu, P. Y. Huang, D. Broido, L. Shi, G. Chen, and Z. Ren, "Unusual high thermal conductivity in boron arsenide bulk crystals," *Science*, 07 2018.
- [108] B. Rethfeld, A. Kaiser, M. Vicanek, and G. Simon, "Ultrafast dynamics of nonequilibrium electrons in metals under femtosecond laser irradiation," *Phys. Rev. B*, vol. 65, p. 214303, May 2002.

- [109] R. Cheaito, J. C. Duda, T. E. Beechem, K. Hattar, J. F. Ihlefeld, D. L. Medlin, M. A. Rodriguez, M. J. Campion, E. S. Piekos, and P. E. Hopkins, "Experimental investigation of size effects on the thermal conductivity of silicon-germanium alloy thin films," *Phys. Rev. Lett.*, vol. 109, p. 195901, Nov 2012.
- [110] J. Liu, S. Ju, Y. Ding, and R. Yang, "Size effect on the thermal conductivity of ultrathin polystyrene films," *Applied Physics Letters*, vol. 104, no. 15, p. 153110, 2014.
- [111] B. F. Donovan, B. M. Foley, J. F. Ihlefeld, J.-P. Maria, and P. E. Hopkins, "Spectral phonon scattering effects on the thermal conductivity of nano-grained barium titanate," *Applied Physics Letters*, vol. 105, p. 082907, 2017/09/16 2014.
- [112] B. M. Foley, H. J. Brown-Shaklee, J. C. Duda, R. Cheaito, B. J. Gibbons, D. Medlin, J. F. Ihlefeld, and P. E. Hopkins, "Thermal conductivity of nano-grained srtio3 thin films," *Applied Physics Letters*, vol. 101, p. 231908, 2017/09/16 2012.
- [113] L. Chen, J. L. Braun, B. F. Donovan, P. E. Hopkins, and S. J. Poon, "Ballistic transport of long wavelength phonons and thermal conductivity accumulation in nanograned silicon-germanium alloys," *Applied Physics Letters*, vol. 111, p. 131902, 2017/09/27 2017.
- [114] K. E. Meyer, R. Cheaito, E. Paisley, C. T. Shelton, J. L. Braun, J.-P. Maria, J. F. Ihlefeld, and P. E. Hopkins, "Crystalline coherence length effects on the thermal conductivity of mgo thin films," *Journal of Materials Science*, vol. 51, no. 23, pp. 10408–10417, 2016.
- [115] Y. K. Koh and D. G. Cahill, "Frequency dependence of the thermal conductivity of semiconductor alloys," *Phys. Rev. B*, vol. 76, p. 075207, Aug 2007.
- [116] K. T. Regner, D. P. Sellan, Z. Su, C. H. Amon, A. J. H. McGaughey, and J. A. Malen, "Broadband phonon mean free path contributions to thermal conductivity measured using frequency domain thermoreflectance," *Nat. Commun.*, vol. 4, p. 1640, 03 2013.
- [117] A. J. Minnich, J. A. Johnson, A. J. Schmidt, K. Esfarjani, M. S. Dresselhaus, K. A. Nelson, and G. Chen, "Thermal conductivity spectroscopy technique to measure phonon mean free paths," *Phys. Rev. Lett.*, vol. 107, p. 095901, Aug 2011.
- [118] Y. Hu, L. Zeng, A. J. Minnich, M. S. Dresselhaus, and G. Chen, "Spectral mapping of thermal conductivity through nanoscale ballistic transport," *Nat Nano*, vol. 10, pp. 701–706, 08 2015.
- [119] A. J. Schmidt, *Optical Characterization of Thermal Transport from the Nanoscale to the Macroscale*. PhD thesis, MIT, 2008.
- [120] J. L. Braun and P. E. Hopkins, "Upper limit to the thermal penetration depth during modulated heating of multilayer thin films with pulsed and continuous wave lasers: A numerical study," *Journal of Applied Physics*, vol. 121, no. 17, p. 175107, 2017.
- [121] J. Yang, E. Ziade, and A. J. Schmidt, "Modeling optical absorption for thermoreflectance measurements," *Journal of Applied Physics*, vol. 119, no. 9, p. 095107, 2016.
- [122] H. S. Carslaw and J. C. Jaeger, "Conduction of heat in solids," *Oxford: Clarendon Press, 1959, 2nd ed.*, 1959.
- [123] W. S. Capinski, H. J. Maris, T. Ruf, M. Cardona, K. Ploog, and D. S. Katzer, "Thermal-conductivity measurements of gaas/alsas superlattices using a picosecond optical pump-and-probe technique," *Physical Review B*, vol. 59, pp. 8105–8113, 03 1999.
- [124] M. C. George, M. A. Rodriguez, M. S. Kent, G. L. Brennecka, and P. E. Hopkins, "Thermal conductivity of self-assembling symmetric block copolymer thin films of polystyrene-block-poly(methyl methacrylate)," *Journal of Heat Transfer*, vol. 138, pp. 024505–024505–5, 10 2015.

- [125] Z. Guo, D. Lee, Y. Liu, F. Sun, A. Sliwinski, H. Gao, P. C. Burns, L. Huang, and T. Luo, “Tuning the thermal conductivity of solar cell polymers through side chain engineering,” *Physical Chemistry Chemical Physics*, vol. 16, no. 17, pp. 7764–7771, 2014.
- [126] P. E. Hopkins, “Thermal transport across solid interfaces with nanoscale imperfections: Effects of roughness, disorder, dislocations, and bonding on thermal boundary conductance,” *ISRN Mech. Eng.*, vol. 2013, p. 982586, 2013.
- [127] Y. S. Touloukian and E. H. Buyco, *Thermophysical Properties of Matter - Specific Heat: Metallic Elements and Alloys*, vol. 4. New York, IFI/Plenum, 1970.
- [128] K. T. Regner, A. J. H. McGaughey, and J. A. Malen, “Analytical interpretation of nondiffusive phonon transport in thermoreflectance thermal conductivity measurements,” *Phys. Rev. B*, vol. 90, p. 064302, Aug 2014.
- [129] R. B. Wilson and D. G. Cahill, “Anisotropic failure of fourier theory in time-domain thermoreflectance experiments,” *Nature Communications*, vol. 5, p. 5075 EP, 10 2014.
- [130] K. T. Regner, J. P. Freedman, and J. A. Malen, “Advances in studying phonon mean free path dependent contributions to thermal conductivity,” *Nanoscale and Microscale Thermophysical Engineering*, vol. 19, no. 3, pp. 183–205, 2015.
- [131] H.-S. Yang, D. G. Cahill, X. Liu, J. L. Feldman, R. S. Crandall, B. A. Sperling, and J. R. Abelson, “Anomalously high thermal conductivity of amorphous si deposited by hot-wire chemical vapor deposition,” *Phys. Rev. B*, vol. 81, p. 104203, Mar 2010.
- [132] X. Liu, J. L. Feldman, D. G. Cahill, R. S. Crandall, N. Bernstein, D. M. Photiadis, M. J. Mehl, and D. A. Papaconstantopoulos, “High thermal conductivity of a hydrogenated amorphous silicon film,” *Phys. Rev. Lett.*, vol. 102, p. 035901, Jan 2009.
- [133] C. B. Arnold, P. Serra, and A. Piqué, “Laser direct-write techniques for printing of complex materials,” *MRS Bulletin*, vol. 32, pp. 23–31, 001 2007.
- [134] L. D. Zarzar, B. S. Swartzentruber, B. F. Donovan, P. E. Hopkins, and B. Kaehr, “Using laser-induced thermal voxels to pattern diverse materials at the solid–liquid interface,” *ACS Applied Materials & Interfaces*, vol. 8, pp. 21134–21139, 08 2016.
- [135] P. Delaporte and A.-P. Alloncle, “Laser-induced forward transfer: A high resolution additive manufacturing technology,” *Optics & Laser Technology*, vol. 78, Part A, pp. 33–41, 4 2016.
- [136] J. Steen, William M. ; Mazumder, *Laser Material Processing*. Springer, 2010.
- [137] S. S. Wellershoff, J. Hohlfeld, J. Gündde, and E. Matthias, “The role of electron–phonon coupling in femtosecond laser damage of metals,” *Applied Physics A*, vol. 69, no. 1, pp. S99–S107, 1999.
- [138] G. A. Antonelli, B. Perrin, B. C. Daly, and D. G. Cahill, “Characterization of mechanical and thermal properties using ultrafast optical metrology,” *MRS bulletin*, vol. 31, no. 08, pp. 607–613
- [139] J. Cabanillas-Gonzalez, G. Grancini, and G. Lanzani, “Pump-probe spectroscopy in organic semiconductors: Monitoring fundamental processes of relevance in optoelectronics,” *Advanced Materials*, vol. 23, no. 46, pp. 5468–5485, 2011.
- [140] A. Devizis, V. Vaiciakuskas, and V. Gulbinas, “Ultrafast pump-probe surface plasmon resonance spectroscopy of thin gold films,” *Applied Optics*, vol. 45, no. 11, pp. 2535–2539, 2006.
- [141] B. N. Chichkov, C. Momma, S. Nolte, F. von Alvensleben, and A. Tünnermann, “Femtosecond, picosecond and nanosecond laser ablation of solids,” *Applied Physics A*, vol. 63, no. 2, pp. 109–115, 1996.

- [142] E. G. Gamaly, A. V. Rode, B. Luther-Davies, and V. T. Tikhonchuk, “Ablation of solids by femtosecond lasers: Ablation mechanism and ablation thresholds for metals and dielectrics,” *Physics of Plasmas*, vol. 9, no. 3, pp. 949–957, 2002.
- [143] W. M. Steen, *Laser Surface Treatment*, pp. 172–219. London: Springer London, 1991.
- [144] D. I. Pantelis, E. Bouyiouri, N. Kouloumbi, P. Vassiliou, and A. Koutsomichalis, “Wear and corrosion resistance of laser surface hardened structural steel,” *Surface and Coatings Technology*, vol. 161, pp. 125–134, 12 2002.
- [145] J. Brandrup, E. H. Immergut, E. A. Grulke, A. Abe, and D. R. Bloch, *Polymer handbook*, vol. 7. Wiley New York etc, 1989.
- [146] L. H. Sperling, *Introduction to physical polymer science*. John Wiley & Sons, 2005.
- [147] J. W. Shriver, *Protein structure, stability, and interactions*. Springer [distributor], 2009.
- [148] J. Buchner and T. Kieffhaber, *Protein folding handbook*, vol. 3. Wiley-VCH Weinheim, 2005.
- [149] R. M. Costescu, M. A. Wall, and D. G. Cahill, “Thermal conductance of epitaxial interfaces,” *Phys. Rev. B*, vol. 67, p. 054302, Feb 2003.
- [150] J. Liu, J. Zhu, M. Tian, X. Gu, A. Schmidt, and R. Yang, “Simultaneous measurement of thermal conductivity and heat capacity of bulk and thin film materials using frequency-dependent transient thermoreflectance method,” *Review of Scientific Instruments*, vol. 84, no. 3, p. 034902, 2013.
- [151] D.-W. Oh, S. Kim, J. A. Rogers, D. G. Cahill, and S. Sinha, “Interfacial thermal conductance of transfer-printed metal films,” *Advanced Materials*, vol. 23, no. 43, pp. 5028–5033, 2011.
- [152] J. C. Duda, C. Y. P. Yang, B. M. Foley, R. Cheaito, D. L. Medlin, R. E. Jones, and P. E. Hopkins, “Influence of interfacial properties on thermal transport at gold:silicon contacts,” *Applied Physics Letters*, vol. 102, p. 081902, 2017/08/09 2013.
- [153] D. G. Cahill, “Thermal conductivity measurement from 30 to 750 k: the 3 method,” *Review of Scientific Instruments*, vol. 61, no. 2, pp. 802–808, 1990.
- [154] K. M. McPeak, S. V. Jayanti, S. J. P. Kress, S. Meyer, S. Iotti, A. Rossinelli, and D. J. Norris, “Plasmonic films can easily be better: Rules and recipes,” *ACS Photonics*, vol. 2, pp. 326–333, 03 2015.
- [155] L. Wang, R. Cheaito, J. L. Braun, A. Giri, and P. E. Hopkins, “Thermal conductivity measurements of non-metals via combined time- and frequency-domain thermoreflectance without a metal film transducer,” *Review of Scientific Instruments*, vol. 87, no. 9, p. 094902, 2016.
- [156] R. B. Wilson and D. G. Cahill, “Limits to fourier theory in high thermal conductivity single crystals,” *Applied Physics Letters*, vol. 107, no. 20, p. 203112, 2015.
- [157] M. J. Assael, K. D. Antoniadis, and W. A. Wakeham, “Historical evolution of the transient hot-wire technique,” *International Journal of Thermophysics*, vol. 31, no. 6, pp. 1051–1072, 2010.
- [158] S. E. Gustafsson, “Transient plane source techniques for thermal conductivity and thermal diffusivity measurements of solid materials,” *Review of Scientific Instruments*, vol. 62, pp. 797–804, 2018/05/06 1991.
- [159] W. J. Parker, R. J. Jenkins, C. P. Butler, and G. L. Abbott, “Flash method of determining thermal diffusivity, heat capacity, and thermal conductivity,” *Journal of Applied Physics*, vol. 32, pp. 1679–1684, 2017/06/22 1961.
- [160] D. Zhao, X. Qian, X. Gu, S. A. Jajja, and R. Yang, “Measurement techniques for thermal conductivity and interfacial thermal conductance of bulk and thin film materials,” *Journal of Electronic Packaging*, vol. 138, pp. 040802–040802–19, 10 2016.

- [161] A. L. Pope, B. Zawilski, and T. M. Tritt, "Description of removable sample mount apparatus for rapid thermal conductivity measurements," *Cryogenics*, vol. 41, no. 10, pp. 725–731, 2001.
- [162] J. Yang, C. Maragliano, and A. J. Schmidt, "Thermal property microscopy with frequency domain thermoreflectance," *Review of Scientific Instruments*, vol. 84, no. 10, p. 104904, 2013.
- [163] M. Goni and A. J. Schmidt, "Thermal wave imaging of microelectronics," *Journal of Heat Transfer*, vol. 138, pp. 020911–020911, 01 2016.
- [164] C. Wei, X. Zheng, D. G. Cahill, and J.-C. Zhao, "Invited article: Micron resolution spatially resolved measurement of heat capacity using dual-frequency time-domain thermoreflectance," *Review of Scientific Instruments*, vol. 84, p. 071301, 2017/09/05 2013.
- [165] A. Sood, R. Cheaito, T. Bai, H. Kwon, Y. Wang, C. Li, L. Yates, T. Bouger, S. Graham, M. Asheghi, M. Goorsky, and K. E. Goodson, "Direct visualization of thermal conductivity suppression due to enhanced phonon scattering near individual grain boundaries," *Nano Letters*, vol. 18, no. 6, pp. 3466–3472, 2018.
- [166] V. Mishra, C. L. Hardin, J. E. Garay, and C. Dames, "A 3 omega method to measure an arbitrary anisotropic thermal conductivity tensor," *Review of Scientific Instruments*, vol. 86, p. 054902, 2017/06/17 2015.
- [167] J. L. Braun, C. J. Szwejkowski, A. Giri, and P. E. Hopkins, "On the steady-state temperature rise during laser heating of multilayer thin films in optical pump–probe techniques," *Journal of Heat Transfer*, vol. 140, pp. 052801–052801–10, 02 2018.
- [168] T. Favaloro, J. H. Bahk, and A. Shakouri, "Characterization of the temperature dependence of the thermoreflectance coefficient for conductive thin films," *Review of Scientific Instruments*, vol. 86, p. 024903, 2018/07/02 2015.
- [169] P. E. Hopkins, L. M. Phinney, J. R. Serrano, and T. E. Beechem, "Effects of surface roughness and oxide layer on the thermal boundary conductance at aluminum/silicon interfaces," *Physical Review B*, vol. 82, pp. 085307–, 08 2010.
- [170] M. J. Assael, S. Botsios, K. Gialou, and I. N. Metaxa, "Thermal conductivity of polymethyl methacrylate (pmma) and borosilicate crown glass bk7," *International Journal of Thermophysics*, vol. 26, no. 5, pp. 1595–1605, 2005.
- [171] J. P. Feser, J. Liu, and D. G. Cahill, "Pump-probe measurements of the thermal conductivity tensor for materials lacking in-plane symmetry," *Review of Scientific Instruments*, vol. 85, p. 104903, 2017/01/19 2014.
- [172] X. Qian, P. Jiang, and R. Yang, "Anisotropic thermal conductivity of 4h and 6h silicon carbide measured using time-domain thermoreflectance," *Materials Today Physics*, vol. 3, pp. 70–75, 2017.
- [173] J. W. Yeh, S. K. Chen, S. J. Lin, J. Y. Gan, T. S. Chin, T. T. Shun, C. H. Tsau, and S. Y. Chang, "Nanostructured high-entropy alloys with multiple principal elements: Novel alloy design concepts and outcomes," *Advanced Engineering Materials*, vol. 6, no. 5, pp. 299–303, 2004.
- [174] B. Cantor, I. T. H. Chang, P. Knight, and A. J. B. Vincent, "Microstructural development in equiatomic multi-component alloys," *Materials Science and Engineering: A*, vol. 375–377, pp. 213–218, 7 2004.
- [175] Y. J. Zhou, Y. Zhang, Y. L. Wang, and G. L. Chen, "Solid solution alloys of alcocrfenitix with excellent room-temperature mechanical properties," *Applied Physics Letters*, vol. 90, no. 18, p. 181904, 2007.
- [176] M.-H. Tsai, C.-W. Wang, C.-W. Tsai, W.-J. Shen, J.-W. Yeh, J.-Y. Gan, and W.-W. Wu, "Thermal stability and performance of nbsitatizr high-entropy alloy barrier for copper metallization," *Journal of the Electrochemical Society*, vol. 158, no. 11, pp. H1161–H1165, 2011.

- [177] C.-C. Tung, J.-W. Yeh, T.-t. Shun, S.-K. Chen, Y.-S. Huang, and H.-C. Chen, “On the elemental effect of alcocrcufeni high-entropy alloy system,” *Materials Letters*, vol. 61, pp. 1–5, 1 2007.
- [178] Y. L. Chou, Y. C. Wang, J. W. Yeh, and H. C. Shih, “Pitting corrosion of the high-entropy alloy co1.5crfeni1.5ti0.5mo0.1 in chloride-containing sulphate solutions,” *Corrosion Science*, vol. 52, pp. 3481–3491, 10 2010.
- [179] Y.-F. Kao, T.-D. Lee, S.-K. Chen, and Y.-S. Chang, “Electrochemical passive properties of alxcofreni ($x = 0, 0.25, 0.50, 1.00$) alloys in sulfuric acids,” *Corrosion Science*, vol. 52, pp. 1026–1034, 3 2010.
- [180] M.-H. Chuang, M.-H. Tsai, W.-R. Wang, S.-J. Lin, and J.-W. Yeh, “Microstructure and wear behavior of alxco1.5crfeni1.5tiy high-entropy alloys,” *Acta Materialia*, vol. 59, pp. 6308–6317, 9 2011.
- [181] H.-P. Chou, Y.-S. Chang, S.-K. Chen, and J.-W. Yeh, “Microstructure, thermophysical and electrical properties in alxcofreni ($0x2$) high-entropy alloys,” *Materials Science and Engineering: B*, vol. 163, no. 3, pp. 184–189, 2009.
- [182] C.-L. Lu, S.-Y. Lu, J.-W. Yeh, and W.-K. Hsu, “Thermal expansion and enhanced heat transfer in high-entropy alloys,” *Journal of Applied Crystallography*, vol. 46, no. 3, pp. 736–739, 2013.
- [183] Z. Fan, H. Wang, Y. Wu, X. Liu, and Z. Lu, “Thermoelectric high-entropy alloys with low lattice thermal conductivity,” *RSC Advances*, vol. 6, no. 57, pp. 52164–52170, 2016.
- [184] C. M. Rost, E. Sachet, T. Borman, A. Moballegh, E. C. Dickey, D. Hou, J. L. Jones, S. Curtarolo, and J.-P. Maria, “Entropy-stabilized oxides,” *Nat Commun*, vol. 6, p. 8485, 09 2015.
- [185] D. Berardan, S. Franger, A. K. Meena, and N. Dragoe, “Room temperature lithium superionic conductivity in high entropy oxides,” *Journal of Materials Chemistry A*, vol. 4, no. 24, pp. 9536–9541, 2016.
- [186] S. Zhai, J. Rojas, N. Ahlborg, K. Lim, M. F. Toney, H. Jin, W. C. Chueh, and A. Majumdar, “The use of polycation oxides to lower the temperature of two-step thermochemical water splitting,” *Energy & Environmental Science*, vol. 11, pp. 2172–2178, 2018.
- [187] R. Liu, H. Chen, K. Zhao, Y. Qin, B. Jiang, T. Zhang, G. Sha, X. Shi, C. Uher, W. Zhang, and L. Chen, “Entropy as a gene-like performance indicator promoting thermoelectric materials,” *Advanced Materials*, vol. 29, no. 38, pp. 1702712–n/a, 2017.
- [188] M. Lim, Z. Rak, J. L. Braun, C. M. Rost, G. N. Kotsonis, P. E. Hopkins, J.-P. Maria, and D. W. Brenner, “Influence of mass and charge disorder on the phonon thermal conductivity of entropy stabilized oxides determined by molecular dynamics simulations,” *Journal of Applied Physics*, vol. 125, no. 5, p. 055105, 2019.
- [189] W.-L. Ong, E. S. O’Brien, P. S. M. Dougherty, D. W. Paley, C. Fred Higgs III, A. J. H. McGaughey, J. A. Malen, and X. Roy, “Orientational order controls crystalline and amorphous thermal transport in superatomic crystals,” *Nature Materials*, vol. 16, pp. 83 – 88, 09 2016.
- [190] D. T. Morelli, V. Jovovic, and J. P. Heremans, “Intrinsically minimal thermal conductivity in cubic $\text{Al}_{1-x}\text{Cr}_x\text{O}_3$ semiconductors,” *Physical Review Letters*, vol. 101, pp. 035901–, 07 2008.
- [191] J. Ma, O. Delaire, A. F. May, C. E. Carlton, M. A. McGuire, L. H. VanBebber, D. L. Abernathy, G. Ehlers, T. Hong, A. Huq, W. Tian, V. M. Keppens, Y. Shao-Horn, and B. C. Sales, “Glass-like phonon scattering from a spontaneous nanostructure in $\text{Ag}_3\text{Sb}_2\text{Te}_3$,” *Nature Nanotechnology*, vol. 8, pp. 445 EP –, 06 2013.
- [192] Y. Zhang, T. T. Zuo, Z. Tang, M. C. Gao, K. A. Dahmen, P. K. Liaw, and Z. P. Lu, “Microstructures and properties of high-entropy alloys,” *Progress in Materials Science*, vol. 61, pp. 1–93, 4 2014.

- [193] J. Yan, F. Liu, G. Ma, B. Gong, J. Zhu, X. Wang, W. Ao, C. Zhang, Y. Li, and J. Li, “Suppression of the lattice thermal conductivity in nbfesb-based half-heusler thermoelectric materials through high entropy effects,” *Scripta Materialia*, vol. 157, pp. 129–134, 2018.
- [194] A. Giri, J. L. Braun, C. Rost-Barber, and P. E. Hopkins, “On the minimum limit to thermal conductivity of multi-atom component crystalline solid solutions based on impurity mass scattering,” *Scripta Materialia*, vol. 138, pp. 134–138, 09 2017.
- [195] I. Suzuki, “Thermal expansion of periclase and olivine, and their anharmonic properties,” *Journal of Physics of the Earth*, vol. 23, no. 2, pp. 145–159, 1975.
- [196] S. Calvin, *XAFS for Everyone*. No. 1, Boca Raton: CRC, 2014.
- [197] G. S. Knapp, M. V. Nevitt, A. T. Aldred, and T. K. Klippert, “An EXAFS study of interionic distances in complex lanthanide oxides,” *Journal of Physics and Chemistry of Solids*, vol. 46, pp. 1321–1325, jan 1985.
- [198] S. Velu, K. Suzuki, C. S. Gopinath, H. Yoshida, and T. Hattori, “XPS, XANES and EXAFS investigations of CuO/ZnO/Al₂O₃/ZrO₂ mixed oxide catalysts,” *Physical Chemistry Chemical Physics*, vol. 4, pp. 1990–1999, may 2002.
- [199] D. Grandjean, H. L. Castricum, J. C. Van Den Heuvel, and B. M. Weckhuysen, “New highly mixed phases in ball-milled Cu/ZnO catalysts as established by EXAFS and XANES,” in *AIP Conference Proceedings*, vol. 882, pp. 636–638, 2007.
- [200] C. M. Rost, Z. Rak, D. W. Brenner, and J.-P. Maria, “Local structure of the mgxnixcoxcuxzn_{0(x=0.2)} entropy-stabilized oxide: An exafs study,” *Journal of the American Ceramic Society*, vol. 100, no. 6, pp. 2732–2738, 2017.
- [201] M. Newville, “Ifeffit: interactive xafs analysis and feff fitting,” *Journal of Synchrotron Radiation*, vol. 8, no. 2, pp. 322–324, 2001.
- [202] B. Ravel and M. Newville, “ATHENA, ARTEMIS, HEPHAESTUS: Data analysis for X-ray absorption spectroscopy using IFEFFIT,” *Journal of Synchrotron Radiation*, vol. 12, no. 4, pp. 537–541, 2005.
- [203] Z. Rak, C. M. Rost, M. Lim, P. Sarker, C. Toher, S. Curtarolo, J. P. Maria, and D. W. Brenner, “Charge compensation and electrostatic transferability in three entropy-stabilized oxides: Results from density functional theory calculations,” *Journal of Applied Physics*, vol. 120, p. 095105, 2018/01/15 2016.
- [204] E. Wuchina, E. Opila, M. Opeka, W. Fahrenholtz, and I. Talmy, “Uhtcs: ultra-high temperature ceramic materials for extreme environment applications,” *The Electrochemical Society Interface*, vol. 16, no. 4, p. 30, 2007.
- [205] W. G. Fahrenholtz, E. J. Wuchina, W. E. Lee, and Y. Zhou, *Ultra-high temperature ceramics: materials for extreme environment applications*. John Wiley & Sons, 2014.
- [206] Q.-J. Hong and A. van de Walle, “Prediction of the material with highest known melting point from ab initio molecular dynamics calculations,” *Physical Review B*, vol. 92, pp. 020104–, 07 2015.
- [207] M. M. Opeka, I. G. Talmy, and J. A. Zaykoski, “Oxidation-based materials selection for 2000°C + hypersonic aerosurfaces: Theoretical considerations and historical experience,” *Journal of Materials Science*, vol. 39, no. 19, pp. 5887–5904, 2004.
- [208] S. D. Kasen, *Thermal Management at Hypersonic Leading Edges*. PhD thesis, University of Virginia, 2013.
- [209] D. Bérardan, S. Franger, D. Dragoe, A. K. Meena, and N. Dragoe, “Colossal dielectric constant in high entropy oxides,” *physica status solidi (RRL) – Rapid Research Letters*, vol. 10, no. 4, pp. 328–333, 2016.

- [210] S. Jiang, T. Hu, J. Gild, N. Zhou, J. Nie, M. Qin, T. Harrington, K. Vecchio, and J. Luo, “A new class of high-entropy perovskite oxides,” *Scripta Materialia*, vol. 142, pp. 116 – 120, 2018.
- [211] R. Djenadic, A. Sarkar, O. Clemens, C. Loho, M. Botros, V. S. K. Chakravadhanula, C. Kübel, S. S. Bhattacharya, A. S. Gandhi, and H. Hahn, “Multicomponent equiatomic rare earth oxides,” *Materials Research Letters*, vol. 5, no. 2, pp. 102–109, 2017.
- [212] S. J. Skinner and J. A. Kilner, “Oxygen ion conductors,” *Materials Today*, vol. 6, no. 3, pp. 30 – 37, 2003.
- [213] X. Cao, R. Vassen, and D. Stoever, “Ceramic materials for thermal barrier coatings,” *Journal of the European Ceramic Society*, vol. 24, no. 1, pp. 1 – 10, 2004.
- [214] Y.-P. Fu, S.-H. Chen, and J.-J. Huang, “Preparation and characterization of ce0.8m0.2o2 (m=y, gd, sm, nd, la) solid electrolyte materials for solid oxide fuel cells,” *International Journal of Hydrogen Energy*, vol. 35, no. 2, pp. 745 – 752, 2010.
- [215] J. Gild, M. Samiee, J. L. Braun, T. Harrington, H. Vega, P. E. Hopkins, K. Vecchio, and J. Luo, “High-entropy fluorite oxides,” *Journal of the European Ceramic Society*, vol. 38, no. 10, pp. 3578–3584, 2018.
- [216] D. T. Morelli, “Thermal conductivity and thermoelectric power of titanium carbide single crystals,” *Phys. Rev. B*, vol. 44, pp. 5453–5458, Sep 1991.
- [217] P. Sarker, T. Harrington, C. Toher, C. Osse, M. Samiee, J.-P. Maria, D. W. Brenner, K. S. Vecchio, and S. Curtarolo, “High-entropy high-hardness metal carbides discovered by entropy descriptors,” *Nature Communications*, vol. 9, no. 1, p. 4980, 2018.
- [218] T. J. Harrington, J. Gild, P. Sarker, C. Toher, C. M. Rost, O. F. Dippo, C. McElfresh, K. Kaufmann, E. Marin, L. Borowski, P. E. Hopkins, J. Luo, S. Curtarolo, D. W. Brenner, and K. S. Vecchio, “Phase stability and mechanical properties of novel high entropy transition metal carbides,” *Acta Materialia*, vol. 166, pp. 271 – 280, 2019.
- [219] Y. Touloukian, R. Powell, C. Ho, and P. Klemens, “Thermophysical properties of matter-the tprc data series. volume 2. thermal conductivity-nonmetallic solids,” tech. rep., THERMOPHYSICAL AND ELECTRONIC PROPERTIES INFORMATION ANALYSIS CENTER . . . , 1971.
- [220] W. S. Williams, “The thermal conductivity of metallic ceramics,” *JOM*, vol. 50, pp. 62–66, Jun 1998.
- [221] M. M. Opeka, I. G. Talmy, E. J. Wuchina, J. A. Zaykoski, and S. J. Causey, “Mechanical, thermal, and oxidation properties of refractory hafnium and zirconium compounds,” *Journal of the European Ceramic Society*, vol. 19, no. 13, pp. 2405 – 2414, 1999.
- [222] M. Farzaneh, K. Maize, D. Lüerßen, J. A. Summers, P. M. Mayer, P. E. Raad, K. P. Pipe, A. Shakouri, R. J. Ram, and J. A. Hudgings, “Ccd-based thermoreflectance microscopy: principles and applications,” *Journal of Physics D: Applied Physics*, vol. 42, no. 14, p. 143001, 2009.
- [223] B. Vermeersch, J.-H. Bahk, J. Christofferson, and A. Shakouri, “Thermoreflectance imaging of sub 100 ns pulsed cooling in high-speed thermoelectric microcoolers,” *Journal of Applied Physics*, vol. 113, p. 104502, 2018/02/21 2013.
- [224] A. Ziabari, P. Torres, B. Vermeersch, Y. Xuan, X. Cartoixà, A. Torelló, J.-H. Bahk, Y. R. Koh, M. Parsa, P. D. Ye, F. X. Alvarez, and A. Shakouri, “Full-field thermal imaging of quasiballistic crosstalk reduction in nanoscale devices,” *Nature Communications*, vol. 9, no. 1, p. 255, 2018.
- [225] J. Gild, Y. Zhang, T. Harrington, S. Jiang, T. Hu, M. C. Quinn, W. M. Mellor, N. Zhou, K. Vecchio, and J. Luo, “High-entropy metal diborides: A new class of high-entropy materials and a new type of ultrahigh temperature ceramics,” *Scientific Reports*, vol. 6, p. 37946, 2016.

- [226] J. J. Petrovic, “Mosi₂-based high-temperature structural silicides,” *MRS Bulletin*, vol. 18, no. 7, pp. 35–41, 1993.
- [227] B. Song, P. Feng, J. Wang, Y. Ge, G. Wu, X. Wang, and F. Akhtar, “Oxidation properties of self-propagating high temperature synthesized niobium disilicide,” *Corrosion Science*, vol. 85, pp. 311–317, 2014.
- [228] S. Raj, “A preliminary assessment of the properties of a chromium silicide alloy for aerospace applications,” *Materials Science and Engineering: A*, vol. 192, pp. 583–589, 1995.
- [229] J. Gild, J. Braun, K. Kaufmann, E. Marin, T. Harrington, P. Hopkins, K. Vecchio, and J. Luo, “A high-entropy silicide:(mo0. 2nb0. 2ta0. 2ti0. 2w0. 2) si2,” *arXiv preprint arXiv:1902.01033*, 2019.
- [230] M. Nakamura, S. Matsumoto, and T. Hirano, “Elastic constants of mosi₂ and wsi₂ single crystals,” *Journal of Materials Science*, vol. 25, no. 7, pp. 3309–3313, 1990.
- [231] H. Zhang, C. Hua, D. Ding, and A. J. Minnich, “Length dependent thermal conductivity measurements yield phonon mean free path spectra in nanostructures,” *Sci. Rep.*, vol. 5, pp. 9121 EP –, 03 2015.
- [232] J. L. Feldman, P. B. Allen, and S. R. Bickham, “Numerical study of low-frequency vibrations in amorphous silicon,” *Phys. Rev. B*, vol. 59, pp. 3551–3559, Feb 1999.
- [233] P. B. Allen and J. L. Feldman, “Thermal conductivity of disordered harmonic solids,” *Phys. Rev. B*, vol. 48, pp. 12581–12588, Nov 1993.
- [234] R. Sultan, A. D. Avery, J. M. Underwood, S. J. Mason, D. Bassett, and B. L. Zink, “Heat transport by long mean free path vibrations in amorphous silicon nitride near room temperature,” *Phys. Rev. B*, vol. 87, p. 214305, Jun 2013.
- [235] F. Yang and C. Dames, “Mean free path spectra as a tool to understand thermal conductivity in bulk and nanostructures,” *Phys. Rev. B*, vol. 87, p. 035437, Jan 2013.
- [236] G. T. Hohensee, R. B. Wilson, and D. G. Cahill, “Thermal conductance of metal–diamond interfaces at high pressure,” *Nat Commun*, vol. 6, p. 6578, 03 2015.
- [237] K. T. Regner, L. C. Wei, and J. A. Malen, “Interpretation of thermoreflectance measurements with a two-temperature model including non-surface heat deposition,” *Journal of Applied Physics*, vol. 118, no. 23, 2015.
- [238] Y. K. Koh, D. G. Cahill, and B. Sun, “Nonlocal theory for heat transport at high frequencies,” *Physical Review B*, vol. 90, pp. 205412–, 11 2014.
- [239] L. Wieczorek, H. Goldsmid, and G. Paul, “Thermal conductivity of amorphous films,” in *Thermal Conductivity 20*, pp. 235–241, Springer, 1989.
- [240] B. S. W. Kuo, J. C. M. Li, and A. W. Schmid, “Thermal conductivity and interface thermal resistance of si film on si substrate determined by photothermal displacement interferometry,” *Applied Physics A*, vol. 55, no. 3, pp. 289–296, 1992.
- [241] D. G. Cahill, M. Katiyar, and J. R. Abelson, “Thermal conductivity of a -si:h thin films,” *Phys. Rev. B*, vol. 50, pp. 6077–6081, Sep 1994.
- [242] H. Wada and T. Kamijoh, “Thermal conductivity of amorphous silicon,” *Japanese Journal of Applied Physics*, vol. 35, no. 5B, p. L648, 1996.
- [243] S. Moon, M. Hatano, M. Lee, and C. P. Grigoropoulos, “Thermal conductivity of amorphous silicon thin films,” *International Journal of Heat and Mass Transfer*, vol. 45, no. 12, pp. 2439 – 2447, 2002.
- [244] B. L. Zink, R. Pietri, and F. Hellman, “Thermal conductivity and specific heat of thin-film amorphous silicon,” *Phys. Rev. Lett.*, vol. 96, p. 055902, Feb 2006.

- [245] Y. He, D. Donadio, and G. Galli, "Heat transport in amorphous silicon: Interplay between morphology and disorder," *Applied Physics Letters*, vol. 98, no. 14, pp. –, 2011.
- [246] C. Thomsen, J. Strait, Z. Vardeny, H. J. Maris, J. Tauc, and J. J. Hauser, "Coherent phonon generation and detection by picosecond light pulses," *Phys. Rev. Lett.*, vol. 53, pp. 989–992, Sep 1984.
- [247] C. Thomsen, H. T. Grahn, H. J. Maris, and J. Tauc, "Surface generation and detection of phonons by picosecond light pulses," *Phys. Rev. B*, vol. 34, pp. 4129–4138, Sep 1986.
- [248] S.-M. Lee and D. G. Cahill, "Heat transport in thin dielectric films," *Journal of Applied Physics*, vol. 81, p. 2590, 1997.
- [249] T. Yamane, N. Nagai, S.-i. Katayama, and M. Todoki, "Measurement of thermal conductivity of silicon dioxide thin films using a 3 method," *Journal of Applied Physics*, vol. 91, no. 12, pp. 9772–9776, 2002.
- [250] A. J. H. McGaughey, E. S. Landry, D. P. Sellan, and C. H. Amon, "Size-dependent model for thin film and nanowire thermal conductivity," *Applied Physics Letters*, vol. 99, no. 13, pp. –, 2011.
- [251] J. Chen, M. Niu, J. Calvin, M. Asplund, S. W. King, B. F. Woodfield, and A. Navrotsky, "Thermodynamics of amorphous sin(o)h dielectric films synthesized by plasma-enhanced chemical vapor deposition," *Journal of the American Ceramic Society*, vol. 101, no. 5, pp. 2017–2027, 2018.
- [252] A. E. Kaloyeros, F. A. Jové, J. Goff, and B. Arkles, "silicon nitride and silicon nitride-rich thin film technologies: Trends in deposition techniques and related applications," *ECS Journal of Solid State Science and Technology*, vol. 6, no. 10, pp. P691–P714, 2017.
- [253] J.-F. Lelièvre, E. Fourmond, A. Kaminski, O. Palais, D. Ballutaud, and M. Lemiti, "Study of the composition of hydrogenated silicon nitride sinx:h for efficient surface and bulk passivation of silicon," *Solar Energy Materials and Solar Cells*, vol. 93, no. 8, pp. 1281 – 1289, 2009.
- [254] B. Swatowska and T. Stapiński, "Amorphous hydrogenated silicon-nitride films for applications in solar cells," *Vacuum*, vol. 82, no. 10, pp. 942 – 946, 2008. Proceedings of the 9th Electron Technology Conference ELTE 2007, Cracow, 4-7 September 2007.
- [255] J. Yoo, J. So, G. Yu, and J. Yi, "Study on hydrogenated silicon nitride for application of high efficiency crystalline silicon solar cells," *Solar Energy Materials and Solar Cells*, vol. 95, no. 1, pp. 7 – 10, 2011. 19th International Photovoltaic Science and Engineering Conference and Exhibition (PVSEC-19) Jeju, Korea, 9-13 November 2009.
- [256] F. Massines, J. Silva, J.-F. Lelièvre, R. Bazinette, J. Vallade, P. Lecouvreur, and S. Pouliquen, "Hydrogenated silicon nitride sinx:h deposited by dielectric barrier discharge for photovoltaics," *Plasma Processes and Polymers*, vol. 13, no. 1, pp. 170–183, 2016.
- [257] S. Duttagupta, F. Ma, B. Hoex, T. Mueller, and A. G. Aberle, "Optimised antireflection coatings using silicon nitride on textured silicon surfaces based on measurements and multidimensional modelling," *Energy Procedia*, vol. 15, pp. 78 – 83, 2012. International Conference on Materials for Advanced Technologies 2011, Symposium O.
- [258] J. Holt, D. Goodwin, A. Gabor, F. Jiang, M. Stavola, and H. A. Atwater, "Hot-wire chemical vapor deposition of high hydrogen content silicon nitride for solar cell passivation and anti-reflection coating applications," *Thin Solid Films*, vol. 430, no. 1, pp. 37 – 40, 2003. Proceedings of the Second International Conference on Cat-CVD (Hot Wire CVD) Process.
- [259] V. Verlaan, C. H. M. van der Werf, Z. S. Houweling, I. G. Romijn, A. W. Weeber, H. F. W. Dekkers, H. D. Goldbach, and R. E. I. Schropp, "Multi-crystalline si solar cells with very fast deposited (180nm/min) passivating hot-wire cvd silicon nitride as antireflection coating," *Progress in Photovoltaics: Research and Applications*, vol. 15, no. 7, pp. 563–573, 2007.

- [260] Y. Kuo, “Plasma enhanced chemical vapor deposited silicon nitride as a gate dielectric film for amorphous silicon thin film transistors—a critical review,” *Vacuum*, vol. 51, no. 4, pp. 741 – 745, 1998.
- [261] L. Wang, H. Qin, W. Zhang, L. Zhang, and D. Yan, “High reliability of vanadyl-phthalocyanine thin-film transistors using silicon nitride gate insulator,” *Thin Solid Films*, vol. 545, pp. 514 – 516, 2013.
- [262] J. Yota, “Effects of deposition method of pecvd silicon nitride as mim capacitor dielectric for gaas hbt technology,” *ECS Transactions*, vol. 35, no. 4, pp. 229–240, 2011.
- [263] F. de Brito Mota, J. F. Justo, and A. Fazzio, “Hydrogen role on the properties of amorphous silicon nitride,” *Journal of Applied Physics*, vol. 86, no. 4, pp. 1843–1847, 1999.
- [264] C. Boehme and G. Lucovsky, “H loss mechanism during anneal of silicon nitride: Chemical dissociation,” *Journal of Applied Physics*, vol. 88, no. 10, pp. 6055–6059, 2000.
- [265] J. L. Braun, S. W. King, A. Giri, J. T. Gaskins, M. Sato, T. Fujiseki, H. Fujiwara, and P. E. Hopkins, “Breaking network connectivity leads to ultralow thermal conductivities in fully dense amorphous solids,” *Applied Physics Letters*, vol. 109, no. 19, p. 191905, 2016.
- [266] C. H. Mastrangelo, Y.-C. Tai, and R. S. Muller, “Thermophysical properties of low-residual stress, silicon-rich, lpcvd silicon nitride films,” *Sensors and Actuators A: Physical*, vol. 23, no. 1, pp. 856 – 860, 1990. Proceedings of the 5th International Conference on Solid-State Sensors and Actuators and Eurosensors III.
- [267] A. J. Griffin, F. R. Brotzen, and P. J. Loos, “The effective transverse thermal conductivity of amorphous si₃n₄ thin films,” *Journal of Applied Physics*, vol. 76, no. 7, pp. 4007–4011, 1994.
- [268] B. Zink and F. Hellman, “Specific heat and thermal conductivity of low-stress amorphous si–n membranes,” *Solid State Communications*, vol. 129, no. 3, pp. 199 – 204, 2004.
- [269] A. Jain and K. E. Goodson, “Measurement of the thermal conductivity and heat capacity of freestanding shape memory thin films using the 3method,” *Journal of Heat Transfer*, vol. 130, pp. 102402–102402–7, 08 2008.
- [270] D. R. Queen and F. Hellman, “Thin film nanocalorimeter for heat capacity measurements of 30 nm films,” *Review of Scientific Instruments*, vol. 80, no. 6, p. 063901, 2009.
- [271] H. Ftouni, C. Blanc, D. Tainoff, A. D. Fefferman, M. Defoort, K. J. Lulla, J. Richard, E. Collin, and O. Bourgeois, “Thermal conductivity of silicon nitride membranes is not sensitive to stress,” *Phys. Rev. B*, vol. 92, p. 125439, Sep 2015.
- [272] A. Sikora, H. Ftouni, J. Richard, C. Hébert, D. Eon, F. Omnes, and O. Bourgeois, “Highly sensitive thermal conductivity measurements of suspended membranes (sin and diamond) using a 3-völklein method,” *Review of Scientific Instruments*, vol. 83, no. 5, p. 054902, 2012.
- [273] X. Zhang and C. P. Grigoropoulos, “Thermal conductivity and diffusivity of freestanding silicon nitride thin films,” *Review of Scientific Instruments*, vol. 66, no. 2, pp. 1115–1120, 1995.
- [274] B. Lee, J. S. Lee, S. U. Kim, K. Kim, O. Kwon, S. Lee, J. H. Kim, and D. S. Lim, “Simultaneous measurement of thermal conductivity and interface thermal conductance of diamond thin film,” *Journal of Vacuum Science & Technology B: Microelectronics and Nanometer Structures Processing, Measurement, and Phenomena*, vol. 27, no. 6, pp. 2408–2412, 2009.
- [275] N. Bodenschatz, A. Liemert, S. Schnurr, U. Wiedwald, and P. Zieman, “Extending the 3 method: Thermal conductivity characterization of thin films,” *Review of Scientific Instruments*, vol. 84, no. 8, p. 084904, 2013.
- [276] A. Irace and P. M. Sarro, “Measurement of thermal conductivity and diffusivity of single and multilayer membranes,” *Sensors and Actuators A: Physical*, vol. 76, no. 1, pp. 323 – 328, 1999.

- [277] S. Bai, Z. Tang, Z. Huang, and J. Yu, "Thermal characterization of Si₃N₄ thin films using transient thermoreflectance technique," *IEEE Transactions on Industrial Electronics*, vol. 56, pp. 3238–3243, Aug 2009.
- [278] N. Stojanovic, J. Yun, E. B. K. Washington, J. M. Berg, M. W. Holtz, and H. Temkin, "Thin-film thermal conductivity measurement using microelectrothermal test structures and finite-element-model-based data analysis," *Journal of Microelectromechanical Systems*, vol. 16, no. 5, pp. 1269–1275, 2007.
- [279] T. Coquil, E. K. Richman, N. J. Hutchinson, S. H. Tolbert, and L. Pilon, "Thermal conductivity of cubic and hexagonal mesoporous silica thin films," *Journal of Applied Physics*, vol. 106, no. 3, p. 034910, 2009.
- [280] M. Bogner, A. Hofer, G. Benstetter, H. Gruber, and R. Y. Fu, "Differential 3 method for measuring thermal conductivity of aln and si3n4 thin films," *Thin Solid Films*, vol. 591, pp. 267 – 270, 2015. Selected papers from 16th International Conference on Thin Films, October 13-16, 2014, Dubrovnik, Croatia.
- [281] S. Govorkov, W. Ruderman, M. W. Horn, R. B. Goodman, and M. Rothschild, "A new method for measuring thermal conductivity of thin films," *Review of Scientific Instruments*, vol. 68, no. 10, pp. 3828–3834, 1997.
- [282] S. V. Garimella, "Advances in mesoscale thermal management technologies for microelectronics," *Microelectronics Journal*, vol. 37, no. 11, pp. 1165 – 1185, 2006.
- [283] P. Eriksson, J. Y. Andersson, and G. Stemme, "Thermal characterization of surface-micromachined silicon nitride membranes for thermal infrared detectors," *Journal of Microelectromechanical Systems*, vol. 6, pp. 55–61, March 1997.
- [284] M. T. Alam, M. P. Manoharan, M. A. Haque, C. Muratore, and A. Voevodin, "Influence of strain on thermal conductivity of silicon nitride thin films," *Journal of Micromechanics and Microengineering*, vol. 22, no. 4, p. 045001, 2012.
- [285] R. Sultan, A. D. Avery, G. Stiehl, and B. L. Zink, "Thermal conductivity of micromachined low-stress silicon-nitride beams from 77 to 325 k," *Journal of Applied Physics*, vol. 105, no. 4, p. 043501, 2009.
- [286] J. L. Braun, C. M. Rost, M. Lim, A. Giri, D. H. Olson, G. N. Kotsonis, G. Stan, D. W. Brenner, J.-P. Maria, and P. E. Hopkins, "Charge-induced disorder controls the thermal conductivity of entropy-stabilized oxides," *Advanced Materials*, vol. 30, no. 51, p. 1805004, 2018.
- [287] R. Bousbih, W. Dimassi, I. Haddadi, and H. Ezzaouia, "The effect of thermal annealing on the properties of pecvd hydrogenated silicon nitride," *physica status solidi (c)*, vol. 9, no. 10-11, pp. 2189–2193, 2012.
- [288] S. P. Singh, P. Srivastava, S. Ghosh, S. A. Khan, and G. V. Prakash, "Phase stabilization by rapid thermal annealing in amorphous hydrogenated silicon nitride film," *Journal of Physics: Condensed Matter*, vol. 21, p. 095010, feb 2009.
- [289] M. G. Ghossoub, J.-H. Lee, O. T. Baris, D. G. Cahill, and S. Sinha, "Percolation of thermal conductivity in amorphous fluorocarbons," *Physical Review B*, vol. 82, pp. 195441–, 11 2010.
- [290] D. V. Tsu, G. Lucovsky, and M. J. Mantini, "Local atomic structure in thin films of silicon nitride and silicon diimide produced by remote plasma-enhanced chemical-vapor deposition," *Phys. Rev. B*, vol. 33, pp. 7069–7076, May 1986.
- [291] M. Maeda and H. Nakamura, "Hydrogen bonding configurations in silicon nitride films prepared by plasmaenhanced deposition," *Journal of Applied Physics*, vol. 58, no. 1, pp. 484–489, 1985.
- [292] R. FESSENDEN, "The infrared spectra of some silazanes and disilazanes1," *The Journal of Organic Chemistry*, vol. 25, no. 12, pp. 2191–2193, 1960.
- [293] M. H. Brodsky, M. Cardona, and J. J. Cuomo, "Infrared and raman spectra of the silicon-hydrogen bonds in amorphous silicon prepared by glow discharge and sputtering," *Phys. Rev. B*, vol. 16, pp. 3556–3571, Oct 1977.

- [294] Z. Yin and F. W. Smith, “Free-energy model for bonding in amorphous covalent alloys,” *Phys. Rev. B*, vol. 43, pp. 4507–4510, Feb 1991.
- [295] J. Bruyère, B. Reynes, C. Savall, and C. Roch, “Annealing of silicon nitride thin films prepared by plasma-enhanced chemical vapor deposition with helium dilution,” *Thin Solid Films*, vol. 221, no. 1, pp. 65 – 71, 1992.
- [296] J. L. Braun, D. H. Olson, J. T. Gaskins, and P. E. Hopkins, “A steady-state thermoreflectance method to measure thermal conductivity,” *Review of Scientific Instruments*, vol. 90, no. 2, p. 024905, 2019.
- [297] A. Giri, J. L. Braun, D. M. Shima, S. Addamane, G. Balakrishnan, and P. E. Hopkins, “Experimental evidence of suppression of subterahertz phonons and thermal conductivity in gaas/als superlattices due to extrinsic scattering processes,” *The Journal of Physical Chemistry C*, vol. 122, no. 51, pp. 29577–29585, 2018.
- [298] E. L. Radue, J. A. Tomko, A. Giri, J. L. Braun, X. Zhou, O. V. Prezhdo, E. L. Runnerstrom, J.-P. Maria, and P. E. Hopkins, “Hot electron thermoreflectance coefficient of gold during electron–phonon nonequilibrium,” *ACS Photonics*, vol. 5, no. 12, pp. 4880–4887, 2018.
- [299] A. Giri, S. W. King, W. A. Lanford, A. B. Mei, D. Merrill, L. Li, R. Oviedo, J. Richards, D. H. Olson, J. L. Braun, J. T. Gaskins, F. Deangelis, A. Henry, and P. E. Hopkins, “Interfacial defect vibrations enhance thermal transport in amorphous multilayers with ultrahigh thermal boundary conductance,” *Advanced Materials*, vol. 30, no. 44, p. 1804097, 2018.
- [300] S. Alaie, M. G. Baboly, Y.-B. Jiang, S. Rempe, D. H. Anjum, S. Chaieb, B. F. Donovan, A. Giri, C. J. Szwejkowski, J. T. Gaskins, M. M. M. Elahi, D. F. Goettler, J. Braun, P. E. Hopkins, and Z. C. Leseman, “Reduction and increase in thermal conductivity of si irradiated with ga+ via focused ion beam,” *ACS Applied Materials & Interfaces*, vol. 10, no. 43, pp. 37679–37684, 2018. PMID: 30280889.
- [301] D. H. Olson, C. M. Rost, J. T. Gaskins, C. J. Szwejkowski, J. L. Braun, and P. E. Hopkins, “Size effects on the cross-plane thermal conductivity of transparent conducting indium tin oxide and fluorine tin oxide thin films,” *IEEE Transactions on Components, Packaging and Manufacturing Technology*, vol. 9, pp. 51–57, Jan 2019.
- [302] J. A. Tomko, D. H. Olson, J. L. Braun, A. P. Kelliher, B. Kaehr, and P. E. Hopkins, “Substrate thermal conductivity controls the ability to manufacture microstructures via laser-induced direct write,” *Applied Physics Letters*, vol. 112, p. 051906, 2018/04/25 2018.
- [303] A. Giri, J. L. Braun, and P. E. Hopkins, “Reduced dependence of thermal conductivity on temperature and pressure of multi-atom component crystalline solid solutions,” *Journal of Applied Physics*, vol. 123, p. 015106, 2018/01/17 2018.
- [304] A. Giri, J. L. Braun, J. A. Tomko, and P. E. Hopkins, “Reducing the thermal conductivity of chemically ordered binary alloys below the alloy limit via the alteration of phonon dispersion relations,” *Applied Physics Letters*, vol. 110, p. 233112, 2018/04/25 2017.
- [305] B. F. Donovan, J. A. Tomko, A. Giri, D. H. Olson, J. L. Braun, J. T. Gaskins, and P. E. Hopkins, “Localized thin film damage sourced and monitored via pump-probe modulated thermoreflectance,” *Review of Scientific Instruments*, vol. 88, p. 054903, 2018/04/25 2017.
- [306] A. Giri, J. L. Braun, and P. E. Hopkins, “Implications of interfacial bond strength on the spectral contributions to thermal boundary conductance across solid, liquid, and gas interfaces: A molecular dynamics study,” *The Journal of Physical Chemistry C*, vol. 120, pp. 24847–24856, 11 2016.
- [307] A. Giri, J. L. Braun, and P. E. Hopkins, “Effect of crystalline/amorphous interfaces on thermal transport across confined thin films and superlattices,” *Journal of Applied Physics*, vol. 119, no. 23, p. 235305, 2016.